Fracking magma: A field and experimental investigation of hydrofracturing in volcanic systems

Holly E. Unwin

Lancaster Environment Centre and

British Geological Survey

This thesis is submitted in partial fulfilment of the requirement for the award of the
degree of Doctor of Philosophy

February 2023

Abstract

Rhyolite eruptions typically begin with the explosive ejection of pyroclastic material, with the potential to form widespread ash plumes that can have worldwide impacts. These eruptions then transition to effusive activity, characterised by the gentler emission of lava. Due to the scarcity of rhyolite eruptions, the processes that control the dynamics of these eruptions are poorly understood, despite the potentially significant hazards. Tuffisites — pyroclast-filled fractures that form within and adjacent to silicic volcanic vents at different stages of an eruption — are thought to provide insights into the processes that control the formation and evolution of silicic volcanic vents, and therefore influence the dynamics of a resulting eruption. Tuffisites are more permeable than the surrounding country rock, leading to suggestions that tuffisites may be able to allow significant volumes of gas to escape the conduit, potentially reducing sufficient excess pressure to moderate the explosivity of an eruption and change its hazards.

This thesis aims to uncover new details about the formation of tuffisites and constrain whether tuffisite-enabled outgassing might be significant on the timescale of an eruption (Animation 1, Appendix A.1). By extrapolating this knowledge of tuffisite formation to the evolution of silicic vents, this thesis then aims to use tuffisites to gain insights into the processes that control eruption dynamics. This work finds that tuffisites form throughout the evolution of silicic vents, above the level of fragmentation in the conduit. Tuffisites can form by the injection of multiple pulses of pyroclastic material into a fracture, and therefore can be interpreted as records of fluctuations of the fluid pressure within the volcanic conduit during an eruption. By combining particle-size distributions with porosity and permeability measurements, this thesis finds that the opening of the fractures that host tuffisites can allow for the pulsed escape of large volumes of gas from the volcanic conduit, potentially influencing the dynamics of an eruption.

Contents

3

7

List of Figures

List of Tables

Acknowledgements

Thank you to my wonderful team of supervisors, Hugh, Fabian, Emrys, Mike, and Rob, for giving me the confidence to follow my ideas and chase my dreams. You have all inspired and pushed me to be the best scientist that I can, even through the challenges of a global pandemic. Thank you all for sharing your knowledge and time with me so generously, and for many, many hours of discussion, without which this thesis would not have been possible.

This thesis also would not have been possible without a wider group of collaborators and friends who have supported me throughout my PhD. Particular thanks go to Mike H and Annabelle for stepping in to help keep this thesis on track when my data collection plans were cancelled by lockdowns, even though your own time was short. I have been lucky to be surrounded by an incredible group of friends in Lancaster and beyond who have encouraged me throughout my PhD journey — thank you for all the late night discussions and adventures.

Thank you to my parents for always encouraging me to follow my dreams and inspiring me to work hard. Thank you, and also Anne and Richard, for welcoming lost PhD students into your home during a pandemic and providing all the tea, biscuits, cake, and walks needed for ideas to turn into a thesis. Finally, thank you Adrian for all your support, without which this thesis would not have been possible. Thank you reminding me to leave my laptop from time to time and for all your help finishing this thesis on the other side of the world.

Declaration

I declare that, other than where the contribution of others is specified, this thesis is entirely my own work and has not been submitted for the award of a degree at this or any other university.

This thesis is 56,252 words in length excluding the Abstract, contents pages, references, and Appendix, and is therefore within the required word limit.

Holly E. Unwin

Multi-author declaration

Please find below a list of publications included in this thesis with information regarding my contributions to each of the publications.

Chapter 3

Pressure-Driven Opening and Filling of a Volcanic Hydrofracture Recorded by Tuffisite at Húsafell, Iceland: A Potential Seismic Source

Holly E. Unwin, Hugh Tuffen, Emrys R. Phillips, Fabian B. Wadsworth, Mike R. James

Published in Frontiers in Earth Sciences, 2021, Vol.9
https://doi.org/10.3389/feart.2021.668058

HEU designed the study with assistance from all co-authors. HEU, HT and FBW carried out fieldwork in Iceland. HEU analysed samples collected with assistance from ERP and HT and devised the formation model with assistance from HT, FBW and MRJ. HEU wrote the manuscript with revisions following comments by all co-authors.

Chapter 4

The exposed Mule Creek vent deposits record the structure of a volcanic conduit during a hybrid explosive-effusive eruption

Holly E. Unwin, Hugh Tuffen, Fabian B. Wadsworth, Emrys R. Phillips, Mike R. James, Annabelle Foster, Stephan Kolzenburg, Jonathan M. Castro, Lucy A. Porritt

Published in Bulletin of Volcanology, 2023. 85(28).
https://doi.org/10.1007/s00445-023-01638-z

HEU designed the study with assistance from HT, ERP and MRJ. HT, SK, JMC and LAP carried out fieldwork at Mule Creek and collected samples that were analysed by HEU with assistance from FBW, ERP and AF. HEU devised the vent formation model

with assistance from FBW, HT, MRJ and AF. HEU wrote the manuscript with revisions following comments by all co-authors.

Chapter 5

Do tuffisites make good outgassing pathways?

Holly. E. Unwin, Fabian B. Wadsworth, Hugh Tuffen, Michael J. Heap, Adrian White, Annabelle Foster, Mike R. James, Emrys R. Phillips

In preparation for submission for publication in Earth and Planetary Science Letters

HEU designed the study with assistance from FBW and HT. Fieldwork to collect samples was completed by HEU, HT, FBW and AW. HEU collected and analysed the grain-size data with assistance from FBW, AW, AF, MRJ and ERP. MJH measured porosity and permeability of samples (originally planned to be measured by HEU and MJH but not possible due to Covid-19). HEU wrote the manuscript with revisions following comments by all co-authors.

The co-authors of these publications have signed below to confirm this.

Yours sincerely

Holly E. Unwin

Coauthors: Hugh Tuffen, Fabian B. Wadsworth, Emrys R. Phillips, M. R. James, M. J. Heap, White, A., Foster, A., Castro, J. M., Kolzenberg, S., Porritt, L. A.

1   Introduction

Explosive volcanic eruptions are one of the most dangerous phenomena on Earth, with the formation of large plumes potentially impacting wide areas. The scarcity of these events, however, means that the processes that control the evolution of these eruptions are poorly understood. Improving our understanding of these processes is key for improving our understanding of rhyolite eruption dynamics and therefore better forecasting of associated volcanic hazards.

The aim of this thesis is to explore the processes occurring during the evolution of silicic conduits. This exploration is centred around the formation of tuffisites — pyroclast-filled fractures that form within and adjacent to volcanic vents. Tuffisites have been suggested to be miniature conduits, with many processes occurring during tuffisite formation also occurring during the formation of silicic conduits, albeit over larger spatial scales (Schipper et al., 2021). By gaining new insights into the processes controlling tuffisite formation, this thesis aims to extrapolate these processes to the conduit to learn more about the controls of the dynamics of silicic eruptions. This is achieved through three subsidiary aims:

1. Reconstruct the evolution of fluid pressure during the lifetime of an external tuffisite, from fracture initiation to the formation of a sintered tuffisite fill.

2. Constrain the controls on the morphology of tuffisites that form during the evolution of silicic volcanic vents, and extrapolate these to silicic vents to learn more about the processes controlling vent evolution.

3. Characterise the timescales of external tuffisite formation and the evolution of tuffisite porosity and permeability to appraise whether tuffisites can act as pathways for significant outgassing from the conduit zone.

1.1 Outline of work

This thesis consists of seven chapters. Chapter 1 outlines the aims and structure of this thesis. Chapter 2 provides an overview of the literature on the evolution of silicic vents, highlighting the potential importance of tuffisites and how these might provide insights into the processes that control eruption dynamics. This chapter also summarises the literature on tuffisites and their formation, as well as providing an overview of our understanding of particle-filled fractures found in other environments and how this might help us to further understand tuffisite formation.

After this review, three data chapters are presented that provide insights into the processes of tuffisite formation, their relationship to the surrounding silicic volcanic vent, and the role that tuffisites might play during vent evolution.

Chapter 3 examines the morphology and internal structure of a large tuffisite at the dissected Húsafell central volcano, west Iceland, which provides an insight into the processes controlling the deposition of pyroclasts within fractures. This work demonstrates that the tuffisite was emplaced by the injection of several pulses of gas-pyroclast mixtures into the fracture to produce multiple sediment units with complex structures and erosive contacts. This pulsed injection is interpreted to reflect fluid pressure changes occurring in the unsteady volcanic conduit during, or in the lead up to, a volcanic eruption. By considering the dimensions of the sediment units emplaced (0.1 m thick and 40 m in length) we find that 1.9–3.3 MPa overpressure would be required to emplace each sediment unit, similar to the overpressure expected just above the level of fragmentation in the conduit, suggesting that tuffisite formation should be a common process.

Chapter 4 explores the characteristics of the different units that form the dissected silicic Mule Creek vent in New Mexico, USA, and considers the relationships of these units with their intersecting tuffisites. This work found that tuffisites are present in every unit of the Mule Creek vent, suggesting that tuffisite formation occurred throughout vent evolution. By comparing the structure of the vent with the tuffisites that intersect it, this chapter explores the similarities and differences between vent and tuffisite evolution, providing new interpretations of the glassy units at the vent margins and the units that intersect

the vent. The chapter presents a model for vent evolution that provides mechanisms for tuffisite formation in each vent unit and considers how the formation of each unit and its tuffisites reflects the processes occurring during different stages of vent evolution.

Chapter 5 expands on the observations and interpretations of the large tuffisite at Húsafell volcano in Chapter 3 to consider whether external tuffisites may act as important outgassing pathways to reduce excess pressure within the volcanic conduit. This chapter combines porosity and permeability data, particle-size distributions, and sintering timescales to determine the potential flux of gas through the tuffisite and how this might have varied during tuffisite evolution. This chapter finds that outgassing through the pore space of external tuffisites, previously considered to be an important outgassing pathway, only permits the escape of a small gas flux. Even when large timescales of outgassing through the pore space are considered, this gas flux is not significant compared to the gas flux that can flow through the fracture as it opens, before it becomes clogged with pyroclasts. Fractures adjacent to the conduit could act as efficient pathways for pulsed outgassing, perhaps allowing a significant flux of gas to escape compared to the vertical gas flux through the conduit during explosive activity.

Chapter 6 provides an integrating discussion on the findings from the individual chapters. This chapter considers the influence of overpressure on the morphology of hydrofractures and constraints on the timescales of fracture formation, as well as considering the role that tuffisites might play in the evolution of silicic vents and potential mechanisms for the formation of internal tuffisites. This chapter also highlights potential avenues for future work that might help improve our understanding of silicic vent formation and the importance of tuffisites.

Chapter 7 then concludes the thesis with a summary of the key findings.

2 Literature review

2.1 Introduction

Magma ascent typically drives the upwards propagation of fractures towards the Earth's surface, opened by high pressure gas-ash mixtures, through which magma and exsolved gases can be transported. If these fractures can continue to propagate until they intersect the surface, they can feed a volcanic eruption. Silicic volcanic eruptions (with magma $<63\%$ SiO_2) generally begin with highly explosive activity (Cassidy et al., 2018). This activity often initiates along fissures, with the explosive ejection of gas and pyroclasts that then quickly localises to activity through single vents (Lara, 2009; McGowan, 2016). Eruptions then transition to effusive activity, involving the relatively gentle eruption of lava. The single vents produced may then be reused as pathways for the ejection of material in later eruptions. Gas pressure within the conduit affects the explosivity of an eruption, and the explosive-effusive transition is thought to represent a shift from closed-system degassing — promoting the rapid ascent of magma and fragmentation — to open-system degassing that allows for gas to escape (Eichelberger et al., 1986; Jaupart and Allègre, 1991).

Explosive volcanic eruptions are one of the most hazardous phenomena on Earth, with the potential to impact wide areas. Increasing our understanding of the processes leading up to, and during, an eruption is crucial for improving the modelling of eruption dynamics and hazard prediction. Recent direct observations of silicic volcanic eruptions at Volcán Chaitén (2008–2009; Castro and Dingwell, 2009) and Cordón Caulle (2011–2012; Schipper et al., 2013) have found that eruptions can show hybrid explosive-effusive activity. Here, the effusion of silicic lava was interrupted by intermittent explosions that ejected explosive material through elongate fractures within the lava filling the vent, occurring simultaneously with lava extrusion (Figure 2.1). These observations have challenged our understanding of silicic eruptions, struggling to account for this hybrid activity.

The hazards and relative rarity of silicic volcanic eruptions, compared to more mafic
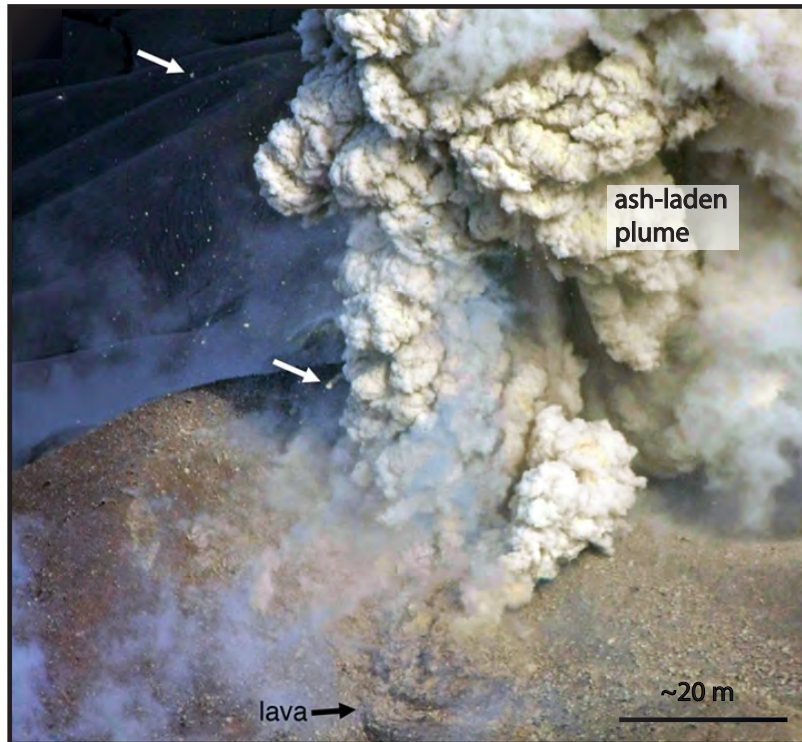
Figure 2.1: Hybrid explosive-effusive activity during the 2011–2012 eruption of Cordón Caulle, Chile, showing the simultaneous ejection of an ash-laden plume and bombs (white arrows) with the effusive on lava. Modified from Castro et al. (2014) and Wadsworth et al. (2022).

systems, make direct observations of eruptive activity both difficult and dangerous to obtain. Our understanding of the processes occurring during silicic volcanic eruptions has been developed by relating the characteristics of preserved silicic vents and ejected pyroclasts to these direct observations of eruptions and their seismic activity. Here, I outline our current knowledge of silicic volcanic eruptions and how they involve through time, highlighting some of the processes of which we only have limited knowledge. I then focus on the formation of tuffisites — particle-filled fractures found within or adjacent to a volcanic conduit, formed by the injection of ash and gas — and discuss how these features, alongside particle-filled fractures in other environments, may help us to discover more about some of the processes occurring during the evolution of silicic systems.

2.2 Preserved silicic vents

Vents are the uppermost part of the conduit system, where at shallow depths ($<$300 m) the conduit flares as it nears the surface. Preserved silicic vents record the structures present in the waning stages of a volcanic eruption, after the explosive-effusive transition, with the centre of the vent clogged with coherent lava. Well-preserved dissected silicic vents, either exposed by erosion or intersected by boreholes (Heiken et al., 1988; Stasiuk et al., 1996; Goto et al., 2008), are rare, but where present these can provide important insights into the processes occurring during an eruption. Different rock units within the vent record different stages of its evolution, and pyroclasts ejected during explosive and transitional activity can also provide a snapshot of processes occurring at an earlier stage of vent evolution (Castro et al., 2014; Saubin et al., 2016; Isgett et al., 2017; Paisley et al., 2019a; Colombier et al., 2020; Schipper et al., 2021).

Silicic volcanic eruptions have been seen to begin with explosive activity along a fissure that has quickly localised to form individual vents (Lara, 2009), matched by observations at older dissected volcanic systems where many lava plugs are preserved in lines, each indicating the location of a former vent (Saemundsson and Noll, 1974; McGowan, 2016). Where vents are dissected, they are seen to have quarried space into the surrounding country rock to produce a characteristic flared shape, into which a pyroclastic breccia unit, vitrophyre or obsidian unit, and lava plug are emplaced in turn (Stasiuk et al., 1996).

The outermost unit of a vent is typically a massive, matrix supported pyroclastic breccia, formed of clasts of the country rock and broken fragments of juvenile material such as lava fragments and pumice clasts (Figure 2.2; Stasiuk et al., 1996). These clasts, $<$2 m across, are found in a matrix of much finer lithic and juvenile clasts ($<$1 cm across; Stasiuk et al., 1996; Goto et al., 2008). This material, and the country rock beyond, can be dissected by tuffisites (particle-filled fractures) that can extend $<$120 m outwards from the vent margin (Heiken et al., 1988; Stasiuk et al., 1996; Goto et al., 2008). Bombs ejected from the volcanic vent can give insight into the structure of the vent during its evolution. The bombs ejected from the vent at Cordón Caulle are often seen to be

composite, formed of welded clasts ranging from vesicular pumice to dense obsidian, as well as containing some rare lithic clasts (Schipper et al., 2021; Wadsworth et al., 2022; Trafton and Giachetti, 2022).

The pyroclastic breccia unit is bordered on the inside by a vitrophyre or obsidian breccia (depending on the degree of post-emplacement hydration), with a gradational boundary between the two units (Figure 2.2). This vitrophyre or obsidian breccia unit is formed of angular glassy clasts that become increasingly elongate and sheared towards the centre of the vent, as well as a few rare lithic clasts (Stasiuk et al., 1996; Furukawa et al., 2021). This breccia can be intersected by an angular network of tuffisites (Tuffen and Dingwell, 2005; Cabrera et al., 2015). The vitrophyre or obsidian breccia then transitions into a coherent vitrophyre or obsidian unit towards the vent centre. Fractures within the vitrophyre or obsidian may be healed back together, leaving only faintly preserved traces of fracturing and healing in the deformation of flow banding (Tuffen et al., 2003; Cabrera et al., 2015; Furukawa et al., 2021). Obsidian pyroclasts ejected from vents, interpreted to be sourced from this vent-lining obsidian unit, have been seen to contain highly distorted vesicles with multi-cuspate morphologies (Gardner et al., 2017, 2019; Wadsworth et al., 2022). Some pyroclasts also contain domains displaying different vesicle textures, separated by boundaries containing xenocrystic material (Gardner et al., 2017).

The vitrophyre grades into the central vent-filling lava unit, which is typically flow banded with flow bands increasing in thickness and becoming more folded and contorted in shape towards the vent centre (Stasiuk et al., 1996). This unit can contain tuffisites, which here are elongate fractures often aligned with flow banding that contain clasts of lava and crystal fragments (Kendrick et al., 2016). As seen in the Cordón Caulle (2011–12) vent, fracture surfaces within the vent-filling lava may be coated by accreted, variably welded particles of ultra-fine ash (Farquharson et al., 2022). Vesicles in the lava towards the vent centre are less sheared than those at the margins (Figure 2.2; Stasiuk et al., 1996; Furukawa et al., 2021). Where flow bands are thickest close to the vent centre, there can be porous bands ~1 cm thick containing subrounded vesicles, alternating with bands of denser material (Stasiuk et al., 1996).
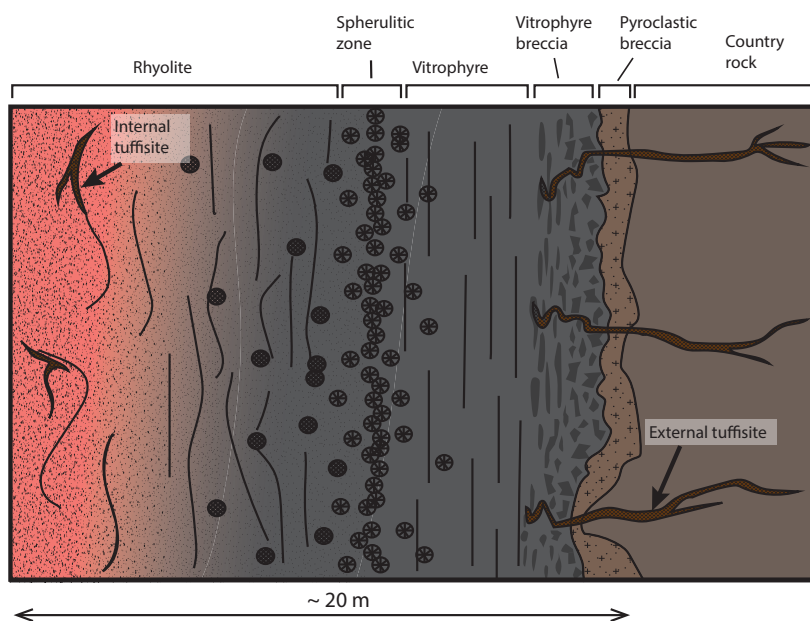
Figure 2.2: Cross-section of the Mule Creek vent showing the typical structure of a silicic vent. The vent quarries space in the country rock, inside of which the vent units are emplaced. The outermost unit of the vent is a pyroclastic breccia, which is bordered on the inside by a vitrophyre or obsidian breccia formed of glassy angular clasts. These angular clasts become gradually more sheared towards the vent centre until a coherent vitrophyre or obsidian unit is formed. At the centre of the vent is a rhyolite lava unit that is more strongly flow banded at its margins than at the vent centre. Nearly all of these units are cross-cut by tuffisites, which are particle-filled fractures found either within or adjacent to the volcanic vent. Redrawn from Stasiuk et al. (1996).

2.2.1 Models for vent evolution

The structure of preserved silicic vents records the processes occurring within the vent
at different stages of its formation, allowing for the creation of models for vent evolution.
The first stage of vent evolution involves the opening of fractures in the country rock by
high pressure gas-ash mixtures (McGowan, 2016). These fractures propagate towards
the surface, providing pathways for the ascent of magma and exsolved gases. This initial
stage of vent formation is highly explosive, quarrying space for the vent within the
surrounding country rock and then ejecting pyroclastic material at the surface (Figure
2.3). Any material that is not able to be ejected will be trapped within the evolving
vent to form the pyroclastic breccia unit (Stasiuk et al., 1996). Continued mixing
and overturning of this pyroclastic breccia could explain an observed lack of internal
structure (Campbell et al., 2013; Kolzenburg and Russell, 2014; Bélanger and Ross, 2018;
Valentine and Cole, 2021). The quarrying of the surrounding country rock is recorded
in the initially high lithic content of the vent-filling pyroclastic breccia, including clasts
broken away from the vent walls (Stasiuk et al., 1996). Welding of the hot clasts of
this pyroclastic breccia could produce a more coherent material able to be fractured
and ejected from the vent, forming composite bombs (Kolzenburg and Russell, 2014;
Schipper et al., 2021; Wadsworth et al., 2022).
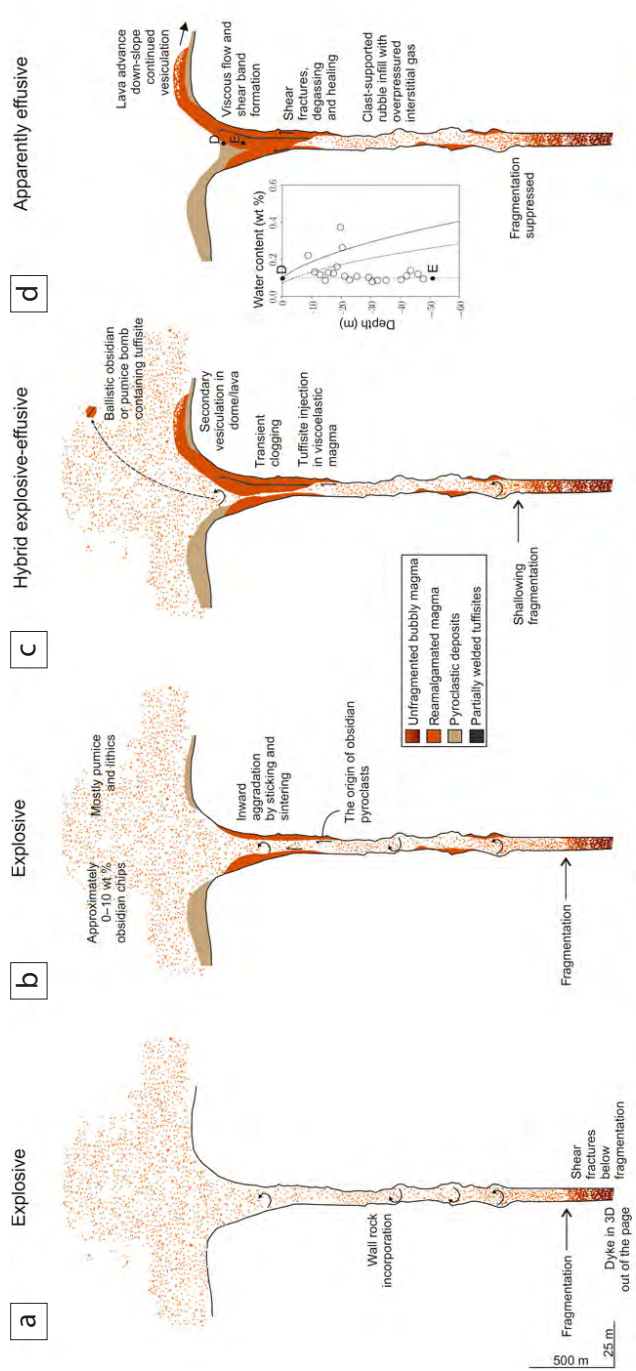
Figure 2.3: A proposed model for the evolution of eruptions at silicic volcanic vents that can provide a mechanism for hybrid explosive effusive activity (a–d; Wadsworth et al., 2020). a) Explosive activity at the start of an eruption ejects fragmented material from the vent. The flow incorporates clasts from the conduit walls that can also be ejected. b) Clasts that remain trapped within the vent accumulate to form pyroclastic breccia. The aggregation of particles on to the conduit walls by sticking and sintering can form re-amalgamated magma that is the origin of vitrophyre or obsidian at conduit margins, as well as vent-filling lava. c): The re-amalgamated magma in the vent can be extruded at the surface to form intact lava (effusive activity), at the same time as material is explosively ejected due to continued fragmentation at depth. This provides a mechanism for hybrid explosive-effusive activity. Fracturing of the accreting material will create obsidian or pumice bombs that can be ejected from the vent, as well as the formation of internal tuffisites. d): The accretion of material in the shallow conduit continues until the whole vent is filled with lava of a clastic origin. This can produce apparently effusive activity at the surface when this lava is extruded while explosive material continues at depth. Reproduced from Wadsworth et al. (2020).

28

The brecciated and coherent vitrophyre or obsidian units form after the emplacement of pyroclastic breccia. These units have been interpreted as part of the lava or as a continuation of clastic material welding together within the vent. If emplaced as a lava, the vitrophyre breccia and vitrophyre units are suggested to have been extruded upwards through the vent, with shearing at the outermost margins causing brecciation and the development of flow banding (Stasiuk et al., 1996). Recognition of distorted vesicles and different domains within obsidian has led to the suggestion that this material originally has a clastic origin, forming by the accretion and welding of ash-sized particles on to the vent walls (Gardner et al., 2017; Wadsworth et al., 2020, 2022; Schipper et al., 2021; Trafton and Giachetti, 2022). Similar textures have been seen in the glassy margins of silicic dykes, interpreted as containing preserved clastic textures (McGowan, 2016; Schmiedel et al., 2021). Two models have been proposed for the emplacement of the final vent-filling lava: the ascent of intact magma from depth that can be extruded upwards through the vent (Schipper et al., 2021) after the explosive-effusive transition had taken place, or the in-situ accretion and welding of pyroclasts to form intact magma in the shallow subsurface (Wadsworth et al., 2020). Both of these models would allow for apparent effusive activity at the surface while fragmentation continued at depth, providing a source of clastic material that could be ejected through the vent-filling lava during periods of hybrid explosive-effusive activity (Wadsworth et al., 2020, 2022; Schipper et al., 2021). However, the second model — assembling magma by the in-situ accretion and welding of pyroclasts — can also account for the preserved clastic textures found within obsidian and lava, suggesting that the vent-filling lava has a clastic origin, rather than being emplaced by the ascent of intact magma from depth (Wadsworth et al., 2020, 2022).

2.2.2 Mechanisms for gas escape

Gas overpressure, created by the exsolution of dissolved volatiles from magma, can help to drive the magma ascent, leading to explosive activity at the surface. The transition from explosive to effusive activity during an eruption is poorly understood, and further complicated by observations of hybrid explosive-effusive activity (Schipper et al., 2013).

The explosive-effusive transition has been suggested to be triggered by a transition from closed-system degassing — acting to drive rapid magma ascent and fragmentation — to open-system degassing, allowing gas to escape from magma and reducing the overpressure (e.g. Eichelberger et al., 1986). This change in degassing style has been suggested to occur by one or more of three mechanisms: (1) the formation of a permeable magma foam with bubble-hosted interconnected gas-escape pathways (Figure 2.4a), (2) the formation of connected high-density fracture networks (Figure 2.4b), or (3) wholesale magma fragmentation to pyroclasts (Figure 2.4c). In the first of these models, the coalescence of bubbles in magma forms a permeable foam through which gas escapes; in turn, gas escape leads to foam collapse forming a dense and degassed lava (Eichelberger et al., 1986). Textural evidence for collapsed bubbles is preserved in rhyolitic lavas and pyroclastic deposits as microlite traces (Kano et al., 1997; Tuffen and Castro, 2009), but a collapsing foam is not thought to be able to remove all the porosity from a magma to produce a dense lava, even with shearing (Wadsworth et al., 2020). The second model suggests that gas escape occurs along permeable magma-hosted fracture networks created by high shear stresses, especially close to the conduit walls (Gonnermann and Manga, 2003; Rust et al., 2004; Castro et al., 2012, 2014; Cabrera et al., 2015). Fractures could then seal and heal to produce a dense degassed lava, evidenced by healed fractures (Tuffen and Dingwell, 2005) and tuffisites (Tuffen and Dingwell, 2005; Goto et al., 2008; Cabrera et al., 2015). However, the fractures observed within preserved silicic vents are not sufficiently closely spaced to allow for the required amount of degassing to occur (Castro et al., 2014), without the fractured magma being highly vesicular. Finally, the third model suggests that magma fragments wholesale, and thus allowing thorough outgassing, but that those fragments (pyroclasts) then all sinter back together again, forming degassed and low-porosity lava in the shallow conduit (Wadsworth et al., 2020, 2022). All three of these models would leave a textural and structural record in deposit characteristics that can be tested against exposed shallow conduit observations.

Open-system outgassing may occur vertically or laterally, with lateral outgassing allowing gas to escape from the magma and flow through permeable conduit margins. Mechanisms for lateral outgassing include flow through permeable host rock (Rust et al., 2004; Lavallée et al., 2013; Farquharson et al., 2015), permeable tephra-lined conduit margins
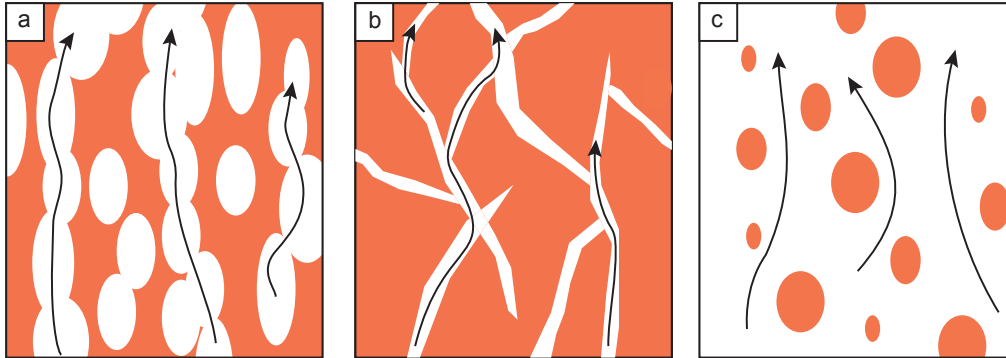
Figure 2.4: Mechanisms for the degassing of magma within volcanic vents. a) Degassing through a permeable magma foam with gas escape pathways formed by interconnected networks of coalesced bubbles (Eichelberger et al., 1986). b) Degassing through a high-density network of fractures intersecting the magma, created by high shear stresses close to the conduit walls (Gonnermann and Manga, 2003; Rust et al., 2004). c) Wholesale fragmentation of magma to pyroclasts allowing degassing by the separation of gas from the solid and liquid phases (Wadsworth et al., 2020, 2022).

(Eichelberger et al., 1986) or permeable particle filled fractures — external tuffisites — created by the injection of ash-gas mixtures into fractures within the conduit walls (Heiken et al., 1988). By contrast, open-system vertical outgassing requires either long-range magma permeability, such as a high porosity magma foam with vertical interconnection of pores, or long-range fractures — such as tuffisites.

2.2.3 Tuffisites — a definition

Tuffisites were first described by Cloos (1941) as fractures, found in basaltic diatremes, created by prying open the host rock. These fractures are filled with fine grained tuff and lithic fragments. In the literature most of the uses of the term relate to tuffisites in diatremes, where authors have found veins filled with tuff, often with unusual mineral assemblages, thought to be emplaced by the injection of gas or water and particles into fractures in the country rock (Reynolds, 1952; Garfunkel and Katz, 1967; Deshpande et al., 1971; Stoppa and Lupini, 1993; Stoppa et al., 2003; Mortimer et al., 2013). Mineral-bearing fracture-hosted breccias associated with hydrothermal systems have also been termed tuffisites, thought to be emplaced by late-stage hydrothermal activity (Williams et al., 2000), as have peperite-type veins that formed due to the interaction between magma and wet sediment (Walker and Francis, 1987).

Here, I apply the term tuffisite to silicic volcanic systems, with tuffisites defined as

fractures that are filled with pyroclastic material. Tuffisites have been recognised in a variety of settings in silicic systems: particle-filled fractures in the country rock (Cloos, 1941; Reynolds, 1952; Paithankar, 1967; Dunham, 1967; Heiken et al., 1988; Stasiuk et al., 1996; Goto et al., 2008), clastic margins of dykes and larger intrusions (Hughes, 1971; McGowan, 2016; Kim et al., 2019), and fractures within magma (Stasiuk et al., 1996; Tuffen et al., 2003; Tuffen and Dingwell, 2005; Saubin et al., 2016; Heap et al., 2019; Schipper et al., 2021; Wadsworth et al., 2022). Tuffisite-like features have also been recognised in basaltic pyroclasts (Owen et al., 2019). Tuffisites in silicic systems are found both within and surrounding dissected conduits and have therefore been divided into two categories depending on their relationship with the volcanic conduit: external tuffisites and internal tuffisites. External tuffisites are particle-filled fractures hosted in the country rock adjacent to the volcanic conduit or intrusion and can be considered as a record of the early fractures that would have been connected to form a pathway for initial magma ascent. Internal tuffisites are particle-filled fractures that instead form in hot magma within the volcanic conduit itself.

2.2.4 Seismicity at silicic volcanic vents

Direct observations of silicic eruptions can give key insights into how the surface expression of an eruption evolves through time, but it is not possible to directly observe the changes in the processes occurring beneath the surface and the vent structure. Seismic events during both precursory and eruptive phases can give real-time information about the subsurface, acting as a useful tool for hazard prediction (Chouet, 1996; Voight et al., 1998). Linking volcano seismicity to direct surface-based observations therefore has great potential to allow us to understand, in real time, critical details of the shifting architecture and behaviour of the subsurface vent. The structures and textures that are preserved at silicic vents are the geological record of seismic trigger mechanisms (e.g. Tuffen et al., 2003), and a key challenge is to clearly place the inferred seismicity into the timeline of an eruption.

Long-period (LP) seismic events at volcanoes are often interpreted as resonance created by subsurface fluid movement, such as the movement of rising magma, hydrothermal

fluids, or gases (Chouet and Matoza, 2013). The presence of fluid within the conduit creates a velocity contrast, trapping acoustic energy within the conduit and producing resonance. The duration of any resonance is dependent on how rapidly this energy is dissipated. A greater contrast in sound speed between the fluid within the conduit and the surrounding rock will create a longer-lived signal. The presence of gas, whether as bubbles within magma or gas-ash mixtures above the level of fragmentation in the conduit, creates a sharp velocity contrast between the fluid and the surrounding solid rock (Chouet, 1996), with very long-lived signals best explained by dusty or misty gases carrying particles <10 μm across (Kumagai and Chouet, 1999, 2000; Taguchi et al., 2021).

LP events occur regularly in the lead up to and during volcanic eruptions and often occur in swarms with similar waveforms, indicating that they reflect the periodic excitation of repetitive, non-destructive sources (Neuberg et al., 2006). Individual LP events a few seconds long can be superimposed to produce swarms several hours to ~1 week in length (Molina et al., 2004; Green and Neuberg, 2006). Various potential sources of LP events have been suggested, including the repeated excitation of fractures within or adjacent to the volcanic conduit (Chouet, 1996), frictional stick-slip at the margins of an extruding magma plug (Iverson, 2008), and gas escape through a magma plug and depressurisation (Bell et al., 2017).

The periodic explosive venting of ash and gas at the surface during Vulcanian eruptions is associated with LP events, further suggesting that this seismicity is linked to gas escape (Cruz and Chouet, 1997). However, interpreting the source mechanisms of seismic events generated by multi-phase fluids under dynamic volcanic conditions is challenging, and will require integration of interpretations from seismic signals with field evidence and modelling to better understand volcanic behaviour (Chouet and Matoza, 2013).

2.2.5   Gaps in our knowledge of conduit processes

Processes controlling the evolution of silicic volcanic systems prior to and during eruptions remain poorly understood. To improve hazard prediction we need to be able to determine

the dynamics of an eruption, requiring a greater understanding of how silicic systems evolve through time. The review above highlights multiple unanswered questions regarding the dynamics of silicic volcanic systems:

1. How do silicic vents open and close?

2. What are the controls on eruption style and what is the trigger of explosive-effusive transitions?

3. How does gas escape from the conduit?

4. What is the source of seismicity at silicic vents?

Tuffisites — pyroclast-filled fractures found within and adjacent to volcanic vents — have been suggested to be mini conduits, with many processes in tuffisites matching those seen in conduits, only separated by differences in scale (Schipper et al., 2021). Improving our understanding of tuffisites therefore has potential to help unravel many of the processes occurring during the evolution of silicic vents. Tuffisites and their formation have been linked to all of these questions above, with tuffisites thought to be both efficient outgassing pathways that may reduce sufficient excess pressure to moderate eruption style, and a potential source of LP seismic events detected at silicic volcanoes. The aim of this thesis is to improve understanding of the processes occurring during tuffisite formation, and to then extrapolate these upwards to the conduit-scale to gain new insights into the processes controlling eruption dynamics.

2.3   Tuffisite formation

Tuffisites are particle-filled fractures that form within (internal tuffisites) or adjacent to (external tuffisites) volcanic conduits. Here, I outline the characteristics of tuffisites, existing models for their formation, and current knowledge of the role that they may play as outgassing pathways.
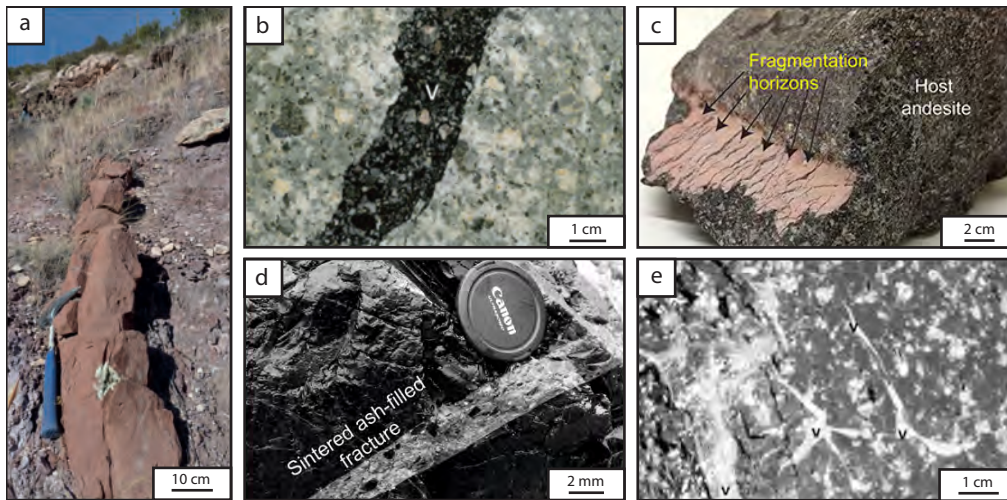
Figure 2.5: Images of tuffisites hosted by the country rock (a and b), lava (c), and vitrophyre/obsidian (d and e). a) A large tuffisite >20 cm thick intersecting the pyroclastic apron at the margins of the Mule Creek vent. Photo taken by Jonathan Castro. b) A tuffisite (labelled v) intersecting pyroclastic breccia from Unzen volcano, Japan (Goto et al., 2008). c) A tuffisite vein within andesite from Volcán de Colima, Mexico (Kendrick et al., 2016). The tuffisite surface shows parallel lenses of sintered material interpreted as fragmentation horizons. d) A tuffisite hosted by an obsidian bomb from Volcán Chaitén, Chile, filled with partially sintered pyroclastic material. This tuffisite (BTB) is the most studied (e.g. Castro et al., 2014; Saubin et al., 2016; Heap et al., 2019). e) A network of angular tuffisites (labelled v) within obsidian at þumall conduit, SE Rauðfossafjöll, Iceland (Tuffen et al., 2003; Tuffen and Dingwell, 2005)

2.3.1 Tuffisite morphology

Tuffisites have been found to be common features both within volcanic conduits and in the adjacent country rock (Stasiuk et al., 1996; Tuffen et al., 2003; Tuffen and Dingwell, 2005). Tuffisites are highly variable in size, ranging from millimetres to metres in thickness and can be up to tens of metres long. Many show internal structure, recording evidence of the injection of a particle-laden fluid into the fracture, from which particles were deposited. All tuffisites in and around silicic conduits are particle-filled fractures, but the morphology of tuffisites varies depending on the characteristics of their host rock.

2.3.1.1 Tuffisites hosted by country rock (external tuffisites)

Tuffisites hosted in the country rock adjacent to the volcanic conduit typically have sharp-edged margins and are clearly fracture-hosted (Reynolds, 1952; Dunham, 1967). These tuffisites form veins usually a few cm in width but fractures up to 2 m wide and

>120 m long have been found (Figure 2.5a; Dunham, 1967; Heiken et al., 1988; Stasiuk et al., 1996; Robertson et al., 1998). External tuffisites are common features in the country rock surrounding silicic conduits, though the source and tips of tuffisites are typically not seen (Heiken et al., 1988; Stasiuk et al., 1996). There is no visible offset between the walls of these tuffisites, suggesting no lateral displacement has occurred during fracture opening. External tuffisites have been seen to originate in the brecciated vitrophyre or obsidian at the conduit margins, weaving around clasts before dividing into smaller forked pathways towards the fracture tip (Stasiuk et al., 1996).

External tuffisites contain angular-subrounded clasts of the host rock, with particle sizes ranging from <1 mm to ∼30 cm depending on the fracture width (Figure 2.5b; Dunham, 1967; Heiken et al., 1988). The majority of such tuffisites are formed of glassy fragments (up to 80%; Dunham, 1967), as well as clasts of rhyolite and phenocryst fragments <5 mm across (Stasiuk et al., 1996). External tuffisites can have a complex internal structure, with the centre of the tuffisite width often formed of a coarser grain-size than the tuffisite margins, and features such as graded bedding and cross-lamination are common (Dunham, 1967; Heiken et al., 1988; Stasiuk et al., 1996).

2.3.1.2 Within-conduit tuffisites (internal tuffisites)

Tuffisites found within the conduit itself — internal tuffisites — form networks of fractures (Tuffen et al., 2003; Tuffen and Dingwell, 2005; Kendrick et al., 2016). The particles within these tuffisites can be variably sintered together (Colombier et al., 2020), and are typically more sintered than those found within external tuffisites (Kolzenburg et al., 2019). Here I have separated these tuffisites into two categories due to their different characteristics: tuffisites found within lava and tuffisites hosted by obsidian or vitrophyre.

2.3.1.3 Lava-hosted tuffisites (internal tuffisites)

Internal tuffisites have been found within andesitic, dacitic, and rhyolitic lava that plugs dissected vents and active dome complexes, forming networks of cross-cutting veins

typically 1–50 mm thick that continue for up to several metres in length (Stasiuk et al., 1996; Kolzenburg et al., 2012; Black et al., 2016; Kendrick et al., 2016). Tuffisites are found to be more common towards the centre and top of dissected vent plugs (Stasiuk et al., 1996) and show a variety of morphologies. Most fractures have sharp edges, though where the host material is pumiceous, clastic material has been seen in the vesicles surrounding the tuffisite (Kendrick et al., 2016; Paisley et al., 2019a). Other tuffisites are more closely aligned with flow banding, with cuspate boundaries that give the tuffisites a pinch and swell shape in cross-section (Stasiuk et al., 1996), or can be sub-parallel lenses of material with graded boundaries, interpreted to be fragmentation horizons (Figure 2.5c; Kendrick et al., 2016). The host material has been seen to backflow into the fracture, indicating that it could still flow at the time of tuffisite emplacement (Kendrick et al., 2016).

The fill of lava-hosted tuffisites is mostly formed of clasts of the host lava and crystal fragments, with clasts typically <1 cm and angular–subangular in shape (Stasiuk et al., 1996; Goto et al., 2008; Kolzenburg et al., 2012). The fill material is often poorly sorted and rare rounded lithics <20 mm across can be present (Kolzenburg et al., 2012; Kendrick et al., 2016). Tuffisites may or may not contain glass in their fill (Kolzenburg et al., 2012; Kendrick et al., 2016). The internal structure of these tuffisites can be complex, with material often showing fine laminations or cross-lamination and truncated beds (Stasiuk et al., 1996; Black et al., 2016; Paisley et al., 2019a). Clasts of the host material can be found at tuffisite margins, separated from the wall by narrow fractures (Kendrick et al., 2016).

2.3.1.4 Obsidian-hosted tuffisites (internal tuffisites)

Internal tuffisites hosted in obsidian (or vitrophyre if hydrated) have most commonly been studied in volcanic bombs due to the scarcity of well-preserved silicic conduits (Figure 2.5d; Castro et al., 2012, 2014; Cabrera et al., 2015; Saubin et al., 2016; Heap et al., 2019; Paisley et al., 2019a), though some obsidian-hosted tuffisites have been found in situ at the margins of silicic conduits (Figure 2.5e; Stasiuk et al., 1996; Tuffen et al., 2003; Tuffen and Dingwell, 2005; Cabrera et al., 2015). These tuffisites are networks

of angular fractures <60 mm thick and <5 m in length, typically a few centimetres long (Tuffen et al., 2003; Tuffen and Dingwell, 2005). The tuffisites are often strongly sheared, with measurable shear displacement across the fractures, and aligned parallel to flow banding within the obsidian (Stasiuk et al., 1996; Tuffen et al., 2003; Tuffen and Dingwell, 2005). The opposite fracture walls can be slightly mismatched in appearance, suggested abrasive wear of the walls during fracture opening (Tuffen and Dingwell, 2005). Fractures can be connected by irregular-shaped particle-filled voids up to 80 mm across (reservoir zones; Tuffen and Dingwell, 2005). Cross-cutting fractures are common, producing a fracture network, though older nearly fully healed veins can be detected only by microlite-rich lines in the obsidian (Tuffen and Dingwell, 2005; Cabrera et al., 2015). Tuffisites within vitrophyre breccia at the Mule Creek vent wind around and between clasts of vitrophyre (Stasiuk et al., 1996).

The particles within obsidian-hosted tuffisites are typically 10–200 μm across and can vary from angular to rounded in shape (Tuffen et al., 2003; Tuffen and Dingwell, 2005; Heap et al., 2019). The clasts are mostly glassy fragments and lithics, although juvenile clasts (>60 μm across) and phenocryst fragments are often also present (Castro et al., 2014; Saubin et al., 2016; Heap et al., 2019). The glassy fragments are typically strongly sintered together until almost no longer identifiable, with the remaining porosity concentrated around lithics (Heap et al., 2019). The interiors of juvenile clasts can be vesiculated with a dense glassy rim (Saubin et al., 2016; Heap et al., 2019). Particles within tuffisites are often arranged with a complex structure, displaying banding (0.2–20 mm thick), cross-lamination, and jigsaw-fit clasts (Tuffen and Dingwell, 2005; Cabrera et al., 2015). The most fine-grained particles are found towards the fracture margins (Tuffen et al., 2003).

2.3.2 Relationships between tuffisites and the conduit

Tuffisites have been reported in nearly all units of dissected silicic conduits (Stasiuk et al., 1996) suggesting that their formation is a common process. This is matched by observations of tuffisites at the eruptions of Chaiten (2008–2009) and Cordon Caulle (2011–2012), where in the opening days of the eruptions ejected bombs were found to be

intersected by tuffisites (Lara, 2009; Castro et al., 2012; Pallister et al., 2013; Schipper et al., 2013), and tuffisites were also found in lavas produced later in the eruptions (Castro et al., 2014). These observations suggest that there is a continued source of clastic material available for tuffisite evolution at different stages of vent formation (Wadsworth et al., 2022).

Clastic material has also been found within fractures that are not preserved as tuffisites, indicating that the movement of gas-pyroclast mixtures may also be common (McGowan, 2016; Farquharson et al., 2022). Clastic material that lines the margins of silicic dykes indicates that the first material to be deposited within the fracture is clastic, before magma emplacement (McGowan, 2016; Kim et al., 2019; Saubin et al., 2019). Fracture surfaces coated with ultra-fine ash, interpreted to form by the accretion of particles during highly pulsatory ash venting, also suggests that clastic material may be captured and stored beneath the surface, rather than ejected (Farquharson et al., 2022).

2.3.3 Tuffisite formation mechanisms

The location, fracture morphology, and characteristics of the particle fill of tuffisites have been interpreted as recording the processes occurring during fracture formation. The complex structures within tuffisites, such as laminations and cross-lamination, suggest that they are formed by the injection of a particle-laden fluid into the fracture (Cloos, 1941; Heiken et al., 1988; Stasiuk et al., 1996). The preserved tuffisites show the final state of the particle-filled fracture, but by considering the incremental deposition of material within tuffisites and their internal structures, we can discover more about the processes occurring during tuffisite formation. Some material may have been carried through the tuffisite without deposition occurring, or deposited and re-eroded from the fracture, causing some stages of tuffisite formation to be missing from the preserved deposit. The period of time before particle deposition begins is particularly poorly understood as there is no physical record of this in the deposit.

2.3.3.1   Country-rock hosted tuffisites

Tuffisite opening

Tuffisites hosted in the country rock are thought to form by the tensile (Mode I) fracturing of the country rock by a high-pressure gas-pyroclast mixture (Heiken et al., 1988). Tensile fracturing can occur when the fluid pressure, P_f exceeds the compressive stress, σ, and the tensile strength, T, of the country rock (Hubbert and Willis, 1957). The condition for failure is therefore

$$P_f > \sigma + T. \tag{2.1}$$

Fractures will therefore typically open in an orientation parallel to the least compressive stress, σ_3, as fracturing in this orientation requires the smallest fluid overpressure. Any pre-existing weaknesses within the country rock, such as unit contacts or bedding planes, will often be exploited in fracture opening due to a lower tensile strength (Scholz, 1968). This process of hydrofracturing or hydraulic fracture formation is the mechanism interpreted as opening magmatic dykes and sills (Rubin, 1993), initiating the formation of volcanic conduits, and forming fractures in other environments such as sand injectites and glacial hydrofractures (van der Meer et al., 2009; Hurst et al., 2011; Phillips et al., 2013). Gas-pyroclast mixtures are thought to be injected into silicic dykes before during fracture opening, before magma emplacement occurs (McGowan, 2016).

If there are pre-existing fractures in the host rock then these will only require sufficient fluid overpressure to overcome the compressive stress, and Eq.2.1 becomes $P_f > \sigma$ for fracture opening. If present, pre-existing weaknesses or fractures may therefore control the direction of the fractures formed instead of the direction of the least compressive stress. Once a fracture has been opened, the fluid overpressure is able to hold the fracture open if it is equal to or exceeds the least compressive stress. During this time, fluid and any particles it is carrying can be injected into the fracture, with the deposition of particles forming the tuffisite fill (Cloos, 1941; Heiken et al., 1988). The presence of beds and erosive surfaces within the tuffisite fill has been interpreted as evidence for tuffisite formation occurring in multiple steps, suggesting multiple pulses

of fluid are injected into the fracture (Heiken et al., 1988). Once the fluid pressure drops sufficiently the fracture will close around the deposited particles, thought to form a more permeable pathway for gas escape from the conduit. If sufficiently hot, particles within the tuffisites can sinter together, reducing tuffisite permeability through time. The relatively lower degree of sintering seen in external tuffisites, compared to within internal tuffisites, suggests that external tuffisites injected into the cold country rock cool more rapidly than tuffisites within magma, limiting the progression of sintering (Kolzenburg et al., 2019).

Source of pyroclastic material

Clasts of host rock found within external tuffisites are interpreted as pieces broken away from the fracture walls during fracture opening that are transported and then deposited within the tuffisite (Stasiuk et al., 1996; Goto et al., 2008). The pyroclasts injected into fractures to form tuffisites must be sourced from fragmentation in the adjacent vent. This fragmentation has been suggested to be local, with the failure of conduit wall rock generating an energetic strain wave capable of fragmenting nearby magma (Lavallée et al., 2012; Benson et al., 2012). More recently, silicic magma columns have been suggested to fragment at <2 km depth, providing a deeper and less localised source of pyroclastic material for tuffisite formation (Figure 2.6; Wadsworth et al., 2020, 2022). The unsteady nature of Subplinian–Vulcanian eruptions produces pressure fluctuations that could drive fracture opening and tuffisite formation.

2.3.3.2 Within-conduit tuffisites

Tuffisite opening

Both lava-hosted and obsidian-hosted internal tuffisites have been suggested to form within the magma while it is still hot and able to flow, interpreted from observations of viscous backfill of the surrounding magma into fractures (Tuffen et al., 2003; Goto et al., 2008; Kendrick et al., 2016). Tuffisites are fractures injected with pyroclastic material, and tuffisite formation therefore requires the brittle failure of viscoelastic magma. Elastic shear stresses in magma decay over a relaxation time defined as $\lambda_r = \mu/G$, where μ is
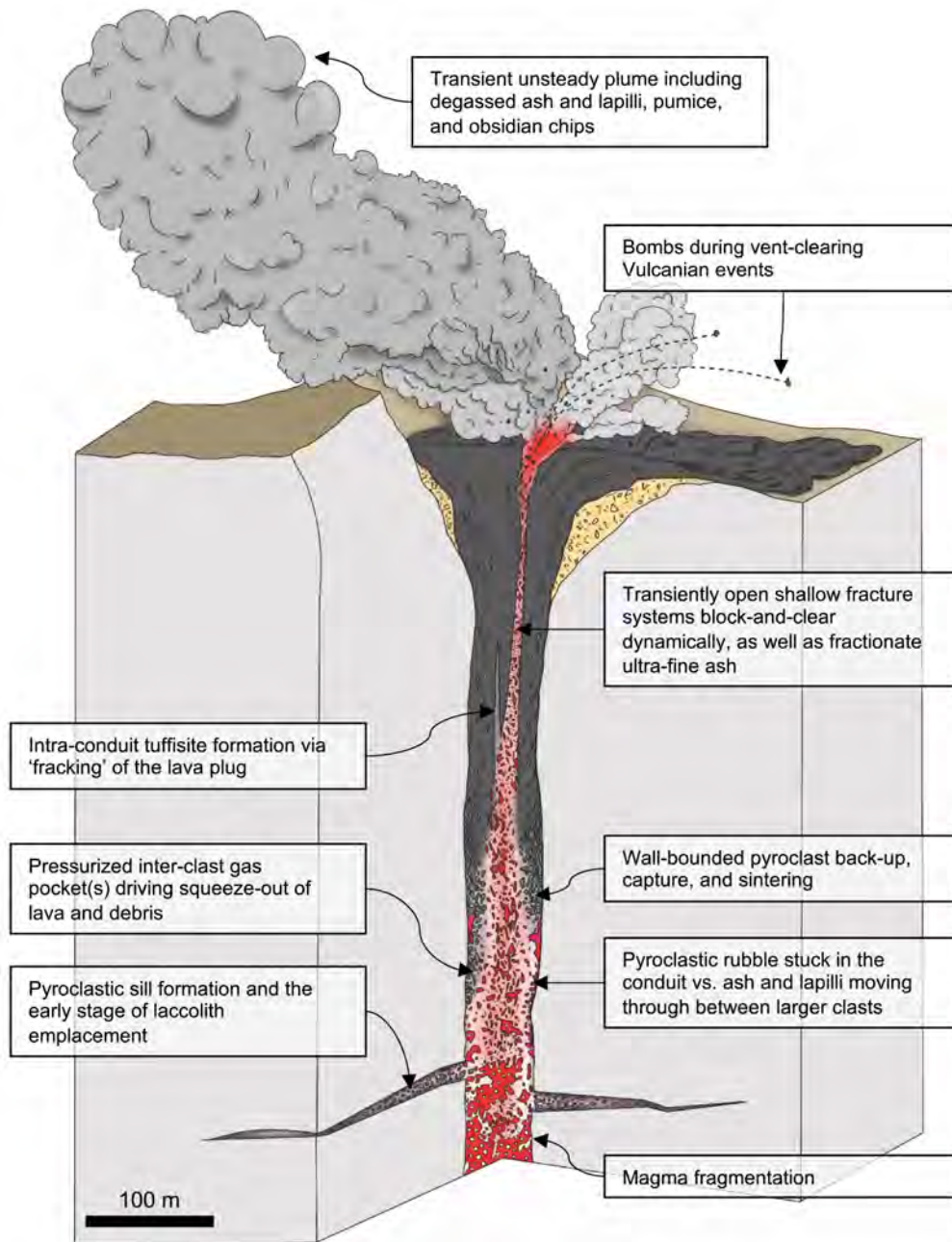
Figure 2.6: A model for hybrid explosive-effusive activity at Cordón Caulle, including potential settings for tuffisite formation (Wadsworth et al., 2022). External tuffisites form within the country rock above the depth of fragmentation, potentially creating pyroclastic sills if tuffisites are sufficiently large. Tuffisites forming within the vent-filling lava represent transient fracture systems with pyroclastic material sourced from continued fragmentation at depth.

the fluid viscosity and G is the elastic shear modulus, found to be $\sim 10^{1}0$ Pa and broadly independent of temperature and composition (Maxwell, 1867; Dingwell and Webb, 1990; Simmons et al., 1998). The characteristic time of magma flow, λ, is $1/\dot{\gamma}$, where $\dot{\gamma}$ is the strain rate. By comparing this relaxation time with the characteristic time of flow a criterion for brittle failure can be created, the scale-independent Weissenberg number (W_i):

$$Wi = \frac{\lambda_r}{\lambda} = \frac{\mu}{G}\dot{\gamma}. \tag{2.2}$$

The field of brittle deformation, where magma is unrelaxed, is defined as values where $W_i \gg 1$, while values where $W_i \ll 1$ indicate the field of viscous deformation (Wadsworth et al., 2018). A large strain rate, such as that expected close to the conduit walls during magma ascent in the shallow conduit, can therefore trigger brittle deformation (Goto, 1999; Gonnermann and Manga, 2003; Holland et al., 2011). Higher-viscosity magmas (dependent on magma composition, concentration of volatiles and temperature) will be able to form shear fractures at a lower strain rate than lower-viscosity magmas, allowing fracturing of magma to occur more centrally in the conduit (Tuffen et al., 2003) and perhaps be an inevitable consequence during the ascent of silicic magmas (Gonnermann and Manga, 2003; Wadsworth et al., 2018).

Source of pyroclastic material

Clasts in tuffisites formed within conduits were initially interpreted as entirely derived from the fracture walls by grinding during shearing (Tuffen et al., 2003). The presence of lithics in tuffisites within conduits (Kolzenburg et al., 2012; Castro et al., 2014; Saubin et al., 2016; Heap et al., 2019) and the discovery of heterogeneous H_2O and trace metal concentrations within tuffisites (Berlo et al., 2013; Saubin et al., 2016) suggest that a large proportion of the tuffisite fill has a source that is distant from the local fracture walls, with some clasts carried from significantly deeper within the conduit (Saubin et al., 2016).

Models for tuffisite formation within magma have suggested that tuffisite formation represents the nucleation point of fragmentation events that tear magma apart (Kendrick et al., 2016), or that pyroclastic material is produced from foamy magma directly

beneath a plug, with fragmentation driven by the pressure drop that occurs during vein opening (Saubin et al., 2016). McGowan (2016) used textural analysis of the obsidian walls of tuffisites at Þumall conduit to show that the host magma was highly vesicular at the moment of tuffisite injection, and had subsequently undergone almost complete collapse into dense melt. If fragmentation could be very localised due to a porosity-controlled fragmentation threshold, then tuffisite formation could perhaps quarry areas of more vesicular material (Saubin et al., 2016). These models, however, do not have a clear mechanism to transport lithics and pyroclasts from depth into tuffisites. Pyroclasts transported from depth have been suggested to instead be sourced from deeper magmatic fragmentation, with the silicic magma column expected to be fragmented above 2 km depth (Wadsworth et al., 2020). Conduit-blocking magma is thought to be assembled by the accretion and sintering of pyroclastic material, and within-conduit tuffisites represent fractures through conduit-blocking magma in which particles were deposited (Figure 2.6; Schipper et al., 2021; Wadsworth et al., 2022). These fractures could have provided pathways for material to reach the surface during hybrid explosive-effusive activity (Wadsworth et al., 2020, 2022; Schipper et al., 2021).

2.3.4 Welding within tuffisites

If pyroclasts are sufficiently hot to deform viscously when deposited, the particles can weld together. Welding can be seen in many different volcanic settings, such as in pyroclastic density currents (Branney and Kokelaar, 2002), fall deposits (Giachetti et al., 2021), ignimbrites infilling conduits (Kano et al., 1997), at the margins of vents lined with obsidian (Gardner et al., 2017; Wadsworth et al., 2020), on fracture surfaces (Farquharson et al., 2022), and in tuffisite veins (Stasiuk et al., 1996; Tuffen et al., 2003; Kendrick et al., 2016; Gardner et al., 2018; Heap et al., 2019; Kolzenburg et al., 2019). This process of welding is associated with the strengthening of materials (Kolzenburg et al., 2012; Vasseur et al., 2013) and reduction in porosity and permeability through time (Farquharson et al., 2017; Heap et al., 2019; Wadsworth et al., 2021). The reduction in permeability during welding suggests that conduit outgassing through tuffisites can only be transient, limited by the time taken for welding to significantly reduce the potential

gas flux (Farquharson et al., 2017; Heap et al., 2019).

Welding can occur when particles are above the glass transition temperature, T_g, and particles that cool more slowly therefore have a longer time period over which welding can take place, allowing more complete welding to occur. Particles injected into tuffisites in cold country rock will cool rapidly, permitting only partial welding to take place and preserving a greater porosity and permeability than in tuffisites of similar dimensions found within the conduit (Kolzenburg et al., 2019).

Welding is driven by the stresses acting on the particles due to surface tension and confining stress. This process is opposed by the gas pressure, which acts to prevent the reduction in porosity, and the viscosity of the particles (Wadsworth et al., 2016, 2019). The rate of change of porosity, $\frac{d\phi}{dt}$, is given by

$$\frac{d\phi}{dt} = -\frac{3\Delta P}{4\mu}\phi - \frac{3\Gamma}{2\mu\langle a_i \rangle \zeta} \left(\frac{\phi_i}{1-\phi_i} \right)^{\frac{1}{3}} \phi^{\frac{2}{3}} (1-\phi)^{\frac{1}{3}} \tag{2.3}$$

where ϕ_i is the initial porosity, ΔP is the difference between the pressure of the gas phase and stress acting on the particles involved in the welding, μ is the viscosity of the hot particles, Γ is the interfacial tension between the gas and the particle, and $\langle a_i \rangle$ is the mean size of the pore spaces between the welding particles, which relates to the particle-size (Wadsworth et al., 2016, 2019). During welding, the stress that is acting on the particles is that closing the fracture and driving particle compaction. In contrast, the gas pressure acts to hold the pore space open, and therefore, the greater the gas pressure (and so the smaller the value of ΔP) the less rapidly sintering can occur (Farquharson et al., 2017). The reduction in porosity as welding continues can alter the gas pressure in the pore space of the sintering material. Following on from work by Sparks et al. (1999), Farquharson et al. (2017) define three regimes that define the controls on pore pressure during welding: 1. Pore pressure can equilibrate through outgassing sufficiently rapidly to prevent an increase in pore pressure; 2. The molecular diffusion of water can occur fast enough to compensate for the porosity reduction and prevent pore pressure increases; 3. Reduction in pore pressure is too rapid to be compensated for by outgassing or molecular diffusion and the pore pressure increases during welding.

Most studies calculating characteristic welding timescales have considered the case when $\Delta P \to 0$, in which welding occurs most slowly in the absence of confining stress (e.g. Schipper et al., 2021; Giachetti et al., 2021; Farquharson et al., 2022). In this case Eq. 2.3 can be approximated by $\phi \approx \phi_i \exp\left(-3t/2\lambda\right)$, where $\lambda = \zeta\mu\langle a_i\rangle\Gamma$ is the welding timescale in the $\Delta P = 0$ regime (Wadsworth et al., 2014, 2016). Here, ζ is a correction factor that accounts for the polydispersivity of the particle-size distribution (Wadsworth et al., 2017).

The welding timescale is dependent on the size and viscosity of the sintering particles, as well as the presence of any confining stress (if considered). Tuffisites have been found to contain particles up to several centimetres across, with the fine-grained matrix involved in sintering typically containing particles <20 μm in diameter (Saubin et al., 2016; Heap et al., 2019). Estimates of the welding timescale for such a tuffisite matrix suggest that tuffisites may remain permeable for minutes to tens of hours in the absence of external forces, or seconds to minutes if external forces are applied, depending on the temperature considered (Gardner et al., 2018; Heap et al., 2019). Similar timescales have been estimated for welding of fine-grained material within the conduit (Wadsworth et al., 2020; Schipper et al., 2021; Farquharson et al., 2022).

2.3.5 Tuffisites as potential outgassing pathways

Tuffisites have been found to have a greater permeability than the surrounding host rock, suggesting that they could make efficient pathways for outgassing (Kolzenburg et al., 2012, 2019; Kendrick et al., 2016; Heap et al., 2019). The ability of a tuffisite to act as an outgassing pathway will depend on how tuffisite permeability varies through time as the pyroclasts weld together. Other key factors will include how long tuffisites act as outgassing pathways for, and how large a volume of melt is available to be degassed.

The permeability of preserved tuffisites have been measured to be $\sim 10^{-11}$–10^{-14} m^2 in crystal-rich intermediate lava (Kendrick et al., 2016) and $\sim 10^{-15}$ m^2 in rhyolitic obsidian (Heap et al., 2019). It should be noted that these measured permeabilities are the permeability of exhumed tuffisites, and therefore do not necessarily reflect the

permeability of tuffisites actively acting as outgassing pathways during an eruption.

The opening of external tuffisites within the country rock has been proposed to be able to reduce excess pressure from within the conduit by increasing the permeability of the conduit walls, allowing lateral outgassing to occur (Heiken et al., 1988; Stasiuk et al., 1996). Internal tuffisites within the conduit have been as interpreted pathways that could permit long-range outgassing through connected high-density fracture networks within the conduit or at conduit margins (Gonnermann and Manga, 2003; Rust et al., 2004; Castro et al., 2012; Cabrera et al., 2015; Kendrick et al., 2016), or as evidence recording the wholesale fragmentation of magma to pyroclasts, allowing for efficient degassing to occur through gas-pyroclast separation (Wadsworth et al., 2020, 2022). Clasts with H_2O rich cores within internal (within-conduit) tuffisites have been interpreted to have been transported hundreds of metres up the conduit, suggesting that they can be long-range features (Saubin et al., 2016), but these fractures within magma are thought to not be sufficiently closely spaced to allow for efficient degassing to occur, unless the fractured magma were highly vesicular (Castro et al., 2014).

Gas escape is thought to occur through the pore space between the particles within the tuffisite, allowing reduction of excess pressure within the conduit until gas flow is limited by sintering (Saubin et al., 2016; Gardner et al., 2018; Schipper et al., 2021). External tuffisites (within the country rock) may make particularly efficient outgassing pathways as rapid cooling will limit the degree of welding that can occur, producing tuffisites with a greater permeability (Kolzenburg et al., 2019). The more rapid welding timescales for internal tuffisites have led to suggestions that fractures can become rapidly clogged within a magma plug, restricting gas flow and allowing pressurisation to occur (Cassidy et al., 2015; Heap et al., 2019).

The potential of tuffisites to act as outgassing pathways will be dependent on the length of time that tuffisites remain permeable, allowing outgassing to occur. The characteristic welding timescales of tuffisites have been found to be seconds to tens of hours, depending on the welding conditions (temperature, particle viscosity, and external stresses; Gardner et al., 2018; Heap et al., 2019), and this is suggested as an estimate for the length of time for which efficient outgassing could take place. This is the timescale beyond which

the tuffisite pathway will become effectively sealed, and the opening of a new fracture would be required to reinvigorate outgassing.

The lifetime of tuffisites has also been inferred from the dissolved water and trace element diffusion gradients occurring around tuffisites, which indicate that tuffisites may allow for outgassing to be sustained over a period of ~15 min to ~1 day (Castro et al., 2012, 2014; Berlo et al., 2013; Saubin et al., 2016; Heap et al., 2019; Paisley et al., 2019a). Tuffisites have been shown to degas a volume of melt over ten times the volume of the vein itself, and this process has been shown to impose chemical heterogeneity, with gas fluxing through veins shown to scavenge trace metals from the surrounding melt (Berlo et al., 2013; Paisley et al., 2019b). H_2O concentrations in glass-walled tuffisites have indicated that tuffisite formation is associated with transient pressure drops of a few megapascals, as well as recording the ephemeral development of overpressure within tuffisite veins due to blockages (Castro et al., 2014).

2.3.6 Tuffisites as a source of volcanic earthquakes

The source of LP events at volcanic conduits is thought to be the repeated injection of gas-ash mixtures into fractures (Chouet, 1996; Kumagai and Chouet, 2000) as the injection of ash-gas mixtures into fractures could produce long-lasting signals. As tuffisites are pyroclast-filled fractures, they have been suggested to be the fossil record of LP events (Tuffen et al., 2003; Molina et al., 2004). The fractures modelled as the source of LP seismic events are thought to be <200 m in length and a few cm in width, similar to the dimensions of tuffisites adjacent to conduits (Heiken et al., 1988; Molina et al., 2004; Arciniega-Ceballos et al., 2012; Torres et al., 2021). Tuffisite formation involves the repeated injection of gas-ash mixtures into fractures, providing a non-destructive repetitive source for LP events (Arciniega-Ceballos et al., 2012). Changes in the observed complex frequencies and Q values (attenuation factor) of resonating fractures through time have been suggested to reflect the filling of fractures with ash particles that sinter through time (Molina et al., 2004; Taguchi et al., 2018).

The formation of internal tuffisites, in particular, has been interpreted as the mechanism

for the generation of LP events (Tuffen et al., 2003; Molina et al., 2004; Tuffen and Dingwell, 2005; Neuberg et al., 2006; Torres et al., 2021). The brittle failure of magma at high strain rates towards the conduit margins during internal tuffisite generation could provide a suitable seismic source, with repeated opening and healing of fractures able to provide a repeatable mechanism with a minimum repeat time of tens of seconds if magma is continually ascending in the seismogenic window (Neuberg et al., 2006; Chouet and Matoza, 2013).

LP events have notably preceded Vulcanian explosions — events triggered by the cyclic pressurisation of magma within the conduit (Stix et al., 1997; Torres et al., 2021). Increasingly frequent LP events have merged into tremor prior to a large explosion at Tungurahua (Bell et al., 2018). The resonance of fractures within a magma plug has been suggested to be the source of LP events, with the sealing of previously pervasive fractures allowing pressurisation beneath the magma plug in the lead up to an explosion (Butcher et al., 2020). This is similar to the models for the formation of tuffisites within a magma plug (Saubin et al., 2016) or intersecting magma assembling in the shallow conduit by the accretion of particles (Wadsworth et al., 2020). Internal tuffisites dissecting the plug material are thought to represent previous outgassing pathways through welding conduit-filling rubble that are now clogged with particles (Wadsworth et al., 2022).

2.3.7   Gaps in our knowledge of tuffisite formation

Tuffisites have been suggested to act as permeable pathways that can allow for the escape of significant volumes of gas from the conduit zone, potentially reducing excess pressure from the conduit zone and moderating eruption explosivity. Despite this potential importance, the processes occurring during the formation of tuffisites are not well understood, preventing the potential significance of tuffisites as outgassing pathways from being confirmed. This exploration of our knowledge of tuffisites and tuffisite formation highlights some gaps in our understanding:

1. When do tuffisites form during magma ascent and vent evolution?

2. How do within-conduit tuffisites form?

3. What controls the morphology of tuffisites?

4. What overpressure is required for tuffisite emplacement?

5. Are tuffisites emplaced by a single multi-phase fluid pulse?

6. What are the characteristics of the fluid injected into fractures to form tuffisites?

7. Do tuffisites represent efficient outgassing pathways? How long would these pathways remain active for?

Investigations into the morphology and internal structure of tuffisites, as well as their relationship to the surrounding volcanic conduit, may help to improve our understanding. Tuffisites, and in particular external tuffisites, are poorly studied compared to the particle-filled fractures found in other environments, such as glacial hydrofractures and sand injectites. The knowledge of non-volcanic water-opened fractures (or hydrofractures) could be applied to the volcanic setting to learn more about tuffisite formation. In the following section I outline the existing knowledge of particle-filled fractures in non-volcanic environments and consider how this might assist in answering some of the questions about tuffisites that are posed above.

2.4 Particle-filled fractures in other environments

Particle-filled fractures with similar appearances to tuffisites also exist in sedimentary environments, where they are opened by high pressure water and are therefore known as hydrofractures. Below I outline the characteristics of glacial hydrofractures, sand injectites, and human-made hydrofractures alongside the mechanisms for their formation, before considering how they might vary from tuffisites in a volcanic environment.

2.4.1 Hydrofracture characteristics

2.4.1.1 Glacial hydrofractures

In glacial environments, hydrofractures can intersect the glacial sediment or bedrock to form particle-filled fractures that may be up to ∼1 m in thickness and ∼10 m in length
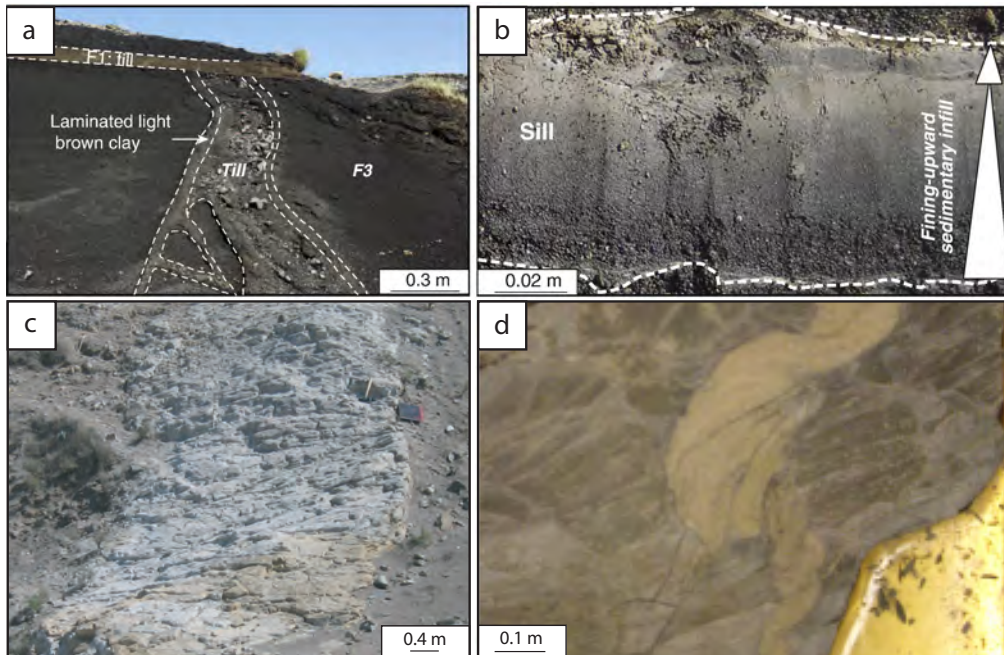
Figure 2.7: Particle-filled hydrofractures found in sedimentary environments. a) and b) Glacial hydrofractures found as part of a large hydrofracture network at Sólheimajökull, Iceland (Ravier et al., 2015). a) Glacial hydrofractures with a finer laminated margin and a coarser grained centre. b) A glacial hydrofracture containing fining upwards sequences within the sedimentary fill. c) A sand injectite with a banded structure (bands 0.1–0.25 m thick) from the Panoche Giant Injectite Complex. The right edge of the injectite as a wavy structure with striations and a polished surface interpreted to be formed by erosion during injection (Vigorito et al., 2008). d) A columnar sandstone injectite within a core with a spiral axis geometry. Small sandstone injections fill partings in the host mudstone adjacent to the injectite (Hurst et al., 2011).

(Rijsdijk et al., 1999; van der Meer et al., 2009). The material within the hydrofracture is more fine-grained at the fracture margins than the fracture centre, with clay-silt rich fracture margins crudely coarsening to sand-sized grains in the centre (Figure 2.7a). The hydrofracture fills are commonly bedded and can also contain complex sedimentary structures such as laminations, cross-laminations, and soft-sediment deformation (Figure 2.7b; Phillips et al., 2013; Ravier et al., 2015; Sigfúsdóttir et al., 2019). Sediment packages can be traced for up to 1 m, with each individual lamina able to be traced for a few tens of cm (Phillips et al., 2013). Different beds are often separated by erosional surfaces that suggest a complex depositional history.

2.4.1.2 Sand injectites

The majority of clastic dykes or sand injectites do not show an internal structure and are instead massive (Peterson, 1968). The hydrofractures are typically filled with sand, and features such as flute marks, scours, and grooves record on the wall rock surface how the injected sand interacted with the host strata during injection (Figure 2.7c; Kane, 2010; Hurst et al., 2011; Cobain et al., 2015). Where internal structures are present, they are less complex than those seen in glacial hydrofractures, with laminations within the hydrofracture arranged either parallel, or less commonly perpendicular to, the dyke walls (Figure 2.7d). Larger clasts, such as host rock clasts sourced from the walls, can be concentrated either towards the hydrofracture centre or walls, and cross-cutting channel structures and graded bedding can also be seen (Obermeier, 1996; Hurst et al., 2011).

2.4.1.3 Human-made hydrofractures

Human-made hydrofractures, generated by the hydrocarbon industry, are often injected with particles to hold (prop) the fracture open to allow for continued fluid flow. These hydrofractures are rarely seen as they are produced beneath the surface but have been uncovered after formation by mine-back (Warpinski et al., 1981; Schmidt et al., 1981), allowing for comparison with model data (Cipolla et al., 2008). Experiments injecting human-made hydrofractures with multiple pulses of different coloured sand have created fractures containing multiple unstructured beds of different coloured sand, and have also found that sand is distributed unevenly along the fracture (Schmidt et al., 1981).

2.4.2 Formation of hydrofractures

In sedimentary environments the creation of overpressure is related to the ability to expel fluids during rapid burial or disequilibrium compaction, such as during the formation and deformation of sedimentary basins, or due to the presence of meltwater in a glacial environment (Cosgrove, 2001; Jolly and Lonergan, 2002). The reduction in pore space during burial will act to expel fluids, with the fluid pressure increasing if fluids cannot

escape sufficiently rapidly, for example due to rapid compaction or surrounding low permeability rock. Compaction during burial reduces the porosity and permeability, further hindering fluid escape. The trapped fluid is no longer at equilibrium, and the fluid pressure increases at a rate greater than the hydrostatic pressure during burial, generating overpressure (Maltman, 1994). If this overpressure is sufficiently large it can fracture the surrounding rock to produce a hydrofracture into which the fluid and any remobilised particles can be injected.

2.4.3 Transporting and depositing particles within hydrofractures

Hydrofracturing is driven by high pressure fluids. The pressure gradient generated along the fracture when it opens controls the velocity of the fluid injected into it, and therefore, the capacity of the flow to carry particles. A greater pressure gradient along a hydrofracture will produce a greater fluid velocity. Particle deposition within the fracture is also dependent on fluid velocity, with a slowing of fluid flow increasing the likelihood of particle deposition, while faster fluid velocities have the potential to erode particles already deposited.

The pressure gradient within a fracture drives the fluid motion, but changes in the permeability of a fluid pathway can indirectly influence the fluid pressure gradient, producing local variations in the fluid velocity. As the velocity of the injected fluid decreases it will deposit particles in the hydrofracture, reducing its permeability and, as the fluid can no longer flow as easily, the fluid pressure gradient along the fracture in this area will increase through time (Kern et al., 1959). A greater fluid pressure gradient in this area of the hydrofracture will increase the fluid velocity, allowing for particles previously deposited to be re-entrained by the fluid, reducing the blockage and increasing the permeabiliy of the fracture. This process can repeat to produce fluctuations in the size of the fluid pressure gradient through time (Kern et al., 1959). At the equilibrium velocity the current is sufficiently fast to avoid depositing the particles it is carrying, but also is not at a sufficiently fast velocity re-entrain any particles already deposited.

2.4.4 Formation of fill microstructures

Microstructures in the fills of hydrofractures, such as laminations and soft-sediment deformation, can provide details about the flow of the injected fluid and its characteristics. The beds and structures produced within the fill can be used to interpret how the fluid velocity and particle density of the fluid changed during hydrofracture formation. As the fluid velocity through the fracture is controlled by the pressure gradient, erosive surfaces within the fills of glacial hydrofractures can be interpreted as a record of the variations in fluid pressure during hydrofracture formation (Phillips et al., 2013; Ravier et al., 2015).

The particles injected into clastic dykes have typically been assumed to be sourced from the surrounding sediment by fluidisation, where the movement of the pore fluid in response to a pressure gradient imposes a sufficeient drag force on the surrounding grains to entrain them (Maltman, 1994; Jolly and Lonergan, 2002). Fluidisation produces massive or structureless deposits, as are seen in the centres of many sand injectites (Hurst et al., 2011; Sherry et al., 2012). Small, irregularly shaped, and structureless areas of glacial hydrofractures have also been explained by fluidisation occurring after particle deposition, destroying any original structures (Phillips et al., 2013).

Well-defined laminations found within hydrofractures cannot be explained by fluidisation, particularly in the absence of visible water-escape structures. Fluidised sediment can only contain laminations if they are primary depositional structures from a source bed of sediment that itself contained laminations. Within the context of peperites, fluidisation has also been suggested as a mechanism for destroying existing laminations in the source sediment (Skilling et al., 2002). Two alternative theories have been suggested for the formation of laminations within hydrofractures: varying the rheology of fluidised material and the 'squeezed-in clastic dyke model' (le Heron and Etienne, 2005).

The first theory involves the injection of initially fluidised material in a single pulse. Rheological differences in the injected sediment, for example due to different grain sizes, will produce separation of material into beds by plastic deformation during injection (Maltman, 1994). To allow this segregation to occur, this model would require sustained

injection of material over a relatively long timescale. This model may be able to explain some of the banding seen parallel to the walls of clastic dykes but not more complex structures and is complicated by debates as to whether flow within hydrofractures is laminar or turbulent (Hurst et al., 2011; Cobain et al., 2015).

The second model has multiple phases of fluid injection into a hydrofracture, with repeated hydraulic fracturing, fracture widening and deposition of pulses of sediment on the fracture walls. Repeated fracturing and sediment deposition would produce complex fracture fills (le Heron and Etienne, 2005). Multiple phases of injection could explain truncated laminations and erosion seen within hydrofractures and also areas of cross-lamination, requiring deposition from diffuse currents (Phillips et al., 2013).

The complex structures seen within glacial hydrofractures have been interpreted as emplacement by multiple fluid pulses into the fracture, while greater variability in the structure of sand injectites means that their emplacement mechanism is less well understood. The importance of these different mechanisms for sediment emplacement will depend on how rapidly sediment is emplaced and the flow dynamics within these fractures.

2.4.5 Interpreting hydrofracture fills as records of fluid pressure through time

If the sediment within glacial hydrofractures is emplaced by multiple externally-created fluid pulses, then the injection of a new fluid pulse must represent an increase in the fluid pressure gradient across a fracture, potentially producing erosion and then the deposition of new material (Phillips et al., 2013). In this way, the microstructures in the fills of glacial hydrofractures have been interpreted as records of the fluid pressure fluctuation during the hydrofracture evolution (Dionne and Shilts, 1974; Christiansen et al., 1982; Phillips et al., 2013; Ravier et al., 2015).

The greatest fluid pressure gradient across a hydrofracture will be related to the fracture opening, especially if a new fracture must be propagated rather than opening a pre-existing weakness (Figure 2.8a). When the fluid velocity wanes, deposition can occur within the

fracture if the fluid velocity is sufficiently slow to cross the deposition threshold. A subsequent fluid pulse is likely to be lower pressure than the initial fracture opening, as the fluid is now only reopening the already existing hydrofracture (Figure 2.8b). The injection of this new pulse may produce erosion and then the deposition of new sediment units once the fluid velocity wanes (Phillips et al., 2013; Ravier et al., 2015). Each erosive surface within a hydrofracture may therefore represent a new fluid pulse injected into the hydrofracture, with erosion occurring at the peak in overpressure associated with the start of the fluid injection. A change in the fluid pressure of the source could increase the fluid pressure available for hydrofracturing, producing larger injections with the ability of erode or remobilise large volumes of material within the fracture (Figure 2.8c).
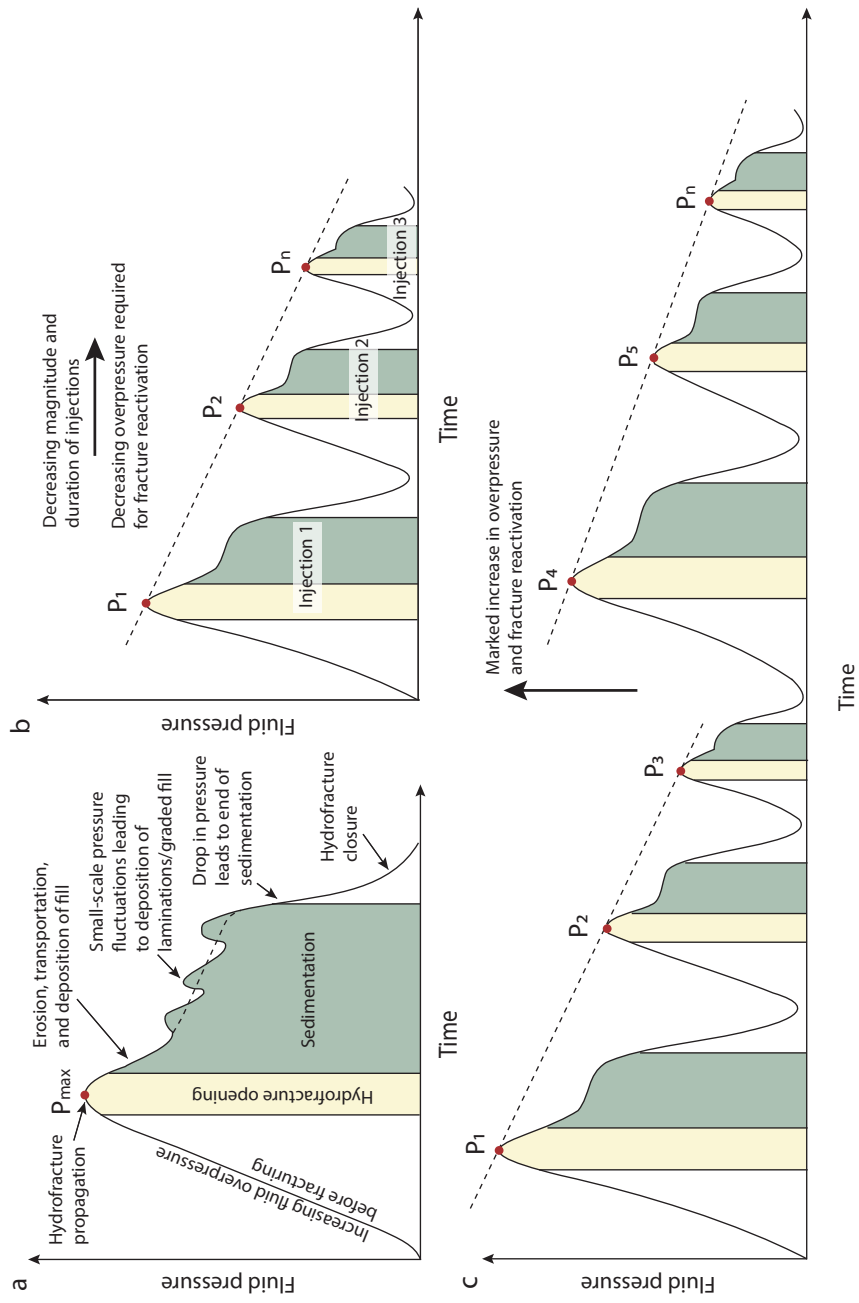
Figure 2.8: Theoretical evolution of fluid pressure through time within a hydrofracture, modified from Phillips et al. (2013). a) The greatest fluid pressure will occur at the time of fracture opening, after which flow through the fracture will reduce the excess pressure. A drop in the fluid pressure of the source through time will decrease the fluid pressure gradient across the fracture, resulting in a lower fluid velocity and potentially particle deposition. Smaller fluctuations in fluid pressure could drive the formation of laminations or graded bedding within the sediment fill, either driven by changes in the source or local pressure changes due to particles filling the fracture and restricting flow. This process will repeat each time a new injection into the fracture occurs. b) If the injections of fluid occur as part of an overall trend of waning fluid pressure, later injections will be smaller in magnitude, perhaps eroding and depositing less material within the fracture or occurring for a shorter duration. c) A marked increase in pressure through time, most likely due to a change in the pressure of the source, could reactivate the hydrofracture and cause large amounts of erosion of pre-existing material before later deposition.

57

The source of the peaks in overpressure may be due to fluctuations in the source, but could also be driven by internal variations within the fracture, for example clogging of the fracture with particles locally limiting fluid flow and producing localised overpressures. Hydrofractures in the laboratory have been seen to propagate in a step-wise manner (Chen et al., 2015), and a sudden increase in fracture length could also create localised increases in fluid pressure gradient that could produce erosive structures that may be misinterpreted as the injection of new fluid pulses.

2.4.6 Gaps in our knowledge of hydrofractures in other environments

Particle-filled hydrofractures in non-volcanic environments are much better studied than tuffisites, but there are multiple gaps in our understanding of the processes occurring during hydrofracture formation. Some outstanding questions include:

1. How great an overpressure is required for hydrofracture emplacement and how fast are the resulting fluid velocities?

2. Do structures within hydrofractures represent pulsed or continuous flow?

3. How quickly are hydrofractures emplaced?

4. Why are sand injectites typically massive in structure unlike glacial hydrofractures, and do these differences reflect contrasting flow dynamics within fractures?

While tuffisites are currently much less studied than hydrofractures in non-volcanic environments, the high temperature and high pressure environment of tuffisites may allow for some knowledge of tuffisites to be eventually applied back to sedimentary environments. For example, the welding of particles within tuffisites may be able to provide an overall emplacement timescale (Wadsworth et al., 2017), and H_2O concentrations within glass-walled tuffisites have also been used to estimate tuffisite formation pressures (Castro et al., 2014).

2.4.7 Comparing hydrofractures and tuffisites

Tuffisites have very a similar appearance to hydrofractures in sedimentary environments but will have formed in a much higher temperature and likely higher pressure environment, which could lead to differences in the mechanism of their formation. The hot sticky particles injected into tuffisites may influence sedimentation, and the injection of a low viscosity ash-gas mixture into a fracture will potentially produce quite different fluid dynamics to the injection of water. The source of overpressure producing tuffisites is much clearer than in the sedimentary environment, with high pressure fluids available to open new fractures. The greater formation pressures of tuffisites compared to sedimentary hydrofractures may produce fractures of different morphologies, and also suggest that fluid may be injected at a much greater velocity into tuffisites, perhaps altering the structures produced within the particle fill. The pressure within the volcanic conduit that is driving tuffisite formation is likely to be more variable than the fluid pressure in the sedimentary environment, which might cause tuffisites to be emplaced in a more pulsatory manner than sedimentary hydrofractures.

2.5 Conclusions

Improving our understanding of the processes occurring during the evolution of silicic vents and explosive volcanic eruptions is necessary to improve the modelling of eruption dynamics and hazard forecasting. This will require bringing together our understanding from direct observations of eruptions, field evidence, and seismic measurements to create a consistent model that can describe the evolution of silicic systems and their behaviour through time. Tuffisites have been suggested to act as efficient outgassing pathways allowing for the reduction of excess pressure from the conduit zone, as well as a potential source of seismicity in the lead up to and during eruptions. The recognition that there are similarities between tuffisites and conduits has led to the suggestion that they may form by the same processes, with differences only in scale. By investigating the characteristics of tuffisites, we can therefore gain an insight into both tuffisite formation and the evolution of silicic vents through time.

3 Pressure-Driven Opening and Filling of a Volcanic Hydrofracture Recorded by Tuffisite at Húsafell, Iceland: A Potential Seismic Source

Holly E. Unwin, Hugh Tuffen, Emrys Phillips, Fabian B. Wadsworth and Mike R. James

Abstract

The opening of magmatic hydraulic fractures is an integral part of magma ascent, the triggering of volcano seismicity, and defusing the explosivity of ongoing eruptions via the outgassing of magmatic volatiles. If filled with pyroclastic particles, these fractures can be recorded as tuffisites. Tuffisites are therefore thought to play a key role in both initiating eruptions and controlling their dynamics, and yet their genesis remains poorly understood. Here we characterise the processes, pressures and timescales involved in tuffisite evolution within the country rock through analysis of the sedimentary facies and structures of a large sub-horizontal tuffisite vein, 0.9 m thick and minimum 40 m in length, at the dissected Húsafell volcano, western Iceland. The vein occurs where a propagating rhyolitic sheet intrusion stalled at a depth of $\sim$500 m beneath a relatively strong layer of welded ignimbrite. Laminations, cross-stratification, channels, and internal injections indicate erosion and deposition in multiple fluid pulses, controlled by fluctuations in local fluid pressure and changes in fluid-particle concentration. The field evidence suggests that this tuffisite was emplaced by as many as twenty pulses, depositing sedimentary units with varying characteristics. Assuming that each sedimentary unit ($\sim$0.1 m thick and minimum 40 m in length) is emplaced by a single fluid pulse, we estimate fluid overpressures of $\sim$1.9–3.3 MPa would be required to emplace each unit. The Húsafell tuffisite records the repeated injection of an ash-laden fluid within an extensive

subhorizontal fracture, and may therefore represent the fossil record of a low-frequency seismic swarm associated with fracture propagation and reactivation. The particles within the tuffisite cool and compact through time, causing the rheology of the tuffisite fill to evolve and influencing the nature of the structures being formed as new material is injected during subsequent fluid pulses. As this new material is emplaced, the deformation style of the surrounding tuffisite is strongly dependent on its evolving rheology, which will also control the evolution of pressure and the system permeability. Interpreting tuffisites as the fossil record of fluid-driven hydrofracture opening and evolution can place new constraints on the cycles of pressurisation and outgassing that accompany the opening of magmatic pathways, key to improving interpretations of volcanic unrest and hazard forecasting.

3.1 Introduction

Magma ascent typically requires the upward propagation of fractures in the shallow crust, producing pathways to transport magma and exsolved gases. Fracture formation is controlled by fluid pressure, the surrounding stress field, and country rock properties (Rubin, 1995; Gudmundsson, 2011; Geshi et al., 2012). Whereas mafic dyke emplacement models account for the associated fracturing of country rock (e.g., Taisne and Jaupart, 2009; Rivalta et al., 2015), this aspect has received surprisingly little attention for silicic magma. As fragmentation is expected to be characteristic of the ascent of silicic magma within the upper two kilometres of the crust (Wadsworth et al., 2020), the first silicic magma entering a propagating fracture tip will be in a fragmental state (e.g., Heiken et al., 1988). The opening of silicic magma pathways will therefore differ from their mafic equivalents, with a gas-pyroclast mixture at the propagating fracture tip, rather than intact magma following an initial gas pocket (Rubin, 1995). Field evidence suggests that fractures in silicic systems may also open laterally as off-shoots from a main sub-vertical fracture network or conduit (Stasiuk et al., 1996). A tuffisite is formed where the fragmented material is transported and deposited within the opening fracture system. The scarcity of well-exposed fossil silicic conduit systems has hindered advances in understanding, and a principal motivation for this study is to provide the

most detailed description of a tuffisite within such a silicic system.

Documented shallow silicic conduit systems, whether exposed by erosion (Stasiuk et al., 1996; Tuffen and Dingwell, 2005), intercepted by boreholes (Eichelberger et al., 1986; Heiken et al., 1988) or reconstructed from ejected pyroclasts (Castro et al., 2014; Isgett et al., 2017; Colombier et al., 2020), have a number of key characteristics. The main conduit is plugged by coherent magma, which may contain healed clastic textures that indicate cycles of fracture, ephemeral clastic transport, and healing (internal tuffisite veins in Figure 3.1; Tuffen and Dingwell, 2005). Where the conduit walls are exposed, tuffisite veins are observed propagating into the country rock (external tuffisite veins in Figure 3.1; Stasiuk et al., 1996; Heiken et al., 1988). Diverse clast types in internal and external tuffisites indicate fracture-enabled material transport over distances of hundreds of metres within the shallow conduit systems (Saubin et al., 2016).

Tuffisites have been invoked as outgassing pathways (Jaupart, 1998; Castro et al., 2012, 2014; Berlo et al., 2013; Farquharson et al., 2017; Heap et al., 2019; Kolzenburg et al., 2019), providing focussed loci for gas escape, in contrast with more widely distributed gas leakage through permeable country rocks (e.g., Eichelberger et al., 1986; Rust et al., 2004; Lavallée et al., 2013; Farquharson et al., 2015). In particular, external tuffisites have been touted as pathways for significant escape of magmatic gases from the main conduit zone, perhaps dissipating sufficient gas pressure to trigger a change in eruption style from explosive toward dominantly effusive (Stasiuk et al., 1996; Castro et al., 2014). However, the details of how this transition takes place remain contested, and existing models of tuffisite-enabled outgassing, which hinge upon the temporal evolution of permeability, are necessarily simplistic.

The permeability of tuffisites is transient as deposition will clog the fracture (e.g., Tuffen et al., 2003; Saubin et al., 2016; Heap et al., 2019), and sintering of deposited particles will further decrease permeability, slowing outgassing (Stasiuk et al., 1996; Okumura and Sasaki, 2014; Wadsworth et al., 2016; Gardner et al., 2018). Current models of the permeability evolution of external tuffisites assume instantaneous filling of the entire tuffisite by a single pulse of particles (Kolzenburg et al., 2019; Wadsworth et al., 2021).

Improved understanding of outgassing through external tuffisites needs to build upon geological evidence from dissected systems, which preserve details of tuffisite deposition. Unsteady flow in the volcanic conduit produces pressure fluctuations that control the formation and input of material into the evolving tuffisite. A basic but enigmatic question is whether tuffisites are "single-pulse", carrying only one pulse of particle-laden gas, or whether they are repeatedly reactivated — as inferred in source models for low-frequency volcanic earthquakes that involve the repetitive, non-destructive resonance of a stationary fluid-filled crack (Figure 3.1; Chouet, 1996; Kumagai and Chouet, 2000). Low-frequency seismic events can cluster into swarms whose shifting waveforms indicate a systematic change in the nature of crack resonance, interpreted as particles progressively filling a fracture system (Molina et al., 2004). Seismic trigger models appealing to crack resonance (e.g., Chouet, 1996) require the injection of pressurised fluid into a fracture tens or hundreds of metres in length. Although this is consistent with the geochemically-inferred extent of tuffisite veins in the Chaitén conduit (Castro et al., 2014; Saubin et al., 2016), there is little detailed documentation of such extensive tuffisite systems in the geological record. Tighter constraints on the longevity of fluid flow through tuffisite veins will assist modelling of both pre-eruptive unrest and eruption dynamics, thus improving forecasting of volcanic hazards.

In this paper we begin to address this knowledge gap by interpreting the structures in the fill of a large (0.9 m wide, 40 m long) tuffisite emanating from a silicic conduit at Húsafell volcano in west Iceland (Saubin et al., 2019), interpreted as recording fluctuations in fluid pressure and variations in the fluid characteristics during tuffisite formation. By identifying individual depositional units and the relationships between them, we have been able to constrain the fluid pressure required for tuffisite formation, as well as the timescales involved.

3.1.1   Characteristics and formation of tuffisites

Tuffisites are particle-filled fractures found within volcanic conduits or the surrounding country rock (Figure 3.1; Heiken et al., 1988; Tuffen et al., 2003). Internal tuffisites form within volcanic conduits and propagate through hot magma when stresses rise

63
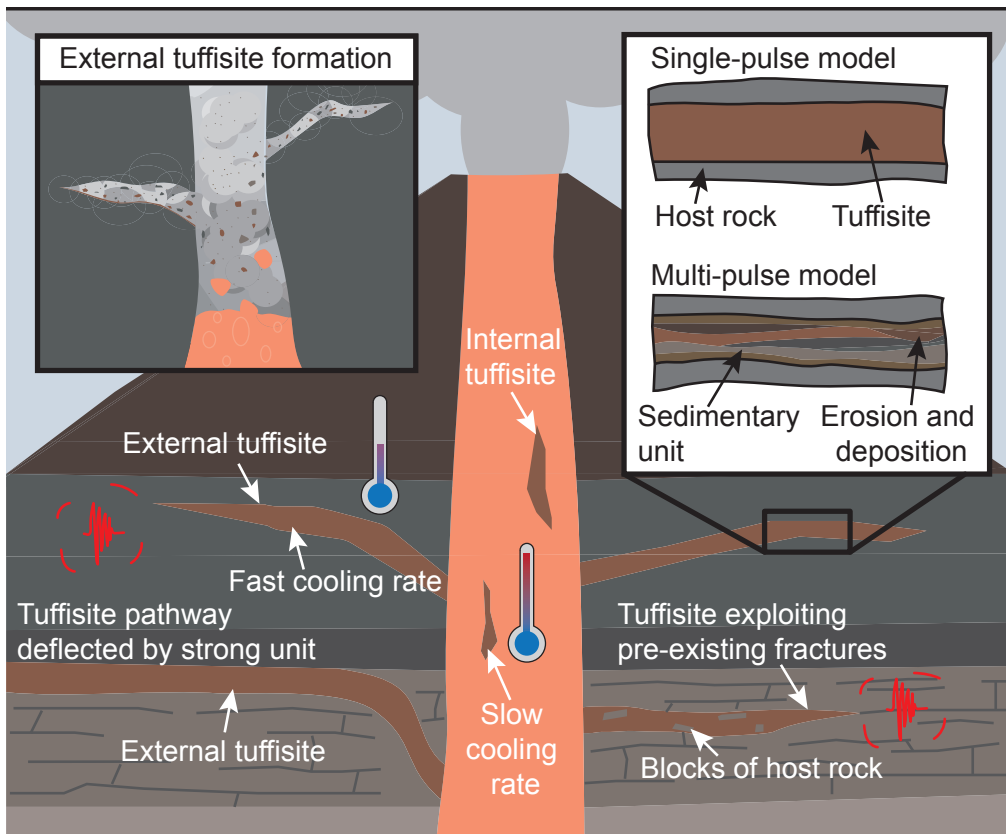
Figure 3.1: Schematic showing the position of internal and external tuffisites with relation to the volcanic conduit. Internal tuffisites form within volcanic conduits, propagating through hot magma itself. External tuffisites form in the country rock surrounding the conduit when the fluid pressure exceeds the strength of the country rock. The morphology of external tuffisites, like magmatic dykes and sills, is influenced by the characteristics of the host rock. Tuffisites can be guided by pre-existing fractures, exploiting the easiest pathway for propagation. Strong units may act as barriers to fracture propagation, deflecting or temporarily stalling a propagating fracture. External tuffisites will cool more rapidly than internal tuffisites, as they are injected into the cold country rock. Tuffisites formed by only one pulse of material will have a simple internal structure, typically with fine-grained margins grading into a coarser-grained centre. Tuffisites formed by multiple pulses have a more complex structure, with multiple sedimentary units that may have erosive boundaries.

to meet or exceed the strength of the magma (equivalently, the rates of deformation imparted by those rising stresses exceed the inverse relaxation time of the magma and cause mode 2 or 3 fractures; Tuffen and Dingwell, 2005). Such internal tuffisites form interconnected networks of fractures (Kendrick et al., 2016; McGowan, 2016; Saubin et al., 2016; Paisley et al., 2019a). By contrast, external tuffisites form in country rock when the fluid pressure exceeds the country rock strength, and must also overcome the lithostatic stress exerted by the overlying rock to widen (mode 1 fractures; Hubbert and Willis, 1957). This mechanism is comparable to the formation of magmatic dykes and sills (Rubin, 1995), glacial hydrofractures (Rijsdijk et al., 1999; Van Der Meer et al., 1999; Phillips et al., 2013; Phillips and Hughes, 2014) and sand injectites (Cosgrove, 2001; Boehm and Moore, 2002; Cobain et al., 2015). The similarities of external tuffisites to hydrofractures in sedimentary settings lead us to interpret tuffisites as a sub-set of hydrofractures, though the different temperature, pressure and fluid characteristics of tuffisites (Heiken et al., 1988; Castro et al., 2012) to the water-opened hydrofractures of other environments (Jonk, 2010) must be acknowledged.

External tuffisites are particle-filled sub-vertical or sub-horizontal fractures that are connected to the conduit, often following weaknesses such as pre-existing fractures (Figure 3.1; Stasiuk et al., 1996). These tuffisites range from millimetres to over a metre in width and from tens of centimetres to tens of metres in length, and branch to form smaller fractures toward the tip of the main vein (Heiken et al., 1988; Stasiuk et al., 1996). Tuffisites are filled with lithic and juvenile clasts, including pumice and dense lava fragments, with clasts ranging from microns to centimetres in size (McGowan, 2016; Saubin et al., 2016).

In both internal and external tuffisites, clasts may be organised into different layers or units, resembling bedding (Heiken et al., 1988; Tuffen et al., 2003; Tuffen and Dingwell, 2005), or the tuffisite interior may lack obvious internal structure (Saubin et al., 2016). The presence of bedded units and structures such as cross-stratification and graded bedding suggest substantial fluid flow through the fracture (Heiken et al., 1988; Tuffen et al., 2003; van der Meer et al., 2009; Hurst et al., 2011; Phillips et al., 2013).

At the sub-surface depth of tuffisite formation (<2 km) the silicic magma column is likely

to be fragmented (Wadsworth et al., 2020), providing a ready source of clastic material to be injected into hydrofractures within the country rock. Explosive volcanic eruptions and the associated volcanic ash plumes are unsteady, with pressure fluctuations that can drive fracture and tuffisite formation. Once a sufficient critical fluid pressure is reached, a hydrofracture can be opened. Hydrofracture opening produces a drop in fluid pressure in the gas-ash dispersion, creating a pressure gradient that facilitates the transport and injection of gas and particles into the evolving fracture system (Heiken et al., 1988; Jolly and Lonergan, 2002). Spatial or temporal variations in fluid velocity inside the fracture can lead to changes in fracture thickness, particle settling or erosion of the deposited particles, potentially developing sedimentary structures such as cross-bedding (Kern et al., 1959; Heiken et al., 1988; Phillips et al., 2013). Large particles can initially prop open the fracture as it closes, maintaining its permeability, but through time the fracture may become clogged with finer particles (Farquharson et al., 2017; Heap et al., 2019). In many tuffisites, there is evidence that the particles compact and sinter together at the end of the tuffisite lifecycle, further reducing permeability and limiting the period of degassing (Tuffen et al., 2003; Heap et al., 2019). The ability of a tuffisite to sinter is related to its temperature, and the melt proportion, such that only melt-rich tuffisites that can remain sufficiently insulated from cooling can sinter and weld shut (Wadsworth et al., 2014, 2021; Kolzenburg et al., 2019).

The lifetime of a tuffisite has been inferred using the timescales of welding and compaction, together with dissolved water and trace element diffusion gradients around veins. Inferred timescales for gas transport within veins range from ∼15 min to ∼1 day (Castro et al., 2012; Berlo et al., 2013; Saubin et al., 2016; Paisley et al., 2019b; Wadsworth et al., 2019). H_2O concentrations in glass-walled tuffisites allow for estimates of the pressure changes associated with tuffisite formation, including transient pressure drops on fracture opening of a few megapascals, and also, in some instances, the ephemeral development of overpressure inside the tuffisite due to blockages (Castro et al., 2014).

3.2 Location and geological setting of the Húsafell study area

Húsafell volcano, in west Iceland (80 km NE of Reykjavik), was active at 3–2.5 Ma, with three phases of silicic volcanism separated by glacial events and mafic eruptions (Sæmundsson and Noll, 1974; Figure 3.2). The first phase of activity began with the emplacement of dacitic lavas >100 m thick, exposed to the west of Húsafell (Figure 3.2), followed by the deposition of the Hraunfossar ignimbrite. The second phase of activity was more explosive, consisting of rhyolitic ash-dominated fall deposits and ignimbrites, including the Deildargil ignimbrite, well-exposed in the valley of Deildargil, the location of this study (Sæmundsson and Noll, 1974). In the third phase of activity numerous dacitic and rhyolitic lavas, rhyolitic ash-dominated fall deposits and ignimbrites were emplaced before the volcano was buried by a thick succession of basalt lava flows originating east of Húsafell. Large volumes of ignimbrite were emplaced and, during the final phase, numerous SW–NE dipping silicic dykes, sheets, domes, and vents were formed (Sæmundsson and Noll, 1974). These features have been dissected in the valley of Deildargil (140 m above sea level), where there is a silicic intrusion emplaced at ~500 m depth, as inferred from magmatic $OH-$ in hydrous glasses (McGowan, 2016). This intrusion outcrops as multiple segments along the valley, cross-cutting a series of ignimbrites, conglomerates, and basaltic lavas (Saubin et al., 2019). The ignimbrite appears to have deflected the ascending rhyolitic sheet, temporarily stalling its ascent (McGowan, 2016). A near-horizontal tuffisite ~0.9 m wide and 40 m long cuts through the contact separating a lower densely welded ignimbrite from an overlying more friable, less densely welded ignimbrite (Figure 3.3). Lack of exposure at both ends of the tuffisite outcrop prevents the preservation of the true length of the tuffisite and the fracture tip, but provides a detailed view of the structures within the tuffisite fill.

3.3 Field methods

The Húsafell tuffisite provides an opportunity to analyse the facies and structures of a tuffisite in detail. The field evidence is key for the reconstruction of tuffisite evolution and interpretation as a record of fluid pressure through time. Vertical graphic logs were

67
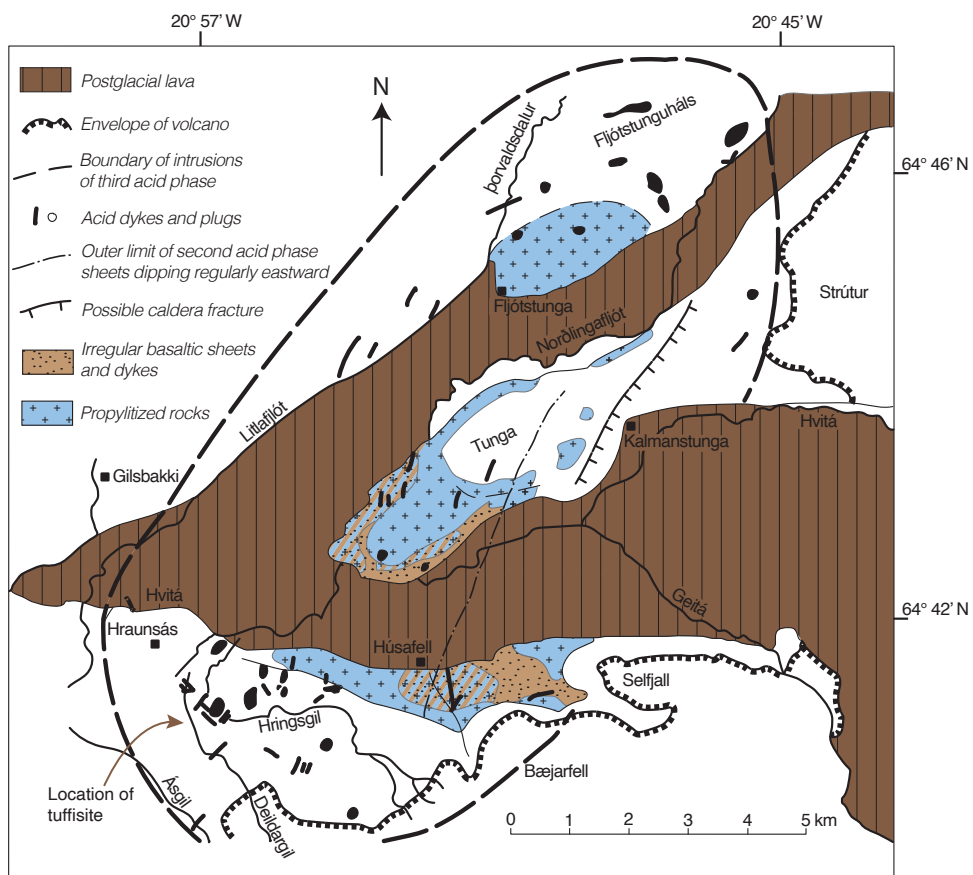
Figure 3.2: Map of the geology of the Húsafell area with the location of the tuffisite, in Deildargil. Adapted from Sæmundsson and Noll (1974).

taken every ~2 m along the main body of the tuffisite, recording the characteristics of each unit including particle-size and details of any structures present within the unit. Different units were identified by changes in particle-size, clast abundances or composition. The composition of the clasts and matrix material was established in the field with aid of a hand lens. The northern end of the tuffisite forms part of a vertical cliff outcrop, with sections that could not be accessed for logging in the field. Graphic logs were instead produced from high resolution panorama-style photographs of the outcrop, ground-truthed using observations of the same units accessible laterally, where possible. These photographs were also used to connect logs to create a structural interpretation of the whole outcrop. Oriented samples collected across the length of the outcrop were thin sectioned, enabling the examination of the range of microstructures present within the different units identified within the tuffisite.

3.4   Field observations

3.4.1   The Tuffisite Morphology and Broad Structure

The tuffisite occurs horizontally along the contact between two ignimbrite units, forming a sill of pyroclastic material (Figure 3.3). The tuffisite fill is composed of a mixture of rhyolitic pumice, dense obsidian and ash shards, together with fragments of the surrounding ignimbrite. The unit beneath the tuffisite and forming its lower boundary is a welded ignimbrite unit composed of massive glass (black ignimbrite), while the unit above the tuffisite and forming its roof is much more friable, fractured, and devitrified (red ignimbrite; Figure 3.3; Saubin et al., 2019). The black ignimbrite is laterally heterogeneous, appearing less densely welded to the south. Abundant near-horizontal platy fracturing within the red ignimbrite pre-dated tuffisite formation, and facilitated the detachment and incorporation of red ignimbrite blocks into the tuffisite. The wall rock lithology appears to have controlled the morphology of the tuffisite margin, with a sharp planar contact at the tuffisite base, against the black ignimbrite, and a more irregular upper margin as the tuffisite was guided by and exploited weaknesses in the overlying red ignimbrite (Figure 3.3). Although the upper margin is not planar, the

69

tuffisite does not form offshoots into the roof rock. The tuffisite is offset by two minor faults along its length, displacing it by about 20 cm, and there are numerous sub-vertical fractures through the tuffisite that also cross-cut the overlying red ignimbrite.
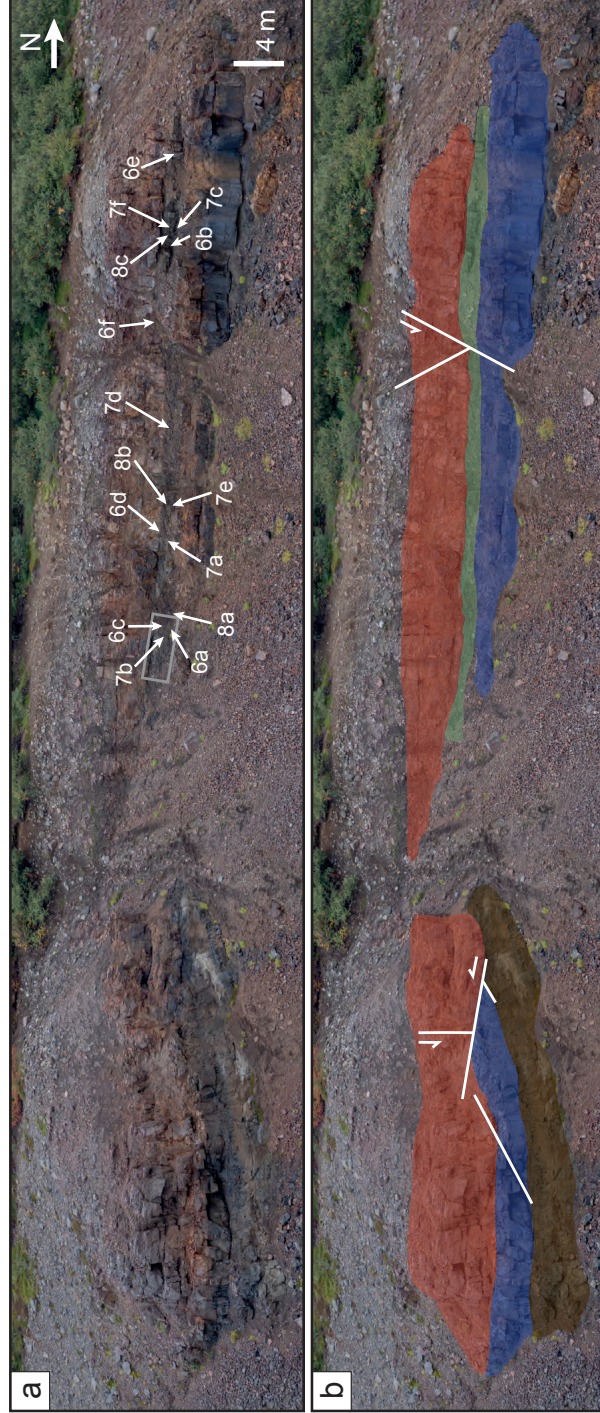
Figure 3.3: Photograph (a) and interpretation (b) of the intrusive system. The upper red ignimbrite is coloured red, lower welded black ignimbrite in blue, the tuffisitic sill in green, and magmatic intrusion in brown. The grey box shows the position of the photograph shown in Figure 3.4, and labels indicate the position of the photographs in Figures 3.6–3.8.

The tuffisite has a well-defined but locally complex internal structure consisting of 0.5–20 cm thick units aligned roughly parallel to the tuffisite walls (Figure 3.4). We adopt a strategy for distinguishing individual depositional units that is based on the following characteristics: grain-size, clast composition, colour, internal structure, and the presence of erosion surfaces.

Most units are laterally continuous for several metres, but thinner units seldom extend >1 m, and such laterally discontinuous units pinch out at the edges after 0.3–1 m. The sequence of units fines upwards from the tuffisite base, but the grain-size increases again immediately above a number of prominent erosive contacts, with material clearly cross-cutting the units underneath. This fining upwards sequence is also interrupted by discontinuous coarse-grained units (Figure 3.5). All of the units show evidence for a degree of sintering — evidenced by induration — but while some areas show greater sintering, to moderately well-sintered, the degree of sintering does not appear to vary systematically along the tuffisite.

3.4.2 Facies Descriptions

The different characteristics of the tuffisite units allow them to be divided into facies of different grain sizes, described here in order, moving upwards from the tuffisite base in an overall fining-upwards sequence. Individual facies are then divided into subfacies of units, defined by the presence or absence of internal structure. Each facies is named according to the pyroclastic lithofacies naming scheme of Branney and Kokelaar (2002) and the characteristics of each facies within the Húsafell tuffisite are summarised in Table 3.1.

3.4.2.1 Massive Lithic Breccia (mlBr)

At the very base of the tuffisite, where preserved, is a massive <20 cm thick breccia unit containing clasts of ignimbrite, derived from the black ignimbrite unit below, as well as subrounded clasts of rhyolitic pumice and dense obsidian (Figures 3.6a,b). This unit forms the base of a <50 cm thick sequence of units, each with a finer grain-size than the
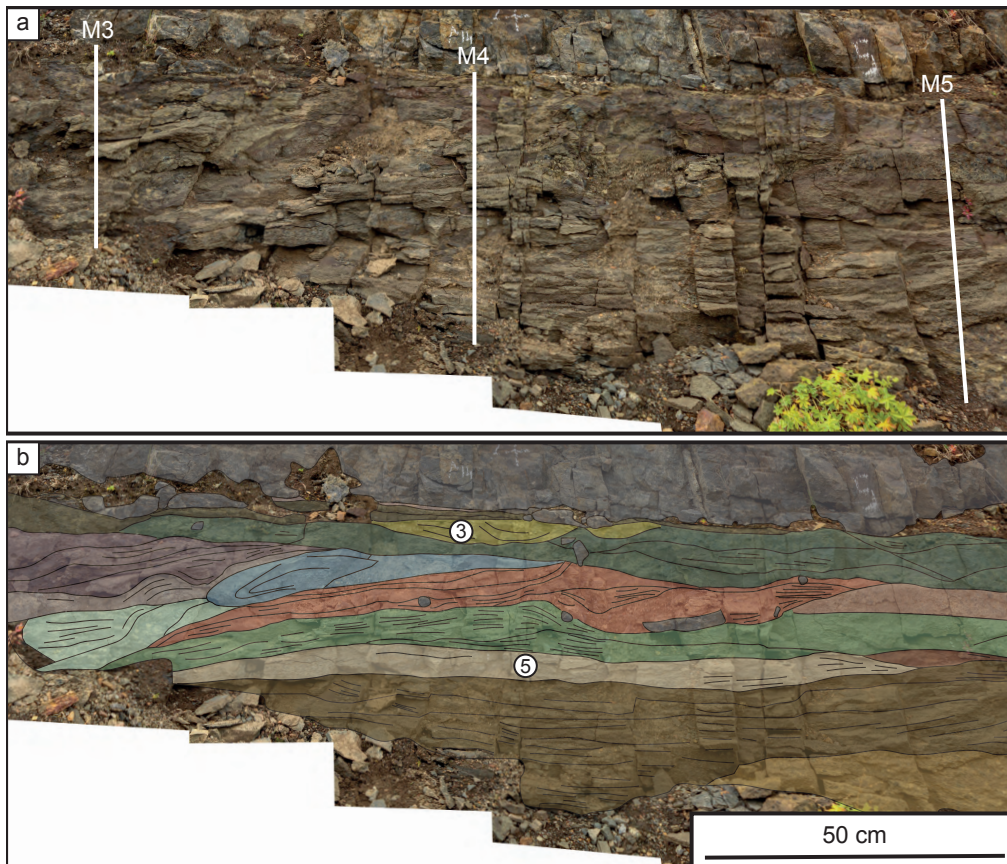
Figure 3.4: Photograph (a) and interpretation (b) showing a closer view of the tuffisite, which has a clear but complex internal structure consisting of many units. M3, M4, and M5 labelled on (a) give the location of the graphic logs shown in Figure 3.5. Labels 3 and 5 mark examples of Structure 3 (channels; Section 3.5.3.3) and Structure 5 (fine rimmed sub-horizontal lenses, interpreted as finger-shaped injections in Section 3.5.3.5). Note how units are dipping toward the S. Colours are schematic to separate units of different appearances in the outcrop.
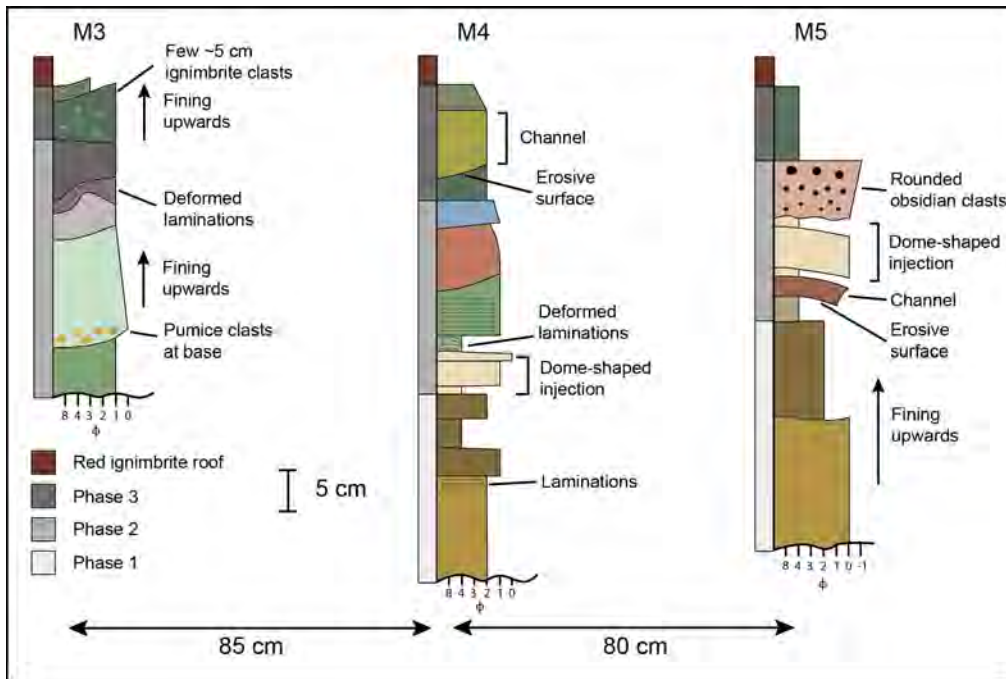
Figure 3.5: Three graphic logs through the tuffisite each spaced about 80 cm apart, hung from the red ignimbrite at the top of the tuffisite. The locations of logs are labelled in Figure 3.4, and beds are given corresponding colours. The tuffisite is composed of fining upwards sequences, interrupted by coarser laterally discontinuous units. The deposition of units can be separated into three different phases, allowing for an overall model of tuffisite emplacement to be interpreted.

units beneath. Other massive breccias are found in the upper 25 cm of the tuffisite and are less laterally continuous as they are cross-cut or truncated by other units.

Table 3.1: Summary of the different tuffisite facies and their characteristics.

	Facies		Clasts	Matrix	Remarks
Lithic breccia	mlBr — Massive lithic breccia	Pumice-rich end member	20–40% rounded, high sphericity pumice 0.2–1 cm across. ≤5% subrounded–angular high sphericity ignimbrite ≤2 cm across.	Yellow-grey, fine lapilli-tuff sized pumice-rich matrix.	Poorly sorted matrix supported lithic breccia, clast supported in places.
			~2% rounded–subangular spherical dense obsidian ≤1 cm across. Rare grey lithics ≤2 cm across.	10% angular dense obsidian chips. ≤2% subangular ignimbrite chips.	Clasts typically show no alignment.
		Ignimbrite-rich end member	~20% subangular-subrounded ignimbrite 1–2 cm across, with aspect ratio ≤2. 2% rounded spherical pumice ≤1 cm across. Rare rounded high sphericity vesicular lithics ≤2 cm across.	Grey-green, fine lapilli-tuff sized pumice-rich matrix. 30% angular dense obsidian chips.	Poorly sorted and matrix supported. Large ignimbrite blocks up to 19 cm across.
	dslBr — Stratified lithic breccia		Clasts unevenly distributed in pockets and varying from 5 to 30% of rock. ≤30% rounded spherical pumice ≤2% cm across. ≤2% subangular ignimbrite ~0.5 cm across, aspect ratio ≤1.5.	Medium lapilli-tuff sized pumice-rich matrix.	Ignimbrite clasts are aligned parallel to tuffisite walls or sub-horizontally defining cross-stratification. Contains irregularly shaped pockets of laminated ash-size material (sT).

		Clasts	Matrix	Notes
Lapilli-tuff	mLT — Massive lapilli-tuff	Pumice-rich end member	10–20% rounded spherical pumice 1–3 mm across. 10% subrounded-angular ignimbrite ≤2 mm across. Rare grey lithics.	Yellow-brown, fine lapilli-tuff sized pumice-rich matrix. 5% dense obsidian chips.	One unit entirely moderately well sorted, medium lapilli-tuff sized pumice grains. More common unit described here.
		Ignimbrite-rich end member	10–30% subrounded-angular ignimbrite clasts ≤2 mm across, aspect ratio ≤1.4. 2% grey lithics ≤1 cm across. ≤2% rounded pumice clasts 0.5–2 mm across.	Grey-green, fine lapilli-tuff sized pumice-rich matrix. 30% angular dense obsidian chips ≤0.5 mm across.	Ignimbrite clasts may show alignment parallel to tuffisite walls.
	dsLT — Stratified lapilli-tuff		≤20% rounded spherical pumice clasts in pockets generally 2–3 mm across, largest 3 cm across. ≤5% subangular ignimbrite ≤5 mm across. ≤5% rounded obsidian 3 mm across.	Pumice-rich with ≤20% subangular dense obsidian chips.	Often interbedded with sT. Ignimbrite clasts aligned parallel to tuffisite walls. Cross-stratification, graded beds and laminated lenses.
Tuff	mT — massive tuff		≤5% rounded-subrounded ignimbrite clasts ≤1 cm across. ≤2% rounded pumice clasts ~0.25 mm across.	Moderately well sintered material that weathers red.	Ignimbrite clasts can show some alignment parallel to tuffisite walls.
	sT — Stratified tuff		Rare subangular-subrounded ignimbrite clasts up to 2 cm across, aspect ratio ≤1.4.	Well sorted glassy shards of pumice and dense obsidian.	Laminated material commonly showing cross-stratification, graded beds and soft sediment deformation.

The units form a spectrum between two end-members of pumice-rich and ignimbrite-rich breccias. The pumice-rich end-member is matrix-supported with 25–30% clasts, but may be locally clast-supported, with ≤50% clasts, and larger clasts appear more rounded. The ignimbrite-rich end-member is less clast rich, with clasts forming around 20% of the rock. More details on the componentry of both end-members can be found in Table 3.1. The clasts show no alignment or arrangement.

3.4.2.2   Stratified Lithic Breccia (dslBr)

Breccia units <10 cm thick show alignment of clasts, particularly ignimbrite clasts. Most ignimbrite clasts have been derived from the overlying red ignimbrite. These units are typically finer than those of mlBr, with ≤2 cm clasts that are unevenly distributed (Figure 3.6c). Pumice clasts are typically seen in a greater concentration toward the top of each unit. These breccias are found in the upper 30 cm of the tuffisite, but are never the uppermost unit. The units can be laterally continuous for several metres but are typically crosscut or truncated by other units, creating erosive upper and lower boundaries.

3.4.2.3   Massive Lapilli Tuff (mLT)

The majority of the tuffisite consists of lenticular to laterally persistent, poorly sorted units of lapilli-tuff that form the centre of the tuffisite (Figures 3.6d,e). These units are usually part of a poorly defined fining upwards sequence, deposited as a series of southwards dipping units that are crosscut by later material. Coarse lapilli also forms discontinuous flat-based units with rounded tops. These massive units vary from about 8–30 cm in thickness and form a spectrum between pumiceous and ignimbrite-rich end members. The pumice-rich end-member is almost entirely formed of fine lapilli-sized pumice grains with sparse ignimbrite and obsidian particles, and forms the uppermost unit of the tuffisite, trapped between clasts of red ignimbrite (Figure 3.6f). The componentry of a more typical pumiceous unit is given in Table 3.1.
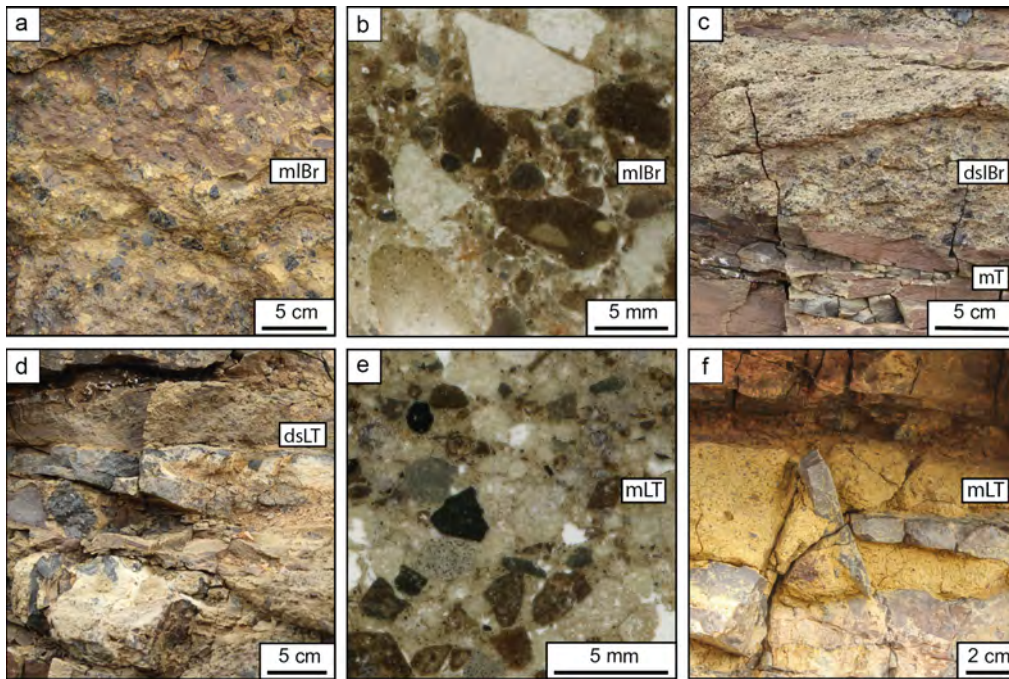
Figure 3.6: Photographs of different facies of coarse-grained material found in the tuffisite. Labels give the facies present in each image and are also listed in brackets. a) Massive breccia with pumice and obsidian clasts at the base of the tuffisite (Facies mlBr). b) Thin section of a massive breccia unit (Facies mlBr). c) Breccia unit with aligned clasts of red ignimbrite (Facies dsBr) with laminated tuff beneath (Facies sT) containing a coarser lens of medium lapilli grains. d) Massive lapilli-tuff (Facies mLT) separated from the units beneath by large clasts of red ignimbrite. e) Thin section with structureless units of coarse lapilli grains (Facies mLT). f) Yellow-orange pumiceous end member of Facies mLT, interfingered between clasts of red ignimbrite.
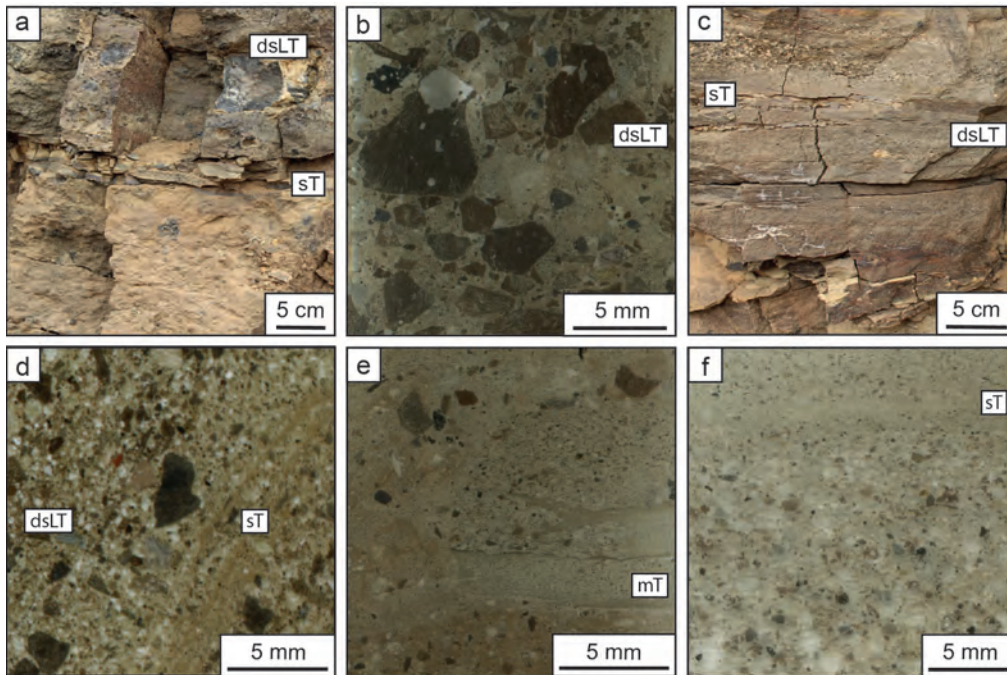
Figure 3.7: Photographs of the finer grained facies of the tuffisite. Labels give the facies present in each image and are also listed in brackets. a) Thinly bedded medium grained lapilli-tuff horizons of finer material (Facies dsLT) above large ignimbrite clasts. b) Thin section of a poorly sorted coarse lapilli-tuff showing some alignment of grains (Facies dsLT). c) Finely laminated and cross-stratified tuff (Facies sT) with thinly bedded medium grained lapilli-tuff beneath (Facies dsLT). d) Thin section of fine grained lapilli-tuff showing grain alignment (Facies dsLT), and finer horizons of ash-sized material (Facies sT). e) Thin section containing a discontinuous veinlet of massive fine material that coarsens toward the centre (Facies mT). f) Coarse lapilli-tuff fining upwards into Facies sT.

3.4.2.4   Stratified Lapilli Tuff (dsLT)

Units of lapilli-tuff found toward the tuffisite centre are often interbedded with thin horizons of finer grained material (Figure 3.7a). These units are typically 2–10 cm thick and may be laterally continuous for tens of centimetres or pinch out, forming lenses. Fine to coarse lapilli are mixed with occasional larger clasts to produce moderately to poorly sorted lapilli-tuffs (Figure 3.7b).

The units show a variety of different structures, including cross-stratification with foresets about 5 cm thick, defined by horizons of finer grained red material and the alignment of ignimbrite clasts. Graded beds of coarse to fine lapilli can be seen in both outcrop and thin-section scale, with both fining and coarsening upwards units (Figures 3.7c,d). Lenses of lapilli reach 15 cm in width and coarsen upwards, showing internal laminations, representing the migration of bedforms within the active hydrofracture.

79

3.4.2.5 Massive Tuff (mT)

The finest-grained massive units, which have ash-sized particles deposited in $\leq$5 cm thick units, are only seen in the upper half of the tuffisite fill, and their friable nature makes the rock prone to erosion. The rock weathers red and consistently appears to be moderately well-sintered. This facies also forms veinlets, with finer-grained margins and coarser centres, that cross-cut the surrounding tuffisite (Figure 3.7e).

3.4.2.6 Stratified Tuff (sT)

The majority of ash-sized material in the tuffisite forms thin ($\leq$2 cm thick) beds comprised of many sub-millimetre laminations of darker and finer material. Many of the laminae can be readily followed laterally for >20 cm, while other laminae crosscut one another or are more lenticular in shape, pinching out after a few centimetres (Figures 3.7a,c). This facies is often found interbedded with coarser-grained material, forming narrow laminated horizons. Cross lamination is very common, with foresets $\leq$3 mm thick.

The well-sorted nature of the finely laminated material is apparent in both outcrop and thin section. Glassy shards of obsidian give particles an angular shape. This material contains far fewer ignimbrite clasts than the coarser material mentioned above. In thin section, particles appear neatly organised into laminae that may grade into one another (Figures 3.7d,f).

3.4.3 Tuffisite Structures

The tuffisite contains a variety of structures that preserve key evidence for emplacement processes. Interpretation of these features will provide constraints on the processes occurring during tuffisite formation, and the fluid pressure required for its emplacement.

3.4.3.1 Structure 1: Entrainment of Clasts and Blocks

There are a number of $\leq$30 cm ignimbritic country rock blocks at the tuffisite base, consisting of roof material (Figures 3.6d,f, 3.7a, 3.8a). These elongated blocks are locally balanced on their end, and thus clearly rotated, but the surrounding finer sediment is massive, showing no variations in grain-size or clast distribution. Smaller clasts can
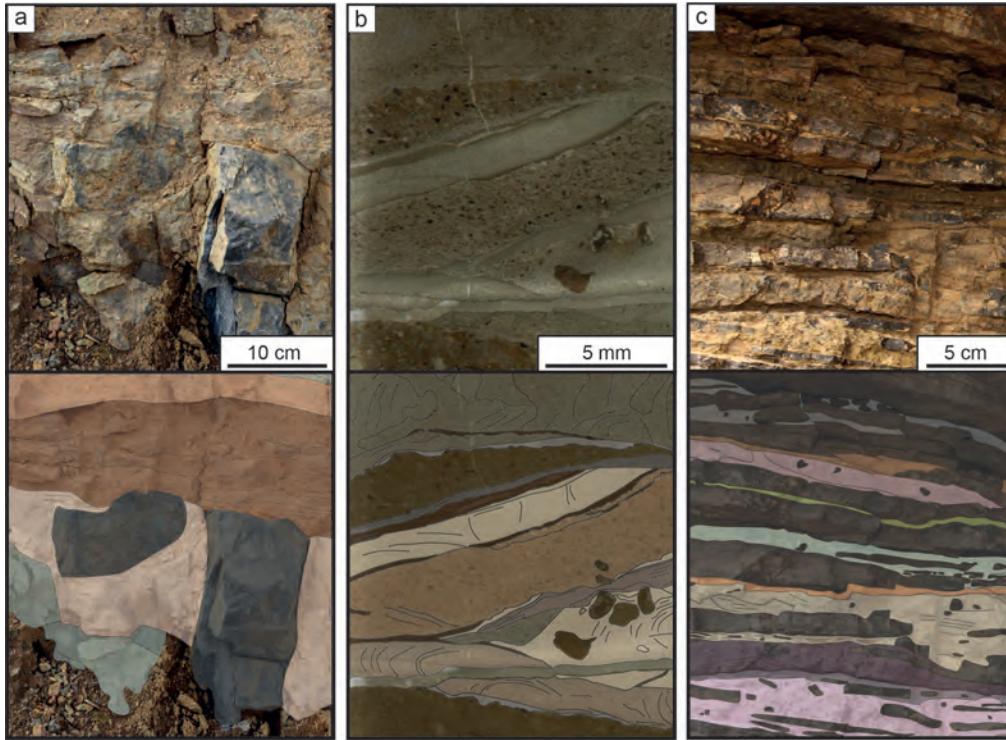
Figure 3.8: Structures seen in the tuffisite fill with photographs (top) and interpretations (bottom). a) A large block of red ignimbrite stood on its end at the base of the tuffisite surrounded by massive sediment (Structure 1). b) A thin section with particle-filled veinlets that have finely laminated material at their walls and a coarser massive centre (Structure 2). c) Ribbons of tuffisite interfingered with red ignimbrite sheets (Structure 4).

show shadow zones, with finer material clearly deposited on the southern side of $\sim$2 cm ignimbrite clasts.

3.4.3.2 Structure 2: Internal Veins

There are numerous places where the tuffisite fill is crosscut by thin veinlets of ash-sized material that do not follow bedding, indicating that they formed later than the main unit they cross-cut (Figures 3.7e, 3.8b). These features appear to be widespread, visible both in outcrop (veinlets $\sim$3 cm thick) and in many of the thin sections produced (veinlets <0.5 mm thick).

The cross-cutting material is always very fine-grained. In outcrop it often appears to be laminated, although the sub-millimetre laminations cannot be traced for more than a few centimetres before they are crosscut by another lamination. The margins of the cross-cutting veinlets are very fine, and the material crudely coarsens inwards. This is

best seen in thin section (Figures 3.7e, 3.8b), where injections have very fine-grained and laminated edges, and where wide enough, then coarsen into fine lapilli-sized material at their centres. The presence of multiple cross-cutting generations of veins indicates a repeated process. There is no visible deformation of the cross-cutting vein walls, which appear sharp, even in thin section. In outcrop, crosscutting veinlets follow sub-vertical fractures for ≤20 cm. Veinlets separate units with a very similar appearance. Some vein edge laminations have undergone soft-sediment deformation, forming a C-shape that spans the width of the unit and indicates a flow direction toward the concave edge of the C-shape, or toward the south (Figure 3.8b).

3.4.3.3   Structure 3: Channels

There are discontinuous units found in the upper half of the tuffisite, with rounded bases and approximately flat tops, that pinch out at both ends after 10–30 cm (Figure 3.4b). The structure is filled with coarse lapilli (Facies dsLT) and fines upwards into finer lapilli and ash-sized material, which is either laminated or deposited in much thinner beds. These units crosscut and erode the underlying units, indicating that their formation occurred during the later stages of infilling the tuffisite.

3.4.3.4   Structure 4: Interfingered Tuffisite and Ignimbrite Sheets

The tuffisite passes through a section of red ignimbrite that is stratigraphically higher at the northern end of the outcrop, due to the presence of a fault. Here, the tuffisite contains many elongate, sub-horizontal fragments of red ignimbrite host rock 2–15 cm thick, with an aspect ratio ∼5:1, each separated by a thin ribbon of sediment ≤10 cm in thickness (Figures 3.6f, 3.8c). The red ignimbrite sheets are all positioned in the uppermost third of the tuffisite width, although some red ignimbrite blocks are found lower down, typically at the base (Structure 1; Figure 3.8a). The long axis of each red ignimbrite block is aligned largely parallel to the fracture population in the country rock, but with some local rotation, and some larger red ignimbrite sheets are fractured vertically into multiple jigsaw-fit fragments arranged in one horizon. Adjacent red ignimbrite sheets can also appear displaced by linear sub-vertical fractures, sometimes filled with particles. In one area, the red ignimbrite blocks are arranged at a shallow angle to the tuffisite walls, giving the impression of cross-bedding or imbrication.

The sediment deposited between the red ignimbrite sheets, along both horizontal and vertical fractures, is composed of massive lapilli or ash-sized grains (Facies mLT or mT). Narrower gaps between ignimbrite clasts are infilled with finer sediment than those where the clasts are more widely spaced. The margins of each ribbon of tuffisite are slightly finer grained than the centre, similar to the internal veins (Structure 2). The sediment in the areas containing many ignimbrite clasts shows no internal structure, but prominent sedimentary structures, including cross-bedding and graded beds, do occur at the tuffisite base, where red ignimbrite clasts are absent (Facies dsLT).

3.4.3.5   Structure 5: Fine Rimmed Sub-Horizontal Lenses

Some units of massive, coarse to medium lapilli (Facies mLT) are discontinuous, continuing for a few metres before gradually pinching out laterally at both ends (Figure 3.4b). These units are found in the centre of the width of the tuffisite and, while they feature frequently in the main tuffisite, examples are less apparent where the tuffisite is interfingered with red ignimbrite sheets at the northern end of the outcrop. These units are typically ~20 cm thick at their central thickest point and have a flat base and a domed top that deforms the overlying clastic vein fill. The shape of these structures in 3D is not visible in outcrop. The overlying laminated material typically has laminations that are deformed, dipping toward the edges of the underlying lens. Occasionally these units are non-conformable, sitting on an erosive surface that crosscuts bedding in the unit beneath.

The edges of the structure are composed of ash-sized material, deposited in laminations that are parallel to the unit edge (Facies sT), even where it pinches out laterally. Here, the laminations form concentric curves on the unit edge. Toward the centre of the unit the material coarsens, over a distance of 10 cm, to medium lapilli. The centre contains ≤2 cm clasts of ignimbrite and obsidian and lacks internal structure.

3.5   Interpretation

The tuffisite consists of a number of units, which can be divided into facies based on their grain-size and internal structure, and contains structures such as channels, lenses and internal veins (Section 3.4). These features preserve key evidence for emplacement processes, recording fluctuations in the fluid pressure and particle volume fraction of the

suspending fluid.

3.5.1 Direction of Fluid Flow

The tuffisite consists of multiple units separated by erosion surfaces and, while the units are mostly horizontal, cross-cutting relationships indicate how the tuffisite may have evolved through time. The southwards dip of units in the middle of the tuffisite, along with cross-stratification, suggests that the injected fluid flowed southwards, eroding the underlying material and depositing multiple dipping units (foresets) to produce a structure that migrated laterally over time (Figures 3.4b, 3.9). Field evidence suggests that a subsequent pulse of higher velocity fluid eroded the top of this structure, followed by the deposition of the unconformable overlying unit. Shadows behind clasts and soft-sediment deformation in internal injections also suggest fluid flow toward the south. In some areas of the outcrop, the fluid flow direction interpreted from cross-stratification is inconsistent, indicating a range of fluid flow directions. This inconsistency could perhaps be explained by backflow, potentially driven by fluid pressure variations as different fluid flow pathways become blocked, or forward-flow with waxing or waning velocity producing eddies.

3.5.2 A Record of Fluid Pressure Fluctuations

Units of varying grain sizes and sedimentary structures inside the tuffisite fill can be interpreted as records of changes in the local velocity of the fluid flowing through the fracture, controlled by spatial and temporal variations in the fluid pressure gradient (Cosgrove, 2001; van der Meer et al., 2009; Phillips et al., 2013). These fluctuations in fluid pressure could be produced externally, controlled by the pressure source, or internally, controlled by processes occurring within the fracture itself.

Volcanic eruptions are rarely steady-state, and so the input of fluid from the unsteady volcanic conduit will be necessarily transient and varying on different timescales. On the longest timescale of days to weeks, the fluid pressure will decrease from a maximum close to the onset of the eruption to lower values as magma discharge wanes. The progressive opening of pathways, for example propagating fractures to shallower depths, will increase fracture volume, lowering the fluid pressure on a timescale of seconds to hours. At the shortest timescale, instabilities within the volcanic conduit, due to unsteady flow, would

84
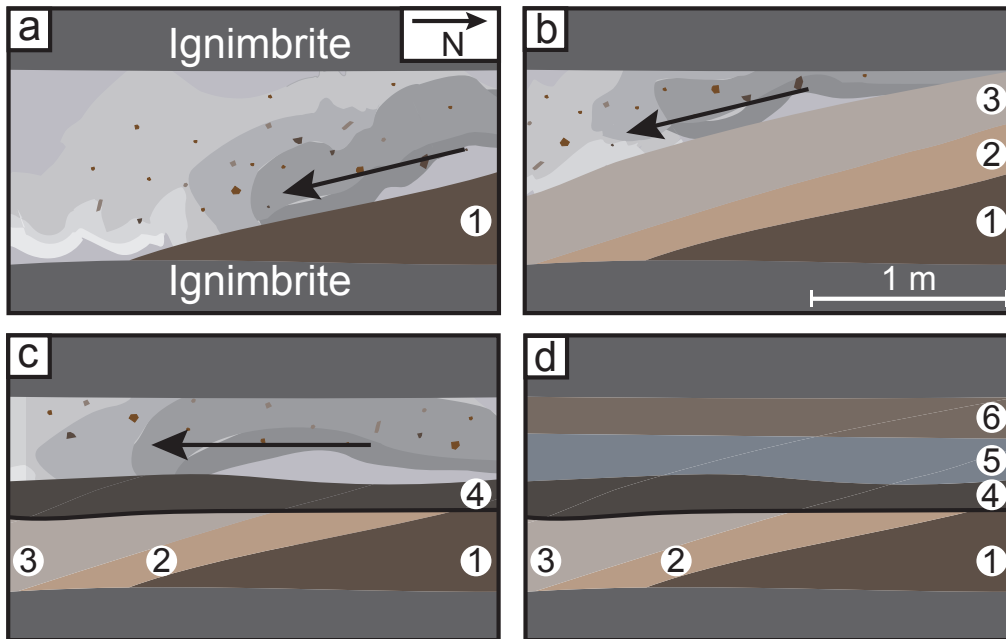
Figure 3.9: Schematic showing the deposition of southwards dipping units in the tuffisite. a) Fluid flow toward the south deposits a tuffisite unit (1) with a shallow angle. b) The next tuffisite units (2 and 3) are deposited above, also dipping at a shallow angle to the south, producing a laterally migrating structure. c) An increase in fluid velocity, driven by a fluctuation in fluid pressure, allows the previous material to be eroded. The next tuffisite unit (4) is unconformably deposited above. d) The final tuffisite units (5 and 6) are deposited.

be able to produce fluctuations in fluid pressure with a timescale of seconds. Fluid pressure fluctuations at each of these timescales will be recorded by the facies and structures of the tuffisite fill.

Even if the source pressure were theoretically constant, internal processes acting within the hydrofracture would still result in fluid pressure fluctuations (Perkins and Kern, 1961). Instabilities in fluid flow can be spontaneously generated within the hydrofracture, producing fluid pressure oscillations that would be superimposed on the fluid pressure variations generated externally. Variations in the width of a hydrofracture along its length could locally alter the fluid pressure (Perkins and Kern, 1961), and the deposition and sintering of particles can clog fluid pathways, lowering the permeability (Farquharson et al., 2017; Heap et al., 2019; Kolzenburg et al., 2019) and therefore changing the hydraulic transport properties of the system. Changes in the fluid pressure gradient along the fracture produce local fluctuations in flow velocity, leading to spatial and temporal changes in (1) erosion when the local fluid velocity is relatively high, (2) deposition when the local fluid velocity is relatively low, and (3) bypassing flow at intermediate flow velocities leading to neither erosion nor deposition. Deposition within

the hydrofracture will reduce the space available for fluid flow, locally increasing the fluid pressure until a fluid velocity is reached that can erode the recently deposited sediment (Kern et al., 1959). Once erosion opens more space to accommodate fluid flow the fluid pressure gradient will fall, and so will the fluid velocity, resulting in renewed deposition. In this way, the fluid velocity inside the fracture will always fluctuate. If the source pressure is constant, then these fluctuations may occur around an equilibrium value, at which sediment is not eroded and particles being carried by the fluid are not deposited but transported through the hydrofracture (Kern et al., 1959).

Based on the reasoning explored above, there are three possible origins of the fluid fluctuations recorded by the sedimentary fill within the tuffisite at Húsafell: (1) the source pressure was broadly steady, but instabilities within the tuffisite itself could still produce fluid pressure oscillations; (2) the source pressure was unsteady but waning, leading to fluid pressure oscillations, superimposed on an overall depositional fill; and (3) the source pressure waxed and waned through time, producing a more complex fill formed by deposition then erosion and re-working of sediment that would perhaps contain little systematic variation. The potential magnitude of the pressure fluctuations generated by these different origins is unclear, preventing individual facies changes or structures within the tuffisite from being linked to fluid pressure fluctuations of one particular origin.

Fluctuations in the fluid pressure create the conditions of erosion and deposition needed to produce sedimentary structures, and the presence or absence of structures in different units additionally reflects the particle concentration of the transporting fluid. Some units (facies dslBr, dsLT, and sT) display complex structures such as cross-bedding, laminations, and graded beds, while other units (facies mlBr, mLT, and mT) display less-structured, massive features. These differences can be interpreted as the result of low vs. high particle concentration in the bypassing flow, leading to laminated vs. massive deposits [e.g., indicate deposition from a fluid with a low particle concentration, rather than due to the injection of a slurry with a high particle concentration, which is inferred for massive units (facies mlBr, mLT, and mT; Sparks, 1976; Allen, 1982; Walker, 1984)], or as the result of highly unsteady vs. sustained and steady current conditions at the time of deposition (e.g., Branney and Kokelaar, 2002).

3.5.3 Interpretation of Structures

3.5.3.1 Structure 1: Entrainment of Clasts and Blocks

Large clasts and blocks of the surrounding ignimbrite within the tuffisite would have required a high fluid velocity to be transported along the fracture, and indicate the minimum width of the open fracture system. One of these blocks of red ignimbrite (Figure 3.8a) is positioned on its narrow end, and so is likely to have been rolled along the base of the fracture before being deposited in that orientation. There is a notable lack of variation and structure in the surrounding units of breccia and coarse lapilli, even adjacent to large obstructing objects in the flow path such as the red ignimbrite block. This is further evidence that at times the fluid had a high particle concentration, giving it the characteristics of a mass-flow or slurry (Fisher et al., 1983; Branney and Kokelaar, 2002), while at other times the formation of cross-lamination indicates that the particle concentration was significantly lower.

3.5.3.2 Structure 2: Internal Veins

Cross-cutting units of massive material, often bordered by material of a smaller grain-size, are interpreted as injections (Figure 3.8b). These features appear similar to many centimetre scale hydrofractures reported in glacial environments and sand injectites, with fine-grained edges and a coarser centre (van der Meer et al., 2009; Hurst et al., 2011; Phillips et al., 2013; Phillips and Kearsey, 2020). We interpret the structures as smaller-scale hydrofractures injected into the earlier formed fill of the larger tuffisite, representing self-intrusion. Where the earlier deposited fill has gained cohesion, due to compaction and the sintering of tuffisite material, an increase in fluid pressure can exceed the overburden and strength of incipiently sinter-bonded clast-clast contacts, enabling the fracturing of this fill and injection of an internal vein.

Such pressurized fluid injection and self-intrusion opens a new more permeable pathway through the earlier tuffisite fill, leading to localised fluid flow and eventually particle deposition. The fine-grained material is the easiest to mobilise and is the first injected into the new fracture, filtering into the host rock and sealing any fluid pathways (Phillips and Kearsey, 2020), similar to the formation of mudcake during well drilling (Ferguson and Klotz, 1954; Dewan and Chenevert, 2001). Once the fracture has widened coarser

material can be injected, with variations in fluid pressure as the fracture fills producing laminations that can be later deformed by fluid flow, as is seen in both sand injectites and hydrofractures in glacial environments (e.g., Scott et al., 2009; Ravier et al., 2014).

The fractures have well-defined straight edges, indicating that the unit overlying the injection must have been sufficiently compacted and consolidated to behave as a cohesive unit. This may reflect sintering-driven strengthening (e.g., Tuffen and Dingwell, 2005; Wadsworth et al., 2016). Cross-stratification indicates that the fluid particle concentration must have been relatively low, with particles deposited inside a void rather than as part of a slurry (Tuffen et al., 2003; Phillips et al., 2013). Even these small injections appear to have involved deposition from multiple pulses of material, generating beds and fine laminations.

3.5.3.3 Structure 3: Channel Structures

Channel structures in the Húsafell tuffisite represent preferential fluid pathways. Channels indicate that pulses of material are not only injected within previously deposited material, but can also erode the underlying material as would be expected in a normal sedimentary sequence (Figure 3.4b). This ability to erode represents large local variations in fluid velocity, so that the fluid can transport previously deposited particles. As the unit beneath sinters and strengthens through time it will become more difficult to erode, and channel formation will therefore only be possible if the pre-existing material is not significantly sintered. Channel formation will be favoured where the frequency of injections is high, allowing for rapid erosion before material can sinter, or the cooling rate is high (fast), preventing significant sintering from occurring. To produce the channel structures in the tuffisite, the fluid velocity must initially be sufficient to erode material. A slowing of the fluid flow then allows for deposition on the erosion surface, forming multiple dipping layers (Branney and Kokelaar, 2002). After another period of erosion, unconformable overlying beds could be deposited. The channel structures indicate a rough direction of fluid flow within the tuffisite, with a component of flow into or out of the plane of the outcrop, rather than parallel along the face of the outcrop.

Figure 3.10: Schematic showing the formation of interfingered tuffisite veins and sheets (Structure 4). (a) The fluid opens multiple pathways along weaknesses in the red ignimbrite, allowing for fluid flow and particle deposition in each fracture. (b) Material is deposited inside each fracture, with fine material first deposited at the edges and coarser material toward the centre. (c) Fractures are interlinked, and through time dominant fluid pathways form, widening certain fractures while others narrow and become clogged with particles.

3.5.3.4 Structure 4: Fracking Through Ignimbrite

The tuffisite is seen to form multiple pathways through red ignimbrite blocks to the north of the fault guided gully (Figures 3.6f, 3.8c). The red ignimbrite fragments are aligned, and long segments have been vertically fractured into shorter tabular blocks that form horizons of ignimbrite clasts. The preferential shape alignment of the blocks, made of the red ignimbrite roof material, suggests they did not simply fall on to the underlying sediment once separated, as this would trigger greater disaggregation and reorganisation of the ignimbrite clasts. Instead, we infer that tuffisitic fluid injection within the red ignimbrite exploited and opened pre-existing sub-horizontal fractures, thus separating the rock into multiple tabular fragments, between which particles were then deposited, similar to mud-rafting seen in sand injectites (Figures 3.10a,b; Duranti and Hurst, 2004; Scott et al., 2009). The ignimbrite fragments essentially host small tuffisites within the larger tuffisite.

The fluid pathways between the red ignimbrite blocks are considered to have formed a network that shifted through time as new fractures opened or pathways became clogged with material. Larger grains would be unable to pass through initially narrow pathways, filtering material until wider dominant fluid pathways were developed (Figure 3.10c). Although the exact timing is unknown, we consider that these pathways formed as fluid pressure increased at a late stage of tuffisite evolution, when sintering-driven pathway clogging reduced permeable gas escape, driving the opening of new fracture pathways within the overlying ignimbrite. Alternatively, if opened as the tuffisite formed, the structure could represent early pathways that were later refined into a more dominant fluid pathway at the base of the tuffisite.
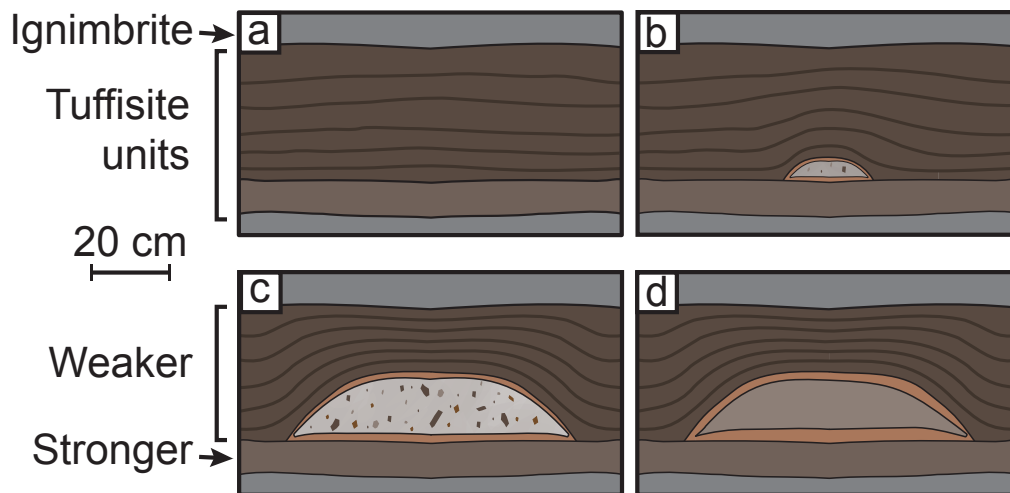
Figure 3.11: Schematic showing the formation of fine rimmed subhorizontal lenses (Structure 5) as finger-shaped injections. a) Fluid flowing perpendicular to the plane of the outcrop opens a pathway between a stronger and weaker unit. b) The widening of the fluid pathway is accommodated by deformation of the weaker material above, forming an intrusion with a domed top and flat base. c and d) Material is deposited inside the intrusion, with fine material deposited first, forming the margins, and coarser material deposited at the centre.

The tuffisite has fractured multiple pathways through the overlying red ignimbrite at only this location, although high aspect ratio blocks of ignimbrite locally occur elsewhere within the tuffisite. The prevalence of fluid pathways in this location may stem from an abnormally high fracture density in the ignimbrite close to the fault, which is only a few metres to the south (Figure 3.3).

3.5.3.5 Structure 5: Finger-Shaped Injections

Massive units of sediment, forming structures with a flat base and rounded top, which pinch out laterally, represent larger injections into the surrounding sediment, ≤ 1 m in length, which lifted and deformed the units above (Figure 3.4b). Under conditions in which the interface between two tuffisite units is the pathway of least resistance, high fluid pressure may open this interface and permit further fluid injection, with sediment deposition (Figures 3.11a,b). The mostly massive structure of the injected material suggests that the fluid had a relatively high particle concentration. As space was opened the fine-grained material was injected, coating the fracture walls (Ferguson and Klotz, 1954; Dewan and Chenevert, 2001) before the coarser-grained material was injected, forcing the fracture open further (Figures 3.11c,d).

3.6 A Model for Tuffisite Emplacement

We can combine our observations of sediment characteristics and structures to build an overall model for the emplacement of the tuffisite (Figure 3.12). The southwards dip of units and sedimentary structures, such as cross-stratification, suggest a roughly southwards direction of fluid flow (Figures 3.4, 3.9). The presence of multiple erosion surfaces along the length of the tuffisite is evidence for multiple fluid pulses, which have eroded material beneath and deposited coarser material above (Figure 3.4b).

Gas and pyroclastic material would have fractured a pathway toward the surface until stalled by the strong and densely welded black ignimbrite, requiring a greater fluid pressure to fracture through. The ascending gas and ash may have reached a great enough fluid pressure to fracture the unit, or exploited an easier pathway, perhaps travelling around the edges of the black ignimbrite unit or fracturing the less densely welded section to the south. Once at the base of the weaker and friable red ignimbrite, the pre-existing sub-horizontal fractures would facilitate horizontal propagation rather than further ascent. As the pre-existing fractures were widened, ignimbrite blocks were detached from the tuffisite walls to produce a single fluid pathway, along which particles were deposited.

The evolutionary model established for the emplacement of the Húsafell tuffisite can be divided into three phases.

3.6.1 Phase 1

Phase 1 is characterised by laterally extensive units that are present along nearly the whole length of the tuffisite ($\sim$40 m). The laterally extensive, massive breccia at the base of the tuffisite was deposited first, as a fluid of high particle concentration was injected along the length of the newly opened or propagating fracture, incorporating blocks detached from the country rock (Structure 1; Figures 3.8a, 3.12). Gradual reduction in fluid pressure and thus flow velocity led to the deposition of finer grained, interbedded lapilli-tuffs and tuffs, and the deposition of an overall fining-upwards tuffisite sequence (Figure 3.5). Structures such as cross-lamination and soft-sediment deformation in some of these units represent a drop in the particle concentration of the fluid, allowing for the formation of sedimentary structures.
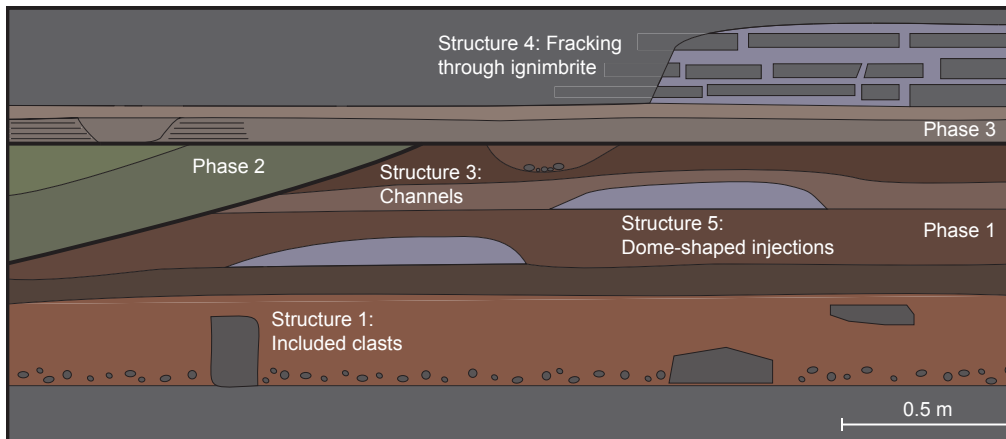
Figure 3.12: Schematic showing the different phases of formation and structures in the tuffisite fill. Phase 1: A laterally extensive fining upwards sequence is deposited, containing large ignimbrite clasts (Structure 1) separated from the country rock. Phase 2: Fining upwards sequences are deposited unconformably above Phase 1, in more localised units, to form structures such as channels (Structure 3) and cross-lamination. Phase 3: Laterally extensive tuffs and lapilli-tuffs are deposited at the top of the tuffisite. As fluid pressure increases material fractures off blocks of ignimbrite from the tuffisite roof (Structure 4) and forms finger-shaped injections at the tuffisite centre (Structure 5).

3.6.2 Phase 2

A new higher velocity fluid pulse produced an erosion surface above the Phase 1 fining upwards sequence, before depositing a similar sequence, which fines upwards from a breccia (basal lag) to lapilli and ash-sized grains (Figures 3.5, 3.12). The units of this second pulse are less laterally extensive, and the increase in internal structures represents deposition in a more open-ended and wider fracture, from a fluid of a lower particle concentration. Increased erosion and reworking of material led to channel formation (Structure 3; Figure 3.4b) and southwards migrating units (Figure 3.9). Internal injections (Structure 2; Figure 3.8b) indicate how local increases in fluid pressure opened new pathways in the surrounding sintering sediment.

3.6.3 Phase 3

Phase 3, the final main pulse of material, was deposited above another erosive surface (Figure 3.12). A lower fluid velocity deposited material as laterally extensive, laminated lapilli-tuffs and tuffs (Facies dsLT and sT; Figure 3.5). Filling of the open space with material demanded the creation of new pathways, made possible by the increasing fluid pressure. Weaknesses in the overlying ignimbrite were exploited, opening more space and producing ribbons of tuffisite interfingered with country rock (Structure 4; Figures

3.8c, 3.10). Where the tuffisite was still hot enough to viscously deform, finger-shaped injections provided another method of opening additional space (Structure 5; Figures 3.4b, 3.11).

3.7 Discussion

3.7.1 Constraints on Tuffisite Emplacement Conditions

To open a hydrofracture, the fluid pressure must be great enough to overcome the lithostatic pressure P_L, induce tensile failure in the surrounding coherent material by overcoming the tensile strength P_T, and widen the hydrofracture by elastically deforming the surrounding material requiring pressure P_W. Inelastic deformation is possible but not considered here as there has been no visible deformation of the fracture walls. The required fluid pressure is therefore

$$P = P_T + P_L + P_W, \tag{3.1}$$

where P_L is calculated using $P_L = \rho \mathrm{g} h$, with ρ representing the density of the overlying material, g acceleration due to gravity, and h the depth of the hydrofracture from the Earth's surface. While the tensile strength of a welded ignimbrite with a typical porosity of $\sim$0.3 may be $\sim$2–5 MPa (Heap et al., 2021), injections are seen to occur along pre-existing weaknesses, such as unit contacts or fractures, that can be assumed to have a lower tensile strength. The value of P_T is therefore assumed to be very small compared to P_L and P_W, and so is not considered in pressure estimates below. P_W can be given in terms of the fracture width, W, and fracture length, L, as (Gudmundsson, 1983)

$$P_W = \frac{E}{2\left(1 - \nu^2\right)} \frac{W}{L}, \tag{3.2}$$

where ν is Poisson's ratio, and E is the Young's modulus. If P_T is negligible, then P_W represents the overpressure (pressure in excess of the ambient P_L) required to open a fracture.

If we assume that the country rock overlying the tuffisite has an average density akin to intercalated lithofacies of pyroclastic, welded, and lava deposits typical of the rhyolitic central volcanoes of Iceland (Ágústsdóttir et al., 2011), we can take an approximate density of $\rho = \rho_0(1 - \phi)$, where ρ_0 is the density of the solid components and ϕ is the

average porosity of the overburden. Approximate values might be $\rho_0 = 1800$ kg.m^{-3} for rhyolite, and $\phi = 0.3$ for volcanic sequences: $\rho = 1260$ kg.m^{-3}. The tuffisite depth below the surface can be estimated as $h = 500$ m via magmatic water concentration in glassy intrusion margins (McGowan, 2016). Taken together, this leads to constraint of $P_L \approx 6.2$ MPa.

In order to calculate the P_W component, we must estimate the scales of the tuffisite W and L, and the properties of the country rock ν and E. Regardless of porosity, the Poisson's ratio for volcanic rocks is relatively tightly constrained with 90% of available data lying within the bounds $0.10 < \nu < 0.35$. $\nu = 0.21$ can be found for a tuff with $\phi = 0.16$ porosity (Özsan and Akn, 2002), which is also the average of a wide range of measurements using a range of volcanic rocks with porosities from 0.01 to 0.2 (see Heap et al., 2020). Therefore, in this study, we take $\nu = 0.21$. To estimate E, Gudmundsson (1983) assumed that $E \approx E_d/2$, where E_d is the dynamic Young's modulus, given by

$$E_d = \frac{V_p^2 \left(1 + \nu\right)\left(1 - \nu\right)\rho}{1 - \nu} \approx 2E \tag{3.3}$$

where V_P is the p-wave velocity of the host rock. Estimates of V_P for porous volcanic rock are $V_P = 1575$ m.s^{-1} (for $\phi = 0.3$; Al-Harthi et al., 1999; Vasseur et al., 2016). These constraints lead to $E \approx 1.4$ GPa. Alternatively, in a review of data for the Young's modulus of volcanic rocks, Heap et al. (2020) find that the majority of the available data for tuff has an arithmetic mean value of $E = 2.4$ GPa and the majority of the data for tuff materials occur in a moderate-to-high porosity cluster with an arithmetic mean of $E = 1.7$ GPa. This leaves us to find characteristic values of W and L.

The structure of the Húsafell tuffisite is interpreted as a record for fluid pressure fluctuations through time. Using Eq. 3.2 and the constraints provided above, we can estimate the fluid pressure required for tuffisite formation and constrain the maximum overpressure reached by the fluid pressure fluctuations. We compare the pressure required to open the crack hosting the Húsafell tuffisite for two contrasting end-member scenarios. The single-shot model involves the opening of the fracture to maximum width in one pressurisation event, and implies rapid deposition of the whole tuffisite fill width in a single fluid injection event, as a single proppant pulse within a fully dilated (0.9 m-thick and 40 m-long) fracture (Figure 3.3). The pulsed emplacement model involves sequential injection of a number of thinner units, with multiple sediment pulses within a partially dilated fracture. While the field evidence of continuous margin-parallel deposits implies

that the pulsed model still involves a 40 m long fracture, the width of each sequential opening event may be significantly smaller than the tuffisite width.

The *single-shot model* demands significant elastic deformation of crack walls, and requires an overpressure of $16 \leq P_W \leq 29$ MPa (lower and upper bound for $E = 1.4$ and $E = 2.4$ GPa, respectively; Figure 3.13). Such a high pressure is much greater than the 2 MPa overpressure predicted at 500 m depth for a conduit of width 30 m and an initial water concentration of 4.6 wt% (Degruyter et al., 2012), similar to the ∼5 wt% water measured in Icelandic rhyolites at Torfajökull (Owen et al., 2013). The model by Degruyter et al. (2012) predicts an overpressure of 16–29 MPa only occurs at depths of ∼2 km for a conduit with the same parameters as above. Conduit constriction, not considered by the Degruyter et al. (2012) model, may allow greater gas pressures to be produced at shallower depths; Castro et al. (2016) find that at 300 m depth, reducing conduit width from 400 m to only 25 m can increase the gas pressure by ∼7 MPa. However, even with conduit constriction, a total pressure of 22–35 MPa at 500 m depth is unfeasible. Additionally, such a high fluid pressure would vastly exceed the tensile strength of all country rock lithologies, and be expected to induce significant damage, which is not seen. We therefore conclude that the emplacement of the tuffisite as one single unit requires an unrealistically high gas pressure at 500 m depth, and is therefore untenable as a model.

The pulsed emplacement model requires a more modest P_W compared with the single-shot model, because the pressure required for each incremental injection scales with the partial dilation width (Eq. 3.2). Many of the tuffisite units, particularly the coarser grained facies (mlBr and dslBr) are visibly continuous across the whole length of the outcrop, and we therefore choose a model unit length of 40 m. Some of the finer-grained tuffisite units are less laterally continuous, but this discontinuity is interpreted as occurring due to erosion, rather than representing the original depositional length of the unit. Field evidence suggests that the tuffisite was deposited in 3 main phases, separated by erosional surfaces (Figure 3.12). Each phase consists of multiple units of varying characteristics, and often with erosive boundaries. The three phases are therefore interpreted to reflect changes in depositional style as the tuffisite evolves, and are each formed of multiple fluid pulses. The model unit width is taken to be 10 cm, the average width of units of facies mlBR, dslBR, mLT, and dsLT. Units of facies mT and sT are typically thinner than 10 cm and are the least laterally continuous. We suggest that the formation of many of these thinner units is driven by internal fluid pressure fluctuations
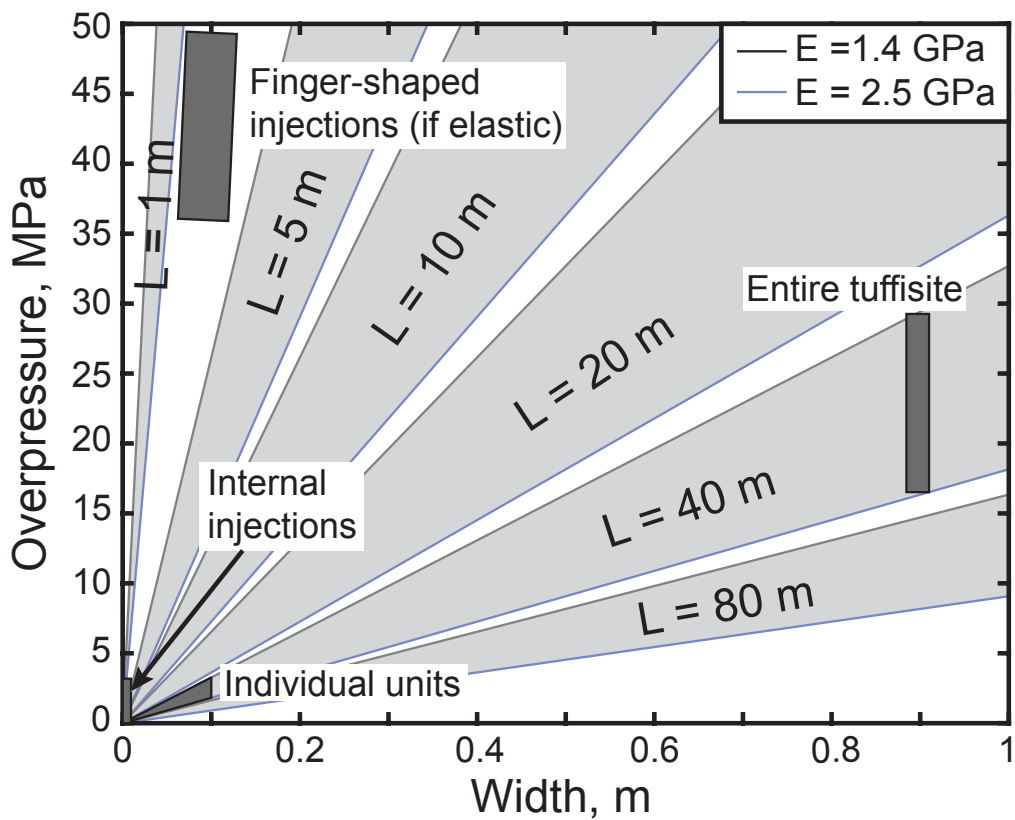
Figure 3.13: The fluid overpressure required to open tuffisites as a function of fracture width, according to Eq. 3.2, for different fracture lengths (Gudmundsson, 1983). Plotted pressure fields show the required fluid overpressure to form the tuffisite as a single pulse, or as many individual units, and to form the internal and finger-shaped injections seen. The overpressure estimate for finger-shaped injections plotted is for the elastic model (Eq. 3.2), but viscous deformation of the surrounding units would decrease the overpressure required.

within the tuffisite, rather than by fluid pressure variations of the source.

Using the range for E given above ($E = 1.4$ to $E = 2.4$ GPa), injection of a 10 cm-thick, 40 m-long unit, consistent with the emplacement of the entire tuffisite fill in nine successive pulses, would require overpressure of $1.9 \leq P_w \leq 3.3$ MPa (Figure 3.13). Attainment of this lower P_W value is far more plausible, and is similar to previous estimates for the overpressure forming tuffisites (Heiken et al., 1988; Saubin et al., 2016) and rhyolitic conduit systems (Benson et al., 2012; Castro et al., 2016). At 500 m depth the model by Degruyter et al. (2012) predicts 2–3 MPa of gas overpressure at 500 m depth for a conduit width of 30 m, consistent with our estimates and our field evidence found here.

We note that the analysis presented above could be repeated, but for a case of a non-porous overlying country rock, for which ρ and V_P, and therefore P_L and P_W, would be higher. However, we note that our estimate of $\phi = 0.3$ is typical of a rhyolitic central volcano dominated by pyroclastic sequences.

The single-shot model appears to be infeasible for a thick tuffisite such as that at Húsafell, evidenced by its complex internal structure (Figures 3.4, 3.12). The dimensions of the sedimentary units suggest that the tuffisite reached a maximum overpressure of 1.9–3.3 MPa, with fluid pressure fluctuations causing erosion and deposition, producing complex structures. The tuffisite must therefore have formed by pulsatory opening and closing, indicating an unsteady source with fluctuating fluid pressure, though some variation in fluid pressure may be generated by internal processes (see section "A Record of Fluid Pressure Fluctuations"). The overpressure required for tuffisite emplacement, 1.9–3.3 MPa, is similar to the overpressure just above the level of fragmentation, perhaps suggesting that the formation of lateral fractures, able to host tuffisites, is inevitable just above the level of fragmentation. The overpressure estimate is also consistent with the pressure changes inferred from diffusion, with H_2O concentrations in glass-walled tuffisites suggesting transient pressure drops of a few megapascals during fracture opening (Castro et al., 2014).

3.7.2 Emplacing Finger-Shaped Injections (Structure 5)

Field evidence suggests that the finger-shaped injections did not form by fracture opening, subsequent fluid flow and deposition of material, but instead by local distributed deformation

of the material above the injection (Figures 3.4, 3.11). This is more consistent with the viscous intrusion of a granular medium, fingering into locally deformable surroundings. The finger-shaped injections appear similar to structures produced by the slow intrusion of one granular medium into a second fluid-saturated granular medium, as investigated experimentally in 2D Hele Shaw cells (Saffman and Taylor, 1958; Trevelyan et al., 2011). We draw this analogy between the finger-shaped injections and experimental results in order to suggest that the finger-shaped injections represent a low velocity process that is likely to have occurred toward the end of tuffisite evolution (Phase 3). In turn, this would require that the pressures driving these intrusions were lower than expected via application of the analysis presented in Section 3.7.1 (Figure 3.13).

We note some important differences between the observations of the finger-shaped injections and the processes operative in the 2D Hele Shaw cells (Saffman and Taylor, 1958; Trevelyan et al., 2011). Most importantly, the roof material of the finger-shaped injections is locally partially sintered — a process that cannot be simulated in the low-temperature analogue experiments. This observation also points to a slow, lower-pressure, ductile process rather than the rapid, brittle repeated fracture-opening process invoked for the other units in the tuffisite. Sintering of hot pyroclasts above the finger-shaped injections would be a viscous process, and the pressure required to drive that would depend on the balance between the interstitial gas pressure and the squeezing pressure (Wadsworth et al., 2019). The upper bound on the squeezing pressure is the lithostatic pressure of 6.2 MPa (as discussed in Section 3.7.1), but the gas pressure is unconstrained. Viscous deformation of the roof material that is associated with intrusion injection would allow space for the intrusion to be produced without requiring lithostatic pressure to be exceeded. In a particle-filled fracture the gas pressure is less than lithostatic pressure, but could still be sufficient to deform the overlying material, allowing the finger-shaped injections to form at a relative underpressure, particularly as exceeding lithostatic pressure may cause the overlying material to instead be preferentially lifted to form a fracture. In turn, this is consistent with the finger-shaped injections occurring after the high-pressure fluidised formation of the other units, and thus toward the end of tuffisite evolution, with an overall waning fluid pressure at the source (Phase 3).

3.7.3 Tuffisites as a Fossil Record of Fluid Pressure Fluctuations

The structures inside the Húsafell tuffisite provide a detailed record of the fluid pressure fluctuations during its formation. Elastically opening a space 0.1 m wide and 40 m long for each unit to be injected required 1.9–3.3 MPa of fluid overpressure, and as the fluid pressure waned particles could then be deposited. The fluid overpressure therefore appears to have oscillated, reaching a maximum of 1.9–3.3 MPa during tuffisite formation, with fluid pressure increases allowing for the erosion of previous units. Toward the end of tuffisite evolution the fluid pressure continued to wane, with finger-shaped injections formed at a lower fluid pressure than the previous sedimentary units (<1.9–3.3 MPa).

While some smaller tuffisites do appear to have a simple structure formed by a single fluid pulse (e.g., internal tuffisites at Chaitén; Saubin et al., 2016), the complex structure of the Húsafell tuffisite suggests that it was formed by multiple pulses of material injected into the same fracture. The three phases of deposition described in the model above are the minimum number of injections that occurred during the formation of the Húsafell tuffisite — if the units of each individual phase were each formed by a fluid pulse, there could have been around as many as 20 injections of material into the fracture.

3.7.4 Tuffisites as a Seismic Source

Pulsed injection of pressurised fluid into a hydrofracture (pulsed emplacement model) has been previously suggested in the context of seismic swarms at restless volcanoes (e.g., Chouet, 1996; Kumagai and Chouet, 1999). Swarms of long-period earthquakes (also called low-frequency, and here abbreviated to LP) with very similar waveforms can last for a period of a few hours to several days, with inferred trigger mechanisms involving the repeated excitation of pre-existing cracks. LP events are thought to represent a sudden pressure change within a resonated crack, and may superimpose to create sustained harmonic tremor, which has a common source process that differs only in duration (Chouet, 1996). The quality factor, Q, describes the degree of seismic attenuation, with high Q-values representing long-lasting oscillations. To produce long-lasting oscillations with Q significantly greater than 100, there needs to be a large density difference between the fluid and the surrounding rock (Chouet, 1996). Computed synthetic waveforms for fluid-filled cracks indicate that very high Q-values (e.g., $Q = 400$ at Tungurahua Volcano,

Molina et al., 2004) are best explained if the fluid is a dusty or misty gas with low sound speed (Kumagai and Chouet, 2000; Taguchi et al., 2021). In this volcanic scenario, the dust is inferred to be fine-grained particles of volcanic ash.

At Tungurahua volcano, Molina et al. (2004) modelled resonance of a fracture at 1 km depth, with a length:width (L/W) ratio of 2, length:aperture ratio of 104, and length of $\sim$200 m, approximately similar to the Húsafell tuffisite. Molina et al. (2004) attributed the systematically changing Q-value during an LP swarm to incremental filling of the fracture by 10 µm ash particles, with eventual crack clogging proposed to have permitted the pressurisation that culminated in an explosive event. This particle-size broadly matches that of the Húsafell tuffisite, as well as other documented tuffisite veins for which more detailed particle-size analysis has been conducted (e.g., Saubin et al., 2016; Heap et al., 2019). A similar model has been proposed at Galeras volcano, with LP events suggested to represent the propagation and increase in volume of a vertical crack injected by a gas-ash mixture (Taguchi et al., 2018). Both the crack volume and mass fraction of gas within the crack were inferred to have decreased as ash was deposited and welded before the next LP event (Taguchi et al., 2021). We propose that the Húsafell tuffisite represents the fossil record of exactly this type of LP seismic swarm.

Internal tuffisites, which have previously attracted much attention as a potential source of LP earthquakes, are thought to originate in brittle failure events in magma at high strain rates (e.g., Tuffen and Dingwell, 2005; Neuberg et al., 2006). Healing and resealing of these fractures could then permit their repeated reactivation, with a minimum repeat time of a few tens of seconds (Tuffen et al., 2003). However, the modest dimensions of documented internal tuffisites ($\leq$5 m; Tuffen et al., 2003) fall short of the crack dimensions of tens to hundreds of metres in length that are required by crack resonance models (Chouet, 1996; Molina et al., 2004). The small interevent times between LP events are also difficult to explain using the model of magma breaking and healing, unless magma is continually ascending in the seismogenic window (Neuberg et al., 2006; Chouet and Matoza, 2013). We therefore propose that the much more extensive external tuffisite at Húsafell is a better candidate geological record of the LP seismic source process. External tuffisites have the potential to grow to these dimensions, as evidenced by tuffisites at Inyo Domes, California, suggested to extend >120 m from a dyke (Heiken et al., 1988).

Detailed characterisation of seismicity accompanying dyke propagation in Icelandic rift

zones, such as at Bárðarbunga in 2014 (Ágústsdóttir et al., 2016; Eibl et al., 2017; Woods et al., 2019), has shown that dyke propagation in the uppermost Icelandic crust ($<$3 km) is not accompanied by the high-frequency volcano-tectonic (VT) events that are normally characteristic of brittle rock failure. Magmatic pathway propagation is instead thought to involve the widening of pre-existing fractures in weak material (Ágústsdóttir et al., 2016; Woods et al., 2019). Low-amplitude tremor was detected, instead of VT events, and interpreted as a swarm of micro-earthquakes at the propagating dyke tip (Eibl et al., 2017). If we apply this understanding of rift zone seismicity to the structural and lithological context of an Icelandic central volcano then we can speculate on the nature of the seismicity triggered during the opening and lifespan of the Húsafell tuffisite. As the tuffisite initially propagated by widening pre-existing fractures in the weak, overlying red ignimbrite, no high-frequency VT events would have been triggered. Instead, the seismicity would have been low-frequency and solely related to the excitation of pre-existing cracks. However, fracturing of stronger neighbouring formations by the rhyolitic intrusion, such as the underlying conglomerates and black ignimbrite, and overlying basaltic lavas (McGowan, 2016; Saubin et al., 2019), may have involved bursts of seismogenic rupture and small-magnitude higher frequency events. The architecture of diverse country rock lithologies with contrasting mechanical properties therefore guides the spatial distribution and nature of seismicity on the opening and then active magmatic pathway.

3.7.5 Repeated Injections and Deformation Style

The strength of the surrounding tuffisite units must control the location of finger-shaped injections. In a theoretical homogenous tuffisite emplaced in a single pulse, the material closest to the colder country rock should cool most rapidly, and therefore will be less well sintered, weaker, and easier to inject (Kolzenburg et al., 2019). However, in the heterogeneous Húsafell tuffisite, involving emplacement over multiple pulses, the cooling history is more complex. To form a finger-shaped injection the overlying unit requires sufficient cohesion to form a roof, but must maintain the ability to viscously deform at the time of injection, and thus be at high temperature, perhaps aided by additional heat from the injected material. In the Húsafell tuffisite the position of finger-shaped injections will reflect the relative ages and temperatures of material deposited by different fluid pulses. The finger-shaped injections are seen around the centre of the tuffisite width, where slow cooling would allow for the greatest degree of sintering (Kolzenburg

et al., 2019), decreasing permeability and allowing fluid pressure to build, and favouring viscous deformation of the tuffisitic roof material. Fluid is injected along the contact between a slow cooled and well-sintered strong unit below, and a younger unit above, deposited by a later fluid pulse, which was still sufficiently hot to viscously deform.

The tuffisite therefore appears to be self-limiting in its lifetime as a degassing pathway. A less-evolved tuffisite with fewer fluid pulses will be colder, allowing material to be more easily injected, and will remain more permeable, allowing for greater amounts of fluid flow. As more pulses are injected and the tuffisite thickens it will take longer to cool, allowing for more sintering to take place, reducing tuffisite permeability. Waning fluid pressure in a hot tuffisite favours the formation of finger-shaped injections, viscously deforming the overlying layers and reducing permeability further.

3.8 Future Challenges

Tuffisites are a fossil record of the processes occurring during the formation and evolution of magmatic pathways. Quantifying the fluid pressure required to open these fractures, by characterising the mechanical properties of tuffisite host rocks, would inform new models of magma ascent dynamics during pre-eruptive unrest. The field evidence presented here suggests that single-shot models of tuffisite emplacement and associated cooling models are not appropriate, and that a full model for tuffisite emplacement is needed in which fracture width and sedimentation and erosion are coupled in a full dynamic model. Only then could the outgassing flux of tuffisites be properly computed to help assess whether tuffisites can act as pressure release valves capable of modulating the style of silicic eruptions. Finally, swarms of shallow volcanic earthquakes are thought to relate to fluid injection into particle-choked fracture pathways (e.g., Molina et al., 2004). Informing seismic source modelling by using constraints from the tuffisite fossil record could yield improved understanding of the nature of volcanic unrest and its relationship with subsurface magma movement.

3.9 Conclusion

Our characterisation of a particle-filled hydrofracture provides insights into tuffisite formation processes. Complex structures indicate that the tuffisite was formed by multiple fluid pulses, controlled by fluctuations in the fluid pressure, and variations in

the fill characteristics record changes in the fluid-particle concentration of the injected fluid. The dimensions of each sedimentary unit (40 m long and 0.1 m thick) can be used to estimate that an overpressure of $\sim$1.9–3.3 MPa was required for their formation, assuming only elastic deformation of the surrounding material, giving a total required pressure of $\sim$9 MPa at 500 m depth including lithostatic pressure. The overpressure, as recorded by sedimentary structures in the tuffisite, appears to have reached a maximum of $\sim$1.9–3.3 MPa, similar to the expected gas pressure just above the region of magma fragmentation within the main conduit, before waning at the end of tuffisite evolution. Viscous deformation can be seen around some injections, suggesting that if a tuffisite can become thick enough to sufficiently insulate material toward the end of its lifetime, injections can occur at a lower fluid pressure, deforming the surrounding material and causing permeability to rapidly decrease. The Húsafell tuffisite has similar dimensions to fractures filling with ash that have been modelled as the source of LP seismic swarms, providing a fossil record of otherwise unobservable processes that are a key component of volcanic unrest.

4 The exposed Mule Creek vent deposits record the structure of a volcanic conduit during a hybrid explosive-effusive eruption

Holly E. Unwin, Hugh Tuffen, Fabian B. Wadsworth, Emrys R. Phillips, Mike R. James, Annabelle Foster, Stephan Kolzenburg, Jonathan M. Castro, Lucy A. Porritt

Abstract

Silicic volcanic eruptions commonly begin with the explosive ejection of pyroclastic material, before transitioning to gentler effusion-dominated activity. Well-exposed dissected silicic systems are scarce and poorly studied, hindering the advances in our understanding of the explosive-effusive transition needed to improve interpretations of volcanic unrest and hazard forecasting. The Mule Creek vent (New Mexico, USA) is a dissected silicic conduit that records the processes controlling conduit formation and evolution, and the role tuffisites (fractures filled with variably welded pyroclasts) play in conduit dynamics. Here, we use decimetre-scale photo-mapping of lithostratigraphic units and thin section analysis to differentiate and interpret three dominant emplacement styles during vent evolution. First, there was repeated deposition and erosion of pyroclastic material at the conduit walls, recorded by erosive surfaces in pyroclastic breccia and agglomerates at the conduit margins. Second, sub-vertical domains of dense melt-dominated magma were emplaced and preserved as glass-dominated vitrophyre and brecciated vitrophyre, with the textural hallmarks of assembly from welding of pyroclasts. Finally, the sub-horizontal fracturing of previously deposited lithologies produced laterally cross-cutting tuffisites. The vent deposits track the widening and then narrowing of the conduit through time and reflect progressive insulation and generally higher temperatures towards the conduit centre as pyroclasts accumulate. Welding of pyroclastic fill and the formation of dense vitrophyres towards the conduit centre lowers deposit porosity and effective wall permeability. This drives localised gas pressure increases and results in gas-driven fracturing, generating tuffisites, which act as transient outgassing pathways. The structure

of the Mule Creek vent records an explosive-effusive transition, constraining the processes controlling conduit evolution and aiding our interpretation of volcanic unrest.

4.1   Introduction

Silicic volcanic eruptions are preceded by the opening of fractures driven by high pressure gas-ash mixtures (McGowan, 2016), often in fissures (Lara, 2009). These fissures then localise to single vents (Schipper et al., 2013). The first pyroclastic deposits recording this opening phase of explosive eruptions typically involve a high proportion of lithics, diagnostic of country rock fracturing and vent-clearing and widening (e.g. Stasiuk et al., 1996; Campbell et al., 2013; Schipper et al., 2013). The volcanic conduit is the ascent pathway along which material is transported towards the surface, and the vent is the uppermost part of this conduit system, which often flares as it approaches within ∼300–500 m of the surface (Wilson and Head, 1981; Cataldo et al., 2013). In silicic systems, the eruption onset is often characterised by high-energy explosive activity (Cassidy et al., 2018) involving the eruption of gas and pyroclastic material, before transitioning to effusive activity dominated by the comparatively gentle eruption of lava (Eichelberger et al., 1986). The switch between explosive and effusive activity is thought to broadly represent a transition from closed-system degassing to more open-system outgassing, where gas can escape from the magma and the conduit system, releasing gas pressure (Eichelberger et al., 1986; Jaupart and Allègre, 1991).

Open-system outgassing may occur vertically or laterally, with lateral outgassing allowing gas to escape from the magma and flow through permeable conduit margins, either through permeable host rock (Jaupart and Allègre, 1991; Rust et al., 2004; Lavallée et al., 2013; Farquharson et al., 2015; Kolzenburg et al., 2019), permeable tephra-lined conduit margins (Rust et al., 2004) or permeable particle filled fractures — known as external tuffisites — created by the injection of ash-gas mixtures into fractures within the conduit walls (Cloos, 1941; Heiken et al., 1988; Goto et al., 2008; Chapter 3). In contrast, open-system vertical outgassing requires either long-range magma permeability (e.g. an extensive magmatic foam), long-range fractures (such as internal tuffisites), a compacting column of fragmental material within the vent (Kolzenburg and Russell, 2014), or dynamic outgassing during fragmentation and explosive eruption, before welding (Wadsworth et al., 2020). Internal tuffisites have been proposed to form in hot magma within a volcanic conduit when shear stresses reach or exceed the strength

of the magma, forming interconnected fracture networks (Kendrick et al., 2016; Saubin et al., 2016). Tuffisites in magma have been touted as permeable outgassing pathways, potentially allowing sufficient outgassing to moderate eruption explosivity (Jaupart, 1998; Castro et al., 2012, 2014; Berlo et al., 2013; Farquharson et al., 2017; Heap et al., 2019; Kolzenburg et al., 2019). However, tuffisite permeability is only transient as welding progressively destroys pore space between hot fracture-propping particles (Stasiuk et al., 1996; Tuffen et al., 2003; Heap et al., 2019; Kolzenburg et al., 2019; Wadsworth et al., 2021).

Direct observations of silicic eruptive activity at Volcán Chaitén (2008–2009) and Cordón Caulle (2011–2012), both in Chile, show that the effusive eruption of silicic lava is interrupted by intermittent explosions (hybrid activity), with gas and ash erupted through fractures in the vent-filling lava itself (Castro and Dingwell, 2009; Castro et al., 2013; Schipper et al., 2013). The recognition that fragmented material trapped in lava-hosted fractures can weld to produce a continuous melt by viscous sintering (Gardner et al., 2018, 2019; Wadsworth et al., 2019, 2021; Farquharson et al., 2022), and the discovery of obsidian clasts and bombs formed of welded fragments (Cabrera et al., 2015; Gardner et al., 2017; Giachetti et al., 2021; Schipper et al., 2021), has led to models suggesting that the accretion of clastic material on to the conduit walls could form both obsidian pyroclasts (Gardner et al., 2017, 2019) and silicic lava (Wadsworth et al., 2020, 2022). Simultaneous explosive and effusive activity has been explained by continued fragmentation at depth, with effusive lava formed by either material accreting and welding at the conduit walls (Wadsworth et al., 2020), or a rising column of intact and degassing magma that does not fill the entire conduit (Schipper et al., 2021).

Dissected mafic and ultramafic systems, such as diatremes, are more common and better studied than silicic vents (e.g. White and Ross, 2011; Valentine and White, 2012; Ross et al., 2017). Diatremes and silicic vents share many similarities, with both formed of an inverse cone-shaped body of pyroclastic material created by blasting and then deposition, and a complex internal structure formed by the continued overturning of previously deposited material (e.g. Ross and White, 2006; Schipper et al., 2021; Valentine and Cole, 2021; Wadsworth et al., 2022). Comparing and contrasting these systems would help to improve our understanding of both groups. Dissected silicic vents provide an opportunity to examine structures and textures of an upper conduit system and test the diverse hypotheses for vent processes described above. The Mule Creek vent, New Mexico (USA), is a classic example of a dissected silicic vent and is a type-locality for
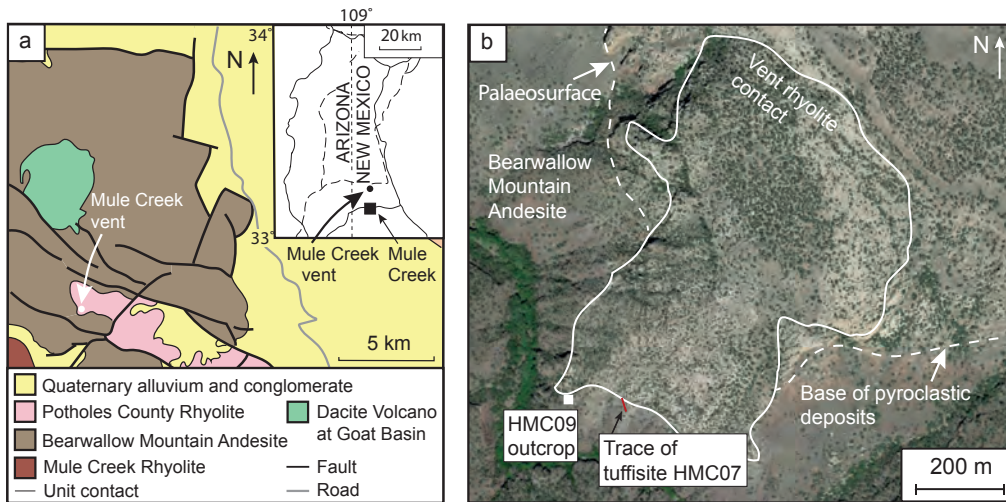
Figure 4.1: a) Location and geological setting of the Mule Creek Vent 8 km north of Mule Creek, Gila National Forest, New Mexico, USA; modified from Stasiuk et al. (1996) and Ratté et al. (2004). The geological map indicates the position of the Mule Creek Vent within the north-west trending Potholes County graben. b) Map view of the Mule Creek vent with the vent rhyolite lava contact, base of the pyroclastic deposit and sample locations marked. Map imagery: Google, ©2022 Maxar Technologies, NMRGIS, USDA Farm Service Agency.

examining the relationships between tuffisites and the vent that they intersect (Figures 4.1a and 4.1b; Stasiuk et al., 1996). Many features of the Mule Creek vent are described in detail by Stasiuk et al., (1996). Here, we build on their observations, focusing on a large outcrop of pyroclastic breccia at the vent margin that provides new insights into the early stages of vent evolution.

4.1.1 Geological setting of the Mule Creek vent

The Mule Creek vent (MCV) is located ∼8 km north of Mule Creek in the Gila National Forest, southwestern New Mexico, USA (Figure 4.1a) and is the best exposed of at least six genetically linked rhyolitic plugs and vents distributed along the north-west trending Potholes Country Graben (Stasiuk et al., 1996; Ratté, 2004), together with voluminous pyroclastic deposits. The MCV was formed during an eruption emplacing the 20–21 Ma Potholes Country rhyolite, a lava flow which is mostly confined within the Potholes Country Graben (Stasiuk et al., 1996). The Mule Creek vent is exposed in a tall canyon 350 m deep, cutting through the ∼23–25 Ma Bearwallow Mountain andesite host rock (Figure 4.1b). The flared shape of the vent towards the canyon rim suggests that the canyon exposes the uppermost ∼350 m of the vent. The upper half of the canyon is encased in bedded rhyolitic tephra up to 150 m thick, emplaced during vent formation,
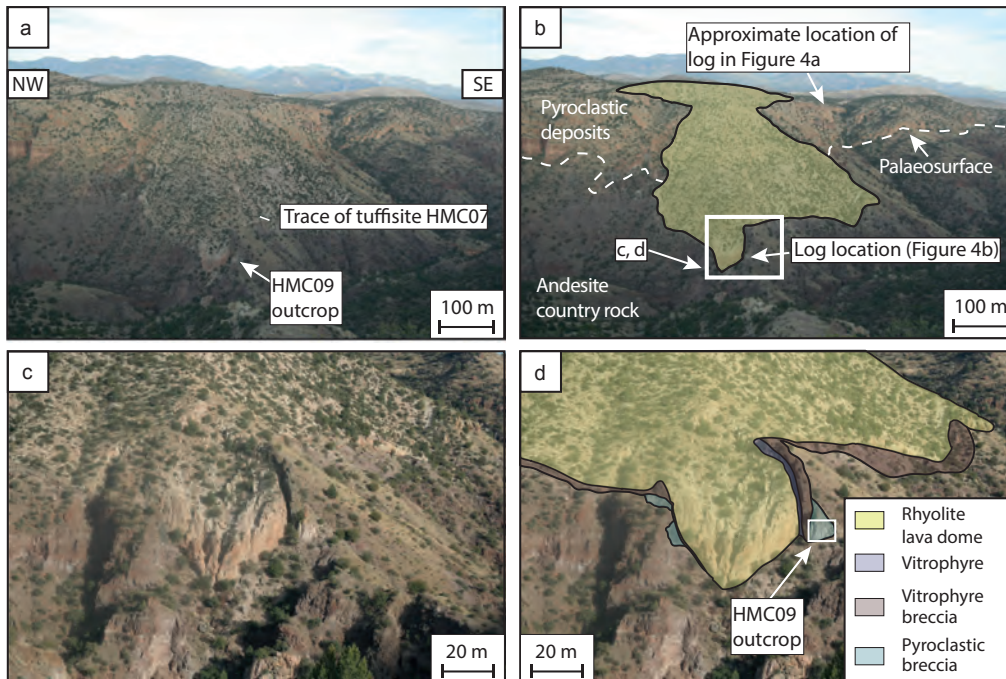
Figure 4.2: Overview photographs of the Mule Creek vent. a) Overview photograph showing the field location, taken looking NE b) The same view as in (a) but with a simplified geological interpretation overlain. c) A zoomed-in photograph showing the structure of the vent more clearly. d) The same view as in (c) but with a simplified geological interpretation overlain. Outcrop names and key features are marked.

indicating the position of the palaeosurface before the formation of the MCV (Figures 4.2a and 4.2b; Ratté, 2004). The Bearwallow Mountain andesite at the canyon base is composed of vesicular brecciated andesite lavas that are red brown to grey in colour. The pyroclastic deposits are sub-horizontally bedded >100 m from the vent, and their dip into the vent increases closer to the contact with the Potholes Country rhyolite lava (Stasiuk et al., 1996).

4.2   Field and analytical methods

A large outcrop of pyroclastic breccia at the vent margin was identified during fieldwork at the MCV in 2010 (HMC09, Figures 4.1b and 4.2), with a greater thickness and more complex internal structure than that described by Stasiuk et al. (1996). Samples and photographs of the MCV units and intersecting tuffisites were collected, enabling the multiscale (macro and micro) analysis of the four different vent units (pyroclastic breccia, vitrophyre breccia, vitrophyre, and central rhyolite lava) and their intersecting tuffisites. Thin sections were prepared from a sub-set of the hand-specimens and have been used

as part of a detailed microstructural study. In addition, polished thin sections were examined using a Hitachi SU-70 high resolution scanning electron microscope with a 15 kV beam voltage and 15 mm working distance. Backscattered-electron (BSE) images of the tuffisite matrix were taken of all samples at an appropriate scale to capture ~200 grains in each image for particle-size distributions, with the collected images each 1280 x 960 pixels. The area of the pyroclastic breccia imaged to produce the particle-size distribution was 0.016 mm^2 at x800 magnification with a scale of 17.5 pixels/μm. The area of vitrophyre breccia imaged was 0.1 mm^2 at x300 magnification with a scale of 3.0 pixels/μm.

Particle-size distributions for particles within tuffisites were determined by measuring the area of particles in backscattered-electron images using ImageJ (Schneider et al., 2012). The low contrast between particles and their touching margins prevented effective image thresholding for particle detection (Lormand et al., 2018). Therefore, the margins of each particle were traced manually. The traced particles were then separated out and each particle measured individually using ImageJ. The particle area data collected reflects 2D slices through 3D samples in the thin section, but will here be referred to as particle-size for simplicity.

The particle area was converted to an equivalent diameter for each particle using $d = \sqrt{4A/\pi}$, where A is the measured particle area and d is the equivalent spherical particle diameter. The circularity of the average particle in each image ranged from ~0.74 to 0.85, calculated with the in-built algorithm within ImageJ (imagej.nih.gov/ij; Schneider et al., 2012). Any particle with an equivalent diameter less than 10 pixels across or an area greater than 1% of the measured image area were considered not to be sufficiently well represented in the data and were filtered out (Shea et al., 2010). The particles were sorted into a series of geometric bins, with the smallest bin equal to the minimum size threshold (10 pixels in diameter) and each subsequent bin $10^{0.1}$ larger than the previous. The histogram was then normalised so that the sum of the areas is equal to one, converting to particle area fraction. While these particle-size distributions are taken from only one sample in a tuffisite in and one in a tuffisite in the vitrophyre breccia, the images locations have been chosen to as representative as possible for that sample. In is unknown how representative these samples might be for tuffisites in those units due to limited sample material, but the particle-size distributions found are given to simply consider the formation time of these tuffisites (considering sintering timescales) and also to compare to the particle-size distributions calculated for tuffisites elsewhere.

4.3 Field observations

The MCV is composed of a series of four major vent units, with the outermost unit comprising a pyroclastic breccia in contact with the andesite country rock (Figures 4.2c, 4.2d and 4.3; Stasiuk et al., 1996). The pyroclastic breccia is bordered on the inside edge by two dark-coloured units with a glassy appearance (i.e. nominally aphyric albeit with some microlite-dominated flow bands), termed by Stasiuk et al. (1996) as a vitrophyre breccia and a vitrophyre. The vitrophyre breccia is composed of heavily fractured clasts of glassy material, and borders the pyroclastic breccia. The vitrophyre breccia becomes less heavily fractured and more sheared towards the centre to form a vitrophyre unit formed of more coherent glass (Figures 4.3a and 4.3b). The vitrophyre unit grades into a flow-banded rhyolite lava at the vent centre (Stasiuk et al., 1996). The vent units are intersected by particle-filled fractures known as tuffisite veins, which form either steeply dipping and aligned features or sub-horizontal structures (Figures 4.3a and 4.3b). Tuffisites injected into the walls of the MCV are defined as external tuffisites, and may be constrained to an individual vent unit or in some cases cross-cut multiple vent units. These external tuffisite veins are filled with fragments of their host rock, as well as ash-sized particles that preserve sedimentary structures such as laminations.

The following sections describe field and sample observations that augment and supplement those described by Stasiuk et al. (1996). We report observations on a locality down-slope (~250 m deeper) from those investigated by Stasiuk et al. (1996), focusing on the pyroclastic breccia, vitrophyre breccia and vitrophyre units, and tuffisites (HMC09; Figures 4.2c and 4.2d).

4.3.1 Pyroclastic breccia and apron

Pyroclastic deposits around the vent form a $\leq$ 150 m thick apron (Figure 4.1b; Stasiuk et al., 1996), with subunits closer to the rhyolite lava contact dipping more steeply ($\leq$ 20 °) into the vent than those further away (Figure 4.3b), and commonly showing evidence of gravitational slumping. At distances >100 m from the rhyolite lava contact the pyroclastic deposits are approximately sub-horizontally stratified or dip away from the vent ($\leq$ 5 °). A transect through this pyroclastic apron at the canyon rim reveals that they become relatively less lithic-rich (fewer non-juvenile clasts) and increasingly pumice-dominated moving stratigraphically up-section (Figure 4.4a; Stasiuk et al. 1996).
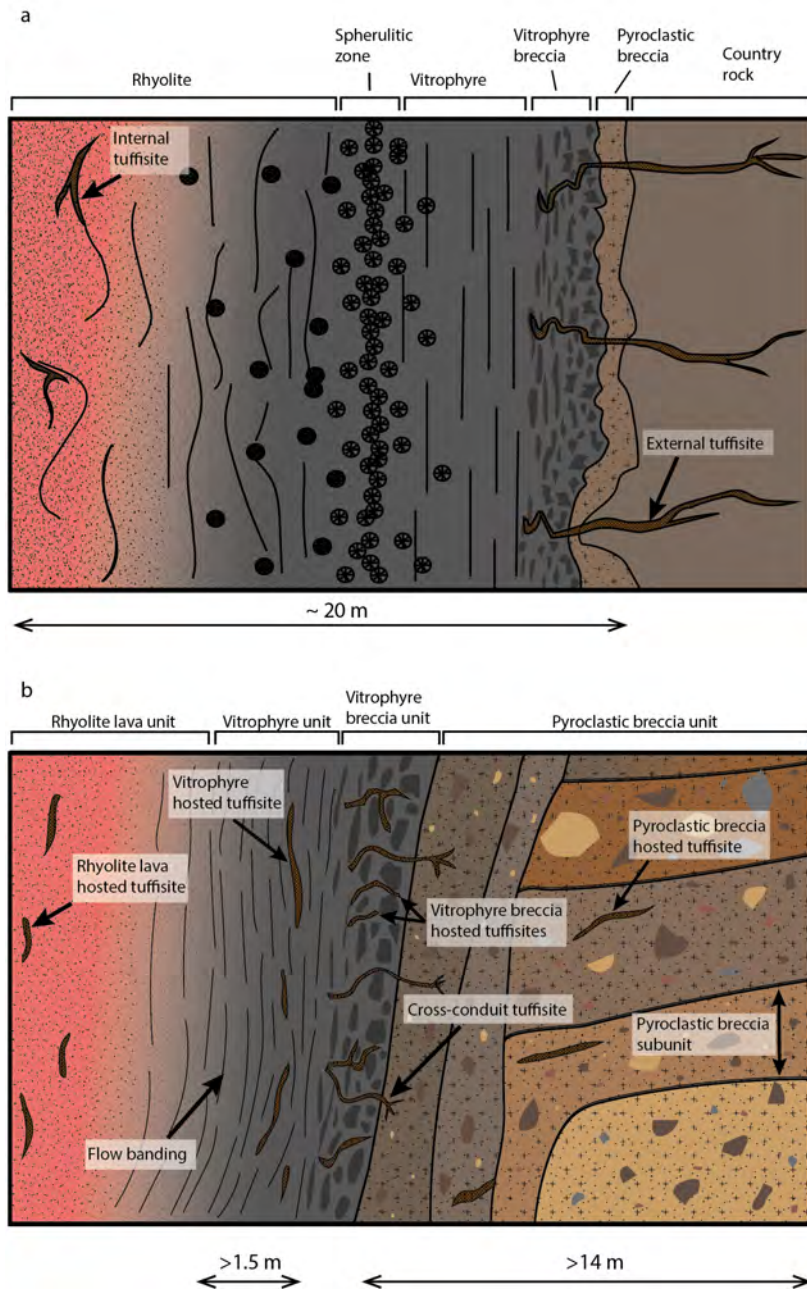
Figure 4.3: Schematics showing the structure of the Mule Creek vent in cross-section. Numbers in circles indicate figures that show the textures of the different features drawn here. a) Vent structure towards the canyon rim as identified by Stasiuk et al. (1996). b) Conduit structure as identified from the outcrop HMC09 — see Figures 4.1b and 4.2d for location. The outermost part of the vent consists of pyroclastic breccia, which is texturally very similar to the surrounding pyroclastic apron. Adjacent to the pyroclastic breccia is a unit of vitrophyre breccia, with glassy, often jigsaw-fit clasts that become more sheared and compacted towards the vent centre. The vitrophyre breccia grades inwards to become a more coherent vitrophyre unit. The vitrophyre grades into the rhyolite lava unit that forms the vent centre. The rhyolite lava unit is flow banded with flow bands that become more widely spaced towards the vent centre. Every unit of the conduit is cross-cut by tuffisite veins, with subvertical tuffisites in the rhyolite lava and vitrophyre units. In the vitrophyre breccia and pyroclastic breccia, tuffisites dip less steeply. Some tuffisites are laterally continuous, up to 13 m in length, while other tuffisites can only be followed for up to 50 cm.

111
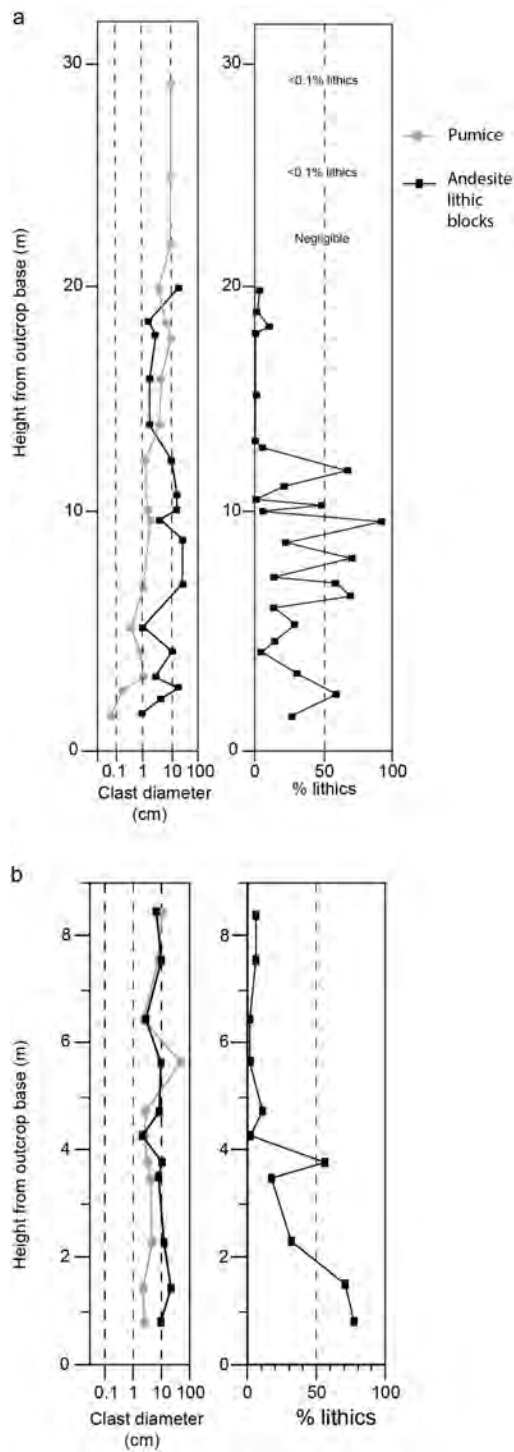
Figure 4.4: Logs of the maximum clast size and % lithics in the different pyroclastic breccia subunits in a) Stasiuk et al. (1996), measured close to the canyon rim and b) this study in outcrop HMC09. Componentry was completed at outcrop-scale (clasts >2 cm across). Locations of both logs are marked on Figure 4.2b. The trace of the log from outcrop HMC09 is drawn on Figure 4.6b.
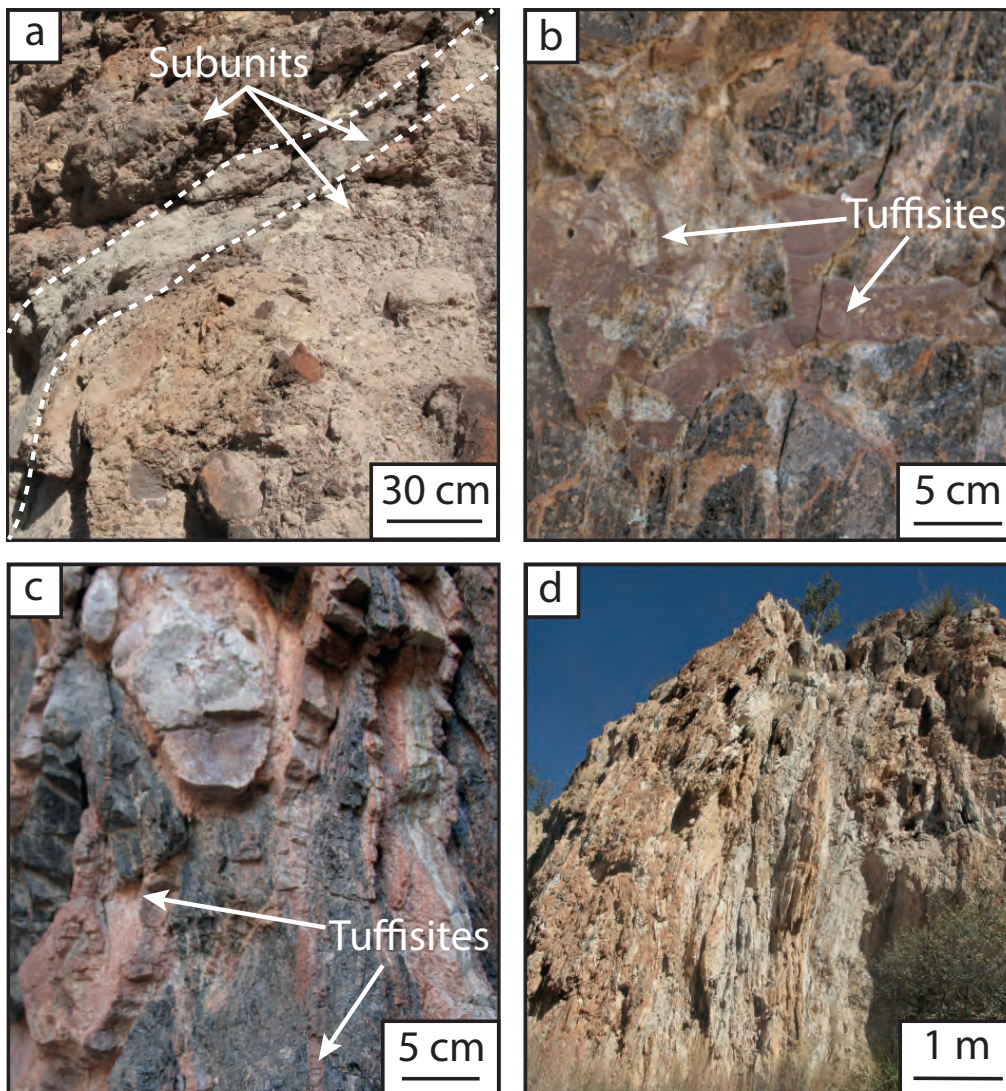
Figure 4.5: Images of the main units within the Mule Creek vent. a) Pyroclastic breccia consisting of multiple different subunits of varying grain-size. b) Vitrophyre breccia consisting of vitrophyre clasts (black/dark grey in colour) heavily dissected by tuffisite veins (red-brown in colour). c) More coherent vitrophyre unit with vertical banding, with vitrophyre (black/dark grey in colour) intersected by tuffisites (red-brown in colour) and late-stage mineralisation (white in colour). d) Central vent rhyolite lava showing well-developed platy fracturing.
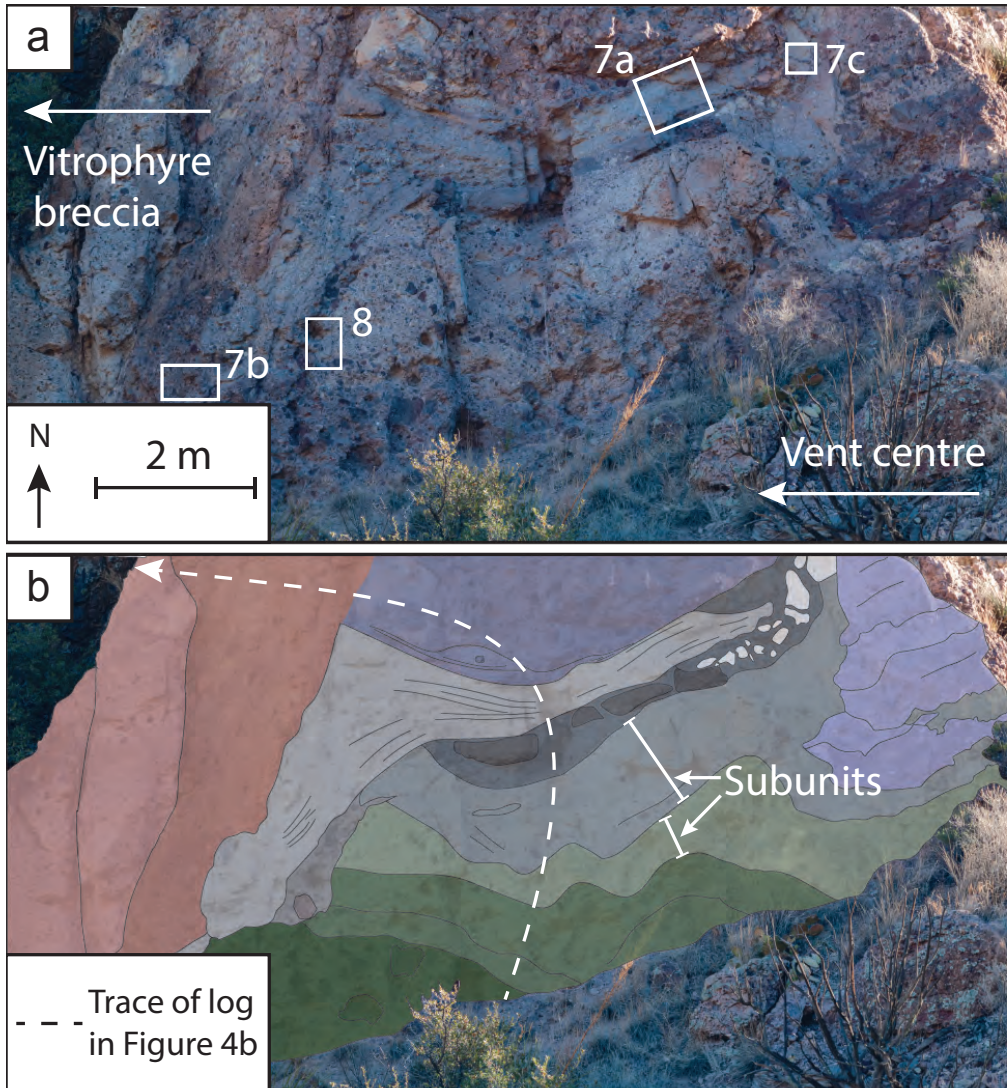
Figure 4.6: Photograph (a) and interpretation (b) of outcrop HMC09. The pyroclastic breccia is composed of multiple cross-cutting subunits, suggesting repeated erosion and deposition of material. The black line shows the trace of the lithostratigraphic log in Figure 4.4b. The coloured subunits in (b) highlight rock subunits of different characteristics, such as different proportions of lithics. Different colours are used to distinguish between subunits of different appearances.

The outermost unit of the MCV is a pyroclastic breccia that is in contact with either the pyroclastic apron or the Bearwallow Mountain andesite country rock (Stasiuk et al. 1996). Clasts in the pyroclastic breccia are composed of rounded pumice and angular lithic fragments derived from the Bearwallow Mountain andesite (Figure 4.5a). Close to the canyon rim, Stasiuk et al. (1996) recorded the pyroclastic breccia as being 0.2–2 m thick and infilling irregularities at the vent margin. This study focuses on the characteristics of a much thicker (>14 m) pyroclastic breccia sequence exposed closer to the base of the canyon on the eastern side of the vent (HMC09, Figures 4.2a, 4.2d and 4.6). This outcrop is ∼100 m deeper than the base of pyroclastic apron mapped by Stasiuk et al. (1996), which can be seen in satellite imagery and field photographs to be higher up the canyon wall (Figures 4.1b and 4.2b). We therefore interpret this outcrop of pyroclastic material as representing part of the pyroclastic breccia emplaced within the evolving vent during its formation, rather than as part of the pyroclastic apron, though these two deposits may be related to one another (Valentine and Cole, 2021).

The structure of the pyroclastic breccia is complex, formed of multiple stratified subunits distinguished by their overall grain-size and componentry. The outer subunits are exposed at the base of the outcrop where they form sub-horizontal layers that grade into one another (Figure 4.6). Closer to the vent centre, the pyroclastic breccia subunits dip steeply towards the vent centre before becoming sub-vertical, with a greater number of steep erosive surfaces. Many subunits contain slump features and steeply dipping extensional faults that offset subunit contacts by up to tens of centimetres (Figure 4.7a). Faults are differentiated from slump or erosive features as more planar features, confined to the pyroclastic breccia, that offset sections of an identifiable subunit.

The different subunits of the pyroclastic breccia contain subangular clasts of the andesite host rock as well as rounded pumice clasts. There are varying clast sizes, with coarser subunits containing ≤ 30 cm lithic (non-juvenile) clasts and ≤ 80 cm pumice clasts, while finer grained deposits contain ≤ 2 cm clasts (Figure 4.6). Sedimentary structures such as graded beds and coarser lenses of material are common in the finer grained subunits (Figures 4.7a and 4.7b). A transect through the outcrop indicates highest lithic content towards its base (Figure 4.4b). Some jigsaw-fit clasts are separated by thin ribbons of pyroclastic breccia (Figure 4.7c). In some layers of pyroclastic breccia the intergranular space between the larger clasts is filled with a matrix of densely welded fine-grained < 5 μm particles (Figure 4.7b).
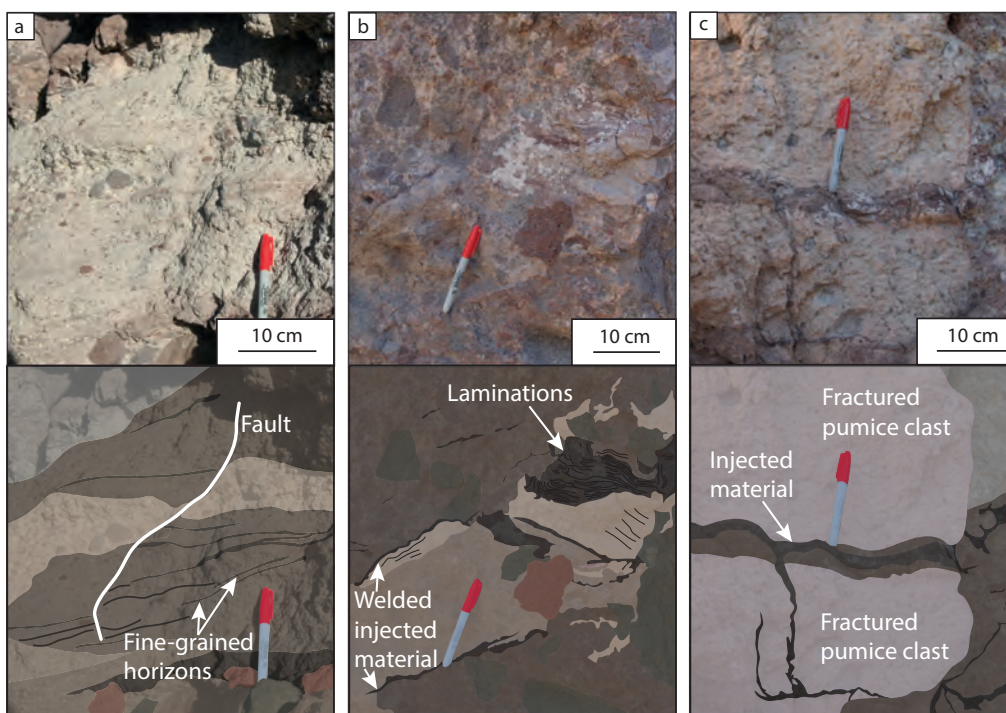
Figure 4.7: Photographs of structural features in the pyroclastic breccia (top) and interpretations (bottom). Different colours are used to distinguish between subunits of different appearances. a) A finer grained subunit within the pyroclastic breccia showing laminations, cross-lamination and coarser lenses of lapilli-sized material, offset by a small fault. b) Finer grained horizons of ash-sized particles cross-cutting the surrounding pyroclastic breccia. c) A fractured pumice clast ∼50 cm across injected with clastic material.
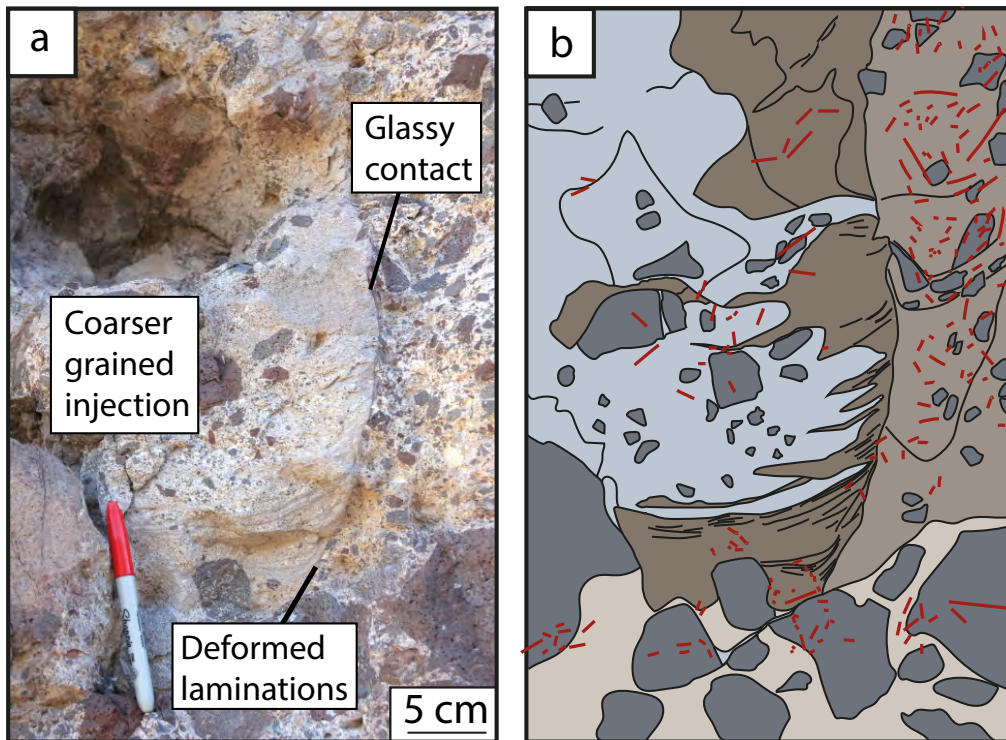
Figure 4.8: Photograph a) and interpretation b) of the pyroclastic breccia surrounding a steeply dipping glassy contact within the pyroclastic breccia that separates finer laminated material from a much coarser-grained subunit. Laminations in the finer material onlap onto the glassy contact. Different colours are used to distinguish between subunits of different appearances.

The nature of the contacts between the various layers of pyroclastic material are highly variable, ranging from sharp, steeply inclined sub-vertical margins marked by a distinct, narrow glassy 'rind', defined by its low vesicularity and absence of visible clasts at outcrop scale, to more complex and highly irregular morphologies with 'feather-like' interdigitating contacts. An example of a highly complex feather-like contact is shown in Figure 4.8 where a laminated pyroclastic deposit composed of fine lapilli and ash-sized grains is cross-cut by a relatively younger lithic breccia. Within a few centimetres of a subvertical contact running down the centre of the photograph (Figure 4.8a) the lamination is deflected upwards to become parallel to this glassy boundary (Figure 4.8b).

The vitrophyre breccia and vitrophyre (Figure 4.3) are lithologically very similar, forming subvertical dark-coloured units with a glassy texture (Figures 4.5b and 4.5c). These units are both non-vesicular. The vitrophyre breccia is a 0–3 m thick unit composed of mostly angular-subangular vitrophyre clasts (ranging from 1–10 cm across) and a few rare andesite clasts ∼3 cm across (Figure 4.5b; Stasiuk et al., 1996). The vitrophyre

117

clasts often show a jigsaw-type fit, separated by red-coloured welded clastic material, suggesting in-situ fracturing of the material. However, Stasiuk et al. (1996) recorded some clast imbrication, suggesting at least some localized transport of clasts. Close to the contact with the vitrophyre (<50 cm from contact) clasts become more elongate than those further from the contact, indicative of shear deformation parallel to the vent margins, and clasts are also more strongly welded together (Stasiuk et al., 1996).

The vitrophyre unit is typically ∼1 m thick but locally reaches 7 m. Elsewhere within the vent this vitrophyre unit is absent (Stasiuk et al., 1996). Flow bands 1–100 μm thick in the vitrophyre are seen to be parallel to the vent margins in oriented samples, but can be contorted and discordant where the contact is irregular (Figure 4.5c; Stasiuk et al., 1996). The vitrophyre grades into the central rhyolite lava unit.

4.3.2   Flow-banded rhyolite lava

The innermost 25 m (measured from an approximate conduit centre-line close to the canyon base) of the MCV is composed of grey to pink flow banded rhyolite lava (Figures 4.3 and 4.5d). The flow banding is more narrowly-spaced (<0.5 mm thick) towards the margins of the rhyolite lava compared with the unit centre (Figure 4.3b). Towards the centre of the MCV the flow banding becomes relatively wider-spaced and increasingly deformed by open to tight, steeply inclined isoclinal folds (Stasiuk et al., 1996). The flow bands consist of layers mostly defined by variations in the degree of vesicularity of the rhyolite lava, with some layers containing clearly visible, open subrounded vesicles, while other layers are less vesicular in appearance and display deformed coalesced vesicles (Stasiuk et al., 1996). Some flow bands are instead defined by alternating bands of aligned microlites and cryptocrystalline rhyolite. The coarsely flow banded rhyolite lava at the very centre of the conduit is the most vesicular compared with the outer parts of this unit at outcrop scale (Stasiuk et al., 1996). This unit shows well-developed sub-vertical platy fracturing (Figure 4.5d). Small sub-millimetre spherulites in the centre of the rhyolite lava increase in size and abundance towards the rhyolite lava margins, before decreasing once again where the rhyolite lava grades into the adjacent vitrophyre unit over a zone approximately 1 m thick (Stasiuk et al., 1996).

4.3.3 Pyroclast-filled fractures

Pyroclast-filled fractures have been recognized in each different unit of the MCV (Figure 4.3) and typically form cross-cutting veins that record fluid transport and injection into the host rock. The size of these veins varies considerably from laterally extensive features which are >30 m in length to much shorter veins that can only be followed for ~2 cm. The morphology of the pyroclast-filled veins varies depending on their host lithology. Consequently, we have divided the veins into the following categories — those hosted in (1) country rock; (2) pyroclastic breccia; (3) vitrophyre or vitrophyre breccia; (4) cross-cutting multiple units and (5) flow-banded rhyolite lava. The characteristics of the pyroclast-filled veins within each host rock are summarized in Table 4.1. Many of these observations are similar to those made closer to the top of the canyon by Stasiuk et al. (1996).

Table 4.1: The characteristics of the pyroclast-filled veins found within the different units of the Mule Creek vent

	Country rock		Pyroclastic breccia	Vitrophyre breccia	Vitrophyre	Cross-cutting multiple host rock units	Rhyolite lava
	Bearwallow Mountain andesite	Pyroclastic apron					
Fracture morphology and margins	Irregularly shaped fracture margins		Diffuse margins giving a wispy appearance	Sharp-edged fracture networks	Sub-vertical sharp-edged fractures parallel to banding in vitrophyre	Diffuse margins coated with fine ash-sized particles	Wavy fractures with poorly defined margins parallel to flow banding
Fracture length	Fractures typically laterally continuous for a few metres		Generally tens of cm in length but up to 13 m long	Wider main fractures show a greater degree of fracturing of their vitrophyre walls	Fractures laterally continuous for <1 m	Fractures up to 30 m in length	Fractures ~ 10 cm in length
	Extend up to 10 m into country rock before branching into networks of veins <1 cm wide				Small perpendicular offshoot fractures extend a few cm from the main fracture	Extend from the margin of the vitrophyre breccia, through the vitrophyre and into the country rock	
Fracture width	Fractures up to 10 cm in width	Fractures up to 20 cm in width	Fractures typically <5 cm in width	Fractures up to ~1 cm in width	Fractures up to ~5 mm in width	Fractures up to ~20 cm in width	Fractures typically ~2 cm wide
Fracture fill	Well sorted homogeneous lapilli-sized grains		Welded ash-sized particles < 5 μm across	Ash-sized particles, angular vitrophyre clasts, and crystal fragments	Brown-coloured altered devitrified material at fracture centre	Welded ash-sized particles < 5 μm across to lapilli-sized grains	Multiple domains of well sintered ash-sized particles

120

	Fracture fill			Internal structures			
Subangular rhyolite lava clasts <5 mm across and quartz and feldspar phenocrysts	Andesite clasts <1 cm across close to vein margins		Laminations and cross-lamination common	More complex internal structure than andesite-hosted veins	Jigsaw-fit andesite clasts at vein margins	Soft sediment deformation of vein adjacent material	
	Rare andesite clasts						
Particles fill pore spaces between large clasts in the breccia	Large clasts sourced from the breccia protrude across vein margins		Laminations, cross-laminations and climbing ripples	Internal self-injections		Soft sediment deformation of vein adjacent material	
Fracture margins lined with welded vitrophyre clasts up to 20μm across	Horizons of fine grained material weave through welded blocks of vitrophyre clasts		No laminations or cross-lamination	Wider fractures contain multiple domains of material separated by sharp erosive contacts		Narrower fractures have a more simple internal structure with fewer domains	
Large clasts in the fracture centre sourced from the surrounding host rock			Fuzzy alteration affects the fracture walls along the length of the fracture	Most veins too narrow to contain visible internal structure	Continuous pale band of glassy material at centre of largest fractures	Lamination, cross-lamination and graded bedding	Multiple domains separated by sharp well-defined erosive to graded contacts
							Soft sediment deformation of vein adjacent material when hosted by pyroclastic breccia or pyroclastic apron
Few quartz and feldspar phenocrysts <0.5 mm across			Laminations and graded bedding			Multiple domains separated by sharp erosive contacts	Soft sediment deformation to produce deformed laminations

4.3.3.1 Pyroclast-filled veins hosted in the country rock

The mostly sub-horizontal pyroclast-filled veins ($\sim$2 cm in width) within the country rock extend into the surrounding Bearwallow Mountain andesite or pyroclastic apron (Figure 4.3; Stasiuk et al., 1996). The veins divide into multiple narrower veins ($<$1 cm in width) at their tips to produce a branching network (Figures 4.3, 4.9a and 4.9b; Stasiuk et al., 1996). The veins are filled with a matrix of red, oxidised, ash-sized particles with fragments of quartz and feldspar phenocrysts and larger ($<$1 cm across), subangular clasts of rhyolite lava and andesite (Stasiuk et al., 1996). Laminations and cross-laminations are common in the finer ash-sized particles found at the fracture margins.

4.3.3.2 Pyroclast-filled veins hosted in the pyroclastic breccia

Pyroclast-filled veins in the pyroclastic breccia are typically $\sim$ 5 cm in width with diffuse margins, giving veins a wispy appearance (Figures 4.9c and 4.9d). The fill is entirely composed of ash-sized particles that are typically welded ($<$5 μm across; Figures 4.10a and 4.10b). This material has a similar appearance to the matrix of the pyroclastic breccia and the material forming tuffisites in the country rock, suggesting a similar composition. The finest material is at the fracture margins where it forms sub-horizontal to irregular, finely laminated features that infill originally open pore spaces and/or voids within the host breccia. Clasts of host material also sometimes protrude across vein margins (Figure 4.11a) and clasts from the host breccia that are substantially larger than those of the surrounding vein material can also be found at vein centres (Figure 4.11a). This is in contrast to tuffisites seen elsewhere that occur within fractures. Within the pyroclastic breccia, the clast-filled veins were observed forming isolated areas of fine-grained material that are not apparently connected to the margin of a pyroclastic breccia subunit, though could be connected in 3D.

The pyroclastic breccia hosted veins typically contain complex internal structures, including laminations, climbing ripples and internal self-injections (Figure 4.11b). The host pyroclastic breccia adjacent to the veins has experienced soft-sediment deformation, with localised vein-adjacent fluidisation producing complex structures including disharmonic folds, cuspate to irregular boundaries between the laminated vein and breccia (Figure 4.11a), and the disruption of the matrix to the breccia to form 'ball-like' structures enclosed
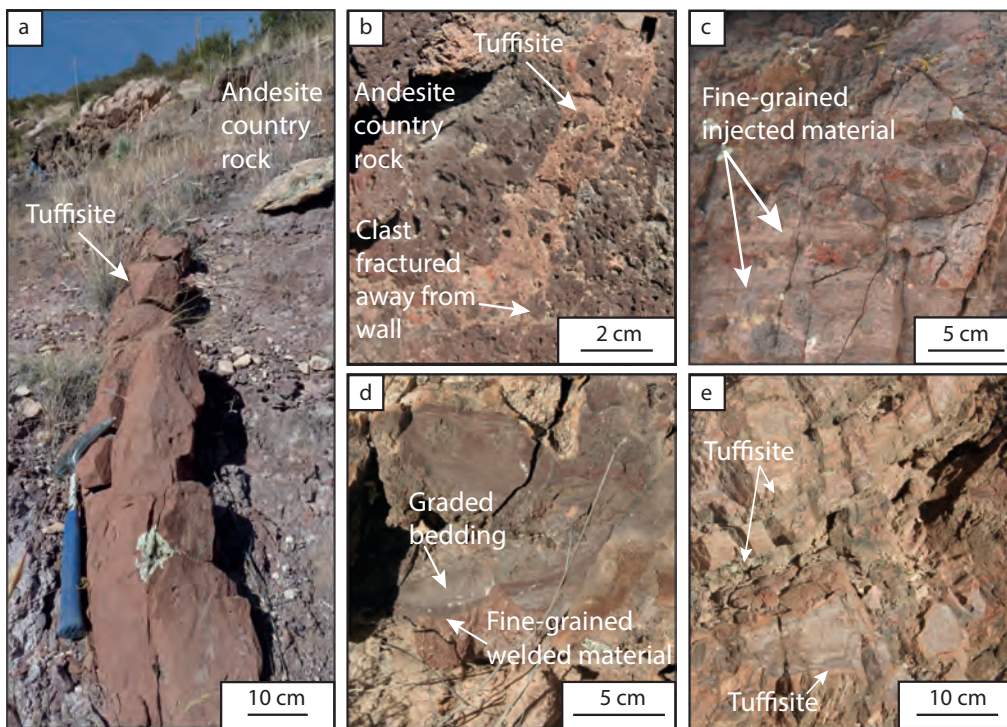
Figure 4.9: Photographs of tuffisites in different units of the Mule Creek vent. a) Tuffisite (red, in centre of image) in the andesite country rock surrounding the vent. b) Tuffisite in the andesite country rock containing clasts derived from the tuffisite walls. c) Sub-horizontal fine-grained tuffisites cross-cut pyroclastic breccia. d) Tuffisite hosted in pyroclastic breccia displays complex laminations and graded bedding. e) Tuffisites within the vent rhyolite form a network of veins with a glassy appearance.
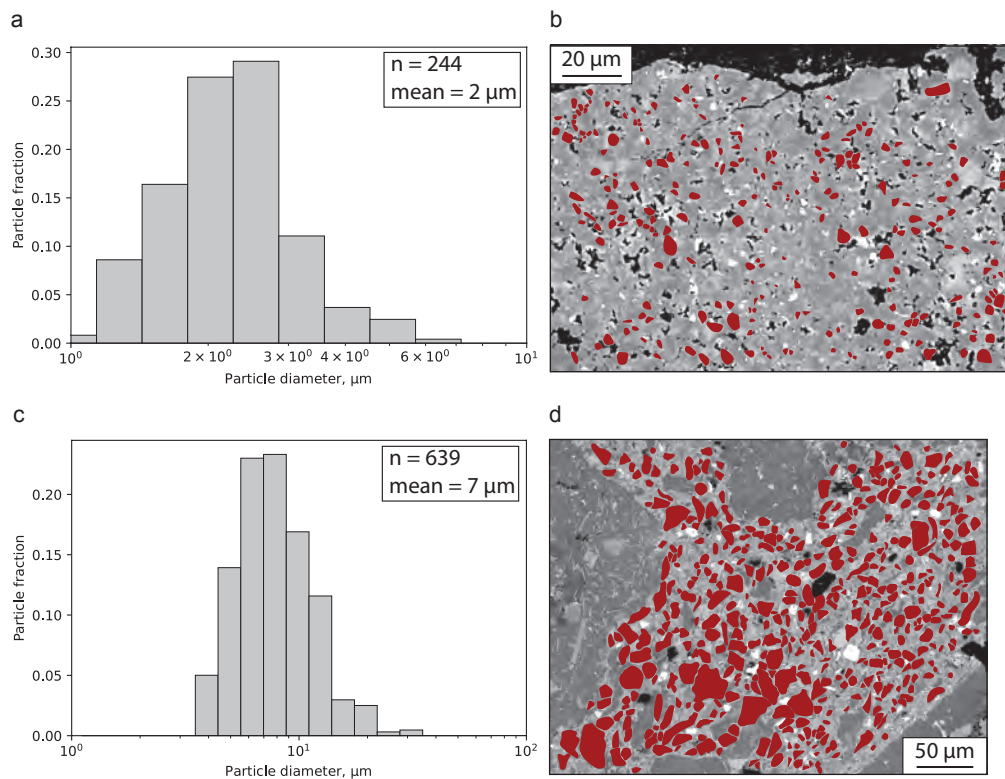
Figure 4.10: Particle-size distributions of tuffisites from SEM images. The particles measured are coloured in red in the SEM image, and n is the number of particles measured. a) and b) Particles forming a diffuse tuffisite within the pore space of the pyroclastic breccia. Image location is given in Figure 4.11a. c) and d) Particles forming a tuffisite within the vitrophyre breccia. The location of the SEM image is given in Figure 4.11d. The original untraced images can be found in Appendix A.2 (Figure A.1).

within the vein (Figures 4.11b and 4.11c). Soft-sediment deformation of the host pyroclastic breccia was also observed and associated with the fragmentation of these fine-grained pyroclast-filled veins themselves, which are broken up into jigsaw-fit clasts of densely welded material.

4.3.3.3   Pyroclast-filled veins hosted in the vitrophyre and vitrophyre-breccia

Pyroclast-filled veins within the vitrophyre are mostly oriented sub-vertically, parallel to the banding within the vitrophyre (Figure 4.5c). Most of the veins are too narrow (<1 mm in width) to contain visible internal structure and are filled with brown coloured altered devitrified material, with fuzzy local alteration also affecting the fracture walls along the fracture length.

Many pyroclast-filled veins within the vitrophyre-breccia have the same appearance
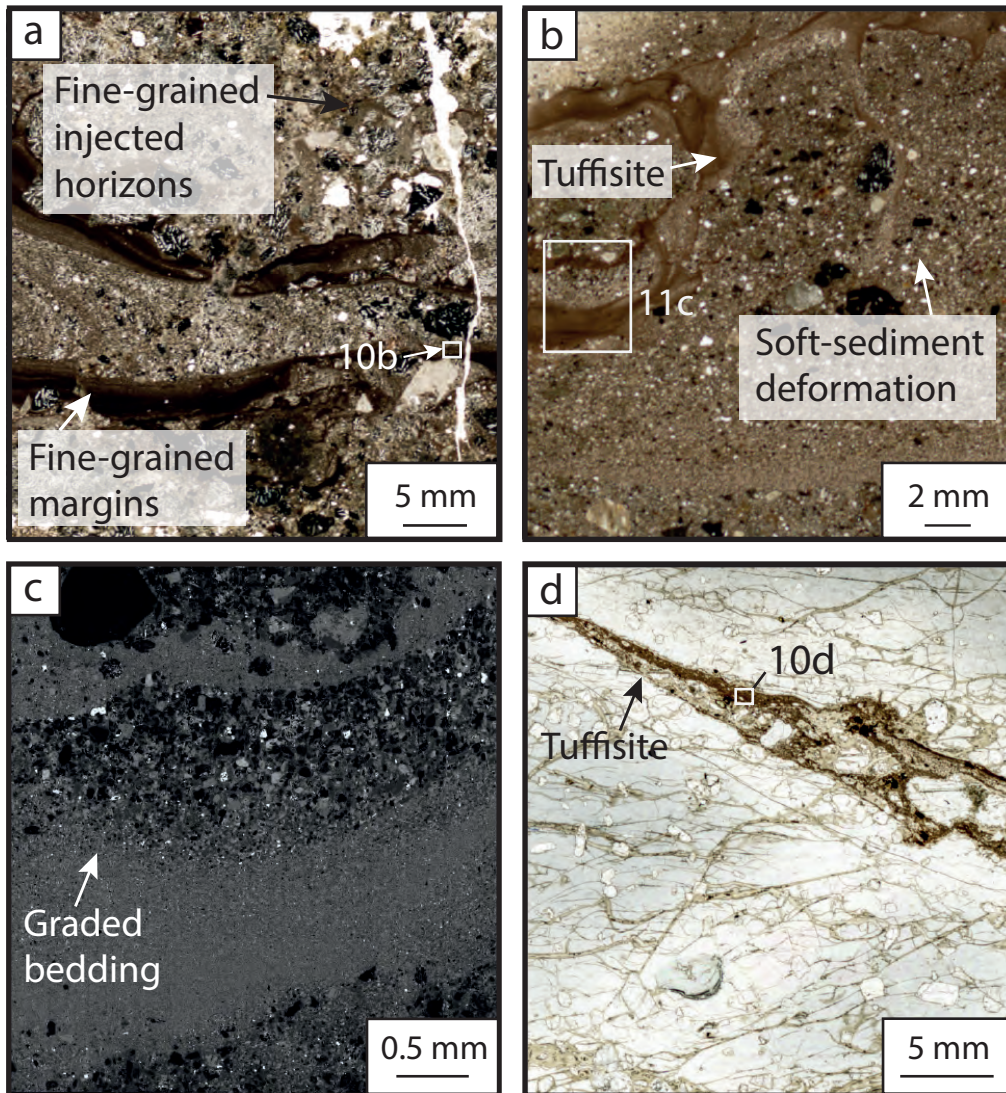
Figure 4.11: Photomicrographs and SEM images tuffisites within the pyroclastic breccia and vitrophyre breccia. White labelled boxes indicate the position of SEM images within the larger scale image. a) Photomicrograph of a tuffisite within the pyroclastic breccia, with finely laminated margins. The injected material grades into coarser particles towards the tuffisite centre. b) Photomicrograph of tuffisite in the pyroclastic breccia, with irregular margins, formed of fine-grained laminated material, and a coarser centre. c) Backscattered electron image of fine-grained injection within the pyroclastic breccia. Small ash-sized particles fill the pore space of the host breccia. d) Sharp-edged tuffisite within the vitrophyre breccia containing different phases of injected material separated by erosive surfaces.

as those in the vitrophyre. However, some fractures within the vitrophyre breccia are larger, up to 1 cm in width, and contain either discontinuous laminae or irregular patches or clasts of clastic material resulting in complex internal structures (Figures 4.5b and 4.11d). The fracture margins are often lined with vitrophyre fragments up to 20 μm across (Figure 4.10c) that are welded — locally to such an extent that the individual clasts are no longer visible (Figure 4.10d). Horizons of ash-sized particles, angular vitrophyre clasts, and crystal fragments weave between those vitrophyre blocks. The clast-filled veins can also contain irregularly shaped blobs of melt with microlites that can be aligned in sheared clasts (Figure 4.10d). The microlite texture of each of the melt blobs is qualitatively similar and the melt blobs are much more microlite-rich than the surrounding vitrophyre. Narrower veins within the vitrophyre-breccia have structures that are less complex, but often still show cross-cutting relationships. The erosive contacts between the different injected domains are sharp, with no indication of soft-sediment deformation. These veins do not show other internal structures such as cross-bedding or lamination (Figure 4.11d).

4.3.3.4 Cross-conduit pyroclast-filled veins

Pyroclast-filled veins are not restricted to spanning the width of one vent unit, and Stasiuk et al. (1996) reported laterally extensive veins originating in the vitrophyre breccia and continuing outwards through the pyroclastic breccia and into the surrounding andesite country rock. In this study, one laterally extensive vein with a length >30 m was traced through the pyroclastic breccia and into the country rock (HMC07, Figures 4.2a and 4.3b). These veins have a similar appearance to the matrix of the pyroclastic breccia and the pyroclastic breccia-hosted tuffisites, suggesting a similar composition.

4.3.3.5 Pyroclast-filled veins hosted in flow-banded rhyolite lava

The pyroclast-filled veins within the rhyolite lava are typically ∼2 cm wide and tens of centimetres long and steeply dipping, aligned parallel to flow banding within the host rock (Figure 4.9e; Stasiuk et al., 1996). The internal structure of these veins is complex, with sharp well-defined erosive to gradational contacts separating clastic domains with different grain-size. Soft-sediment deformation is clearly seen, with curved walls to injections and deformed laminations. The pyroclast-filled veins can form an angular

network filled with welded material.

4.4   Interpretations

The units of the MCV are interpreted to have all been emplaced during a waning explosive eruption, forming in order from the pyroclastic breccia at its outer margins deposited first, then cross-cut by the accretion of the vitrophyre breccia and vitrophyre, before finally the emplacement of the rhyolite lava within the centre of the evolving vent (Figure 4.12 and Appendix A.3, Animation 2) . Repeated fracturing and the injection of material into the vent units would have been facilitated by pulsations within this overall waning phase.
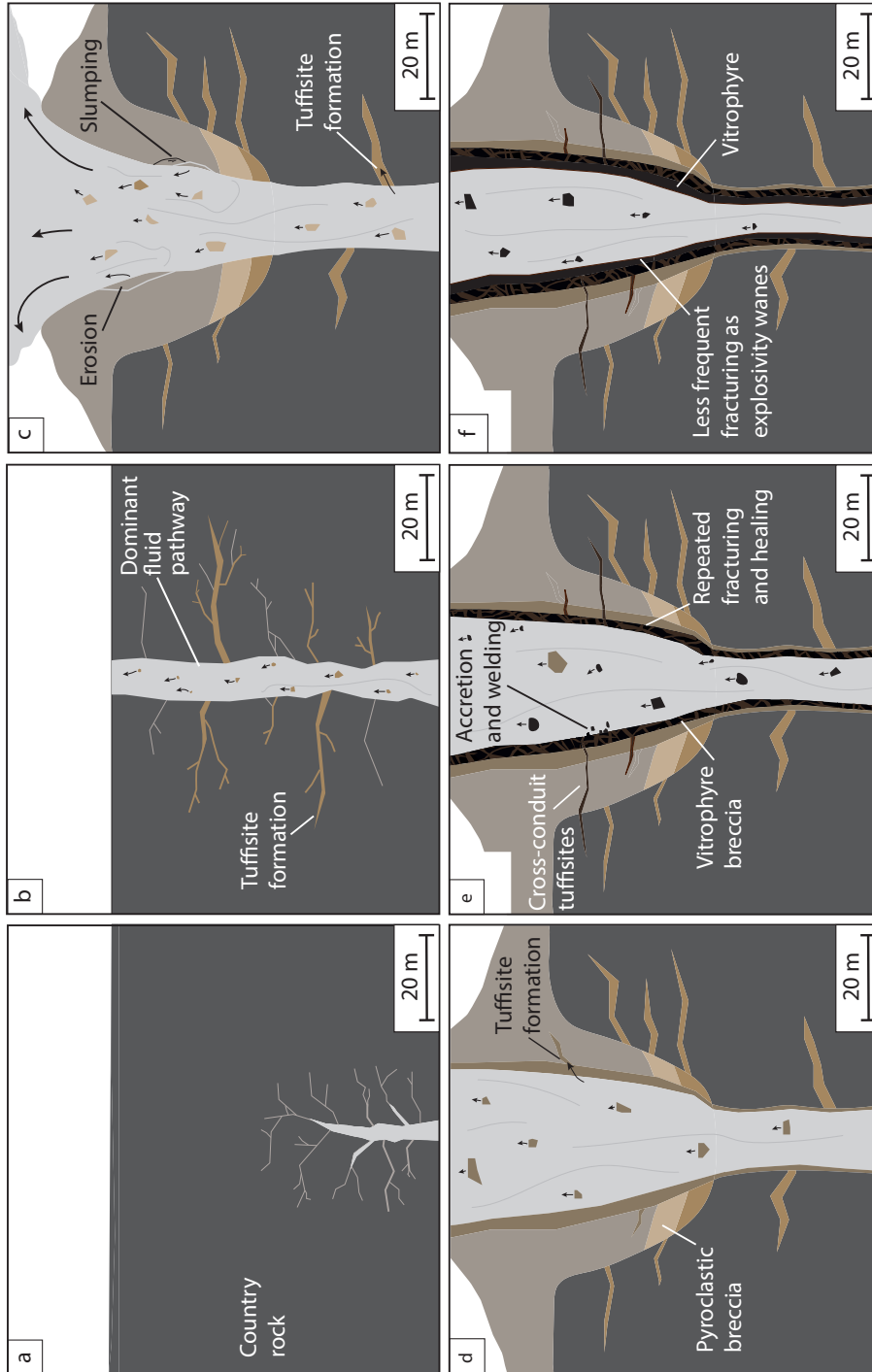
Figure 4.12: Model for the formation of the Mule Creek vent. See animated version of this figure (Animation 2). a) Fractures are opened by a high pressure gas-pyroclast mixture. If preserved, material deposited within these fractures forms tuffisites within the country rock (e.g. Figure 4.9a). b) Continued fracturing forms a network of fractures that can grow in size (thickness and length) due to the quarrying of pyroclastic material. c) Propagation and widening of fractures allows for the formation of a proto-conduit. d) Repeated deposition and erosion as fluid pressure within the developing conduit fluctuations allows for the emplacement of multiple subunits of pyroclastic breccia. Pyroclastic breccia-hosted tuffisites can form (e.g. Figures 4.9b–d). e) Once the conduit reaches a great enough temperature, welding of ash-sized particles at the conduit margins produces the vitrophyre. Repeated fracturing and healing forms the vitrophyre breccia with jigsaw-fit clasts and vitrophyre breccia-hosted tuffisites. Cross-conduit tuffisites that intersect multiple vent units form. f) Once the explosivity drops sufficiently the accreting vitrophyre will not be as greatly fractured, producing a more intact vitrophyre unit. Fracturing of the vitrophyre by high pressure gas-ash mixtures produces tuffisites hosted within the vitrophyre.

4.4.1 Formation of the pyroclastic breccia

The different subunits of the pyroclastic breccia are often separated by erosive surfaces, suggesting repeated cycles of erosion and deposition. The extensional faults seen within the pyroclastic breccia (Figure 4.7a) reflect material collapsing back into the vent at the end of a phase of deposition. Sub-horizontal subunits away from the vent centre are interpreted to have formed first, cross-cut by later subunits deposited closer to the vent centre (Figure 4.12 and Appendix A.3, Animation 2). Welding of the pyroclastic breccia allowed it to transition from a loose pile of fragmented rock and pyroclasts that would have been frequently overturned to a more coherent rock. Later sub-vertical pyroclastic breccia would have been injected through this more coherent material, allowing steeper and better-defined erosive contacts to form. Fractured jigsaw-fit clasts separated by ribbons of clastic material (Figure 4.7c) record a smaller-scale version of this process, with sudden pressure pulses breaking clasts during deposition.

The pyroclastic breccia contains a substantial volumetric proportion of lithic clasts, suggesting that the breccia was emplaced during an early stage of vent formation when explosive processes were quarrying, transporting and depositing clasts of the surrounding country rock (Figure 4.4; Stasiuk et al., 1996). The erosive contacts suggest that significant erosion was still occurring, interspersed with periods of deposition. The lower lithic clast proportion (<10 vol.%) in the later sub-vertical pyroclastic breccia subunits could indicate that earlier breccia subunits acted as a barrier preventing further quarrying of the country rock (Figure 4.4). Through time, subunits became less lithic-rich as the conduit began to stabilise in both size and shape, reducing the overturning of the pyroclastic breccia already deposited and breaking less material from the conduit walls (Valentine and Cole, 2021).

The steep glassy contact (Figure 4.8) is an example of one of the erosive margins between different breccia subunits. Its glassy margin formed via accretion of ash-sized particles to the sub-vertical surface, where they could weld to form dense glass, through the same processes thought to form obsidian or vitrophyre at conduit margins (Gardner et al., 2017). The formation of the glassy margin suggests that this position in the vent was sufficiently hot for welding to occur, and if deposited rapidly enough, this may have helped to strengthen the margin, allowing it to exist at such a steep angle.

4.4.2 Formation of the vitrophyre breccia and vitrophyre

The similarities between the vitrophyre breccia and vitrophyre units, both dark units with a glassy appearance and low vesicularity, suggest that these units are formed of the same material. These units are therefore interpreted to have formed through the same process, with the vitrophyre breccia a brecciated derivative of the vitrophyre. The vitrophyre is formed by the hydration of obsidian due to post-emplacement alteration since its emplacement. Obsidian can form by the accretion of pyroclasts at the conduit margins (Appendix A.4 Animation 3; c.f. Gardner et al., 2017), and if continued this process could also produce a thick unit coating the conduit walls (Wadsworth et al., 2020). This is the same process that we suggest formed the thin, localized glassy contact within the pyroclastic breccia (Figure 4.8; see Section 4.4.1), but here occurring on a far larger scale in terms of both the thickness and vertical continuity of the dense glassy layer formed. The lack of lithics in the vitrophyre breccia and vitrophyre suggest that quarrying of the country rock had decreased by the time these units were emplaced, perhaps due to the source of lithics becoming cut off as the margins of the conduit were no longer country rock, or because explosivity waned.

There are two potential mechanisms by which the vitrophyre could brecciate to form the vitrophyre breccia: either the latter formed through in situ fracture of a coherent vitrophyre, supported by the pseudo-jigsaw-fit appearance of many clasts and the presence of tuffisites, or clasts were eroded and transported from greater depth, before being deposited to form the vitrophyre breccia (Gardner et al., 2017; Wadsworth et al., 2020). Compaction and shearing later altered the shape of these clasts towards the vitrophyre breccia-vitrophyre contact (Figure 4.3), causing them to become more elongate, masking the evidence for these processes across much of the unit.

The persistence of lithics suggests some clasts within the vitrophyre breccia were sourced from elsewhere, perhaps sourced from a greater depth and transported up the conduit to their place of deposition (Stasiuk et al., 1996; Saubin et al., 2016). Imbricated clasts must have been transported at least a few metres before being deposited. Most clasts however have a jigsaw-fit appearance, suggesting that while some clasts may have been transported from elsewhere, the local clast production by in-situ fracturing was more prevalent (Appendix A.4 Animation 3). Shear traction on the assembling vitrophyre walls due to the bypassing high velocity gas and pyroclasts could produce a sufficiently high shear stress, relative to the elastic shear modulus, to brecciate the vent margin

(Wadsworth et al., 2018). If the brecciation of the vitrophyre walls is indicative of high velocity bypassing flow, then the transition to non-brecciated vitrophyre could represent eruption waning and a further reduction in explosivity, as dense conduit-plugging material experienced a lessening degree of damage by pulses of pressurized magmatic fluids.

4.4.3 Formation of tuffisites

The pyroclast-filled veins found cross-cutting the different vent units are interpreted as tuffisites, with all veins except those in the pyroclastic breccia occurring within fractures. We interpret the fracture-hosted tuffisites as hydrofractures driven by pressurised magmatic fluids (gas-pyroclast mixtures) above the fragmentation level in the eruption-feeding conduit (Wadsworth et al., 2020; Chapter 3). Most of the tuffisites seen within the MCV have complex internal structures that must reflect either variations in the fluid velocity along the fracture or changes in fracture width, or both. Variations in fluid velocity can be driven either externally, by gas pressure fluctuations within the volcanic conduit, or internally by local variations in the fracture width, created by pre-existing narrower fracture sections or by clogging the fracture with deposited material (Perkins and Kern, 1961; Cosgrove, 2001; Phillips et al., 2013; Chapter 3). Within the MCV we identify four different phases of tuffisite formation: (1) the formation of tuffisites within the country rock, associated with the opening of the conduit pathway (Figures 4.9a and 4.9b), (2) diffuse tuffisites within the pore space of the pyroclastic breccia (Figures 4.9c and 4.9d), (3) tuffisites hosted within the vitrophyre and vitrophyre breccia (Figures 4.5b, 4.5c and 4.11d) and (4) tuffisites within the central rhyolite lava (Figure 4.9e).

4.4.3.1 Tuffisites in the country rock

Tuffisite veins within the andesite country rock contain clasts of the host rock at their margins that have been fractured away from the vein wall (Figures 4.9a and 4.9b). This fracturing process records the propagation and widening of the fracture network, with country rock tuffisites recording the first stages of vent evolution (Cloos, 1941). These tuffisites record some of the first fractures that were opened as part of the fracture network that developed into the MCV. Parts of the fracture network that have been abandoned and not destroyed during the quarrying of the vent can be filled with pyroclastic material and preserved as tuffisites within the country rock (Figure 4.12 and

Appendix A.3,).

The diffuse margins of tuffisites hosted by the pyroclastic apron reflect the difficulties of opening and propagating a pathway through the highly permeable host rock. Instead, gas escape exploited, and potentially widened, pre-existing open voids and intergranular pore spaces within the breccia, which progressively filled with laminated/stratified ash. Deposition of these tuffisite cavity fills would have led to a locally significant reduction in the permeability of the pyroclastic apron, acting to seal areas of the evolving vent margins.

4.4.3.2 'Early' tuffisites in the pyroclastic breccia

The tuffisites within the pyroclastic breccia are not fracture hosted, but instead comprise fine-grained materials likely swept through the pore space of the surrounding pyroclastic breccia and driven by lateral pressure gradients within the volcanic conduit (Figures 4.11a and 4.11b). Particles carried into the pore space would likely be deposited either where the fluid pressure decreased as it entered a larger void, or where the fluid flux was lowest. These tuffisites leave behind a record of this process in the areas of lower permeability or where fluid flow pathways become blocked. Unlike the tuffisites found in other vent units, these tuffisites are not formed by hydrofracturing, instead representing outgassing through dilation of existing permeable pathways that did not require fracturing to further increase permeability.

The soft sediment deformation surrounding these features reflects the passage of pressurized gas through the pore spaces of the unlithified breccia, which reduced the effective confining pressure, lowered its cohesive strength, and allowed for shifting and slumping. More extensive tuffisites (<13 m in length) may represent areas where the fluid flow within the pyroclastic breccia was more constrained to a single pathway, allowing for more focused deposition of material into a single vein. These more laterally extensive tuffisite veins are consistent with the infilling of the pre-existing intergranular pore spaces and cavities, not only lowering the permeability of the breccia but also reducing the friability of these pyroclastic deposits, facilitating subsequent fracture development.

4.4.3.3 Tuffisites in the vitrophyre and vitrophyre breccia

The morphology of the tuffisites within the vitrophyre and vitrophyre breccia reflects the greater cohesion and lower permeability of the vitrophyre compared to the pyroclastic breccia. The wide variety of tuffisite orientations seen in the vitrophyre breccia (Figure 4.5b) suggest that tuffisite formation is not necessarily controlled by pre-existing fabrics, although the branches at the margins of the tuffisite in Figure 4.11d do exploit pre-existing fractures in the surrounding vitrophyre breccia. The more poorly-developed fabric of the outermost parts of the assembling vitrophyre breccia would act as less of a control on the morphology of intersecting tuffisites than the stronger fabric seen within the vitrophyre. The tuffisites within the vitrophyre and vitrophyre breccia were emplaced after the development of the fabric, once the vitrophyre had cooled sufficiently to have fractured by shearing, producing pathways that tuffisites could easily exploit.

The tuffisites in the vitrophyre breccia are interpreted as fracturing and injecting material into the stationary conduit wall, leading us to consider them to be external tuffisites, rather than internal tuffisites formed by in-situ shear failure of highly viscous magma (c.f. Stasiuk et al., 1996, Tuffen et al., 2003). The interpretation of the vitrophyre forming by accretion at the conduit margins suggests that these tuffisites formed instead as external tuffisites by tensile failure, with some clasts broken from the fracture walls as the fracture opened, and other clasts injected.

Some obsidian-hosted tuffisites described elsewhere are angular particle-filled fractures that have developed tractional bedforms (Tuffen et al., 2003; Tuffen and Dingwell, 2005), and display very similar morphologies and internal structures to the Mule Creek vitrophyre breccia and vitrophyre-hosted tuffisites. These were originally documented at Torfajökull, Iceland and interpreted as internal tuffisites. In that interpretation, the clastic fracture fill was thought to be locally-derived clasts from fracture walls (Tuffen et al., 2003). However, the observations made herein suggest that these similar features may actually have been external tuffisites with clastic fill sourced from an erupting and bypassing dispersion travelling up a volcanic conduit prior to conduit sealing by continued welding. This reinterpretation would provide a source for the trace metal concentrations in the Torfajökull veins, which Berlo et al. (2013) attributed to a genesis that was 'deep' relative to the tuffisite position. Similarly, the observations made here suggest that the pyroclasts filling tuffisites found in vitrophyre-like bombs, such as the bomb documented by Saubin et al. (2016), may be sourced from magmatic

fragmentation, contrary to models that suggest that the fill is formed by disaggregation of a foamy magma directly beneath the vitrophyre. Taken together, these comparisons between the MCV vitrophyre-hosted tuffisites and similar tuffisites found elsewhere lend support to models that envisage the shallow conduit as progressively plugging by sintering of the products of deeper fragmentation (Wadsworth et al., 2020, 2022; Farquharson et al., 2022). We propose that tuffisites can be considered to be predominantly external rather than internal, as a large proportion of their fill is distally derived, and carried through tensile fracture networks within largely passive, conduit-lining dense magma. The particle source is the deeper gas-ash-pyroclast mixture feeding the ongoing eruption, consistent with models for combined explosive-effusive eruption behaviour (Wadsworth et al., 2020), and failure is driven by gas overpressure (Chapter 3). This model provides a distinct fluid and particle source able to fluidise and transport particles within the tuffisite and emphasises the passive role of the dense conduit lining over the timescale of overpressure-driven brittle failure events, even if it remained capable of some viscous deformation.

4.4.3.4 Tuffisites hosted in flow-banded rhyolite lava

Tuffisites within the central flow-banded rhyolite lava (internal tuffisites) have previously been proposed to form by the same mechanisms as those in vitrophyre or obsidian, and are often considered to form when stresses within magma meet or exceed the magma shear strength, opening networks of magma-hosted fractures (Tuffen et al., 2003; Tuffen and Dingwell, 2005; Kendrick et al., 2016; Paisley et al. 2019a). The tuffisites within the rhyolite lava of the MCV are steeply dipping, reflecting either failure parallel to the plane of maximum shear stress, rotation of veins by subsequent viscous flow and shear (Tuffen et al., 2003; Gonnermann and Manga, 2003), or exploitation of weaker pore-rich bands associated with devitrification (Schipper et al., 2015).

The clasts in internal tuffisites have previously been thought to derive entirely locally from fracture walls (Tuffen et al., 2003; Tuffen and Dingwell, 2005), or from a foamy magma immediately beneath, and in contact with, a dense magma plug (Saubin et al., 2016). Neither of these models is consistent with the observed lithic content of internal tuffisites (Heap et al., 2019). Flow banding in the central rhyolite lava at the MCV and the granulation at the margins of lava plugs elsewhere demonstrate that the lava plug is pushed upwards and out of the vent (Pallister et al., 2013; Gaunt et al., 2014).

Tuffisites in the vent centre will therefore also likely be deformed (Tuffen et al., 2003), changing their planar geometry, and obscuring their relationship with particle sources. For this reason, as suggested in Section 4.4.3.3, we propose that it is consistent with our genetic model to assume that what appear to be internal tuffisites, may be consistent with flow-deformed external tuffisites. These fractures within conduit-blocking magma, assembled by the welding of pyroclastic material, provided pathways for pyroclastic material produced by continued fragmentation at depth to reach the surface during hybrid explosive-effusive activity (Wadsworth et al., 2020; 2022; Schipper et al., 2021).

4.5   A model for the formation of the Mule Creek vent

It follows from our interpretation (Section 4.4) that the material at the conduit centre is relatively younger than the material forming the conduit margins, and as such, each conduit unit records a different period of conduit evolution. Tuffisites are found within every unit of the MCV, formed at different stages of conduit evolution and at a variety of scales, with very few cross-cutting the entire conduit width. This indicates that there was a continuous but pulsating supply of pyroclastic material to feed tuffisite formation during vent evolution.

4.5.1   Conduit opening and the erosive formation of the vent structure

The propagation of fractures by pressurised gas-pyroclast mixtures through the overlying andesite created pathways for fluid flow (Figure 4.12a and Appendix A.3, Animation 2). A branched network of fractures formed, exploiting the weakest pathways for fracture opening (e.g. bed/unit contacts, joints, faults). Where this propagating fracture network separated blocks from the surrounding country rock, these could become entrained into the ascending fluid, providing a source of the lithic clasts. Variations in fluid velocity, driven by fluctuating fluid pressure, would have caused pyroclastic material and country rock fragments to be deposited within the opening fractures (Figure 4.12b). Through time the network of fractures was refined into a major pathway with a simpler shape, forming an evolving conduit. Some abandoned pyroclast-filled fractures may be preserved, forming tuffisites that cut through the country rock adjacent to the major pathway.

4.5.2 The onset of vent-filling emplacement of the pyroclastic breccia

Once a vent is opened the initial activity is likely to be purely erosive and would therefore not be recorded in any vent-filling units. The pyroclastic breccia unit was the first within-vent unit emplaced during conduit formation. A relatively high proportion of country rock fragments records the quarrying and filling of space with pyroclastic material and fragments of country rock, together with pyroclastic material (Figure 4.4). The first subunits deposited are subhorizontal, as the quarried-out area is filled with pyroclastic material, but repeated erosion and deposition produces later subunits that dip more steeply towards the conduit centre (Figure 4.12c). The permeable pyroclastic breccia filling the evolving conduit would allow for lateral outgassing from the conduit, with erosion, deposition and slumping causing the fluid pathway to migrate and seal through time. Ash-sized particles transported into the pore space of the surrounding pyroclastic breccia by outgassing can be deposited to form what we term 'diffuse tuffisites' (Figure 4.12d).

At Cordón Caulle, Chile in 2011 and Chaitén, Chile in 2008, the initial purely explosive phase of activity lasted about ten days (Lara, 2009; SERNAGEOMIN-OVDAS, 2011). If the Mule Creek eruption had a similar timescale, the vent-filling breccia would be deposited over a similar period as the purely explosive phase waned and conduit occlusion prevailed, before the dense lava was produced and erupted.

4.5.3 Vent wall steepening and localization: A transition from unwelded pyroclastic breccia to welded vitrophyre breccia

The sustained input of fragmented material from depth would supply material to become trapped within the conduit. The continued deposition of hot material within the conduit and the increasing volume of the accreted deposits would have inhibited cooling of the conduit fill, enabling ever-greater welding of the surrounding pyroclastic breccia subunits (Kolzenburg et al., 2019).

Welding increased the cohesion of the pyroclastic breccia, stabilizing the conduit walls and preventing the overturning of the deposited material. The increased stability would also allow tuffisites hosted within the pyroclastic breccia to become larger and more extensive. As the permeability of the pyroclastic breccia decreased, outgassing

would have been constrained to within the central portion of the conduit and promoted overpressure development, especially if the conduit diameter were to constrict (Castro et al., 2016) due to pyroclastic breccia emplacement at its walls. The gradual heating of the conduit walls during pyroclastic breccia emplacement would have eventually allowed fine-grained ash particles to stick to the conduit margins, allowing a transition to the formation of vitrophyre breccia (Figure 4.12e). The presence of the glassy contact within the pyroclastic breccia (Figure 4.8) suggests that a sufficient temperature for welding at the conduit margins can be reached before the start of vitrophyre breccia and vitrophyre formation. Whether the transition from pyroclastic breccia to vitrophyre breccia can occur will depend on multiple factors, such as the eruption explosivity and the grain-size of material, where higher explosion intensity results in finer grain sizes (Kueppers et al., 2006; Fowler and Scheu, 2016), thus facilitating more efficient welding. The shielding of the surrounding country rock by the pyroclastic breccia would reduce the number of lithics available, and the increased cohesion of the pyroclastic breccia would prevent overturning and reworking (Schipper et al., 2021). A drop in explosivity would also reduce the amount of quarrying that could occur, leaving a supply of ash-sized particles for vitrophyre breccia and vitrophyre formation that contained fewer lithic clasts (Figure 4.12f). The vitrophyre breccia and vitrophyre were nearly entirely formed by the welding of ash-sized particles, with a few rare lithic clasts captured by the accreting material. Coherent vitrophyre, rather than vitrophyre breccia, would have been formed once the explosivity had dropped sufficiently to prevent the repeated fracturing of the accreting material.

Increased overpressure in the constricting conduit opened fractures that would become tuffisites within the vitrophyre and vitrophyre-breccia, now acting as a passive and effectively static 'country rock'. These tuffisites may have cross-cut only the vitrophyre or vitrophyre-breccia, but given greater overpressure the fractures may have propagated further to intersect the pyroclastic breccia or surrounding country rock (Figure 4.12e).

4.5.4   Conduit sealing and the formation of the innermost vent units

Fine-grained, crystal-poor material that sticks to conduit margins can weld to form a dense glass (Gardner et al., 2017), preserved here as vitrophyre (Figures 4.5c and 4.12e). The pressure-driven fracturing of this dense glassy vitrophyre produced the in-situ jigsaw-fit clasts that form the vitrophyre breccia, separated by tuffisites. As the

eruption waned further and erosive quarrying decreased, the accreting vitrophyre at the conduit margin was no longer fragmented and ejected, and merely damaged, until eventually that damage ceased. If the filling of the conduit were promoted by the welding of pyroclastic material and the entire silicic magma column were expected to be wholly fragmented at depth, the central conduit-plugging rhyolite lava would share a similar origin (Wadsworth et al., 2020). The continued accretion and welding of pyroclastic material would have eventually sealed part of or all of the vent, leading to the onset of welded-lava effusion to produce the flow-banded rhyolite lava at the vent centre. A body of magma assembled at shallow depth could then be fractured to produce a network of permeable pathways along which pyroclastic material from below could be transported and deposited to form tuffisites (Wadsworth et al., 2020, 2022).

4.6   Discussion

4.6.1   Similarities between conduits and tuffisites

The initiation of an eruption can be considered as the continued propagation, expansion, and connection of tuffisites that evolve into a conduit. In the shallow subsurface (<2 km depth) the silicic magma column is likely to be fragmented (Wadsworth et al., 2020). The deposition of clastic material within the conduit during the waning phase of an eruption means that preserved, dissected conduits will qualitatively resemble a tuffisite, as each is a pathway for pyroclastic discharge. The characteristics and overall structure of the MCV are remarkably similar to those of the tuffisites intersecting the vent units, albeit on a larger scale. Processes such as repeated erosion and deposition of material, injections, and welding, occur both on a small scale within tuffisites, but also on a much larger scale within the vent units (Schipper et al., 2021).

Once repeated injections of material into a tuffisite allow it to reach a sufficient thickness, the tuffisite centre becomes hot enough for welding and viscous deformation to occur (Chapter 3). The same process at the conduit-scale will allow the pyroclastic breccia to weld and strengthen, changing the conduit pathway through time. Conduits are much larger than tuffisites and so will generally reach greater temperatures and cool more slowly, allowing more complete welding to occur (Kolzenburg et al., 2019). In a conduit where the margins have become sufficiently hot, ash particles can stick to and coat the conduit margins to form a vitrophyre unit (Gardner et al., 2017; Wadsworth

138

et al., 2020). Similarly, sticking and coating of tuffisite vein walls by fine-grained ash can create dense veneers (Farquharson et al., 2022), which will have low permeability relative to the surrounding country rock (Wadsworth et al., 2022).

However, there are many important differences between tuffisites and conduits that control their evolution through time. While tuffisites are the initial stage of conduit evolution, the greater dimensions of a conduit allow for more mixing and overturn of material, preventing the formation and preservation of the complex internal structures seen within tuffisites (Valentine and Cole, 2021). The shape of the vent is likely to create deposits that are more prone to slumping than within tuffisites, controlling the structure of the vent produced. The pressure gradients driving gas and particle flow within the conduit will likely be lower than within a tuffisite, due to the greater dimensions of the conduit, especially during waning activity, controlling the ability for pyroclasts to be re-entrained into the flow and for internal fracturing to occur (Chapter 3). The greater permeability of the conduit margin than tuffisite walls will also help to reduce the pressure gradient within the conduit by allowing for lateral gas escape (Heiken et al., 1988), lowering the flow velocity within the conduit. To inject material into a pre-existing host fracture to form a tuffisite, the fluid pressure must be great enough to displace the surrounding material (Chapter 3), while in a conduit continuous mixing, overturning and soft sediment deformation allows for the emplacement of new material at lower fluid pressures.

4.6.2   Flux through tuffisites during vent evolution

Tuffisites have been suggested to act ubiquitously as permeable pathways along which outgassing can occur, perhaps defusing gas pressure from a conduit (Farquharson et al., 2017; Kolzenburg et al., 2019). Therefore, tuffisite formation is thought to be key to understanding explosive-effusive transitions. By contrast, here, we show that the initial host-rock for 'early' tuffisites is a highly permeable vent-lining breccia (Appendix A.4 Animation 3) that would allow highly efficient outgassing (Eichelberger et al., 1986). 'Early' tuffisites in this host-rock are not necessarily only hydrofracture driven, and instead can also involve invasion of the pyroclastic debris with ash- and clast-laden fluids, which deposit as they percolate (White and Ross, 2011). Such invasion could create deposits that appear superficially tuffisitic, but actually sealed up outgassing routes in pre-existing deposits, without any initial high-permeability opening phase.

Once the conduit walls have been heated sufficiently for welding of fine material at the margins to form the vitrophyre and vitrophyre breccia, these lower permeability units (relative to the pyroclastic breccia) will seal the margins of the conduit, constraining fluid flow and increasing the fluid pressure within the active portion of the conduit. If a sufficient fluid pressure can be achieved to fracture the vitrophyre breccia, tuffisites can form a pathway through the less permeable material and into the more permeable pyroclastic breccia beyond, where outgassing can occur more effectively (Appendix A.4 Animation 3). Tuffisites therefore become necessary for lateral outgassing to occur in this partially or wholly sealed phase of the conduit evolution. Fracturing the dense vitrophyre breccia will require a greater fluid pressure than invading a pathway through the weaker, less compacted pyroclastic breccia, suggesting that once the vitrophyre unit begins to coat the conduit margins a higher fluid pressure can be achieved within the conduit. We propose that this corresponds to the formation of a dense lava plug, accompanied by repetitive Vulcanian explosions. If the dense glassy plug extends to the surface then hybrid activity could occur, as observed at Chaitén in 2008 (transitional phase 2; Pallister et al., 2013) and Cordón Caulle from June 15th 2011 (Castro et al., 2013; Schipper et al., 2013, 2021; Wadsworth et al., 2022).

Fine ash-sized particles, whether injected and deposited within a fracture or deposited within the pore space of coarser-grained material, will rapidly weld, sealing fluid flow pathways and reducing further outgassing. The permeability of these fluid pathways will therefore only be transient. The time-dependent porosity of a welding matrix with time, $\phi(t)$, can be estimated using the 'vented bubble model' (Wadsworth et al., 2019)

$$\frac{d\phi}{dt} = -\frac{3\Delta P}{4\mu}\phi - \frac{3\Gamma}{2\mu\langle a_i\rangle\zeta}\left(\frac{\phi_i}{1-\phi_i}\right)^{\frac{1}{3}}\phi^{\frac{2}{3}}(1-\phi)^{\frac{1}{3}} \tag{4.1}$$

where ϕ_i is the initial porosity, ΔP is the difference in pressure of the gas phase and stress acting on the particles involved in the welding, μ is the viscosity of the hot particles, Γ is the interfacial tension between the gas and the particle, and $\langle a_i\rangle$ is the mean size of the pore spaces between the welding particles (related to the particle-size; Wadsworth et al., 2016). When $\Delta P \to 0$, Eq. 4.1 can be approximated by $\phi \approx \phi_i\exp\left(-3t/(2\lambda)\right)$ where $\lambda = \zeta\mu\langle a_i\rangle/\Gamma$ is the welding timescale in the $\Delta P = 0$ regime (Wadsworth et al., 2014, 2016). Here, ζ is a correction factor that accounts for the polydispersivity of the particle-size distribution (Wadsworth et al., 2017).

Referring to Eq. 4.1, $\Delta P \approx 0$ is justified for the case where the gas and particles are in pressure equilibrium (i.e. the effective pressure is zero). At Mule Creek, this is likely to be the case in the conduit itself (i.e. during vitrophyre formation by welding) or in the early stages of tuffisite formation and welding. As tuffisites seal and gas pressure decays, there may be an increase in the pressure acting to compress the assemblage of particles relative to the gas pressure between the particles, causing ΔP to rise to $\Delta P > 0$, invalidating this simple approximation. Nevertheless, if we use the $\Delta P \approx 0$ assumption, we can give an upper-bound on λ. In order to compute λ, we must convert R_i to $\langle a_i \rangle$ and ζ. To do this, we use the model provided by Wadsworth et al. (2017), which, using the two distributions given in Figure 4.10, yields $\langle a_i \rangle = 2.7 \times 10^{-7}$ m with $\zeta = 17.59$ (Figure 4.10a) and $\langle a_i \rangle = 7.33 \times 10^{-6}$ m with $\zeta = 7.33$ (Figure 4.10c), respectively. Using $\Gamma = 0.22$ N/m (Gardner and Ketcham, 2011), $5 \times 10^7 < \mu < 1.5 \times 10^9$ Pa.s (using Hess and Dingwell, 1996; with a water content of 0.8 wt.% and for 700 and 800 °C from Stasiuk et al., 1996), we find that $18 < \lambda < 540$ min for the 2 μm particles in the tuffisites within the pyroclastic breccia, or $37 < \lambda < 1107$ min for the 7 μm particles in the tuffisites within the vitrophyre breccia. These timescales are far shorter than conduit cooling timescales (Kolzenburg et al., 2019), especially when thermally buffered by an ongoing bypassing eruption, with hot material flowing past the conduit walls, and well within the timescales associated with ongoing silicic eruptions (e.g. Schipper et al., 2013), lava assembly, and effusion (Wadsworth et al., 2020). This process will act more efficiently in early, high energy fragmentation events due to the correlation of grain size and fragmentation energy (Kueppers et al., 2006; Fowler and Scheu, 2016) and slow down during the later waning stages of an eruption — further enhancing the discrepancy in the need for pressure release during the high energy stages and a more efficient outgassing and depressurization during later, waning phases.

The welding timescales in both cases explored here suggest that the welding material could efficiently lower the permeability of any outgassing pathways, potentially sealing them completely. In the pyroclastic breccia, welding of fine-grained intruded material could locally reduce the permeability, but with fluid flow pathways through the unconsolidated and permeable breccia relatively unconstrained, this reduction in permeability would likely not have a great effect on the bulk permeability of the unit. The accretion of the vitrophyre and vitrophyre breccia could quickly seal the conduit margins, rapidly decreasing their permeability. With gas unable to escape laterally through the impermeable vitrophyre and vitrophyre breccia, regular and repeated fracturing would be required to

continually produce new lateral outgassing pathways to replace those sealed by welding.

As tuffisites close, gas pressure drops and ΔP will rise, and therefore, our estimate of the rate of porosity change is a conservative estimate (c.f. Eq. 4.1). Similarly, if the gas pressure rises in tuffisites or between the welding vitrophyre material, Eq. 4.1 predicts that ΔP will drop and can become negative, causing $d\phi/dt$ to be positive, and therefore porosity to increase with time as the gas pushes the sintering system apart again. Fractured masses of sintered particles within tuffisites in the vitrophyre breccia (Figure 4.10d) suggest that this process does occur, perhaps due to the sealing or nearby permeable pathways locally increasing gas pressure (Chapter 3).

4.7 Future Challenges

Tuffisite veins are pervasive throughout the width of the MCV, from the vitrophyre into the country rock, suggesting that they might play a role in influencing conduit dynamics throughout vent evolution. Characterisation of the grain sizes, porosity, and permeability of tuffisites would determine how significant their role in outgassing might be, and whether tuffisites could carry a sufficient flux to defuse pressure within the evolving conduit. Further investigation of conduit walls would help constrain how their permeability and erodibility might vary through time, controlling the lateral outgassing flux through conduit walls and the conduit morphology throughout its evolution. This evolution of the permeability and erodibility of the conduit walls may also influence flow within the conduit, perhaps acting as a control on the steadiness of conduit flow through time. Detailed analysis of textures and H_2O contents across the margins of vents similar to Mule Creek may help to constrain degassing mechanisms. More closely integrating the spatial context provided by analysis at ancient dissected systems with the fragmental but fresh record preserved in pyroclasts from recent silicic eruptions is then needed to further improve our understanding of the processes controlling the explosive-effusive transition. Detailed textural analysis of the different clasts forming the vitrophyre breccia at Mule Creek and similar vents may also help to confirm whether this unit was brecciated in situ or formed of vitrophyre clasts fractured away from the vent margin and redeposited at a shallower depth. Similar structures to the those seen within the Mule Creek vent are seen in basaltic diatremes, and applying and adapting our understanding of vent formation to less silica-rich systems poses an additional challenge.

4.8 Conclusions

The structure of the Mule Creek vent is complex, with the characteristics of the different vent-filling units controlling its morphology during vent evolution. The pyroclastic breccia contains many erosive surfaces, reflecting the repeated deposition, erosion, and overturning of pyroclastic material until sintering and compaction increased its cohesion and more stable conduit walls could form. Heating of the conduit walls and waning explosivity allowed the accretion of ash-sized particles to form the vitrophyre breccia unit, with glassy material repeatedly fractured and re-healed until explosivity waned sufficiently for a more coherent vitrophyre to accrete. The accretion and sintering of pyroclastic material eventually blocked the vent, leading to the eventual effusion of sintered lava and production of flow-banded rhyolite lava at the vent centre.

The tuffisites that intersect every vent unit have complex internal structures, reflecting repeated periods of erosion and deposition within the fractures. Diffuse tuffisites in the pyroclastic breccia record lateral outgassing through the high permeability breccia lining the conduit margins. Repeated periods of erosion and deposition, driven by fluctuations in the conduit fluid pressure, caused the conduit width to vary through time. The accretion of ash-sized particles to form the vitrophyre and vitrophyre breccia would have effectively narrowed the active conduit, sealing the conduit margins and restricting lateral outgassing to the permeable pathways created by tuffisites.

5 Do tuffisites make good outgassing pathways?

An edited version of this chapter is currently in preparation for submission to Earth and Planetary Science Letters.

Holly E. Unwin, Fabian B. Wadsworth, Hugh Tuffen, Michael J. Heap, Adrian White, Annabelle Foster, Mike R. James, Emrys R. Phillips

Abstract

Particle-filled fractures found within the country rock adjacent to volcanic conduits, known as tuffisites, have been suggested to be efficient outgassing pathways. Tuffisites may act as 'volcanic valves', allowing sufficient outgassing to reduce conduit pressure and thereby affect eruption style directly. To date, their efficiency in this role has been estimated via determination of tuffisite permeability, and consideration of how this might vary during tuffisite evolution. However, this approach assumes that preserved tuffisites reflect a static example of the 'valve' as it was when it was active in the volcanic sub-surface. Here, we instead suggest that there are two broad stages of tuffisite formation during which outgassing can occur. First, fracture opening, associated with a rapid gas flux from the volcanic conduit into the country rock that is largely unimpeded by particle deposition. Second, particle deposition and fracture closure, leading to lower relative fluxes albeit potentially sustained for longer times. We consider these two stages in detail and compute the potential outgassing flux for each, based on primary constraints from a large, exceptionally preserved tuffisite associated with rhyolitic volcanism at the dissected Húsafell central volcano, Iceland. For the first stage, we use direct observations and geophysical data from silicic eruptions to propose a general timescale for open fracture outgassing of 10–100 s. For the second stage, we use the porosity, permeability, and particle-size distributions of the tuffisite fill to place constraints on the time it took for the particles to sinter viscously to their current state. Based on this two-step approach, we find that the tuffisite was assembled by multiple pulses each spaced ~12 hours apart. Using scaling approaches, we compute the estimated flux during each stage and find that during the first open-fracture stage, the flux can be ~10^4–10^7 times greater than the potential flux through the second stage during which the tuffisite is sintering closed. Our conclusions are that while tuffisite

formation allows for extensive outgassing, the outgoing magmatic fluid flux is dominated by the initial open phase, which is not captured directly by field evidence.

5.1 Introduction

During an explosive silicic volcanic eruption, it is the rapid expansion of the gas phase in growing bubbles that leads to magma acceleration up the conduit, brittle fragmentation and the production of pyroclasts (Woods and Koyaguchi, 1994). However, if gas can escape from the magma via outgassing, then magma fragmentation may be avoided and magma ascent rates will be slower (Eichelberger et al., 1986; Jaupart and Allègre, 1991). Therefore, the potential for outgassing from magma could directly influence the style of an eruption: explosive or effusive (Degruyter et al., 2012).

The specific dynamics of outgassing from the conduit are largely unconstrained, but a range of conceptual models have been proposed. Of these, perhaps the dominant is lateral outgassing, with gas escaping through gas-permeable magma into permeable conduit wall rocks (Jaupart and Allègre, 1991; Rust et al., 2004; Lavallée et al., 2013; Farquharson et al., 2015; Kolzenburg et al., 2019) or through fractures that dissect the margins of the conduit (Cloos, 1941; Heiken et al., 1988; Stasiuk et al., 1996; Chapter 3). Conduit-margin fractures held open — or 'propped' — by pyroclastic material are known as 'external tuffisites', and have been invoked as efficient pathways for lateral outgassing from the conduit (Jaupart, 1998; Castro et al., 2012, 2014; Berlo et al., 2013; Farquharson et al., 2017; Heap et al., 2019; Kolzenburg et al., 2019). The observation that external tuffisites could be highly permeable (e.g. Heap et al., 2019) has led to the possibility that these features could potentially reduce eruption explosivity (Stasiuk et al., 1996; Castro et al., 2014). However, these external tuffisite features have only rarely been observed directly (Chapter 3) and the dynamics of their formation and evolution has scarcely been considered.

During an energetic silicic explosive eruption, magma fragmentation is thought to occur around 2 km depth below the surface, suggesting that the upper 2 km or more is a dispersion of expanding gas and pyroclasts (Wadsworth et al., 2020, 2022). Calculations suggest that the gas overpressure in this shallow region of conduits can lead to lateral 'fracking' and the opening of fractures in the country rock adjacent to a volcanic conduit by gas-pyroclast mixtures (Heiken et al., 1988; Stasiuk et al., 1996; Chapter 3; Chapter

4). Therefore, it is suggested that the dynamics of lateral, sub-horizontal tuffisites must involve fracture opening, fracture-bounded pyroclast transport, pyroclast deposition, and fracture closure. All of these processes are coupled and difficult to constrain. The first stage of tuffisite formation is fracture opening, during which the gas-pyroclast mixture flows through the fracture and into the country rock (with a pathway that may or may not be ultimately connected to the surface). This first phase can continue until the fluid velocity wanes sufficiently for particle deposition to occur (Kern et al., 1959). Particles are then deposited to form bedded units that can show cross-cutting relationships, as well as structures such as laminations, cross-laminations, and internal injections, all subject to the fluid dynamic regime of transport (Heiken et al., 1988; Tuffen et al., 2003; Phillips et al., 2013). It is proposed that once particles begin to deposit, there is a second stage wherein the gas pressure decreases further and the fracture closes onto the deposited pyroclasts. The pyroclasts will prop the fracture open, preventing it from closing completely, and allowing continued gas escape through the pore space of the deposited sediment unit (Kern et al., 1961; Warpinski et al., 1981; Heiken et al., 1988). If pyroclasts are sufficiently hot when deposited, the particles can weld together through time, reducing permeability and limiting gas escape through inter-particle pore space (Wadsworth et al., 2014, 2021; Kolzenburg et al., 2019). If the gas overpressure increases again due to variations in the source conduit gas pressure, then the tuffisite could re-open, effectively forming sequential pyroclast-laden fluid injections into the same tuffisite. Repetitive or cyclic behaviour like this could emplace more sediment units, repeating these stages of tuffisite formation to assemble tuffisites >20 cm in thickness (Chapter 3).

Both stages of tuffisite formation — flow through the fracture before and during particle deposition and then subsequently through the inter-particle pore space — have the potential to allow outgassing to occur from the conduit. The first stage, largely before particle deposition, should be short in duration relative to the second stage. That first stage has not yet been considered in the computation of outgassing efficiencies (e.g. Heap et al., 2019). Outgassing through tuffisites has only been considered to occur during the second stage of tuffisite formation, with outgassing through inter-particle pore space. Whether outgassing through lateral tuffisites is significant compared to the vertical gas escape up a conduit will depend on the number, dimensions, and permeabilities of tuffisites at the different stages of their evolution, as well as the timescales for which outgassing can occur.

The total length of time for which a tuffisite might be able to act as an outgassing pathway is poorly constrained. Tuffisite lifetimes have been estimated for a specific case of 'within-conduit' (or 'internal') tuffisites, by considering the time required for the deposited pyroclasts to sinter together and reduce tuffisite permeability sufficiently to prevent gas flow. This timescale will depend on the initial temperature at which pyroclasts are emplaced, the cooling rate of pyroclasts, the pyroclast H_2O concentration, any applied stresses (Quane and Russell, 2005; Wadsworth et al., 2019) and the vesiculation of the pyroclasts (Weaver et al., 2022). Estimates of sintering times for internal tuffisites suggest that they remain permeable for minutes to tens of hours in the absence of external forces (in the surface tension regime) or for seconds to minutes if compacting stresses are applied (in the compaction regime; Heap et al., 2019). Estimates of internal tuffisite longevity have also been calculated using H_2O diffusion modelling for internal tuffisites hosted within obsidian bombs and calculations have suggested that internal tuffisites remain sufficiently permeable for gas escape for minutes to tens of hours (Cabrera et al., 2011; Castro et al., 2012; Berlo et al., 2013; Saubin et al., 2016; Heap et al., 2019).

Here the key need to understand tuffisite lifetimes and their overall outgassing potential better is addressed. To do this, this chapter assesses the relative importance of both the proposed first and second stages of tuffisite formation and the potential volume of gas that can escape during each stage, using a large tuffisite at Húsafell volcano, Iceland, as a case study (Figure 5.1a). This potential flux is dependent on the porosity and permeability of the tuffisite during the different stages of tuffisite formation, alongside the duration of each stage, pressure gradient driving tuffisite formation, and tuffisite dimensions. This chapter constrains these variables using a range of evidence, all in order to determine which stage of tuffisite formation contributes the most significant outgassing and estimate the potential gas flux (volume of as escape per second per tuffisite) through the tuffisite at Húsafell to consider whether this could allow for a significant reduction in excess pressure within the conduit.

5.2 Methods

Fieldwork at the Húsafell tuffisite has shown it to have a complex internal structure, composed of many different units separated by their varying particle-sizes and componentry (Figures 5.1b and 5.1c). Large blocks covering the range of different tuffisite units were
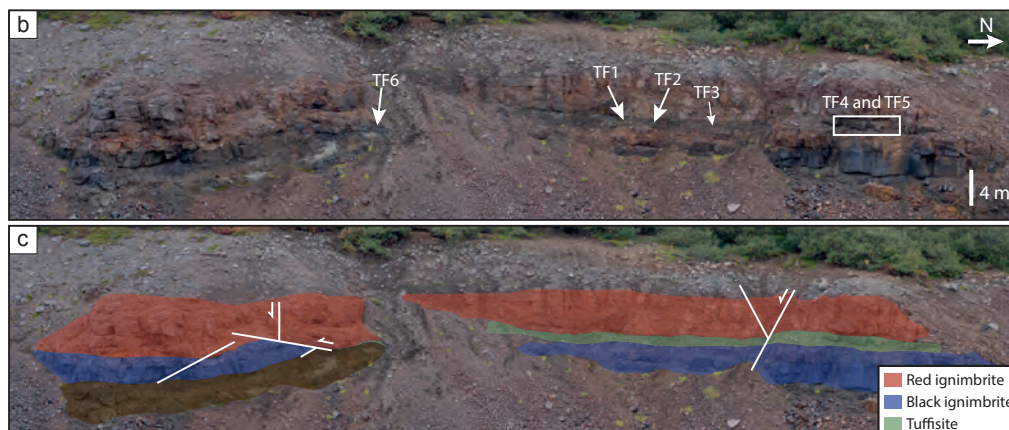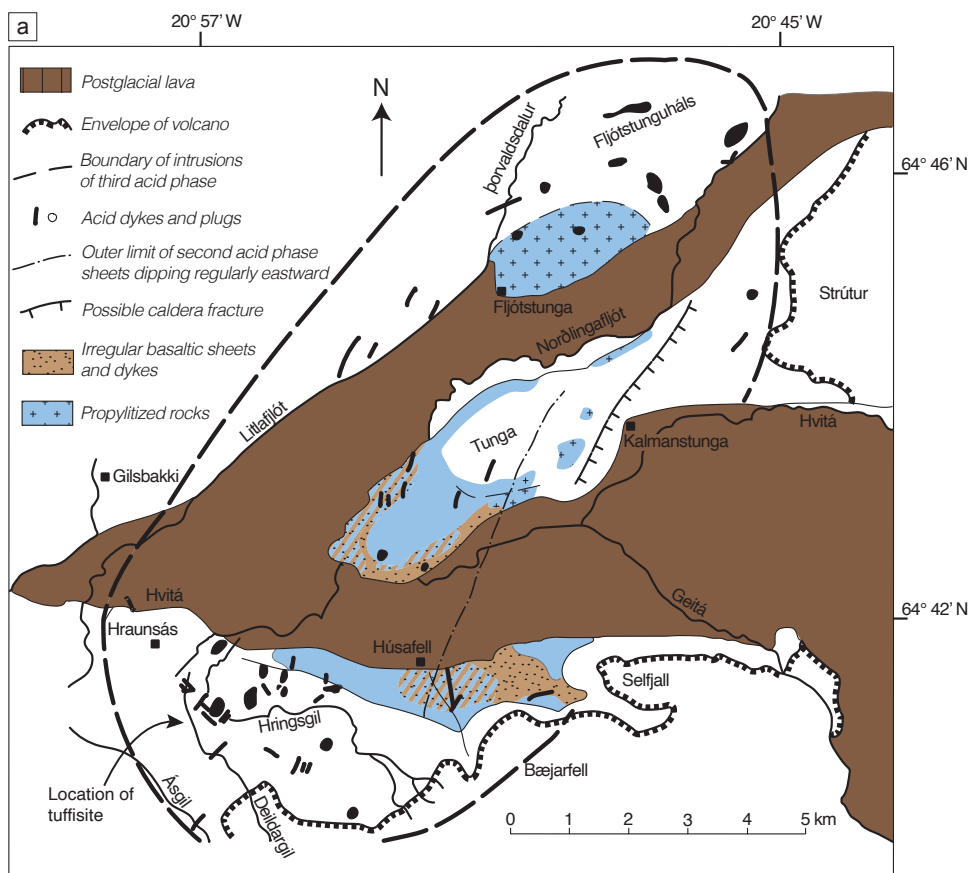
Figure 5.1: The geological setting of the Húsafell tuffisite. a) The location of the Húsafell tuffisite in the valley Deildargil at Húsafell central volcano in west Iceland. Photograph (b) and interpretation (c) of the location of the Húsafell tuffisite, injected along the contact between two ignimbrite country rock units. The locations of the samples used in this study are marked in (b). Samples TF4 and TF5 were taken from the scree beneath northern end of the outcrop, where the cliff-like outcrop prevents direct sampling. These samples appear very similar to particular units in the tuffisite outcrop above, but their exact location is not known.

collected for particle-size analysis, and porosity and permeability measurements (Figure 5.1b). Most samples could be sampled directly from the outcrop, allowing their exact position and orientation to be known.

Particle-size distributions were determined for the different tuffisite units to constrain the sintering time of each unit and therefore the timescale over which outgassing could have occurred through tuffisite pore space. Laboratory measurements of porosity and permeability of the samples constrain the final sintered porosity and permeability of the tuffisite units, indicating how efficient the tuffisite might be as a long-term outgassing pathway.

5.2.1 Particle-size analysis

Samples of the tuffisite were sectioned to allow closer observations and interpretations of their microstructures and particle-size analysis. Polished thin sections were examined using a Hitachi SU-70 high resolution scanning electron microscope at the University of Durham (UK), with a 15 kV beam voltage and 15 mm working distance. Backscattered-electron (BSE) images were taken of all samples at appropriate scales to collect multiple nests of images that capture the full particle-size distribution of the matrix of the different tuffisite units, as these are the particles that will sinter together through time and alter the tuffisite permeability during its evolution. Each nest is composed of images of 2–4 magnifications (typically $\sim$x200–1800 magnification; Appendix A.5, Table A.1) to allow the whole range of particles to be fully imaged (Figure 5.2a). Images were chosen to be representative of the overall sample and the areas imaged are smaller scale than any structures (e.g. laminations) within the sample. These larger sample heterogeneities were accounted for by combining different image nests.

Due to the low contrast between adjacent particles that often overlapped or were partially welded, thresholding the images did not enable individual particle detection, and particle margins needed to be traced manually. The traced outlines of particles with touching margins were then separated out to produce an atlas of particles that ensured each particle could be measured individually (Figures 5.2b and 5.2c). Where possible, large particles formed by the sintering of many smaller particles were included in the grain-size distribution as their component smaller particles (Figure 5.3). Particle areas were then analysed separately for each image within each image nest using ImageJ (Figure 5.2d; Schneider et al., 2012).
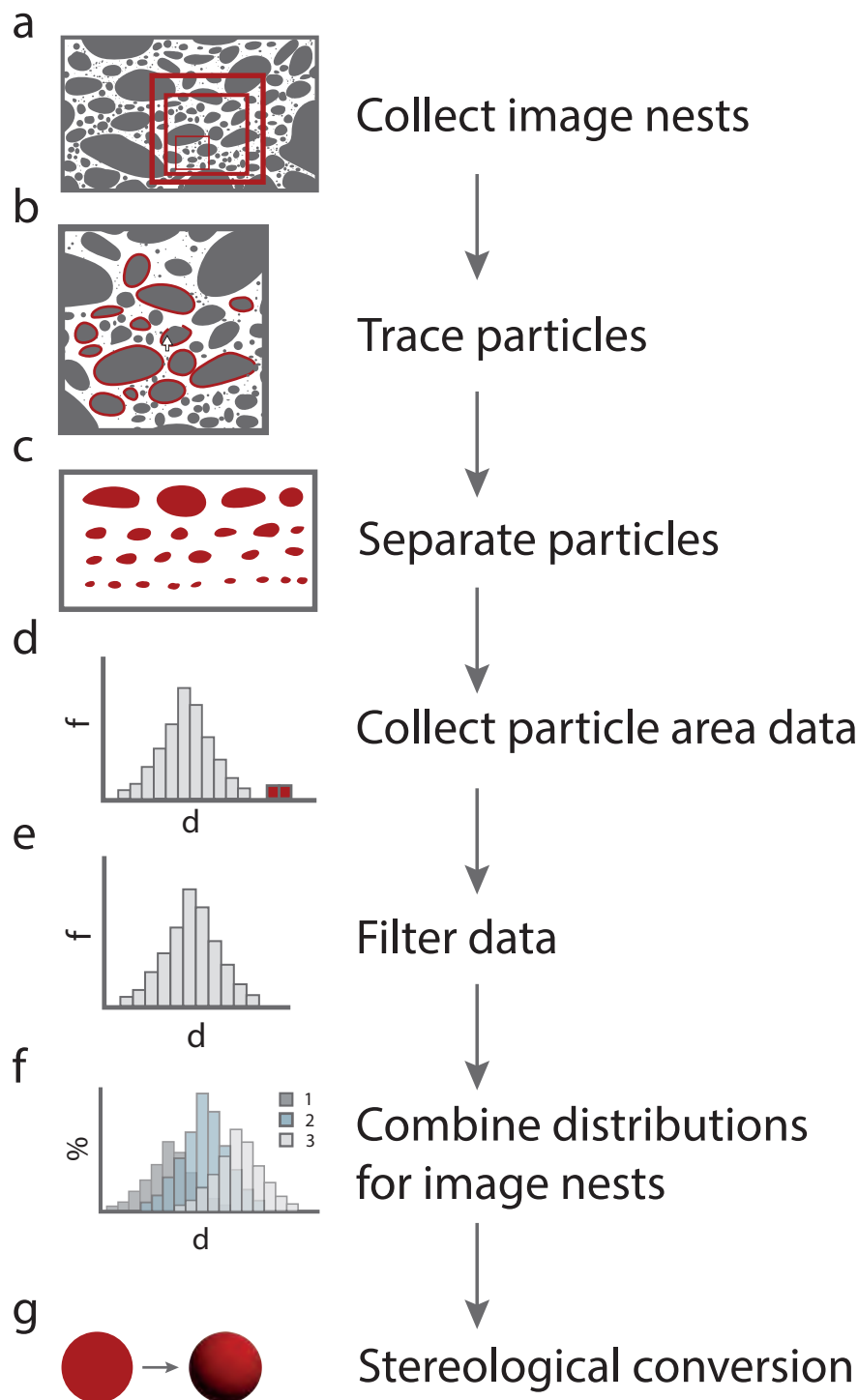
Figure 5.2: The method used to create overall particle-size distributions from sets of nested BSE images for the different units in each thin section. a) Sets of nested BSE images with different magnifications are collected to ensure that the whole particle-size distribution is captured. b) Particle margins in each image are then traced. c) Particles are separated out to ensure that each is measured individually. d) A particle-size distribution for each image is found using ImageJ (Schneider et al., 2012). e) Particle sizes too large or too small to be imaged at each magnification are filtered from the data. f) The particle-size distributions are scaled by their image area to combine them into one overall particle-size distribution for the image nest. g) A stereological conversion (Sahagian and Proussevitch, 1998) spherical particle diameters to be obtained.

The measured particle areas for each image within a nest were combined using a Python code into a single distribution representing all the particles present within the image set (see Appendix A.5, Figure A.2 and Jupyter notebooks in the Appendix B.1 and B.2). The Python code removed particles measured that were too small ($<$10 pixels across, Shea et al., 2010) or too large ($>$1% of the image area) to be correctly represented by each image (Figure 5.2e). At the highest magnification this 10-pixel minimum size allowed particles with a radius of $>$0.33 μm (TF2 and TF3) or $>$0.44 μm (TF1) to be imaged, with any particles smaller than this filtered from the dataset. The particle areas for each image were then placed into bins, and the particle-size distributions were trimmed to combine those for each image at the point at which the normalised frequency of particles of a certain size in one image was exceeded, and so assumed to be better represented, than the normalised frequency of particles in the image of the next lowest magnification in the image nest. Example cumulative distribution plots can be seen in Figure A.3a–c for different magnifications (Appendix A.5.1). The trimmed distribution for each image was then scaled by the fraction of the image that was measured particles to produce a single particle-size distribution (Figures 5.2f and Appendix A.5.1, Figure A.3d). A stereological conversion (Sahagian and Proussevitch, 1998; Shea et al., 2010) was used to convert the particle areas into volumes, allowing the volume fraction for each particle-size to be calculated (Figure 5.2g). Further details can be found in Appendix A.6 and Appendix B.2. The particle-size distributions from each nest could then be scaled by thin section area to produce an average particle-size for each sample collected, to be compared with the porosity and permeability data (Appendix B.3).

5.2.2 Porosity and permeability measurements

Measurements of porosity and permeability were performed at the Strasbourg Institute of Earth and Environment (France). Cylindrical samples 20 mm in diameter were first cored from samples of the different tuffisite units, representing different particle sizes, and the host rocks of the tuffisite (red friable ignimbrite and black densely welded ignimbrite; Chapter 3). Samples were chosen to be representative of the overall units, avoiding small-scale heterogeneities such as sedimentary structures where possible. The samples were precision-ground to lengths of 30–40 mm before being dried in a furnace at 40 °C for at least 48 hours. Samples were thoroughly washed after grinding and had their ends blasted with compressed air to remove any fines produced. The connected porosity of each sample was determined by measuring the skeletal (i.e. connected) volume given

by a Micromeritics AccuPyc II 1340 helium pycnometer and the bulk volume of each sample, calculated from the sample dimensions (assuming that the sample was perfectly cylindrical). The permeability of each cylindrical sample was measured using a gas (nitrogen) permeameter at a confining pressure of 1 MPa (to ensure that the gas flows through the sample instead of between the jacket and the sample edge). Further details can be found in (Appendix A.7; Farquharson et al., 2016; Heap et al., 2017). Details of the magnitude of experimental errors in these measurements are discussed in Appendix A.7.2.1 with example Python code in Appendix B.4.

To measure the permeability of each cylindrical sample, the volumetric flow rate (Q in $m^3.s^{-1}$) through the sample was measured for several different gas pressure differentials, ∇P, where ∇P is defined as

$$\nabla P = \frac{P_{\text{up}}^2 - P_{\text{down}}^2}{2P_{\text{down}}L_s}. \tag{5.1}$$

Here, P_{up} is defined as the upstream gas pressure, P_{down} as the downstream gas pressure (which here is atmospheric pressure and therefore $P_{\text{down}} = 101,325$ Pa) and L_s is the sample length. Eq. 5.1 is for compressible gas flow over short lengths (i.e. for low L_s) and reduces to $\nabla P = (P_{\text{up}} - P_{\text{down}})/L_s$ for incompressible flow (Kushnir et al., 2017). The Darcian permeability of each sample (k_D; in m^2) can then be calculated using

$$k_D = \frac{Q\mu_n}{A\nabla P}, \tag{5.2}$$

where μ_n is the viscosity of nitrogen at room temperature (1.76 x 10^{-5} Pa.s) and A is the circular cross-sectional area of the sample cylinder. Each permeability measurement was then checked to determine if a correction for gas turbulence (Forchheimer correction; Forchheimer, 1901) or gas slippage (Klinkenberg correction; Klinkenberg, 1941) were needed (Appendices A.7.1, A.7.2, and B.4). Measurements of tuffisite samples containing sedimentary structures taken parallel and perpendicular to the structures showed that the permeability is isotropic. Measurements were taken parallel to the sedimentary structures within the tuffisite as this is the expected direction of gas flow.
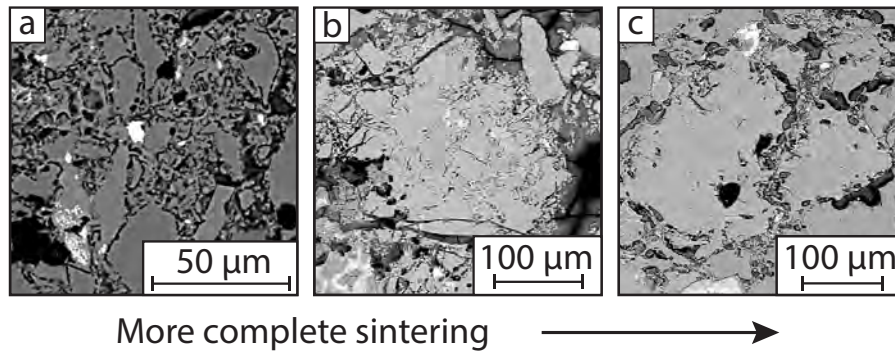
Figure 5.3: BSE images of particles within the tuffisite showing different degrees of sintering. a) Particles are partially sintered and the individual particle margins can still be easily distinguished. b) Particles can still be identified within the more sintered material but the individual particle margins are now unclear, with some particles formed by the sintering of multiple smaller particles. c) Individual original particles can no longer be distinguished once material has sintered further. Sutures between particles are visible in the sintered material, preserving evidence for its origin of smaller particles that are now sintered together.

5.3 Results

5.3.1 Tuffisite porosity and permeability

The permeability and connected porosity of the tuffisite samples was constrained (raw data in Table 5.1). The connected porosity of the different tuffisite samples was found to vary from 0.07 to 0.36, and the permeability varied from 1.93 x 10^{-14} m^2 to 5.09 x 10^{-18} m^2 (Table 5.1). The permeability of one sample was measured both parallel and perpendicular to the tuffisite length to check if the tuffisite samples were isotropic in terms of their permeability, giving similar permeability values of 3.3 x 10^{-15} m^2 (parallel) and 2.6 x 10^{-15} m^2 (perpendicular). The host rocks of the tuffisite (red ignimbrite and black ignimbrite) were found to have a permeability too low to measure in our laboratory setup ($\ll 10^{-18}$ m^2).

Table 5.1: The dimensions of the host rock (Ig-R and Ig-B) and tuffisite (TF) samples and their measured porosity and permeability. Ig-R and Ig-B refer to the red and black ignimbrites respectively. The location of each tuffisite sample is marked in Figure 5.1b.

	Sample length L_s (mm)	Sample diameter (mm)	Bulk volume (cm^3)	Connected porosity	Permeability (m^2)	Correction used
Host rock samples						
Ig-R1	39.93	19.95	12.48	0.13	$\ll 10^{-18}$	—
Ig-R2	40.04	19.96	12.53	0.14	$\ll 10^{-18}$	—
Ig-R3	32.75	19.95	10.24	0.13	$\ll 10^{-18}$	—
Ig-R4	33.19	19.95	10.37	0.13	$\ll 10^{-18}$	—
Ig-B1	39.93	19.94	12.47	0.07	$\ll 10^{-18}$	—
Ig-B2	40.07	19.94	12.51	0.07	$\ll 10^{-18}$	—
Tuffisite samples						
TF1-1	39.89	19.90	12.41	0.23	3.06×10^{-16}	None
TF1-2	39.92	19.92	12.44	0.25	4.95×10^{-16}	Forchheimer
TF2-1	40.01	19.95	12.51	0.10	5.09×10^{-18}	Klinkenberg
TF3-1	39.88	19.95	12.47	0.19	2.71×10^{-15}	Forchheimer
TF4-1	40.00	19.76	12.27	0.36	1.74×10^{-14}	Forchheimer
TF4-2	40.02	19.76	12.27	0.33	1.14×10^{-14}	Forchheimer
TF4-3	40.02	19.79	12.31	0.33	6.74×10^{-15}	Forchheimer
TF4-4	39.85	19.64	12.07	0.36	1.93×10^{-14}	Forchheimer
TF5-1 (parallel)	40.02	19.88	12.42	0.28	3.37×10^{-15}	Forchheimer
TF5-2 (parallel)	33.43	19.90	10.40	0.28	3.19×10^{-15}	Forchheimer
TF5-3 (perpendicular)	40.03	19.95	12.51	0.27	3.14×10^{-15}	Forchheimer
TF5-4 (perpendicular)	39.99	19.93	12.48	0.25	2.13×10^{-15}	Forchheimer
TF6-1	39.91	19.97	12.50	0.09	8.14×10^{-17}	None
TF6-2	40.01	19.94	12.49	0.07	1.03×10^{-16}	None
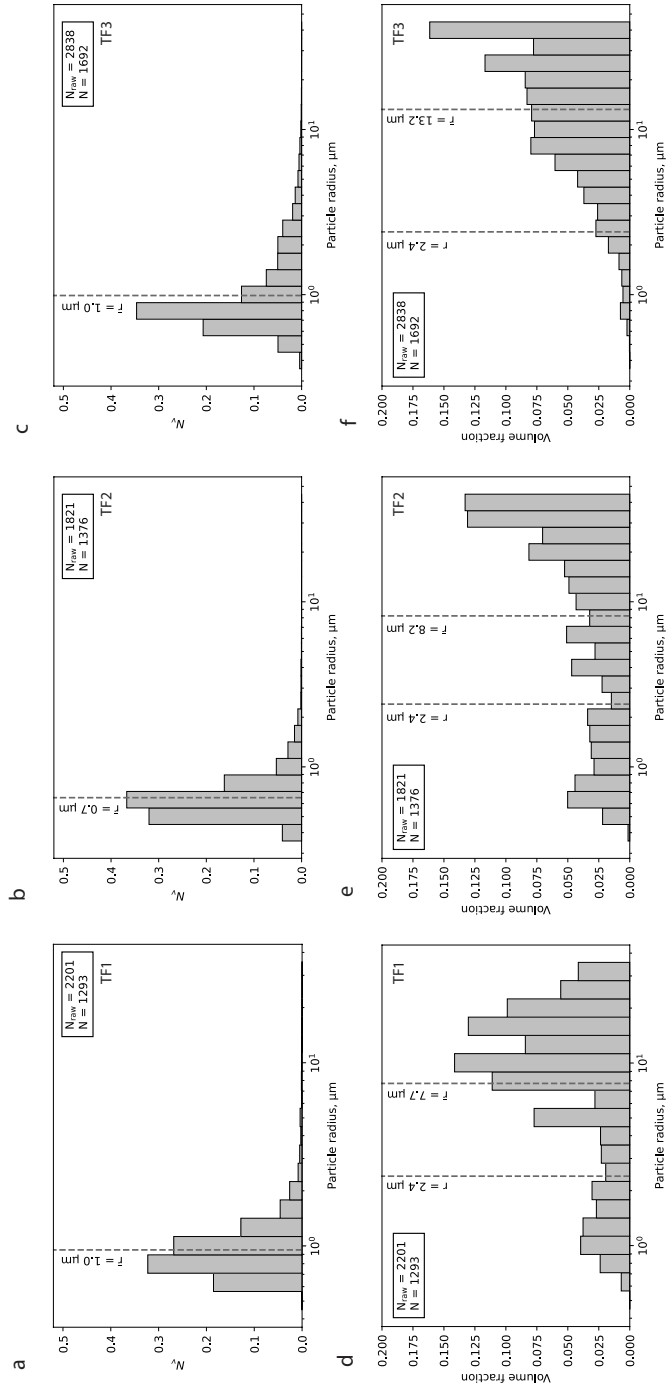
Figure 5.4: Particle-size distributions showing normalised frequency (a–c) and volume fraction (d–f) of particles for the tuffisite samples TF1, TF2, and TF3. N_{raw} is the total number of particles counted within an image nest before filtering, N is the total number of particles that form the final particle-size distribution displayed here, after filtering has taken place and the particle-size distributions for each image within a nest have been combined. r is the modelled best fit particle radius for the porosity and permeability data (2.4 μm) and $\bar{r}$ is the mean particle radius for each sample. The majority of particles measured have a small radius ($\sim$1 μm). The greater volume of particles with a larger radius allows them to dominate in the distribution by volume.

155

5.3.2 Tuffisite particle-size distributions

Samples TF1, TF2 and TF3 were chosen for particle-size distributions as these were sampled directly from the main section of the tuffisite. The highest magnification images (typically x1200–1800) are large enough for particles >0.3 μm to be collected, with the majority of particles measured having a radius <1 μm. The radii of particles in the matrix of these samples after filtering were found to range from ~0.3–60 μm, with the mean particle radius ranging from 0.6–1.0 μm in the different samples (Figures 5.4a–c). Many of the finest grained particles in the images could not be measured as their margins were too obscured by sintering (Figure 5.3). The overall distributions each show a positive skew, also suggesting an absence of identifiable particles of the smallest sizes (<0.5 μm). The samples with a smaller average particle-size are found to have a lower porosity and permeability, as expected (Table 5.1).

The particle frequency distributions were converted into volume fractions for each sample (Figures 5.4d–f). The volume fraction distributions are dominated by the larger particles in the distribution.

5.4 Discussion

5.4.1 Modelling tuffisite permeability

The permeability of our tuffisite samples increases as a function of porosity (Figure 5.5), in agreement with data for tuffisites from Chaitén and Cordón Caulle in Chile (Heap et al., 2019) and volcanic rocks in general (e.g. Farquharson et al., 2015). By combining the particle-size distributions found for the different tuffisite units with the measured porosity permeability data, the particle-size that is controlling the permeability of each sample can be considered, as well as producing a modelled permeability from each particle-size distribution.

Wadsworth et al. (2016) provide a model for predicting the permeability, k, of sintered granular materials, given by

$$k = \frac{2\left(1 - (\phi - \phi_c)\right)}{s^2} \left(\phi - \phi_c\right)^{\bar{e}},$$
(5.3)

where ϕ is the porosity, ϕ_c is the porosity at the percolation threshold at which the

permeability is considered to be zero, s is the specific surface area and $\bar{e}$ is the percolation constant. The value of ϕ_c has been determined to be ~ 0.03 for granular materials across a wide range of particle types and sizes (Wadsworth et al., 2016) and $\bar{e}$ is 4.4 for overlapping particles (Feng et al., 1987). The specific surface area, s, is the ratio of pore surface area within a sample to the sample volume and can be related to the mean of the initial particle-size distribution (see Wadsworth et al., 2016 for full solution). Using the Excel Solver tool the monodisperse particle-size that is controlling the sintered permeability of the measured samples is predicted by finding the best fit value for s. The best fit to the data is found to be with a global $\phi_c = 0.05$ and particles of diameter 4.7 μm, giving an R^2 value of 0.81 (Figure 5.5). As the standard deviation of the original particle-size distribution is not known a polydisperse particle-size distribution cannot be produced. Particles 4.7 μm in diameter, or with a radius of 2.35 μm, are similar in size to the mean particle-size measured directly in the particle-size distributions of the sintered material of samples TF1-3 (Figures 5.4a–c). This particle-size is also similar to that found as the fine fraction in the matrix of internal tuffisites elsewhere (Heap et al., 2019; Saubin et al., 2019) and the ultra-fine ash fraction seen to be trapped by sintering onto fracture surfaces within the vent of the rhyolitic 2011–12 eruption of Cordón Caulle (Farquharson et al., 2022).

The particle-size distributions can be calculated for units of different particle-size within each sample, allowing for the calculation of a predicted sample permeability using Eq. 5.5 and the calculated polydisperse particle-size distribution (Wadsworth et al., 2016). The units with particle-size distributions dominated by the finer particle-sizes provide the best prediction of the sample permeability, suggesting again that the permeability of the sample is controlled by the finer grained material swept into the pore spaces between larger particles.
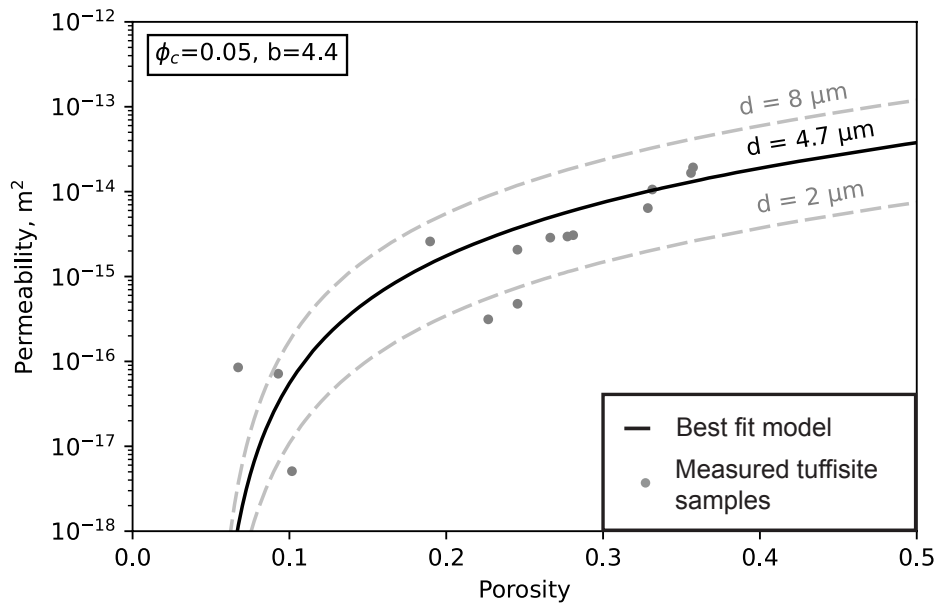
Figure 5.5: Porosity and permeability data for the different tuffisite samples (grey symbols) and the modelled porosity-permeability relationship for packs of monodisperse particles of different diameters, d, using the model of Wadsworth et al. (2016). A particle pack of particles with a diameter of $d = 4.7$ μm gives the best fit for the data (solid black line).

Table 5.2: The variables used in equations and their values, if applicable.

Variable	Definition	Value	Variable	Definition	Value
A	Cross-sectional area	–	P_{up}	Sample upstream pressure	–
a	Fracture size in the third dimension	~ 100 m	P_{down}	Sample downstream pressure	101,325 Pa
$\langle a_i \rangle$	Mean pore size	–	Q	Volumetric flow rate through sample	–
B	Coefficient	10^{10}	Q_v	Fluid flow rate through fracture	–
C	Pore-free heat capacity	1,000 J.kg^{-1}.K^{-1}	q	Fluid flow rate	–
C_f	Fluid heat capacity	1,007 J.kg^{-1}.K^{-1}	s	Specific surface area	–
D_h	Hydraulic diameter	0.18–0.20 m	t_c	Conductive cooling time	–
d_t	Total tuffisite thickness	1.0 m	v	Flow velocity	–
d_{unit}	Thickness of a tuffisite unit	0.1 m	W	Fracture width	$d_{\text{unit}} = 0.1$ m
E	Young's modulus	1.4–2.4 GPa	Γ	Interfacial tension between the gas and the particles	0.3 N.m^{-1}
$\bar{e}$	Percolation constant	4.4	ζ	Correction factor	–
k	Permeability	–	η	Friction factor	0.03
k_1	Initial permeability before sintering	10^{-13} m^2	κ	Pore free thermal diffusivity	2.89 x 10^{-7} m^2.s^{-1}
k_2	Final unit permeability	10^{-15} m^2	κ'	Porous thermal diffusivity (calculated)	2.41 x 10^{-7} m^2.s^{-1}
k_D	Darcian permeability of sample	–	λ	Thermal conductivity (calculated)	0.578 W.m^{-1}.K^{-1}
k_i	Inertial permeability	–	μ	Viscosity of the fluid-particle mixture	1.34 x 10^{-4} Pa.s
k_t	Overall tuffisite permeability	–	μ_f	Viscosity of the fluid	1.0 x 10^{-4} Pa.s
L	Fracture length	40–120 m	μ_n	Viscosity of nitrogen at room temperature	1.76 x 10^{-5}

L_s	Sample length	see Table 5.1	μ_p	Viscosity of hot particles	–
n	Particle fraction of fluid	0.25	ν	Poisson's ratio	0.2
P_1	Upstream fracture pressure	–	ρ	Pore free density	2,000 kg.m^{-3}
P_2	Downstream fracture pressure	101,325 Pa	ρ_f	Fluid density	1 kg.m^{-3}
P_m	Mean pressure	–	ϕ	Porosity	–
ΔP	Pressure difference	–	ϕ_1, ϕ_2	Initial and final porosity	0.4, 0.2
			ϕ_c	Porosity at the percolation threshold	0.03

5.4.2 Predicting tuffisite longevity

5.4.2.1 Degree of tuffisite sintering

The sintering of particles within the Húsafell tuffisite would have altered the porosity and permeability of tuffisite units during their lifetime, influencing the potential outgassing flux. from the conduit. The particles within the units of the Húsafell tuffisite are visibly sintered together (Figure 5.3), with small particles sintering to form larger aggregates. This has, in many cases, completely obscured the original particle margins, which is also indicated by the absence of very fine-grained particles in the particle-size distributions, producing a positive skew in the data (Figure 5.4).

The final laboratory-measured porosity and permeability of the tuffisite indicates the degree of sintering that took place. The ability of particles to sinter is dependent on the particle-size distribution, as well as the particle viscosity, applied pressure, and temperature. By comparing the timescale for the cooling of the emplaced units with their sintering timescale, the length of time for which outgassing through tuffisite pore space could occur can be considered, as well as providing constraints for the emplacement time of the Húsafell tuffisite.

5.4.2.2 The cooling time of Húsafell tuffisite units

The length of time that the particles within a tuffisite unit would have remained hotter than the glass transition temperature will control the length of time available for particles to sinter. A simple approximation for the cooling time scale of the tuffisite units by conduction, t_c, can be given by $t_c = d_{\text{unit}}^2/\kappa$, where d_{unit} is the thickness of the unit being considered and κ is the thermal diffusivity. The thermal diffusivity of the porous tuffisite, κ', can be found using the equation

$$\kappa' = \frac{\lambda\left(1 - \phi_2\right)}{\left(\rho C\left(1 - \phi_2\right) + \rho_f C_f \phi_2\right)\left(1 + \phi_2\right)}, \tag{5.4}$$

where λ is the pore-free thermal conductivity, ϕ_2 is the final porosity, ρ is the density, C is the pore-free heat capacity, ρ_f is the density of the pore-filling fluid, and C_f is the heat capacity of the pore-filling fluid (Connor et al., 1997). The value of λ can be found with $\lambda = \kappa \rho C$, where the best fit value of κ for pore free volcanic material is

2.89 x 10^{-7} $m^2.s^{-1}$ (Bagdassarov and Dingwell, 1994). To calculate κ' the following values are taken: ρ = 2,000 kg.m^{-3}, ρ_f = 1 kg.m^{-3}, C = 1,000 J.kg^{-1}.K^{-1}, C_f = 1,007 J.kg^{-1}.K^{-1}, and ϕ_2 = 0.2. For convenience, the definitions and values of different variables are listed in Table 5.2.

The cooling time for the whole tuffisite thickness (d_t = 1 m), assuming that the tuffisite was emplaced in a single fluid pulse, is ~1,200 hours. However, the structure of the tuffisite suggests that it is formed of a series of 0.1 m-thick units, each emplaced by an individual fluid pulse (Chapter 3). Each 0.1 m-thick unit would have a cooling time of ~12 hours, during which the particles could have remained sufficiently hot to sinter. This is a conservative overestimate because pyroclasts can only sinter when at a temperature above the glass transition temperature and, therefore, sintering will have stopped before the tuffisite cools to the ambient background temperature.

The injected material must be fully sintered or hardened before the gas pressure fully drops to prevent lithostatic pressure from compressing the tuffisite material during fracture closure. The individual units across most of the tuffisite width do not appear to have been viscously deformed by subsequent injection of material, suggesting that the material had time to fully cool to a temperature below the glass transition before the new material was injected (Chapter 3). The cooling time calculated above (~12 hours) is therefore the minimum time between each injection, suggesting that the entire tuffisite was assembled over a period of at least several tens of hours. However, as the next injection could have been emplaced without compacting the previous material if it had cooled to a temperature below the glass transition, rather than the ambient temperature, this minimum value is a conservative overestimate of the time between injections.

The material closer to the centre of the tuffisite, interpreted as being emplaced towards the end of tuffisite evolution, appears to be more sintered, suggesting a slower cooling time perhaps made possible by the increased tuffisite thickness (Chapter 3). Viscous deformation of the surrounding tuffisite units by later injections ('Finger-shaped injections'; Chapter 3) suggests that towards the end of the tuffisite lifetime the newly emplaced material did not have time to cool sufficiently before the next injection to prevent viscous deformation from occurring. This could reflect the better-insulated tuffisite centre preventing sufficient cooling before the next injection to avoid viscous deformation. Higher temperatures at the tuffisite centre would allow for more rapid sintering, perhaps

allowing overpressure to increase more rapidly, resulting in more frequent injections when the critical overpressure threshold to drive fracture opening was reached.

5.4.2.3   Tuffisite sintering time

The sintering of particles in the tuffisite will reduce its porosity and permeability through time, limiting the potential outgassing flux. The measured porosity and permeability of tuffisite samples reflect the final values reached by the tuffisite after sintering had taken place. By considering the time required for the particles within the tuffisite to sinter to their measured porosity, another constraint on the length of time that the tuffisite was active can be found.

The porosity of a sintering granular matrix through time, $\phi(t)$, can be estimated using the 'Vented Bubble model' (Wadsworth et al., 2019, 2021)

$$\frac{d\phi}{dt} = -\frac{3\Delta P}{4\mu}\phi - \frac{3\Gamma}{2\mu\langle a_i\rangle\zeta}\left(\frac{\phi_i}{1-\phi_i}\right)^{\frac{1}{3}}\phi^{\frac{2}{3}}(1-\phi)^{\frac{1}{3}} \tag{5.5}$$

where ΔP is the difference between the pressure of the hot gas and the stress acting on the sintering particles, μ_p is the viscosity of the hot particles, Γ is the interfacial tension between the gas and the particles, $\langle a_i\rangle$ is the mean size of the pore spaces between the sintering particles (which can be related to particle radius — Wadsworth et al., 2016), and ζ is a correction factor that accounts for the polydispersivity of the particle-size distribution (Wadsworth et al., 2017).

The sintering time is dependent on the particle-size, and so the sintering time for the measured polydisperse particle-size distributions of the different tuffisite units is calculated. The viscosity of the sintering particles was determined using Hess and Dingwell (1996) for 800 and 900 °C at 0.1 wt% H_2O (at atmospheric pressure) to 1 wt% H_2O (as measured in an adjacent dyke at Húsafell; McGowan, 2016) to give 7.1 x $10^8 < \mu_p <$2.3 x 10^{10} Pa.s for 0.1 wt% H_2O and 1.9 x $10^6 < \mu_p <$2.5 x 10^7 Pa.s at 1 wt% H_2O. The tuffisite is thought to have been emplaced at 500 m depth (McGowan, 2016), giving a lithostatically imposed melt pressure of 10 MPa, and here $\Gamma = 0.3$ N/m is used (Gardner and Ketcham, 2011). With these inputs, Eq. 5.5 can be solved numerically to give the evolution of $\phi(t)$ during sintering.
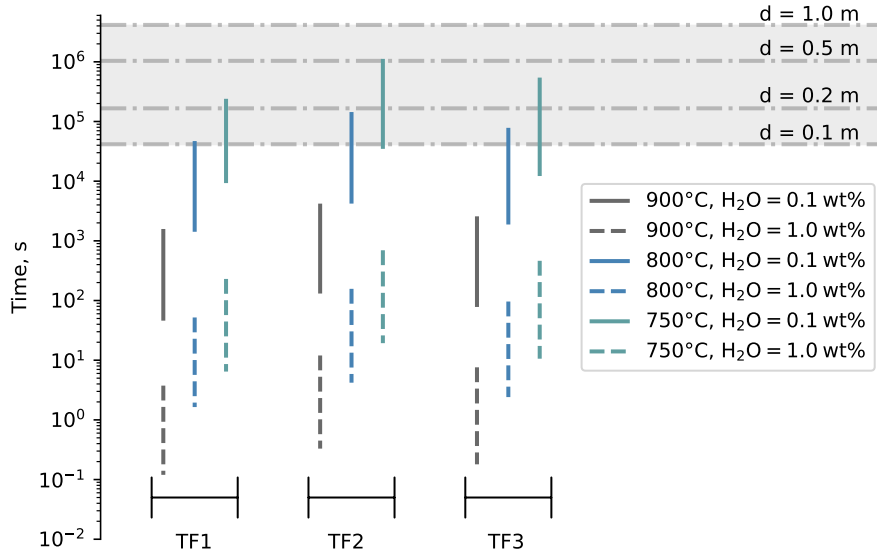
Figure 5.6: The conductive cooling timescales for units of thickness, d (horizontal lines), compared to the modelled sintering times (vertical lines) for each sample (polydisperse particle-size distributions). The sintering times show the time taken for the particle-size distribution, measured for each sample, to sinter to the observed sample porosity for different water contents. Overlap between the two timescales indicates that the calculated conductive cooling and sintering times are approximately equal under those conditions. The vertical lines that fall beneath the horizontal lines indicate that the samples under these conditions would be able to sinter to the observed porosity more rapidly than the unit could cool, suggesting that the samples would have sintered more completely than seen in the tuffisite.

The sintering timescale of the tuffisite unit is dependent on the effective pressure ΔP (Eq. 5.5). If the gas pressure equals the stress on the particles, then $\Delta P = 0$. If the stress on the particles is the lithostatic stress of 10 MPa (Chapter 3), then this condition of $\Delta P = 0$ gives a maximum possible gas pressure of also 10 MPa. Under this pressure equilibrium of $\Delta P = 0$, the sintering time is long and the first term on the right-hand-side of Eq. 5.5 is zero. A gas pressure lower than 10 MPa will produce a larger effective ΔP, and the first term on the right-hand-side will be a function of the pressure, increasing the rate of sintering. The fastest possible sintering will occur at the largest possible ΔP, which is the case where the gas pressure is at atmospheric pressure (0.1 MPa) with sintering occurring in the compaction regime such that $\Delta P \approx 10$ MPa.

The sintering process is estimated using VolcWeld (which is a downloadable implementation of Eq. 5.5 including the effect of diffusive loss of H_2O during sintering; Vasseur and Wadsworth, 2019; Wadsworth et al., 2019, 2021). The full sintering dynamics are solved using this program, and the times at which ϕ matches the observed porosity for a given

sample/unit are outputted. This is taken as the 'sintering time' for that sample to reach its final state. These sintering times vary depending on the particle-size distribution of the different units, giving $\sim 10^2 - 10^6$ s for particles with 0.1 wt% H_2O and $\sim 10^{-1} - 10^3$ s for particles with 1 wt% H_2O. This sintering time can be compared to the conduction cooling time of the tuffisite units to further constrain reasonable conditions for tuffisite emplacement (Figure 5.6a). Conditions for which the sintering time is much more rapid than the cooling time suggest that, under those conditions, the the particles would be expected to be able to sinter to a lower porosity than is seen in the given cooling time. For example, at 1 wt% H_2O, the sintering time is significantly shorter than the cooling time calculated for a 0.1 m-thick unit. If the water content of the particles was lower, as might be expected for small clasts that can degas quickly in a fracture at low pressure, the sintering and cooling times are much closer together, with pyroclasts sintering to the observed porosity in the given cooling time. These values indicate combinations of temperatures and water contents that could have produced the observed tuffisite porosity in units of different thicknesses. These values have been calculated using the final observed particle-size distribution and a sensitivity analysis exploring the effects of adding extra fines to the distribution can be found in Appendix A.8.

This suggests that the sintering material must have had either a low H_2O content or a low temperature to produce the observed porosity in the same time as required for cooling. Comparing the conduction cooling timescales and sintering timescales also suggests that the tuffisite must have been emplaced by multiple fluid pulses, each producing a sediment unit, rather than as one ~ 1 m-thick unit. This is consistent with the complex structure of the tuffisite, composed of many different sediment units with different particle-size distributions (Chapter 3).

5.4.3 Seismic signals and the timescales of early tuffisite formation

The source of long-period (LP) seismic events observed at many active volcanoes is thought to be the repeated fluid-driven excitation of pre-existing cracks, triggered by a sudden pressure change within the resonating fracture (Chouet, 1996). These LP events have been suggested to be linked to tuffisite formation (Tuffen, 2003; Tuffen and Dingwell, 2005; Molina et al., 2006), and may therefore record the start of tuffisite formation (Phase 1), constraining the length of time that this initial phase may last for.

The degree of seismic attenuation in a fracture is described by its Q value, where high Q

values represent long lasting oscillations that require large density differences between the fluid and the surrounding rock. The modelling of synthetic waveforms shows that high Q values are best explained by the injection of a dusty gas with particles <10 μm across (Kumagai and Chouet, 1999, 2000; Molina et al., 2004). Changes in the observed complex frequencies and Q values of resonating fractures through time have been suggested to reflect the filling of a fracture with ash particles that sinter through time (Molina et al., 2004; Taguchi et al., 2018). Internal tuffisites, those that form within the conduit, have been suggested to be the fossil record of these seismic swarms, formed by the brittle fracturing of magma at high relative strain rates (Tuffen et al., 2003; Molina et al., 2004; Tuffen and Dingwell, 2005; Neuberg et al., 2006; Taguchi et al., 2021). Alternatively, Chapter 3 suggested that the greater dimensions of external tuffisites formed by pulsed injection into the country rock could make them a more suitable source for LP earthquakes as they more closely match the inferred dimensions of seismic resonators (Kumagai and Chouet, 1999).

The dimensions of the Húsafell tuffisite and the particle-size of its pyroclast fill are consistent with the requirements of the crack excitation model. The permeability-controlling particle-size at Húsafell (4.7 μm-diameter particles) and the average particle-size (0.6–1.1 μm) correspond to the requirements for <10 μm diameter particles within seismically excited fractures (Kumagai and Chouet, 2000; Molina et al., 2004). Furthermore, the Húsafell particle sizes are close to those measured in tuffisites and particle-coated vent surfaces from recent rhyolite eruptions at Chaitén and Cordón Caulle (<15 μm — Saubin et al., 2016; 10–20 μm — Schipper et al., 2021; 0.05–3 μm — Farquharson et al., 2022) and the dissected rhyolitic vent at Mule Creek (USA) (5–7 μm — Chapter 4).

The duration of different LP events recorded at volcanoes is typically $\sim$10–100 seconds (Molina et al., 2004; Neuberg et al., 2006; Arciniega-Ceballos et al., 2012; Torres et al., 2021). This is also similar to VLP frequencies associated with shallow transport of magmatic fluids in conduit systems (Niu and Song, 2020; Ripepe et al., 2021). Both timescales correspond well with that of pulses of ash and gas venting from fractures at Cordón Caulle (seconds to tens of seconds; Heap et al., 2019; Schipper et al., 2021; Crozier et al., 2022). The pulsatory nature of this explosive ash and gas venting, like the repeated injection of ash and gas into fractures modelled as the sources of LP events, requires multiple pulses of fluid injection through the same pathway. This is exactly what is recorded in the sedimentary structures of the Húsafell tuffisite (Chapter 3). Such pulsations are associated with gas pocket accumulation and release in low-viscosity

basaltic systems (Ripepe et al., 2021) but their origin in silicic systems remains enigmatic.

A key question is whether the pressurisation history of any single resonating fracture/tuffisite, such as the Húsafell tuffisite, will be representative of the broader timescale of the entire upper conduit pressurisation occurring during any specific silicic eruption. As many seismogenic fractures may be active simultaneously, generating distinctive LP event families (Neuberg et al., 2006; Niu and Song, 2020), this may not necessarily be the case. Nonetheless, pressurisation timescales of 2–4 hours recorded by H_2O diffusion gradients around a single bomb-hosted external tuffisite from Chaitén (McGowan et al., 2015) do correspond with the timescale of tilt cycles at Soufriere Hills in Montserrat (Voight et al., 1999; Neuberg et al., 2006) and Santiaguito in Guatemala (Johnson et al., 2008), and are considerably longer than the duration of any individual LP event. This suggests that the pressure history recorded by a single fracture can correspond with the timing of an entire tilt (pressurisation) cycle, rather than one isolated LP event within it, and that therefore the single fracture pressure history can span a number of repetitive, similar LP events within a swarm (e.g. one family history). For one randomly selected fracture to be representative of the whole conduit, inter-fracture connectivity is required, and that is exactly what is evident from observation of the timing of gas-ash discharge from individual fractures in the Cordón Caulle vent (Schipper et al., 2013) and from inferred long-range connectivity within the Chaitén conduit from diverse dissolved magmatic H_2O concentrations in tuffisite-filling clasts (Saubin et al., 2016). Within this conceptual framework, the Húsafell tuffisite is seen as the fossil record of an LP swarm, occurring at a spatially fixed position (e.g. a family), and the inferred timescale of particle injection into the fracture, and its cooling and sintering relates to the duration of the swarm itself. It is speculated that the shorter LP event durations themselves relate to the period of peak fluid pressure, which holds the fracture fully open for tens of seconds, prior to a pressure drop that leads to particle deposition and fracture closing. Temporal changes in LP events within a swarm at Tungurahua (Ecuador) have been interpreted as the fracture filling with particles, increasing the Q value and decreasing the gas weight fraction of the fracture (Molina et al., 2004; Taguchi et al., 2018; Torres et al., 2021).

5.4.4 Flux through the Húsafell tuffisite

Tuffisites are thought to provide permeable pathways for lateral outgassing, potentially carrying sufficient gas flux to defuse pressure during a volcanic eruption and lower explosivity. By combining the permeability of the different tuffisite units with their dimensions and timescales of formation, the potential gas flux able to pass through the Húsafell tuffisite at different stages of its evolution can be constrained.

Before the formation of the fracture hosting the Húsafell tuffisite, the country rock at the conduit margins (with a permeability of $\ll 10^{-18}$ m^2) would have impeded lateral outgassing and the flux of gas through the country rock would have been very small, with permeability controlled by any pre-existing fractures. The fact that pore pressures were eventually sufficient to fracture the country rock is also suggestive of a low rock-mass permeability. Once the gas-pyroclast mixture can open the fracture that will host the tuffisite, the permeability will dramatically increase, with the open fracture pathway allowing for a greater flux of gas to flow, cool, condense, and escape into the country rock beyond. With low-permeability host rock, nearly all of the gas flow would be through the fracture produced, with some leakage along smaller connected fractures. The deposition of fine-grained particles in the pore space of fracture walls or offshoot fractures will help to further constrain fluid flow to the within the tuffisite.

The cooling and condensation of water vapour would reduce the volume of the outgassing fluid, allowing this smaller volume to then flow into the low permeability country rock beyond. In the shallow subsurface where tuffisites form ($\sim$500 m depth), the weight of the overlying material will produce a pressure of $\sim$6.2 MPa (Chapter 3), causing water to be a vapour rather than a supercritical fluid. This water vapour will condense when it crosses the boiling point of water, calculated using the Clausius-Clapeyron relation as $\sim$270 °C, decreasing its volume. At lithostatic pressure ($\sim$6.2 MPa; Chapter 3) the volume of one mole of water vapour can be calculated with the ideal gas law, $PV = n\mathrm{R}T$, where P is the gas pressure, V is the gas volume, n is the number of moles, R is the gas constant (8.31 J.mol^{-1}), and T is the temperature being considered ($\sim$270 °C), giving a volume of 7.2 x 10^{-4} m^3. Assuming that water is incompressible, 1 mole of water has a volume of 1.8 x 10^{-5} m^3. This suggests that the condensation of water reduces the volume of water vapour by a factor of $\sim$40. The temperature of the water vapour injected into the fracture will rapidly cool from the conduit temperature ($\sim$800 °C), also producing a decrease in gas volume before the boiling point is reached. Assuming a

constant pressure, the volume of water vapour is directly proportional to its temperature, according to Charles' law. This decrease in temperature will therefore lead to a decrease in water vapour volume by a factor of $\sim$3, though depressurisation will cause this value to be an overestimate of the overall volume decrease. Overall, the injected water vapour will decrease in volume by a factor of $\sim$120 as it cools and condenses, allowing a much smaller volume of liquid water to flow into the hydrothermal system beyond.

The emplacement of each unit of the tuffisite allows for two different mechanisms for gas escape. Significant outgassing through tuffisites has been suggested to occur though the tuffisite pore space, after particle deposition has occurred and the fracture has closed around the deposited particles. Outgassing may also occur through the fracture at the start of tuffisite formation, before particles are deposited and the fracture closes. Here the flux for these outgassing mechanisms is compared to consider which stage is more significant.

5.4.4.1   Gas flow through a propped pyroclast-filled fracture

Gas can flow through the pore spaces of the tuffisite in the second phase of tuffisite formation, with the permeability of this pathway limited by the particle-size distribution of the tuffisite and the ability of the particles to sinter through time. The particles in the Húsafell tuffisite did not fully sinter, preserving a permeable pathway through which long-term outgassing could occur even after sintering.

For a tuffisite unit with an average particle-size diameter of 4.7 μm (the best fit particle-size diameter for the permeability of the Húsafell tuffisite samples) the permeability is initially $\sim 10^{-13}$ m^2, decreasing to $\sim 10^{-15}$ m^2 over a period of $\sim$12 hours as the particles compact and sinter together. The tuffisite will then remain at this permeability until the next injection of material. Subsequent injections will also have a permeability of initially $\sim 10^{-13}$ m^2, decreasing to $\sim 10^{-15}$ m^2 over a period of $\sim$12 hours, increasing the thickness of sintered material (permeability of $\sim 10^{-15}$ m^2) through time.

The flow rate of gas, q, that is able to pass through the particle pack of a unit is controlled by the difference in fluid pressure along the tuffisite length. ΔP must at least be equal to the overpressure required to hold open a fracture by elastically deforming

the surrounding material, which can be calculated using

$$\Delta P = \frac{E}{2\left(1 - \nu^2\right)}\frac{W}{L},$$

(5.6)

where E is the Young's modulus, ν is the Poisson's ratio, W is the fracture width and L is the fracture length (Gudmundsson, 1983). Here ν is taken to be 0.2 (Özsan and Akın, 2002) and a range of values for E of 1.4–2.4 GPa (Heap et al., 2020) is considered to estimate the required overpressure. The Húsafell tuffisite comprises units each $\sim$0.1 m in thickness and $>$40 m in length (Chapter 3), and d is taken to be 0.1 m. Tuffisites within the country rock have been seen to extend $>$120 m from the conduit margin (Heiken et al., 1988), and the values $L = 40$–120 m are considered. This gives a ΔP of 1.8–3.1 MPa (for $L = 40$ m) or 0.6–1.0 MPa (for $L = 120$ m) for the different values of E.

The fluid flow rate through the propped fracture, q, can be calculated using Forchheimer's law:

$$\frac{dP}{dx} = \frac{-\mu_f}{k}q - \frac{\rho_f}{k_i}q^2,$$

(5.7)

where dP/dx is the pressure gradient along the fracture, μ and ρ are the viscosity and density of the particle-bearing fluid, and k_i is the inertial permeability, related to the permeability, k, according to the relationship $k_i \approx \mathrm{B}k^{3/2}$ (Zhou et al., 2019; Vasseur et al., 2020). For planar fractures this relationship has been found to be true when the coefficient $\mathrm{B} = 10^{1}0$. It is calculated that $\frac{dP}{dx} \approx \Delta P/L$. First order estimations of μ and ρ are calculated using

$$\mu \approx \mu_f/\left(1 - n\right)$$

(5.8)

$$\rho \approx \rho_f\left(1 - n\right) + \rho_p n$$

(5.9)

where μ_f and ρ_f are the viscosity and density of the fluid without particles, n is the fraction of particles, and ρ_p is the density of the particles. This is an approximation, taken for simplicity, that does not consider the relationship between fluid flow and sedimentation rates within the fracture, and how these might vary through time. The ability of the injected fluid-particle mixture to produce the delicate laminations and cross-laminations seen in the tuffisite suggests that the mixture is not a slurry and therefore $n < 0.5$ (Cartwright et al., 2008). Molina et al. (2004) model the particle fraction of the gas-particle mixture injected into a fracture at Tungurahua as $\sim$25% particles, and so $n = 0.25$ is taken as an approximate value. The particle fraction

estimated by Molina et al. (2004) is likely to represent the fluid injected into an actual fracture, and $n = 0.25$ is therefore a maximum value as it is likely that the n of the fluid-particle mixture passing through the pore space of the tuffisite will be lower due to slower fluid velocities and the surrounding deposited pyroclasts restricting particle transport. At atmospheric pressure and 25 °C the density of water vapour is ~0.6 kg.m^{-3}, increasing to ~2.1 kg.m^{-3} at 1 MPa and 750 °C. The pressure and temperature of the gas within the fracture is poorly constrained but here the value for fluid density, ρ_f, is taken to be 1 kg.m^{-3}, between these values. Taking the values $\mu_f = 1$ x 10^{-4} Pa.s, $\rho_f = 1$ kg.m^{-3}, and $\rho_p = 1800$ kg.m^{-3}, it is calculated that the flow rate, q, through the deposited particle for a unit just injected, before sintering ($k_1 = 10^{-13}$ m^2) to be 3.7 x 10^{-6}–5.5 x 10^{-5} m.s^{-1}, and 3.7 x 10^{-8}–5.8 x 10^{-7} m.s^{-1} for a unit that has had sufficient time to sinter to its final permeability ($k_2 = 10^{-15}$ m^2).

The fluid velocity through the tuffisite can be converted into a gas flux by considering the volume of tuffisite allowing outgassing during its evolution. The gas flux, Q_v, can be calculated using $Q_v = qad_t$, where a is the size of the tuffisite in the third dimension. Very little is known about the 3D shape of the Húsafell tuffisite as there is no 3D cross-section preserved in the field. The value for a is therefore taken to be a range of values for a of 1–100 m. Multiplying by the unit thickness ($d_t = d_{unit} = 0.1$ m) and size of the third dimension of the tuffisite ($a = 1$–100 m) gives a range of values for the potential fluid flux through the tuffisite of $Q = 3.7$ x 10^{-7}–5.5 x 10^{-4} m^3.s^{-1} before sintering occurs or 3.7 x 10^{-9}–5.8 x 10^{-6} m^3.s^{-1} after the unit has sintered.

The potential gas flow rate through the tuffisite will increase through time as more units are deposited, creating a greater volume of material more permeable than the host rock through which gas could escape. The calculation above can be expanded to include the injection of multiple different tuffisite units, with each unit assumed to have the same length ($L = 40$–120 m), thickness ($d_{unit} = 0.1$ m), and initial permeability ($k_1 = 10^{-13}$ m^2). All units are assumed to sinter to $k_2 = 10^{-15}$ m^2 before the injection of the subsequent unit (Figure 5.7). The permeability of the individual units is scaled by their thickness to give a permeability of the tuffisite using

$$k_t = \frac{k_1 d_{unit} + k_2 (d_t - d_{unit})}{d_t} \tag{5.10}$$

where d_t is the total thickness of the tuffisite (Farquharson and Wadsworth 2018). The tuffisite will permit the maximum gas flow rate when it has the greatest volume, after all
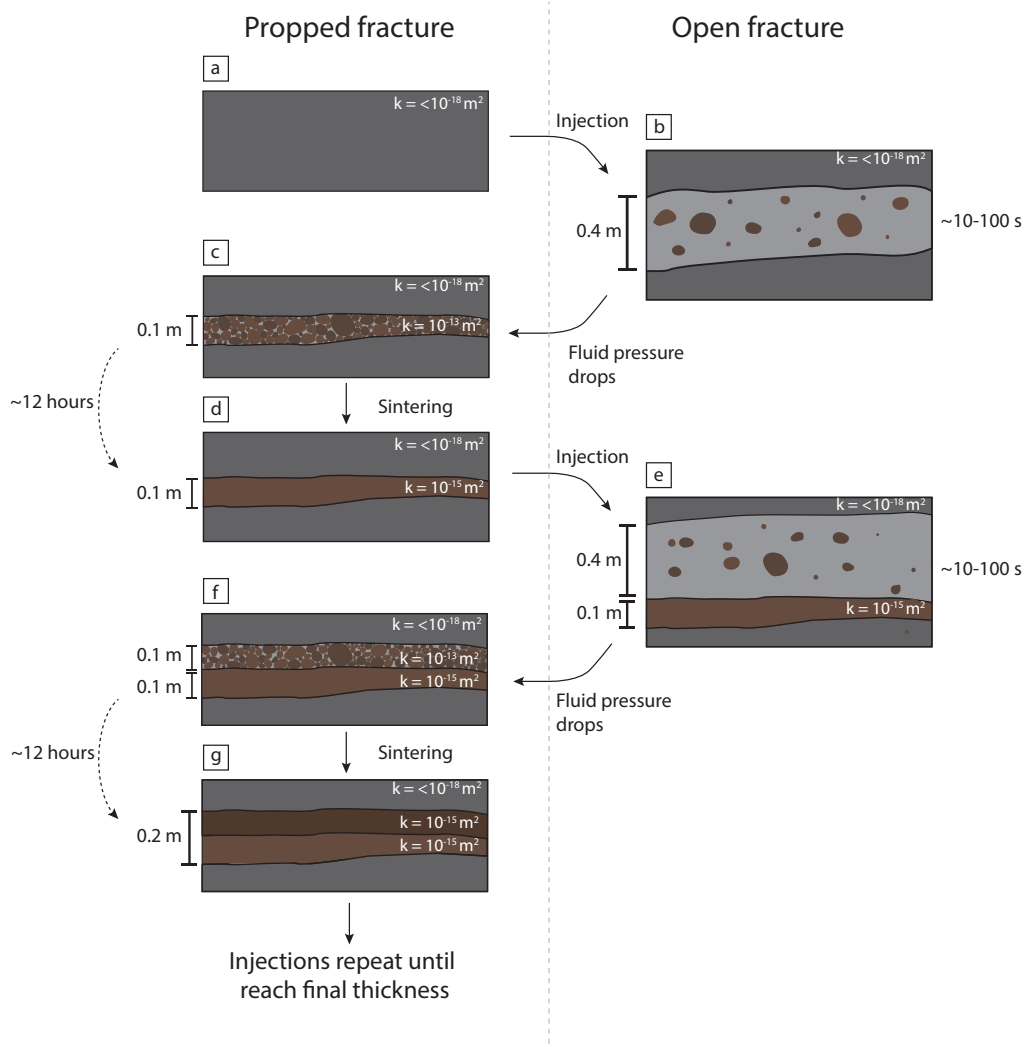
Figure 5.7: Schematic showing the different stages of tuffisite formation. a) The high-pressure gas-pyroclast mixture fractures the low permeability host rock, producing a fracture into which material can be injected. b) The fracture remains open for ∼10–100 s and is about four times the preserved unit width (Molina et al., 2004). c) The fluid pressure drops and particles are deposited. The fracture closes but remains propped open by the deposited particles, allowing gas to still flow through the pore spaces within the particle pack. d) Over a period of up to 12 hours the particles sinter together, reducing the permeability of the particle pack and further restricting gas flow. e) The fracturing process repeats, re-opening the fluid flow pathway for ∼10–100 seconds before the fluid pressure drops. f) The drop in fluid pressure once again closes the fracture, restricting gas flow to through the pore space of the particle pack. The previous tuffisite unit is still present, creating a greater thickness of more permeable material through which gas can flow. g) The newly deposited unit sinters together, lowering its permeability and reducing the possible gas flux. These processes will then continue to repeat, with more pulses emplaced until the final unit thickness is reached.

the units have been emplaced. The total width of the Húsafell tuffisite, d_t, is $\sim$1 m thick, formed of units with a thickness, d_{unit}, of 0.1 m. After 10 injections, when $d_t = 1$ m, the overall permeability of the tuffisite before the newly emplaced unit has sintered, k_t, is 1.09×10^{-14} m^2. This permeability assumes that there are no fractures within the larger tuffisite fill, such as fractures at the boundaries between tuffisite units. This matches our observations in the field, with tuffisite units sintered together at their margins. The lower permeability value of the 1 m thick tuffisite compared to the unsintered tuffisite permeability reflects the increased proportion of less permeable sintered material present. The increased cross-sectional area of the tuffisite will allow for more gas flow to occur for the same pressure gradient. For our range of values of ΔP this gives an estimated fluid velocity through the whole tuffisite of 6.2×10^{-6}–4.1×10^{-7} m.s^{-1}, decreasing to 5.8×10^{-7}–3.7×10^{-8} m.s^{-1} after sintering.

The flux through the tuffisite increases only slightly once the new units are emplaced, from 3.7×10^{-7}–5.5×10^{-4} m^3.s^{-1} (when $d_t = 0.1$ m) to 4.1×10^{-7}–6.2×10^{-4} m^3.s^{-1} (when $d_t = 1$ m), considering the range of values for ΔP, L, and a. The possible gas flux through the tuffisite is strongly controlled by the permeability of the newly deposited unit, with the overall increase in tuffisite thickness not contributing much to the possible gas flux. Assuming that the length of time between each injection is $\sim$12 hours, then the total volume of gas able to flow through the particle pack of the tuffisite during its emplacement (over $\sim$120 hours) is $\sim$0.17–250 m^3 for a pressure gradient, ΔP, of 1.8–3.1 MPa (for $L = 40$ m) or 0.6–1.0 MPa (for $L = 120$ m). Note that the gas flux and volume calculated here are an overestimate, as the newly deposited unit will sinter during the 12 hours after its emplacement, reducing its permeability through time, rather than staying at a permeability of 10^{-13} m^2 for 12 hours.

The potential gas flux able to pass through the particle pack of external tuffisites is only small and would not contribute significantly to pressure dissipation during an eruption due to the low permeability of the propped fracture. However, the preserved permeability of external tuffisites allows them to act as outgassing pathways for long periods of time, over which their outgassing could become significant. Tuffisites may also provide important planes of weakness within the country rock for the opening of future outgassing pathways.

5.4.4.2 Gas flow through an open fracture

An open fracture has a much greater permeability than the tuffisite, potentially allowing for significantly more gas flow to occur, even if only possible for a short duration before the fracture becomes clogged with particles. Here the potential fluid flux that the fracture could carry during the first stage of tuffisite formation is calculated.

The fluid flow velocity within a tuffisite is poorly constrained. Gas-ash venting at the surface has been suggested to represent the surface expression of tuffisites (Heap et al., 2021), with measured ejection velocities of up to 30 m.s^{-1} (Crozier et al., 2022). These vertical surface velocities are likely to not be representative of the velocities within a horizontal tuffisite at depth but provide a useful constraint. In the short period of time before particle deposition begins, the fluid velocity within the fracture must be great enough to particles from being deposited within the fracture. A constraint on the minimum fluid flow velocity within the fracture could be estimated using the Froude number, Fr, which represents the ratio of inertial to gravitational forces within a flow. The formation of cross-laminations within the tuffisite later in its formation may suggest that the flow within the fracture is subcritical (Chapter 3; Fr <1), though this is taken tentatively as depositional regimes for granular flows within fractures are not well understood. At the start of tuffisite formation, it is therefore likely that the fluid flow velocity through the fracture is greater than the fluid velocity at the critical Froude number (where Fr = 1). The Froude number can be calculated using Fr = $v/(g.D)^{1/2}$, where v is the flow velocity, g is acceleration under gravity and D is the depth of flow. This gives a minimum flow velocity of $\sim$1 m.s^{-1} during this first stage of tuffisite formation.

Assuming incompressible flow, the flux through a fracture can be estimated using the Darcy-Weisbach equation, where the flux, Q_v, is given by

$$Q_v = \frac{2\Delta P A^2 D_h}{\rho \eta L},\tag{5.11}$$

where ΔP is the pressure difference across the fracture, A is the cross-sectional area (where $A = aW$ for a rectangular slot), D_h is the hydraulic diameter, ρ_f is the density of the injected fluid, η is a friction factor, and L is the fracture length (40–120 m). The hydraulic diameter, D_h, can be calculated as $D_h = 2aW/(a + W)$ where a is the size of the tuffisite in the third dimension ($a = 1$–100 m) and W is the fracture width

($W = d_{\text{unit}} = 0.1$ m). The friction factor, η, is dependent on the Reynolds number of the flow within the fracture. The Reynolds number, $Re = \rho v D_h / \mu$, is dependent on the density of the gas-pyroclast mixture, ρ, the speed of fluid flow, v, and the viscosity of the fluid, μ. The minimum value for v is calculated above as the fluid velocity at the critical Froude number ($v = \sim 1$ m.s^{-1}), and $\rho = 450$ kg.m^{-3}, and $\mu = 1.3$ x 10^{-4} Pa.s. It is found that the minimum Re value is ~ 6.23 x 10^5–6.92 x 10^5 m.s^{-1}, which will occur once the fluid velocity has waned sufficiently for particle deposition to begin, and so it is expected that the Re number during this first stage of tuffisite formation will exceed this value. At 30 m.s^{-1}, the velocity of particles ejected from gas-ash vents at the surface, the Re value is 1.9 x 10^7–2.1 x 10^7 m.s^{-1}. For turbulent, high Re number, flow within rough-walled fractures, η is found to be 0.03 at Re $= 10^6$ (Francis and Peters, 1980). The value of η is therefore estimated to be ~ 0.03. Placing these values in Eq. 5.11 gives a fluid flux through the fracture of 0.007–4200 m^3.s^{-1}, or for an opening time of 10–100 s the volume is 0.07–4.2 x 10^5 m^3. This is the volume of the gas-pyroclast mixture would be able to escape each time, with a particle fraction of $n=0.25$. The flux of gas able to escape with each injection is therefore 0.005–3200 m^3.s^{-1}, or 0.05–3.2 x 10^5 m^3 during each 10–100 s period before particle deposition. This would allow for 4.5–2.9 x 10^6 m^3 of outgassing during the $\sim$100-hour tuffisite lifetime, assuming 9 fluid injections each lasting 10–100 seconds before particle deposition clogs the fracture.

The possible fluid flux through the pore space of the tuffisite is $\sim 10^4 - 10^7$ times smaller than the possible fluid flow through the open fracture, before flow is limited by particle deposition. This suggests that outgassing in the first stage of tuffisite formation is much more significant than that in the second stage, even when taking into account the relative durations of each stage. To match the possible outgassing in occurring in $\sim$10–100 s during the first stage of tuffisite formation, outgassing through the tuffisite pore space of the Húsafell tuffisite would have to continue for $\sim$15 days to 20 years (assuming the last injected unit remains at $k_1 = 10^{-13}$ m^2). This value is a conservative underestimate as the last injected unit of the tuffisite would sinter to lower porosity during this timeframe.

The estimated gas fluxes can be converted into H_2O fluxes by considering the number of moles of gas able to escape each second and the M_r of H_2O, using the equation $PV = nRT$, where P is the gas pressure, V is the volume of gas emitted per second, n is the number of moles of gas emitted per second, R is the gas constant (8.31 J.mol^{-1}.K^{-1}), and T is the temperature. Multiplying the number of moles of H_2O, n, by the M_r of H_2O (0.018 kg.mol^{-1}) then yields the mass of H_2O emitted per second. The total pressure at

175
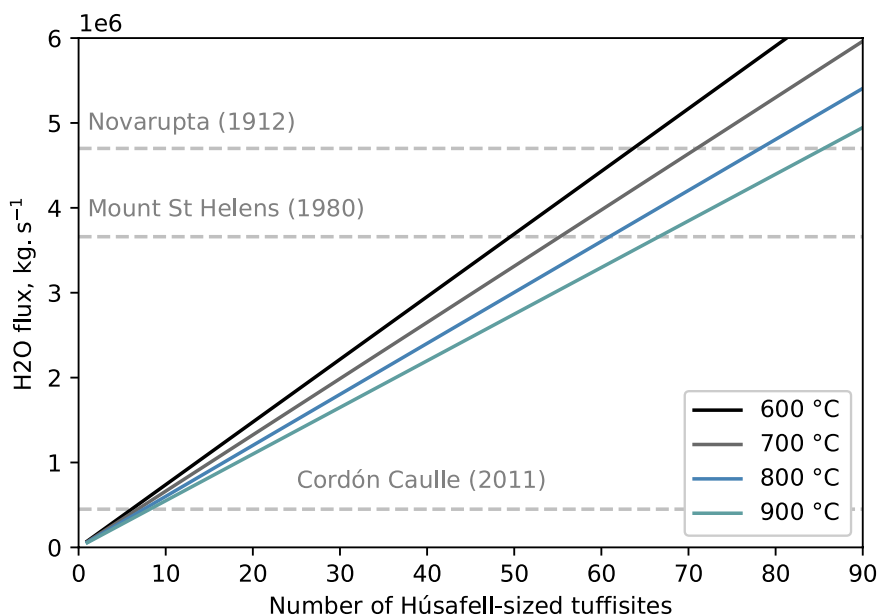
Figure 5.8: The potential flux of H_2O through multiple Húsafell-sized tuffisites compared to the H_2O flux of the eruptions of Novarupta (1912; Fierstein and Hildreth, 1992; Gonnermann and Houghton, 2012); Mount St Helens (1980; Blundy et al., 2008; Degruyter and Bonadonna, 2012) and Cordón Caulle (2011; Castro et al., 2013; Bonadonna et al., 2015). The calculated tuffisite H_2O flux is calculated from the maximum flux (3200 $m^3.s^{-1}$) estimated in Section 5.4.4.2. This potential flux would be possible for only short period, until the tuffisite became clogged with particles, and would therefore allow for pulses of gas to escape.

which the tuffisite forms will be due to the lithostatic pressure (~6.2 MPa; Chapter 3) and the overpressure of tuffisite formation (0.6–3.1 MPa), giving a pressure of ~6.8–9.3 MPa. For this pressure range and the range of fluxes estimated above (0.005–3200 $m^3.s^{-1}$), the H_2O flux would be 0.06–6.0 x 10^4 $kg.s^{-1}$, assuming a temperature of 800 °C. This can be compared to the H_2O flux of different volcanic eruptions to constrain the importance of the tuffisite-enabled outgassing in an eruption, multiplying the calculated mass eruption rate by the wt% H_2O measured in melt inclusions (Figure 5.7). Note that to do this, it is assumed that the discharged H_2O is proportional to the mass flux of associated magma, and so assume that there is no release of gas that had become decoupled from its parent magma. The tuffisite at Húsafell could therefore, during the first 10–100 s of each pulse emplacement, outgas 1–15% of the surface H_2O flux of the eruptions of Novarupta in USA (1912; Fierstein and Hildreth, 1992; Gonnermann and Houghton, 2012), Mount St Helens in USA (1980; Blundy et al., 2008; Degruyter and Bonadonna, 2012) and Cordón Caulle (2011; Castro et al., 2013; Bonadonna et al., 2015).

5.4.5   Implications for tuffisites as outgassing pathways

It is found that the outgassing during the first stage of tuffisite formation is much more significant than later flow through the pore space of the particle-filled fracture, suggesting that tuffisites are a biproduct of an open system, preserving now clogged former gas escape pathways, rather than as a mechanism to open a closed system. These tuffisites are tensile fractures connected to the margin of the conduit that would have allowed for short, pulsed periods of outgassing as fluid was periodically injected into the fracture (Chapter 3). While tuffisite formation would have allowed outgassing, the small size and low permeability of the preserved particle-filled fractures prevents tuffisites from acting as efficient outgassing pathways unless there was a very large network of connected fractures intersecting low-permeability country rock. Previous studies have focused on the permeability of tuffisites and the influence of sintering times on permeability evolution (Heap et al., 2019; Kolzenburg et al., 2019). The relatively small size and low permeability of particle-filled fractures would prevent outgassing through tuffisite pore space from being significant on the timescale of eruptions, even before sintering occurs. The greater permeability of tuffisites than the surrounding country rock, however, may allow long-term outgassing on inter-eruption timescales.

The volume of gas able to escape during the first stage of stage of tuffisite formation, as the fracture opens, will be controlled by the dimensions of the fracture and the length of time the fracture remains open before particle deposition restricts fluid flow. These variables depend on the fluid pressure gradient driving tuffisite formation. With tuffisites forming at the margin of an erupting conduit (Stasiuk et al., 1996; Chapter 4), these variables are therefore controlled by the conduit conditions and how they might vary through time. The complex structure of tuffisites records the evolution of the conduit conditions, with fluid pressure driving tuffisite activity waxing and waning through time (Chapter 3). Unlike plume activity above the surface, the way conduit conditions evolve is poorly understood. This knowledge gap creates uncertainties in the flux calculations, but the potential for pulsed lateral outgassing of large volumes of gas during tuffisite formation suggests that filling this knowledge gap is important for conduit modelling. If connected to the hydrothermal system, tuffisites may be able to act as an efficient pathway for the transport of gas that then condenses and passes into the hydrothermal system. Large lateral outgassing fluxes during tuffisite formation indicate that there is an unknown coupling between flow moving upwards and sideways within the conduit, also

highlighted by the trapping of ultra-fine ash particles beneath the surface (Farquharson et al., 2022).

The processes occurring during outgassing through the fracture at the start of tuffisite formation are not well understood, and improving our understanding of these processes and the period of time before blockage via particle deposition occurs would help to constrain the outgassing flux. Understanding the dynamics of flow of a gas-particle mixture containing hot sticky particles that are able to accrete on to both of the fracture walls and each other is needed to constrain the potential fluid velocities and driving pressures behind tuffisite formation. As particles are deposited, this first outgassing flux must decrease through time to connect to the smaller flux calculated for flow through the inter-particle pore space as the fracture becomes clogged.

The conditions required for tuffisite formation suggest that tuffisites should be common features, but very few country-rock hosted tuffisites have been identified in the field (Heiken et al., 1988; Stasiuk et al., 1996; Chapter 3), perhaps due to poor preservation at dissected silicic vents, or simply a lack of recognition of what to look for. The fractures modelled as the sources of LP earthquakes are typically long ($\sim$100–1000 m in length), suggesting that the opening of these long horizontal fractures would require flexure of the crust, adding additional complications to the shape of tuffisites and therefore the dynamics of fluid flow during tuffisite formation. Tuffisites may act as planes of weakness that can be exploited by future fractures during the creating of later outgassing pathways.

During the first stage of tuffisite formation, with flow through an open fracture, up to 1–15% of the surface H_2O flux seen in explosive volcanic eruptions may be degassed laterally for $\sim$10–100 seconds. While tuffisites have the potential to carry a large flux of gas, perhaps producing a pressure perturbation in the conduit, this drop in pressure would be short-lived with the tuffisite-enabled flux dropping significantly after $\sim$10–100 seconds when the fracture is clogged with particles. If this outgassing can occur with each new pulse into a tuffisite, with new pulses emplaced every 12 hours, then $\sim$400–4000 tuffisites would be required for this outgassing flux to be continuous. This is an unreasonable number of large tuffisites to be positioned around a conduit, and the outgassing enabled by tuffisites will therefore occur in short-lived pulses, even if several tuffisites are present. If tuffisites allowed for a large continuous flux of gas to escape the conduit zone, then tuffisites would be able to reduce significant excess pressure and

potentially moderate eruption explosivity. Each tuffisite will instead produce a relatively short-lived reduction in pressure, and understanding the impact of this pressure reduction on the vertical fluid flow within the conduit and eruption explosivity will require conduit models to consider the coupling between flow moving upwards and sideways within the conduit.

5.4.6 Conclusion

The Húsafell tuffisite has a complex internal structure, comprising multiple cross-cutting units that are interpreted as having been emplaced by multiple injections. The permeability of the tuffisite units of (1.93 x 10^{-14} m^2 to 5.09 x 10^{-18} m^2) suggests that the permeability is controlled by particles ~ 4.7 μm in diameter. These particles are a similar size to those inferred as injected into resonating fractures modelled as the sources of long period volcanic earthquakes. If each injection emplaced a ~ 0.1 m-thick unit then, to align with observations of the degree of sintering, injections would have needed to be at minimum intervals of approximately 12 hours. This suggests that the whole tuffisite, if emplaced by ~ 10 pulses, would have been assembled over a period of ~ 120 hours. It is estimated that the outgassing flux through the pore space each tuffisite unit before sintering would have been ~ 3.7 x 10^{-7}–5.5 x 10^{-4} $m^3 s^{-1}$, with outgassing once subsequent units were emplaced strongly controlled by the permeability of the unsintered unit. A much greater outgassing flux (0.005–3200 $m^3.s^{-1}$ or 0.06–6.0 x 10^4 $kg.s^{-1}$ H_2O) could have occurred at the start of tuffisite formation, before the fracture becomes clogged with particles, suggesting that tuffisite outgassing is much more significant during fracture opening rather than through the pore space of the tuffisite units even when the relative timescales of the two are considered. It is found that tuffisites are a biproduct of an open system, rather than a mechanism for allowing continued gas escape from the conduit zone, allowing significant volumes of pulsed outgassing to occur as new material is injected into the fracture. This highlights a need to better understand the coupling between vertical and horizontal flow within the conduit, as well as how the conduit conditions evolve through time.

6 Discussion

This thesis has combined fieldwork and microstructural analysis to gain an insight into the formation of tuffisites in and around silicic vents. The similarities between tuffisites and silicic vents suggest that they are formed by similar processes, only separated by differences in scale (Chapter 4; Schipper et al., 2021). Alongside the discussion sections provided within each chapter, here I provide some further discussion that is beyond the scope of any individual chapter. This discussion is split into two sections to explore the two main themes of this work: tuffisite formation and the evolution of silicic vents. In the Literature Review (Chapter 2) at the start of this thesis I highlighted multiple open questions about the formation of tuffisites and silicic vents:

1. When do tuffisites form during magma ascent and vent evolution?

2. How do within-conduit tuffisites form?

3. What controls the morphology of tuffisites?

4. What overpressure is required for tuffisite emplacement?

5. Are tuffisites emplaced by a single multi-phase fluid pulse?

6. What are the characteristics of the fluid injected into fractures to form tuffisites?

7. Do tuffisites represent efficient outgassing pathways? How long would these pathways remain active for?

8. How do silicic vents open and close?

9. What are the controls on eruption style and what is the trigger of explosive-effusive transitions?

10. How does gas escape from the conduit?

11. What is the source of seismicity at silicic vents?

Here, I will discuss these key unanswered questions based on the findings of this thesis and provide suggestion for future work to explore these questions further. Firstly, this discussion will consider the different controls of tuffisite formation, and how these might affect tuffisite characteristics, before applying this knowledge to hydrofractures found

in other environments. I then consider the evolution of silicic vents, and the roles that tuffisites might play during vent evolution.

6.1 Tuffisites and sedimentary hydrofractures

Tuffisites display a wide range of morphologies, controlled by the characteristics of the host rock and the evolution of the fluid pressure that drives tuffisite formation. These differences in morphology have led to tuffisites within and around silicic vents to be separated into two categories — internal and external tuffisites — that have been considered to have different formation mechanisms. In the literature review of this thesis I highlighted some gaps in our understanding of tuffisite formation, such as the controls on tuffisite morphology, the characteristics of the fluid into fractures at the start of tuffisite formation, and the overpressure required for tuffisite emplacement. In this section I discuss each of these topics, drawing on examples from tuffisites and cold water-opened hydrofractures forming in sedimentary environments.

The formation of the tuffisite at Húsafell (Chapter 3) was estimated to require an ovepressure of ∼1.9–3.3 MPa to form. This overpressure is similar to that expected just above the level of fragmentation in a silicic conduit (Degruyter et al., 2012), suggesting that tuffisites should be common features in and around silicic conduits, particularly if there are pre-existing fractures that can be exploited (Chapter 3). Despite this, surprisingly few external tuffisites have been recognised in the field. This may be due to several different factors: tuffisites formed of poorly sintered pyroclastic material may have a low preservation potential; many tuffisites are small features that may not be noticed in the field; there may be difficulty distinguishing large tuffisites from non-intrusive pyroclastic deposits; there are a wide range of tuffisite morphologies; and difficulty identifying well-sintered tuffisites from those interpreted as coherent magmatic dykes and sills.

6.1.1 Controls of tuffisite and hydrofracture formation

6.1.1.1 Host-rock controls

The characteristics of the host rock will control the morphology of the fracture produced in hydrofracture formation, and also, alongside the fracture depth, control the fluid

pressure required for fracture opening (Lister and Kerr, 1991). The tensile strength of the host rock, presence of pre-existing fractures, host rock permeability, and the orientation of the external stress field may control the ability to create fractures and the route that the resulting fracture takes (e.g. Gudmundsson, 2011; Kavanagh et al., 2017; Vachon and Hieronymus, 2017).

A host rock with a relatively low tensile strength will require a lower fluid pressure to fracture than one with a greater tensile strength, allowing sufficient pressure to fracture to be more easily achieved. Host rocks with a sufficiently high density of pre-existing fractures to affect the rock mass strength, which can be exploited and reopened, will also allow for fracture formation at relatively low fluid pressures (Rubin 1993). This will control the location of hydrofractures produced and how common they may be.

Tuffisites intersecting highly permeable host rocks, such as pyroclastic breccia, are diffuse and wispy in structure (Chapter 4). This morphology is interpreted to be formed by fine particles being carried in and deposited within the pore space of the host rock, rather than being fracture hosted. Glacial hydrofractures that intersect relatively permeable host rocks also display a similar morphology. Injections into permeable rocks can fluidise the surrounding material more easily (Bear, 1972), allowing fluidisation to control the shape of the injection formed.

Tuffisites that are confined to the pyroclastic breccia display a diffuse and wispy morphology, but those that cross-cut multiple units, including the pyroclastic breccia, instead have well-defined margins and appear to be confined to fractures. This suggests that the change in morphology is due to a change in the permeability of the host material, with earlier tuffisites deposited within the pore space, and later tuffisites instead able to form well-defined fractures through the pyroclastic breccia. This change in the permeability of the pyroclastic breccia through time may be due to welding or alteration, changing the properties of the host material and resulting in tuffisites with different characteristics forming later in vent evolution.

6.1.1.2   Magnitude of overpressure

Overpressure drives hydrofracture formation, opening fractures within the host rock and controlling the velocity at which material is injected into the fracture. The magnitude of the overpressure determines the width of a fracture during injection and the size and

characteristics of the injected unit.

At overpressures just sufficient to break the surrounding rock, assuming only elastic deformation occurs, the resulting fracture will be narrower than those formed at a greater fluid pressure (Gudmundsson, 1983). The smaller the fluid pressure gradient driving hydrofracture formation the lower the fluid velocity of the injected fluid will be, limiting the dimensions of the particles that can be transported into the fracture. The particle size of tuffisites will also be limited by the fracture width. Narrow fractures will be easily clogged with material, restricting fluid flow through the fracture and preventing the development of any more complex microstructures such as cross-lamination. In sedimentary environments, if particles are sourced from nearby sediment by fluidisation, then fewer particles may be entrained into the fluid flow. In the volcanic environment narrow tuffisites injected into cooler country rock will be able to cool rapidly, preventing welding from occurring and allowing them to maintain a greater permeability than larger tuffisites that will cool more slowly (Kolzenburg et al., 2019).

At a high overpressure the opening of the fracture may cause a greater amount of damage to the surrounding rock than fractures opened at lower fluid pressures, allowing a larger flux of gas to escape through the fracture walls. Greater overpressures will open initially wider fractures, producing greater elastic deformation of the fracture walls, but the greater degree of leakiness will prevent the fluid pressure being sustained, potentially limiting width of the preferred fracture if there is not sufficient time to fill the opened space with particles. The length of time that fluid pressure can be sustained locally within a fracture will be dependent on variations of the source, fracture propagation, and the leakiness of the fracture walls. The volume of fluid able to escape through the fracture walls will be controlled by the wall permeability and the supply of fine-grained material that can block fluid flow pathways into the surrounding host rock. A wider fracture and faster fluid velocity will allow for the transportation of larger particles as well as readily allowing for the fluidisation and entrainment of material. Wide tuffisites will cool more slowly, potentially allowing for significant welding and reduction of permeability to occur.

6.1.1.3   Effects of temperature

The high temperatures of tuffisite formation will control the characteristics of tuffisites by influencing fluid flow and sedimentation. The influences of temperature on tuffisite

formation can be considering by comparing tuffisites with low temperature hydrofractures formed in sedimentary environments.

Tuffisites are though to form above the level of fragmentation within the conduit (Chapter 3) and the clasts injected into the tuffisite will therefore initially be at a high temperature, though potentially rapidly cooling once injected into the fracture. The degree of cooling of pyroclasts that will occur before particle deposition is currently not well constrained, and therefore the temperature of the injected clasts is difficult to determine (Chapter 5). Pyroclasts will cool both adiabatically and due to advection during their transport, and as conduction and convective boundary cooling are dependent on particle size, larger particles will remain hotter at the time of particle deposition.

The ability of particles within many tuffisites to weld together after deposition suggests that the particles remain above the glass transition temperature for a sustained period after their deposition (Chapter 5). The material injected into tuffisites will therefore be hot sticky particles with the potential to accrete onto the fracture walls (Farquharson et al., 2022), allowing for deposition by accretion to occur onto both fracture walls simultaneously, rather than only occurring at the base, as in lower-temperature sedimentary hydrofractures. Particles will also be able to stick together during particle transport and sinter to form agglomerates, as has been seen elsewhere in the conduit (Giachetti et al., 2021). This will influence the dynamics of fluid flow during tuffisite formation.

In glacial hydrofractures, remobilisation and fluidisation of material deposited within hydrofractures is common. In tuffisites, deposited sticky sintered particles will be significantly harder to fluidise or erode, limiting the remobilisation of particles. This may potentially reduce the complexity of microstructures generated within tuffisites. However, soft sediment deformation appears to be common in both glacial hydrofractures and tuffisites, suggesting that particulate deposits can still be deformed during sintering, even if remobilisation is prevented (Chapter 3; Chapter 4). Sintering also does not prevent erosion within tuffisites, with many erosive surfaces visible (Chapter 3). These erosive surfaces are, however, more common within the lower-temperature, country rock-hosted external tuffisites than within internal tuffisites, which form at a greater temperature, suggesting that sintering influences the erodibility of tuffisite filling deposits (Chapter 4).

Welding or sintering within tuffisites allows deposits to achieve a significantly lower permeability than deposits within sedimentary hydrofractures, after sufficient time has

elapsed (Kolzenburg et al., 2019). Hot particle accretion onto fracture walls and the decreasing permeability of pre-existing deposits will allow tuffisites to focus fluid flow to within the host fracture. This is also seen within sedimentary hydrofractures, with the coating of hydrofracture walls with fine-grained material that reduces the wall permeability, but sintering will allow this process to occur more efficiently within tuffisites than in sedimentary hydrofractures. This may allow tuffisites to self-pressurise more easily, with internal processes that can locally vary fluid pressure within the fracture (e.g. localised clogging of fluid flow pathways; Chapter 3) having a great capacity to influence fluid pressure and velocity than would be possible without sintering.

6.1.2 Fluid flow and deposition within hydrofractures

The dynamics of fluid flow within fractures will control the microstructures formed by sediment deposition. Examining the size of particles transported into a fracture and the microstructures produced can allow estimation of the injected fluid velocity and identification of a laminar or turbulent flow regime.

The fluid velocity within sand injectites in vertical fractures (dykes) has been estimated by considering the velocity required to exceed the terminal fall velocities of clasts within the fluid, allowing them to be transported upwards, calculated for a single particle (Duranti and Hurst, 2004; Scott et al., 2009; Sherry et al., 2012) or for a particle in a water-particle mixture of a given particle concentration (Ross et al., 2014; Cobain et al., 2015). This has yielded fluid flow velocities of $\sim$0.1–9 m.s^{-1} for single particles in a fluid (calculated for clasts <0.7 m across; Duranti and Hurst, 2004; Scott et al., 2009; Sherry et al., 2012) or up to $\sim$2 m.s^{-1} for a 3 m diameter clast in a fluid-particle suspension (Ross et al., 2014). This suggests that the fluid velocities involved in sand injectite formation are similar to, or perhaps greater, than those in tuffisite formation, with the minimum fluid velocity during injection of the Húsafell tuffisite estimated to be $\sim$1 m.s^{-1} (Chapter 5).

The smaller dimensions and particle sizes of glacial hydrofractures than sand injectites suggest that the fluid velocity during their formation is significantly lower. We can repeat the calculation of fluid velocity in Chapter 5 to estimate the fluid velocity during glacial hydrofracture formation. For a glacial hydrofracture with a hydraulic diameter of $\sim$0.19 m (for a fracture of width of 0.1 m and height of 1 m), the fluid has a velocity of $\sim$1 m.s^{-1} at the critical Froude number (Fr=1), suggested to be the minimum velocity

at the start of hydrofracture formation. This velocity value is similar to that inferred for tuffisites, as the Froude number equation only takes into account the hydraulic diameter and length of the fracture, and not the characteristics of the flowing fluid. The smaller dimensions of glacial hydrofractures than tuffisites suggests that, to produce the similar fluid velocities, the fluid pressure gradient driving glacial hydrofracture formation is smaller than that driving tuffisite formation.

The fluid velocities estimated above allow the Reynolds number of the flow to be calculated, determining if flow is expected to be laminar or turbulent. The Reynolds number for flow through a rectangular duct, Re, is given by

$$Re = \frac{\rho U D_h}{\mu} \tag{6.1}$$

where ρ is the fluid density, U is the fluid velocity, D_h is the hydraulic diameter, and μ is the viscosity of the particle-bearing fluid. As μ and ρ are dependent on the particle fraction of the fluid, these need to be considered before Reynolds numbers can be estimated. The value of μ and ρ can be calculated using:

$$\mu \approx \mu_f \left(1 - n\right) \tag{6.2}$$

$$\rho \approx \rho_f \left(1 - n\right) + \rho_p n \tag{6.3}$$

where μ_f and ρ_f are the viscosity and density of the fluid without particles respectively, ρ_p is the density of particles, and n is the particle fraction of the fluid (Chapter 5).

Sand injectites do not contain the complex structures such as cross-lamination seen in glacial hydrofractures and tuffisites, suggesting that sand injectites are deposited by a fluid with a greater particle concentration than the other particle-filled fracture types (Chapter 3; Phillips et al., 2013). The fluid flow velocities estimated above suggest that the scouring and erosion visible at the margins of sand injectites is created by the injection of a fluid with a high particle fraction, rather than injection of high velocity fluid, as this feature has not been seen in tuffisites of similar inferred injection velocity. However, similar scouring has been seen on particle-coated fracture surfaces that dissect the vent-filling lava emplaced during the 2011–2012 eruption of Cordón Caulle (Farquharson et al., 2022), suggesting greater fluid flow velocities than are found within tuffisites. These fracture surfaces are thought to represent pathways for the

pulsed ejection of gas-pyroclast mixtures seen during the eruption itself (Heap et al., 2019). Video analysis of these gas-pyroclast jets suggests that particles are ejected at velocities >5 m.s^{-1} (Crozier et al., 2022). The fluid-particle concentration for sand injectites has been estimated to range from 0.4–0.54, with 0.54 close to the highest possible for fluidisation to occur (Scott et al., 2009; Ross et al., 2014; Cobain et al., 2015).

The Reynolds number for flow in a rectangular duct is laminar at Re <2300 (White and Xue, 2020). Glacial hydrofractures will have a lower particle concentration, and the presence of fine-grained laminations at the fracture margins and a coarser-grained centre have been interpreted as evidence for laminar flow (Taylor, 1982; Dixon et al., 1995). Using the Reynolds number calculations from Chapter 5 it is possible to consider the dimensions that would be required for a fracture to have laminar flow.

The particle concentration of the fluid involved in glacial hydrofracture formation is poorly constrained but is suggested to be low by the complex structures seen within hydrofractures (Chapter 3; Rijsdijk et al., 1999; van der Meer et al., 2009; Phillips et al., 2013), and so the particle fraction, n, is taken as 0.4 and 0.2. Taking $\mu_f = 1.06$ x 10^{-3} Pa.s, $\rho_f = 1000$ kg.m^{-3}, $\rho_s = 2650$ kg.m^{-3}, and $v = 1$ m.s^{-1} (Cobain et al., 2015), laminar flow will occur in glacial hydrofractures with a hydraulic diameter <3.7 x 10^{-3} m (for $n = 0.4$) or <2.3 x 10^{-3} m (for $n = 0.2$). For a glacial hydrofracture measuring ∼5 m in the third dimension, the fracture will only contain laminar flow if it had a thickness <2 mm (for $n = 0.4$), or <1 mm (for $n = 0.2$). Glacial hydrofractures are therefore likely to contain turbulent flow.

The Re number for flow within tuffisites is estimated to be much higher than that of sedimentary hydrofractures (Chapter 3) due to the gas-particle mixture injected into tuffisites having a lower viscosity than a water-particle mixture. This means that many tuffisites will contain turbulently flowing fluid, unless the fracture width is very small. For a tuffisite with an $n = 0.25$, tuffisites will only be in the laminar regime (Re <2300) if they have a hydraulic diameter of <6.6 x 10^{-4} m. For a tuffisite with a third dimension of 5 m, laminar flow would therefore only be expected in a tuffisite with a width of <0.3 mm. The walls of narrow tuffisites have often been seen to be lined with fine-grained laminated material, and rather than being formed by laminar flow these are perhaps produced by the finest particles being sucked into the pore spaces of the host rock and deposited, with fluid loss through the permeable tuffisite walls important at the start of

tuffisite formation, or by the processes of turbophoresis (Farquharson et al., 2022).

The characteristics of fluid flow through tuffisites and sedimentary hydrofractures will control the internal structures produced. The greater particle concentration of sand injectites than tuffisites or glacial hydrofractures gives those hydrofractures a simpler internal structure (Hurst et al., 2011). Tuffisites and glacial hydrofractures have more similar internal structures, often emplaced by multiple pulses of injected material (Chapter 3; Phillips et al., 2013). The internal structures of both types of particle-filled fractures are surprisingly similar, despite differences in the viscosity of the depositing fluid. This could be related to the behaviour of the hot sticky pyroclasts injected into tuffisites, and closer comparisons between the structures of glacial hydrofractures and tuffisites may help to constrain the rheology of the gas-pyroclast mixture injected into tuffisites. Glacial hydrofractures contain large proportions of mud-sized particles (van der Meer et al., 2009) that will also have the ability to stick and aggregate during flow, as well as being difficult particles to re-entrain once deposition has taken place.

6.1.2.1   Hydrofracture formation time

The velocity of fluids injected into sedimentary hydrofractures and tuffisites will likely overlap, as calculated above. The large fluctuations in fluid overpressure possible within the volcanic conduit (Chapter 3) can readily produce high fluid velocities. In contrast, the creation of similarly large overpressures in sedimentary systems by fluid migration, rapid loading, or thermal pressurisation is more of a challenge (Hurst et al., 2011). The great dimensions of some sand injectites, and large clasts that are transported within them, suggest that large overpressures and high fluid velocities can be involved in sand injectite formation. The trigger of sand injectite formation is poorly understood, though potential suggested trigger mechanisms include seismicity or rapid loading (Jonk, 2010), but the trigger mechanism for their formation is not well understood.

The internal structure of the hydrofracture is controlled by the fluid pressure fluctuations within the fracture during its formation (Chapter 3; Phillips et al., 2013). In a volcanic environment, the overpressure of the source will fluctuate through time during an eruption (Chapter 3), with the ability for fluid pressure fluctuations to inject multiple pulses of fluid into a fracture within a relatively short space of time (∼minutes to days). The evolution of the pressure source for hydrofracture formation in sedimentary environments is much less well understood, but the simple structures of sand injectites

suggest that many are emplaced by only a single fluid pulse (Hurst et al., 2011). The timescales of formation of sedimentary hydrofractures are not well constrained, but if sand injectites are emplaced by a single fluid pulse, these are likely to form in a shorter time than glacial hydrofractures emplaced by many pulses of injected fluid.

Fluid pressure fluctuations within fractures can be generated internally, within the fracture itself, as well as externally due to variations in the pressure source. Drops in pressure due to the propagation of the fracture tip during particle injection could produce variations in fluid velocity within the fracture itself and create complex sedimentary structures by eroding and redepositing material. The clogging of hydrofractures with particles can locally increase the fluid pressure along the fracture, leading to increased fluid velocities and erosion (Kern et al., 1959). These processes could perhaps produce the appearance of injected pulses of fluid within hydrofractures without requiring overall pressure fluctuations of the fluid source. Investigating the microstructures found close to the fracture tip of tuffisites and glacial hydrofractures would allow the importance of fracture propagation for the structures produced to be constrained. These structures could then be compared with structures interpreted as formed by externally driven pressure fluctuations generated by the source to consider the importance of these two mechanisms.

6.1.3 Hydrofractures as fluid flow pathways

Tuffisites and sedimentary hydrofractures can act as permeable pathways for fluid flow through the host material. This is of particular importance for sand injectites, which can bypass impermeable units leading to the loss of hydrocarbons from potential reservoirs (Hurst et al., 2003; Cartwright et al., 2007). Fluid inclusion and stable isotope data suggest that sand injectites can also act as long-term pathways for fluid flow (Hurst et al., 2003), as has been suggested for external tuffisites in volcanic systems. Unlike tuffisites, which will weld to a lower porosity and permeability within minutes to hours of being emplaced, sand injectites will remain permeable, though fluid flow may be limited by the formation of cements. Comparing the dimensions of tuffisites and sand injectites, and further constraining the final permeability of external tuffisites, may help to constrain how important tuffisites may be for long-term gas escape from the conduit zone, and provide insights into the loss of magmatic fluids from magmatic reservoirs.

6.1.4 Hydrofracture summary

Tuffisites display many similarities to hydrofractures of sedimentary systems and comparing their characteristics reveals the influence of temperature on their dynamics. These groups of hydrofractures each have different flow dynamics during their formation and constraining these may help to improve our understanding of the rheology of the gas-pyroclast mixture injected into tuffisites, the transport velocity of particles, and the mechanisms that create fluid pressure fluctuations within fractures during tuffisite evolution.

6.2 Vents

Direct observations of rhyolite eruptions (Volcán Chaitén 2008–2009, and Cordón Caulle 2011–2012) showed that during the transition from explosive to effusive activity, eruptions can be hybrid, with explosive and effusive activity occurring simultaneously from the same location (e.g. Pallister et al., 2013; Schipper et al., 2013; Castro et al., 2014). Inspired by these observations, a new model proposes that rhyolite eruptions are dominantly explosive, with lava 'built' by hot, viscous re-assembly from pyroclasts just beneath the Earth's surface (Wadsworth et al., 2020, 2022). This model expands on earlier work (Gonnermann and Manga, 2003) proposing that subsurface magma fragmentation does not necessarily lead to explosive volcanism at the surface, as clasts and tuffisites can heal and combine to form dense lava (Tuffen et al., 2003). The clastic assembly model (Wadsworth et al., 2020; Wadsworth et al., 2022) is consistent with the structure of the Mule Creek vent (Chapter 4) as well as clastic textures observed within vents elsewhere (Gardner et al., 2017; Schipper et al., 2021; Wadsworth et al., 2022). Here I further discuss the open questions about silicic vents mentioned in the literature review at the start of this thesis, exploring the processes that lead to the explosive-effusive transition and the closure of vents, the ability of tuffisites to act as pathways for gas escape, and potential sources of LP seismicity seen at silicic vents.

6.2.1 The trigger of the explosive-effusive transition

The transition from explosive to effusive activity begins with the start of lava assembly within the vent, before the onset of hybrid explosive-effusive activity seen at the surface (Chapter 4; Wadsworth et al., 2020, 2022). This must relate to the start of the accretion

and welding of captured pyroclasts at the conduit margins, assembling the vitrophyre and vitrophyre breccia units seen at the Mule Creek vent (Chapter 4) as well as later the rhyolite lava that fills the vent. Before welding begins, the majority of pyroclasts are explosively ejected from the vent, or deposited within the vent to form a pyroclastic breccia that can be eroded, redeposited and overturned (Chapter 4; Valentine and Cole 2021). A change in eruption dynamics then allows this material to begin to be accreted on to the conduit margins and weld (Gardner et al., 2017; Wadsworth et al., 2020, 2022). This change in conditions within the conduit allows a large fraction of pyroclasts to be captured and accumulated in the shallow subsurface, where they can reassemble to form lava (Farquharson et al., 2022).

The change in conditions that allows for the start of the capture and accumulation of pyroclasts on to conduit walls, and therefore the assembly of lava, is poorly constrained. This is likely to relate to the waning of flow within the conduit allowing for more particles to remain within the subsurface, or a reduction in the size of pyroclasts allowing for the easier capture of particles on to conduit walls (Chapter 4, Farquharson et al., 2022). The sub-vertical glassy contact within the pyroclastic breccia at Mule Creek is interpreted as an early attempt to start this process of particle capture and welding at the conduit margins (Chapter 4). This suggests that the conditions for the welding of pyroclasts at the conduit margins may be unstably achieved in different parts of the conduit at different times, with the transition from the deposition of pyroclastic breccia to accretion and welding to form vitrophyre able to locally occur multiple times. Only once the conduit has tipped to the correct conditions over a wider area can the accretion of the vitrophyre breccia and vitrophyre truly begin.

6.2.2   External tuffisites as outgassing pathways

The longest tuffisites seen adjacent to and within the Mule Creek vent begin within the vitrophyre breccia, with tuffisites seen to weave around clasts within the vitrophyre breccia before continuing outwards into the pyroclastic breccia and country rock beyond (Chapter 4; Stasiuk et al., 1996). The large size of the tuffisite at Húsafell central volcano (Chapter 3) suggests that this tuffisite may be an example of a large cross-conduit tuffisite that would have originated within the vitrophyre breccia of its host vent. The presence of obsidian clasts within the tuffisite at Húsafell indicate that there was a source of obsidian to be injected into the tuffisite at the time of its formation. During

191

the time of vitrophyre breccia emplacement, the repeated fracturing and quarrying of glassy material at the vent margins could have provided a source of these obsidian clasts (Chapter 4).

Before the accretion and welding of material at vent margins to produce the vitrophyre breccia and vitrophyre, lateral outgassing would be able to occur from the vent into the surrounding permeable pyroclastic breccia (Rust et al., 2004). The emplacement of the vitrophyre and vitrophyre breccia would have effectively sealed the conduit margins, preventing lateral outgassing (Chapter 4). This would increase the importance of tuffisite-enabled outgassing, with the formation of fractures now required to create permeable pathways for lateral gas escape. The timescales of LP events, suggested to be created by tuffisite formation, suggest that tuffisites could act as efficient outgassing pathways for only a short time (∼10–100 s; Chapter 5).

The gas flow through the tuffisite could be restricted by one of three regimes: source waning, particle clogging or entrance sealing. In the first regime, a decrease in the pressure of the source will lead to the closure of the fracture or deposition of clasts within the tuffisites, limiting the tuffisite lifetime and therefore the volume of gas that would be able to escape. In the second regime of particle clogging the timescale for tuffisite outgassing is controlled by how rapidly the fracture becomes clogged with particles, restricting fluid flow (Chapter 5). In this regime a high mass eruption rate would limit the rate of vitrophyre breccia or vitrophyre formation at the conduit margin by the pulsatory erosion of material and high velocities preventing the capture of pyroclasts on collision with the conduit walls. Alternatively, in the final regime of entrance sealing, if the conduit conditions are correct for a large fraction of pyroclasts to be captured and accreted on to the conduit walls, a large volume of accreted material could form rapidly. This rapid accretion could seal the entrance to the tuffisite, limiting the timescale for which outgassing could occur.

Internal tuffisites, those formed within magma, have been suggested to allow for fluid flow to occur until they become blocked by accreting pyroclasts that become captured by the fracture walls (Farquharson et al., 2022). In this second regime, the controls on the timescale of outgassing through both internal and external tuffisites would be the rate of particle accretion and the size of the fracture opening. The pulsed injection of material into external tuffisites (Chapter 3) could then be created by the repeated blocking and reopening of the tuffisite entrance. The fluid overpressure required for

tuffisite emplacement would then be controlled by the tensile strength of the accreting vitrophyre breccia blocking the tuffisite opening. It is likely that these regimes may dominate in different stages of the eruption, with the first fracture clogging regime occurring during more explosive activity, while the second regime of entrance sealing would require lower fluid velocities to allow for the efficient capture and accretion of particles at the conduit margins. Confirming which regime occurs during tuffisite formation would require analysis of the microstructures at the opening (source region) of a preserved tuffisite.

6.2.3   Formation of internal tuffisites

Tuffisites found within volcanic vents, hosted by the vent-filling magma, have been generally interpreted as shear fractures that open when the shear stresses acting on the magma exceed the magma strength. Shear failure is thought to nearly always begin with the formation of tensile fractures that then coalesce to form a shear fracture (Rutter, 1986; Lavallée et al., 2013). While the offset across fracture walls suggests some shear is occurring across the fracture (Tuffen and Dingwell, 2005), the source of particles for vein filling and tuffisite formation is less straightforward. Previously suggested potential particle sources include local abrasion at fracture walls (Tuffen et al., 2003; Tuffen and Dingwell, 2005), or fragmentation of nearby or underlying magma driven by fracture opening and resultant decompression (Lavallée et al., 2012; Saubin et al., 2016). These models struggle to explain the presence of complex structures within tuffisites that suggest emplacement by multiple pulses of injected material, as is evidenced by cross-cutting tuffisite units (Black et al., 2016). The proposal that lava has a clastic origin (Wadsworth et al., 2020, 2022) now allows reconsideration of the formation of internal tuffisites.

The wholesale fragmentation of magma, which can then accrete on to the vent walls at shallow depths to form lava, provides a source of magmatic fluid within the conduit that can drive tensile fluid-driven fracturing and transport clastic material (Wadsworth et al., 2022). This process allows for a single source of fragmented material, rather than requiring repeated fragmentation of volatile-rich or vesicular magma in the adjacent conduit interior (Tuffen et al., 2003) or residing at greater depths (Berlo et al., 2013; Saubin et al., 2016) to produce tuffisites. The similar morphology of internal and external tuffisites suggests similar formation mechanisms, with internal tuffisites injected

into effectively stationary vitrophyre or lava rather than forming during magma ascent (Chapter 4). Internal tuffisites are therefore interpreted as being formed by the tensile fracturing of the assembling body of lava in the shallow conduit by gas-pyroclast mixtures produced by continued fragmentation at depth. The formation of internal tuffisites would therefore involve the fracturing of the welding body of hot pyroclasts in the shallow subsurface. Pressurisation driving tensile failure may be driven by lava accretion restricting fluid flow or welding lowering the permeability of outgassing pathways through the pore spaces of the body of hot pyroclasts. Internal tuffisites could act as outgassing pathways, allowing for the transport of the gas-pyroclast mixture through the assembling lava (Wadsworth et al., 2022) and thus permitting localised volatile depletion around fracture walls (Tuffen et al., 2022). If the fracture reaches the surface, it could provide an opening for explosive venting at the surface, as seen during the 2011–2012 eruption of Cordón Caulle (Schipper et al.,, 2013; Heap et al., 2019; Schipper et al., 2021; Crozier et al., 2022; Farquharson et al., 2022; Wadsworth et al., 2022). Hot fine-grained pyroclasts (<63 μm in diameter), have been seen to become trapped on fracture walls during this turbulent upward transport (Farquharson et al., 2022). The timescales over which their surface-connected internal tuffisites can act as outgassing pathways will depend on how rapidly pyroclasts can accrete within these fractures to block fluid flow, which will be controlled by the impact velocity, viscosity, and size of pyroclasts.

There is the potential for a large number of external tuffisites to be formed at the margin of silicic vents, particularly if there are pre-existing fractures that can be exploited to allow for tuffisite formation at a lower fluid pressure than required to create a new fracture within the host rock (Chapter 3). The high density of fractures seen within the vitrophyre breccia at Mule Creek also suggests that external tuffisite formation is common (Chapter 4). Many internal tuffisites could potentially therefore also be external tuffisites that have been rotated after their formation during the extrusion of the plug. Close analysis of the textures at the margins of internal tuffisites may reveal their interaction with the surrounding lava and indicate whether this later rotation of tuffisites occurs. Useful details may include exploring how often tuffisites follow or intersect flow banding within the lava, and also whether there is a systematic change in tuffisite orientation closer to the plug margins where a greater degree of shearing and therefore rotation may take place than in the vent centre.

Recent investigation of silicic vent evolution and clastogenic processes in silicic conduits (e.g. Wadsworth et al., 2020, Schipper et al., 2021; Tuffen et al., 2022, Wadsworth et

al., 2022) is shedding new light on key processes. However, there remains ample scope to further characterise internal tuffisite textures to better constrain their formation and connectivity with silicic vents. Useful further steps could include investigating how extensive networks of tuffisites within lava might be and considering grain-size distributions and therefore the timescales of internal tuffisite formation. These timescales could then be compared to those estimated for internal tuffisites by diffusion (Berlo et al., 2013; Castro et al., 2014; Paisley et al., 2019a, b). Comparing the componentry of the fills of internal tuffisites with external tuffisites may also provide information about how the source of clastic material is changes through time before and after the explosive-effusive transition has taken place.

6.2.4 Outgassing and sources of LP seismicity at silicic vents

The source of long-period (LP) volcanic earthquakes is thought to be the resonance of gas-ash mixtures injected into fractures (Chouet and Julian, 1985; Chouet, 1996; Kumagai and Chouet, 1999). Internal tuffisites have therefore been suggested to be the 'fossil record' of LP events (Chapter 3; Tuffen et al., 2003; Molina et al., 2004; Tuffen and Dingwell, 2005), and the newly refined model for internal tuffisite formation, to include a phase of wholesale magma fragmentation, may provide new perspectives on source mechanisms. In Chapter 3, external tuffisites are also highlighted as potential LP sources.

Networks of internal tuffisites previously documented at vent and conduit margins were only traceable over <5 metres, due to limited exposure and preservation (Stasiuk et al., 1996; Tuffen et al., 2003; Goto et al., 2008). In contrast, modelled LP source fractures are much greater in dimension (lengths and breadths of tens to hundreds of metres; Molina et al., 2004; Torres et al., 2021) than tuffisites seen. However, volatile concentration heterogeneities in tuffisite fills (Berlo et al., 2013; Saubin et al., 2016) indicate that these fractures do have a far greater vertical connectivity, over tens to over a hundred metres. Wholesale fragmentation would allow for the easy delivery of pyroclasts from depth into fractures within the lava, without requiring localised fragmentation, as well as provide sufficient ash-pyroclast mixtures for fractures to become pervasive within the assembling magma body. This process could create fractures of the size modelled as the source of LP events within an interconnected fracture network. The timescales of LP events ($\sim$10–100 s; Chapter 5), or the period that these fractures could act as

outgassing pathways, would be controlled by the rate that fluid flow within the fracture could be blocked by accretion. These timescales also match the timescales of pulsed venting through fractures within lava seen at Cordón Caulle (Chapter 5; Schipper et al., 2013, Heap et al., 2019; Schipper et al., 2021, Crozier et al., 2022), and agree with short diffusion times of trace metals within lava- and bomb-hosted internal tuffisites (Berlo et al., 2013; Paisley et al., 2019). This evidence all integrates to support the thesis that internal tuffisite are a viable LP event source.

Formation of either internal or external tuffisites may trigger LP events, and different LP swarms may represent either of these processes. To determine which source process applies to a specific LP swarm improved constraints are required on the locations of events with respect to the conduit walls, and a greater understanding of the timescales of internal and external tuffisite formation.

6.2.5 Extending the clastic origin of magma

The recognition of clastic origin of lava has transformed our understanding of the processes occurring during silicic eruptions (Wadsworth et al., 2020, 2022). Conduit models indicate that magma may be fragmented above >2 km depth (Wadsworth et al., 2020), suggesting that textures of intrusions emplaced at greater depths may also preserve their previously overlooked clastic origin. Further characterisation of intrusion margins may capture a gradient of welding at their very edge, with textures becoming more welded away from the intrusion margin. Considering the controls on whether the injected clastic material welds to produce a magmatic dyke or sill, or remains preserved as a clastic dyke or sill, would allow us to better understand the temperature evolution of these features and frequency of injections of material.

Narrow veins of silicic material (thickness of a few centimetres) seen within and around intrusions were originally thought to have a clastic origin in some of the first literature on tuffisites (Dunham, 1967), though no mechanism for the assembly of coherent magma from pyroclasts was known. The high viscosity of silicic magma would make it very difficult to inject into narrow veins (Gudmundsson, 1983), while clastic material can easily form veins a few millimetres in thickness. There are likely to be many more features that are better explained by magma having a clastic origin, and further work is needed to constrain what the characteristics of these injected gas-pyroclast mixtures might be, and the conditions that are required for hot pyroclasts to reassemble and gain

196

coherence.

6.3   Summary and further work

Tuffisites and hydrofractures in sedimentary systems have many similarities, such as similar morphologies, and the potential for complex internal structures that suggest formation by multiple fluid pulses. These hydrofractures from different environments can also be quite different, with structures such as wall-perpendicular laminations commonly seen in sand injectites (Hurst et al., 2011) but not currently recognised in tuffisites, perhaps due to differences in the particle concentration of the injected fluid. Further characterising the similarities and differences between the hydrofractures formed in these different systems could help us to learn about the rheology of the fluids injected and how this controls the resultant sedimentary structures. With the recognition that silicic magma is assembled from the welding of hot pyroclasts, understanding the rheology of gas-pyroclast mixtures, and how these move in the shallow subsurface, will be key for improving the modelling of eruption dynamics and hazard prediction. External tuffisites appear to allow for the escape of large volumes of gas from the conduit zone in short-lived pulses. These ideas need to now be applied to internal tuffisites, to consider how these features form, and their relationship to LP seismic events seen in silicic systems. This would help constrain the processes occurring within the conduit during the explosive-effusive transition and understand what triggers the onset of hybrid activity.

7 Conclusions

This thesis aimed explore the formation of tuffisites to constrain whether tuffisite-enabled outgassing might be significant on the timescale of an eruption. By extrapolating this knowledge of tuffisite formation to the evolution of silicic vents, this worked then aimed to use tuffisites to gain insights into the processes that control eruption dynamics. Here I briefly outline the key findings:

- Tuffisite formation requires an overpressure of a few megapascals, similar to that found just above the level of fragmentation in the conduit. This suggests that tuffisites should be common features.

- Tuffisites can form by multiple pulses of injected fluid, allowing tuffisites to be interpreted as a record of fluid pressure fluctuations within the volcanic conduit through time.

- Tuffisites form by similar processes to silicic volcanic vents, allowing them to be used to gain insights into the processes controlling vent evolution and the style of the associated eruption through time.

- Tuffisites are found in every unit of volcanic vents, indicating that there is a continued source of pyroclastic material after the explosive-effusive transition takes place. This suggests that there is continued fragmentation at depth, allowing for the assembly of lava from the capture and welding of pyroclasts in the shallow vent.

- Large volumes of gas can escape through tuffisites during fracture opening, until the fracture becomes clogged with pyroclasts. This pulsed outgassing may be significant compared to the vertical flux of gas during the explosive phase of an eruption, perhaps able to moderate eruption style.

8 References

Adams, N. K., Houghton, B. F., Fagents, S. A., Hildreth, W. (2006). The transition from explosive to effusive eruptive regime: The example of the 1912 Novarupta eruption, Alaska. GSA Bulletin 118(5–6):620–634. https://doi.org/10.1130/B25768.1

Ágústsdóttir, T., Woods, J., Greenfield, T., Green, R. G., White, R. S., Winder, T., Brandsdóttir, B., Steinthórsson, S., Soosalu, H. (2016). Strike-slip faulting during the 2014 Bárðarbunga-Holuhraun dike intrusion, central Iceland. Geophys. Res. Lett. 43(4):1495–1503. https://doi.org/10.1002/2015GL067423

Ágústsdóttir, T., Gudmundsson, M., Einarsson, P. (2011). A gravity study of silicic domes in the Krafla area, N-Iceland. Jokull 60:135–148.

Al-Harthi, A. A., Al-Amri, R. M., and Shehata, W. M. (1999). The porosity and engineering properties of vesicular basalt in Saudi Arabia. Eng. Geol. 54(3-4):313–320. https://doi.org/10.1016/S0013-7952(99)00050-2

Allen, J. R. L. (1982). Sedimentary Structures: Their Character and Physical Basis, Vol. 2. Amsterdam: Elsevier.

Arciniega-Ceballos, A., Dawson, P., Chouet, B. A. (2012). Long period seismic source characterization at Popocatépetl volcano, Mexico. Geophys. Res. Lett. 39(20). https://doi.org/10.1029/2012GL053494

Bagdassarov, N., Dingwell, D. B. (1994). Thermal properties of vesicular rhyolite. Journal of Volcanology and Geothermal Research 60:179–191. https://doi.org/10.1016/0377-0273(94)90067-1

Bazargan. M., Gudmundsson, A. (2019) Dike-induced stresses and displacements in layered volcanic zones. Journal of Volcanology and Geothermal Research 384:189–205. https://doi.org/10.1016/j.jvolgeores.2019.07.010

Bear, J. (1972). Dynamics of fluids in porous media. Elsevier, New York

Bélanger, C., Ross, P. S. (2018). Origin of nonbedded pyroclastic rocks in the Cathedral Cliff diatreme, Navajo volcanic field, New Mexico. Bull. Volcanol. 80(61). https://doi.org/10.1007/s00445-018-1234-0

Bell, A. F., Hernandez, S., Gaunt, H. E., Mothes, P., Ruiz, M., Sierra, D., Aguaiza, S. (2017). The rise and fall of periodic 'drumbeat' seismicity at Tungurahua volcano, Ecuador. Earth Planet Sci. Lett. 475:58–70. https://doi.org/10.1016/J.EPSL.2017.07.030

Bell, A. F., Naylor, M., Hernandez, S., Main, I. G., Gaunt, H. E., Mothes, P., Ruiz, M. (2018). Volcanic Eruption Forecasts From Accelerating Rates of Drumbeat Long-Period Earthquakes. Geophys. Res. Lett. 45(3):1339–1348. https://doi.org/10.1002/2017GL076429

Benson, P. M., Heap, M. J., Lavallée, Y., Flaws, A., Hess, K.-U., Selvadurai, A. P. S., Dingwell, D. B., Schillinger, B. (2012). Laboratory simulations of tensile fracture development in a volcanic conduit via cyclic magma pressurisation. Earth Planet. Sci. Lett. 349–350:231–239. https://doi.org/10.1016/j.epsl.2012.07.003

Berlo, K., Tuffen, H., Smith, V., Castro, J. M., Pyle, D. M., Mather, T. A., et al. (2013). Element variations in rhyolitic magma resulting from gas transport. Geochim. Cosmochim. Acta 121:436–451. https://doi.org/10.1016/J.GCA.2013. 07.032

Black, B. A., Manga, M., Andrews, B. (2016). Ash production and dispersal from sustained low-intensity Mono-Inyo eruptions. Bull. Volcanol. 78(57). https://doi.org/10.1007/s00445-016-1053-0

Blundy, J., Cashman, K., Rust, A. (2008). Gas Loss and Resorption beneath Mount St. Helens, 1980-1986. American Geophysical Union, Fall Meeting 2008

Boehm, A., and Moore, J. C. (2002). Fluidized sandstone intrusions as an indicator of Paleostress orientation, Santa Cruz, California. Geofluids 2:147–161. https://doi.org/10.1046/j.1468-8123.2002.00026.x

Bonadonna, C., Pistolesi, M., Cioni, R., Degruyter, W., Elissondo, M., Baumann, V. (2015) Dynamics of wind-affected volcanic plumes: The example of the 2011 Cordón Caulle eruption, Chile. J. Geophys. Res. Solid Earth 120(4):2242–2261. https://doi.org/10.1002/2014JB011478

Branney, M. J., and Kokelaar, P. (2002). Chapter 4: conceptualizing deposition: a flow-boundary zone approach. Pyroclastic density currents and the sedimentation of ignimbrite. https://doi.org/10.1144/GSL.MEM.2003.027.01.04

Butcher, S., Bell, A. F., Hernandez, S., Calder, E., Ruiz, M., Mothes, P. (2020). Drumbeat LP "Aftershocks" to a Failed Explosive Eruption at Tungurahua Volcano, Ecuador. Geophys. Res. Lett. 47(16) https://doi.org/10.1029/2020GL088301

Cabrera, A., Weinberg, R. F., Wright, H. M. N., Zlotnik S., Cas, R. A. F. (2011). Melt fracturing and healing: A mechanism for degassing and origin of silicic obsidian. Geology 39(1):67–70. https://doi.org/10.1130/G31355.1

Cabrera, A., Weinberg, R. F., Wright, H. M. N. (2015). Magma fracturing and degassing associated with obsidian formation: The explosive–effusive transition. Journal of Volcanology and Geothermal Research 298:71–84. https://doi.org/10.1016/J.JVOLGEORES.2014.12.014

Campbell, M. E., Russell, J. K., Porritt, L. A. (2013). Thermomechanical milling of accessory lithics in volcanic conduits. Earth Planet Sci. Lett. 377–378:276–286. https://doi.org/10.1016/J.EPSL.2013.07.008

Cartwright, J., Huuse, M., Aplin, A. (2007). Seal bypass systems. Am. Assoc. Pet. Geol. Bull. 91:1141–1166. https://doi.org/10.1306/04090705181

Cartwright, J., James, D., Huuse, M., Vetel, W., Hurst, A. (2008). The geometry and emplacement of conical sandstone intrusions. J. Struct. Geol. 30(7):854–867. https://doi.org/10.1016/J.JSG.2008.03.012

Cassidy, M., Cole, P. D., Hicks, K. E., Varley, N. R., Peters, N., Lerner, A. H. (2015). Rapid and slow: Varying magma ascent rates as a mechanism for Vulcanian explosions. Earth and Planet. Sci. Lett. 420:73-84. https://doi.org/10.1016/j.epsl.2015.03.025

Cassidy, M., Manga, M., Cashman, K., Bachmann, O. (2018). Controls on explosive-effusive volcanic eruption styles. Nat. Commun. 9(2839). https://doi.org/10.1038/s41467-018-05293-3

Castro, J. M., Dingwell, D. B. (2009). Rapid ascent of rhyolitic magma at Chaitén volcano, Chile. Nature 461:780–783. https://doi.org/10.1038/nature08458

Castro, J. M., Cordonnier, B., Tuffen, H., Tobin, M. J., Puskar, L., Martin, M. C., Bechtel, H. A. (2012). The role of melt-fracture degassing in defusing explosive rhyolite eruptions at volcán Chaitén. Earth Planet. Sci. Lett. 333–334:63–69. https://doi.org/10.1016/j.epsl.2012.04.024

Castro, J. M., Schipper, C. I., Mueller, S. P., Militzer, A. S., Amigo, A., Silva Parejas, C., Jacob, D. (2013). Storage and eruption of near-liquidus rhyolite magma at Cordón Caulle, Chile. Bull. Volcanol. 75(702). https://doi.org/10.1007/s00445-013-0702-9

Castro, J. M., Bindeman, I., Tuffen, H., and Schipper, C. I. (2014). Explosive origin of silicic lava: textural and –H2O evidence for pyroclastic degassing during rhyolite effusion. Earth Planet. Sci. Lett. 405:52–61. https://doi.org/10.1016/j.epsl.2014.08.012

Castro, J. M., Cordonnier, B., Schipper, C. I., Tuffen, H., Baumann, T. S., and Feisel, Y. (2016). Rapid laccolith intrusion driven by explosive volcanic eruption. Nat. Commun. 7:13585. https://doi.org/10.1038/ncomms13585

Cataldo, E., Davies, A. G., Wilson, L. (2013). Near-vertical supersonic and shock-free gas/magma flow at ionian volcanoes: Application to Pillan. Icarus 226:1171–1176. https://doi.org/10.1016/j.icarus.2013.06.035

Chen, Y., Nagaya, Y., Ishida, T. (2015). Observations of Fractures Induced by Hydraulic Fracturing in Anisotropic Granite. Rock Mech. Rock. Eng. 48:1455– 1461. https://doi.org/10.1007/s00603-015-0727-9

Chouet, B., Julian, B. R. (1985). Dynamics of an expanding fluid-filled crack. J. Geophys. Res. 90:11187. https://doi.org/10.1029/JB090iB13p11187

Chouet, B. A. (1996). Long-period volcano seismicity: its source and use in eruption forecasting. Nature 380, 309–316. https://doi.org/10.1038/380309a0

Chouet, B. A., and Matoza, R. S. (2013). A multi-decadal view of seismic methods for detecting precursors of magma movement and eruption. J. Volcanol. Geoth. Res. 252:108–175. https://doi.org/10.1016/J.JVOLGEORES.2012.11.013

Christiansen, E. A., Gendzwill, D. J., Meneley, W. A. (1982). Howe lake: a hydrodynamic blowout structure. Can. J. Earth. Sci. 19:1122–1139. https://doi.org/10.1139/e82-097

Cipolla, C. L., Warpinski, N. R., Mayerhofer, M. J. (2008). Hydraulic Fracture Complexity: Diagnosis, Remediation, and Exploitation. In SPE Asia Pacific Oil and Gas Conference and Exhibition. OnePetro. https://doi.org/10.2118/115771-MS

Cloos, H. (1941). Bau unt taetigkeit von tuffschloten; Untersuchungen an dem schwaebischen vulkan. Geol. Rundsch. 709–800. https://doi.org/10.1007/BF01801913

Cobain, S. L., Peakall, J., and Hodgson, D. M. (2015). Indicators of Propagation Direction and Relative Depth in Clastic Injectites: Implications for Laminar Versus Turbulent Flow Processes. Boulder, CO: Geological Society of America. https://doi.org/10.1130/B31209.1

Colombier, M., Burgisser, A., Cáceres, F., Druitt, T., Gurioli, L., Hess, K.-U., Boivin, P., Miallier, D., Dingwell, D. B. (2020). Rheological change and degassing during a trachytic Vulcanian eruption at Kilian volcano, Chaîne des Puys, France. Bull. Volcanol. 82(78). https://doi.org/10.1007/s00445-020-01420-5

Connor, C. B., Lichtner, P. C., Conway, F. M., Hill, B E., Ovsyannikov, A. A., Federchenko, I., Doubik, Y., Shapar, V. N., Taran, Y, A. (1997). Cooling of an igneous dike 20 yr after intrusion. Geology 25(8):711-714. https://doi.org/10.1130/0091-7613(1997)025<0711:COAIDY>2.3.CO;2

Cosgrove, J. W. (2001). Hydraulic fracturing during the formation and deformation of a basin: A factor in the dewatering of low-permeability sediments. AAPG Bull.

85(4):737–748. https://doi.org/10.1306/8626C997-173B-11D7-8645000102C1865D

Crozier, J., Tramontano, S., Forte, P., Oliva, S. J. C., Gonnermann, H. M., Lev, E., Manga, M., Myers, M., Rader, E., Ruprecht, P., Tuffen, H., Paisley, R., Houghton, B. F., Shea, T., Schipper, C. I., Castro, J. M. (2022). Outgassing through magmatic fractures enables effusive eruption of silicic magma. Journal of Volcanology and Geothermal Research 430(107617). https://doi.org/10.1016/j.jvolgeores.2022.107617

Cruz, F. G., Chouet, B. A. (1997). Long-period events, the most characteristic seismicity accompanying the emplacement and extrusion of a lava dome in Galeras Volcano, Colombia, in 1991. Journal of Volcanology and Geothermal Research 77:121–158. https://doi.org/10.1016/S0377- 0273(96)00091-1

Degruyter, W., Bachmann, O., Burgisser, A., Manga, M. (2012). The effects of outgassing on the transition between effusive and explosive silicic eruptions. Earth Planet. Sci. Lett. 349–350:161–170. https://doi.org/10.1016/j.epsl.2012.06.056

Degruyter, W., Bonadonna, C. (2012). Improving on mass flow rate estimates of volcanic eruptions. Geophys. Res. Lett. 39(16). https://doi.org/10.1029/2012GL052566

Deshpande, G. G., Peshwa, V. V., Ghate, N. S. (1971). An unusual mineral assemblage in tuffisite veins at Pimpal-Wandi, District Poona, Maharashtra. Curr Sci 40(4):87-88

Dewan, J. T., Chenevert, M. E. (2001). A model for filtration of water-base mud during drilling: Determination of mudcake parameters. Petrophysics 42:237–250.
Dionne, J.-C., Shilts, W. W. (1974). A Pleistocene Clastic Dike, Upper Chaudière Valley, Québec. Can. J. Earth Sci. 11:1594–1605. https://doi.org/10.1139/e74-158

Dingwell, D. B., Webb, S. L. (1990). Relaxation in silicate melts. European Journal of Mineralogy, 4:427-449.

Dixon, R. J., Schofield, K., Anderton, R., Reynolds, A. D., Alexander, R. W. S., Williams, M. C., Davies, K. G. (1995). Sandstone diapirism and clastic intrusion in the Tertiary submarine fans of the Bruce-Beryl Embayment, Quadrant 9, UKCS. Geological Society, London, Special Publications 94:77–94. https://doi.org/10.1144/GSL.SP.1995.094.01.07

Dunham, A. C. (1967). The felsites, granophyre, explosion breccias and tuffisites of the north-eastern margin of the Tertiary igneous complex of Rhum, Inverness-shire. Quarterly Journal of the Geological Society 123:327–350. https://doi.org/10.1144/gsjgs.123.1.0327

Duranti, D., Hurst, A. (2004). Fluidization and injection in the deep-water sandstones of the Eocene Alba Formation (UK North Sea). Sedimentology 51, 503–529. https://doi.org/10.1111/j.1365-3091.2004.00634.x

Eibl, E. P. S., Bean, C. J., Vogfjörd, K. S., Ying, Y., Lokmer, I., Möllhoff, M., O'Brien, G. S., Pálsson (2017). Tremor-rich shallow dyke formation followed by silent magma flow at Bárðarbunga in Iceland. Nat. Geosci. 10:299–304. https://doi.org/10.1038/ngeo2906

Eichelberger, J. C., Carrigan, C. R., Westrich, H. R., and Price, R. H. (1986). Non-explosive silicic volcanism. Nature 323:598–602. https://doi.org/10.1038/ 323598a0

Farquharson, J., Heap, M. J., Varley, N. R., Baud, P., and Reuschlé, T. (2015). Permeability and porosity relationships of edifice-forming andesites: a combined field and laboratory study. J. Volcanol. Geoth. Res. 297:52–68.

https://doi.org/10.1016/j.jvolgeores.2015.03.016

Farquharson, J. I., Heap, M. J., Lavallée, Y., Varley, N. R., Baud, P. (2016). Evidence for the development of permeability anisotropy in lava domes and volcanic conduits. Journal of Volcanology and Geothermal Research 323:163–185. https://doi.org/10.1016/j.jvolgeores.2016.05.007

Farquharson, J. I., Wadsworth, F. B., Heap, M. J., and Baud, P. (2017). Time-dependent permeability evolution in compacting volcanic fracture systems and implications for gas overpressure. J. Volcanol. Geoth. Res. 339:81–97. https://doi.org/10.1016/J.JVOLGEORES.2017.04.025

Farquharson, J. I., Wadsworth, F. B. (2018). Upscaling permeability in anisotropic volcanic systems. Journal of Volcanology and Geothermal Research 364:35–47. https://doi.org/10.1016/J.JVOLGEORES.2018.09.002

Farquharson, J., Tuffen, H., Wadsworth, F. B., Castro, J. M., Unwin, H. E., Schipper, C. I. (2022). In-conduit capture of sub-micron volcanic ash particles via turbophoresis and sintering. Nat. Commun. 13(1):4713 https://doi.org/10.21203/rs.3.rs-1152244/v1

Feng, S., Halperin, B. I., Sen, P. N. (1987). Transport properties of continuum systems near the percolation threshold. Phys. Rev. B. 35(197). https://doi.org/10.1103/PhysRevB.35.197

Ferguson, C., Klotz, J. A. (1954). Filtration from mud during drilling. J. Petrol. Technol. 6, 30–43. https://doi.org/10.2118/289-g

Fierstein, J., Hildreth, W. (1992). The Plinian eruptions of 1912 at Novarupta, Katmai National Park, Alaska. Bull. Volcanol. 54:646–684. https://doi.org/10.1007/BF00430778

Fisher, R. V., Schmincke, H. U., Van Bogaard, P. (1983). Origin and emplacement of a pyroclastic flow and surge unit at Laacher See, Germany. J. Volcanol. Geoth. Res. 17:375–392. https://doi.org/10.1016/0377-0273(83)90077-X

Forchheimer, P. (1901). Wasserbewegung durch boden. Z. Ver. Dtsch. Ing., 45(50):1781–1788.

Fowler, A. C., Scheu, B. (2016). A theoretical explanation of grain size distributions in explosive rock fragmentation. Proceedings of the Royal Society A: Mathematical, Physical and Engineering Sciences 472(2190). https://doi.org/10.1098/RSPA.2015.0843

Francis, W., Peters, M. C. (1980). The Flow of Fluids. Fuels and Fuel Technology: a summarized manual. 559–569. https://doi.org/10.1016/B978-0-08-025249-0.50101-4

Furukawa, K., Uno, K., Horiuchi, Y., Murohashi, S., Tsuboi, M. (2021). Conduit system, degassing, and flow dynamics of a rhyolite lava: A case study of the Shiroyama lava on Himeshima Island, Japan. Volcanica 4(2):107–134. https://doi.org/10.30909/VOL.04.02.107134

Gardner, J. E., Ketcham, R. A. (2011). Bubble nucleation in rhyolite and dacite melts: Temperature dependence of surface tension. Contributions to Mineralogy and Petrology 162:929–943. https://doi.org/10.1007/s00410-011-0632-5.

Gardner, J. E., Llewellin, E. W., Watkins, J. M., Befus, K. S. (2017). Formation of obsidian pyroclasts by sintering of ash particles in the volcanic conduit. Earth Planet Sci. Lett. 459:252–263. https://doi.org/10.1016/j.epsl.2016.11.037

Gardner, J. E., Wadsworth, F. B., Llewellin, E. W., Watkins, J. M., Coumans, J. P.

(2018). Experimental sintering of ash at conduit conditions and implications for the longevity of tuffisites. Bull. Volcanol. 80(23). https://doi.org/10.1007/s00445-018-1202-8

Gardner, J. E., Wadsworth, F. B., Llewellin, E. W., Watkins, J. M., Coumans, J. P. (2019). Experimental constraints on the textures and origin of obsidian pyroclasts. Bull. Volcanol. 81(22). https://doi.org/10.1007/s00445-019-1283-z

Garfunkel, Z., Katz, A. (1967). New Magmatic Features in Makhtesh Ramon, Southern Israel. Geol. Mag. 104:608–629. https://doi.org/10.1017/S0016756800050275

Gaunt, E. H., Sammonds, P. R., Meredith, P. G., Smith, R., Pallister, J. S. (2014). Pathways for degassing during the lava dome eruption of Mount St. Helens 2004-2008. Geology 42(11):947–950. https://doi.org/10.1130/G35940.1

Geshi, N., Kusumoto, S., Gudmundsson, A. (2012). Effects of mechanical layering of host rocks on dike growth and arrest. J. Volcanol. Geoth. Res. 223–224:74–82. https://doi.org/10.1016/J.JVOLGEORES.2012.02.004

Giachetti, T., Trafton, K. R., Wiejaczka, J., Gardner, J. E., Watkins, J. M., Shea, T., Wright, H. M. N. (2021). The products of primary magma fragmentation finally revealed by pumice agglomerates. Geology 49(11):1307–1311. https://doi.org/10.1130/G48902.1

Gonnermann, H. M., Manga, M. (2003). Explosive volcanism may not be an inevitable consequence of magma fragmentation. Nature 426:432–435. https://doi.org/10.1038/nature02138

Gonnermann, H. M., Houghton, B. F. (2012). Magma degassing during the Plinian eruption of Novarupta, Alaska, 1912. Geochemistry, Geophysics, Geosystems 13(10). https://doi.org/10.1029/2012GC004273

Goto, A. (1999). A new model for volcanic earthquake at Unzen Volcano: Melt Rupture Model. Geophys. Res. Lett. 26:2541–2544. https://doi.org/10.1029/1999GL900569

Goto, Y., Nakada, S., Kurokawa, M., Shimano, T., Sugimoto, T., Sakuma, S., Hoshizumi, H., Yoshimoto, M., Uto, K. (2008). Character and origin of lithofacies in the conduit of Unzen volcano, Japan. Journal of Volcanology and Geothermal Research 175(1–2):45–59. https://doi.org/10.1016/J.JVOLGEORES.2008.03.041

Green, D. N., Neuberg, J. (2006). Waveform classification of volcanic low frequency earthquake swarms and its implication at Soufrière Hills Volcano, Montserrat. Journal of Volcanology and Geothermal Research. 153:51–63. https://doi.org/10.1016/j.jvolgeores.2005.08.003

Gudmundsson, A. (1983). Stress estimates from the length/width ratios of fractures. J. Struct. Geol. 5, 623–626. https://doi.org/10.1016/0191-8141(83)90075-5

Gudmundsson, A. (2011). Deflection of dykes into sills at discontinuities and magma-chamber formation. Tectonophysics 500:50–64. https://doi.org/10.1016/J.TECTO.2009.10.015

Heap, M. J., Kushnir, A. R. L., Gilg, H. A., Wadsworth, F. B., Reuschlé, T., Baud, P. (2017). Microstructural and petrophysical properties of the Permo-Triassic sandstones (Buntsandstein) from the Soultz-sous-Forêts geothermal site (France). Geothermal Energy 5:1–37. https://doi.org/10.1186/s40517-017-0085-9

Heap, M. J., Tuffen, H., Wadsworth, F. B., Reuschlé, T., Castro, J. M., Schipper, C. I. (2019). The permeability evolution of tuffisites and implications for outgassing

through dense rhyolitic magma. J. Geophys. Res. Solid Earth 124:8281–8299. https://doi.org/10.1029/2018JB017035

Heap, M. J., Villeneuve, M., Albino, F., Farquharson, J. I., Brothelande, E., Amelung, F., Got. J.-L. (2020). Towards more realistic values of elastic moduli for volcano modelling. J. Volcanol. Geoth. Res. 390:106684. https://doi.org/10.1016/j.jvolgeores.2019.106684

Heap, M. J., Wadsworth, F. B., Heng, Z., Xu, T., Griffiths, L., Aguilar Velasco, A., Vairé, E., Vistour, M., Reuschlé, T., Troll, V. R., Deegan, F. M., Tang, C. (2021). The tensile strength of volcanic rocks: Experiments and models. J. Volcanol. Geoth. Res. 418:107348. https://doi.org/10.1016/j.jvolgeores.2021.107348

Heiken, G., Wohletz, K., Eichelberger, J. (1988). Fracture fillings and intrusive pyroclasts, Inyo Domes, California. J. Geophys. Res. Solid Earth 93, 4335–4350. https://doi.org/10.1029/JB093iB05p04335

Hess, K.-U., Dingwell, D. B. (1996). Viscosities of hydrous leucogranitic melts: A non-Arrhenian model. American Mineralogist 81:1297–1300. https://doi.org/10.2138/AM-1996-9-1031

Holland, A. S. P., Watson, I. M., Phillips, J. C., Caricchi, L., Dalton, M. P. (2011). Degassing processes during lava dome growth: Insights from Santiaguito lava dome, Guatemala. Journal of Volcanology and Geothermal Research 202:153–166. https://doi.org/10.1016/J.JVOLGEORES.2011.02.004

Hubbert, M. K., Willis, D. G. (1957). Mechanics of hydraulic fracturing. Transact. AIME 210:153–168. https://doi.org/10.2118/686-G

Hughes, C. J. (1971). Anatomy of a granophyre intrusion. Lithos 4:403–415. https://doi.org/10.1016/0024-4937(71)90123-X

Hurst, A., Cartwright, J., Huuse, M., Jonk, R., Schwab, A., Duranti, D., Cronin, B. (2003). Significance of large-scale sand injectites as long-term fluid conduits: evidence from seismic data. Geofluids 3:263–274. https://doi.org/10.1046/j.1468-8123.2003.00066.x

Hurst, A., Scott, A., Vigorito, M. (2011). Physical characteristics of sand injectites. Earth Sci. Rev. 106:215–246. https://doi.org/10.1016/J.EARSCIREV.2011.02.004

Isgett, S. J., Houghton, B. F., Fagents, S. A., Biass, S., Burgisser, A., and Arbaret, L. (2017). Eruptive and shallow conduit dynamics during Vulcanian explosions: insights from the Episode IV block field of the 1912 eruption of Novarupta, Alaska. Bull. Volcanol. 79:1138. https://doi.org/10.1007/s00445-017-1138-4

Iverson, R. M. (2008). Dynamics of seismogenic volcanic extrusion resisted by a solid surface plug, Mount St. Helens, 2004-2005. A Volcano Rekindled: The Renewed Eruption of Mount St. Helens 1750:425–460. https://doi.org/10.3133/PP175021

Jaupart, C., Allegre, C. J. (1991). Gas content, eruption rate and instabilities of eruption regime in silicic volcanoes. Earth Planet Sci. Lett. 102:413–429. https://doi.org/10.1016/0012-821X(91)90032-D

Jaupart, C. (1998). Gas loss from magmas through conduit walls during eruption. Geol. Soc. Spec. Public. 145:73–90. https://doi.org/10.1144/GSL.SP.1996.145.01.05

Jolly, R. J. H., Lonergan, L. (2002). Mechanisms and controls on the formation of sand intrusions. J. Geol. Soc. 159:605–617. https://doi.org/10.1144/0016-764902-025

Johnson, J. B., Lees, J. M., Gerst, A., Sahagian, D., Varley, N. (2008). Long-period

earthquakes and co-eruptive dome inflation seen with particle image velocimetry. Nature 456:377–381. https://doi.org/10.1038/nature07429

Jonk, R. (2010). Sand-rich injectites in the context of short-lived and long-lived fluid flow. Basin Res. 22:603–621. https://doi.org/10.1111/j.1365-2117.2010.00471.x

Kane, I. A. (2010). Development and flow structures of sand injectites: The Hind Sandstone Member injectite complex, Carboniferous, UK. Mar. Pet. Geol. 27:1200–1215. https://doi.org/10.1016/J.MARPETGEO.2010.02.009

Kano, K., Matsuura, H., Yamauchi, S. (1997). Miocene rhyolitic welded tuff infilling a funnel-shaped eruption conduit Shiotani, southeast of Matsue, SW Japan. Bulletin of Volcanology 59:125–135. https://doi.org/10.1007/S004450050180

Kavanagh, J. L., Rogers, B. D., Boutelier, D., Cruden, A. R. (2017). Controls on sill and dyke-sill hybrid geometry and propagation in the crust: The role of fracture toughness. Tectonophysics 698:109–120. https://doi.org/10.1016/j.tecto.2016.12.027

Kendrick, J. E., Lavallée, Y., Varley, N. R., Wadsworth, F. B., Lamb, O. D., and Vasseur, J. (2016). Blowing off steam: tuffisite formation as a regulator for lava dome eruptions. Front. Earth Sci. 4:41. https://doi.org/10.3389/feart.2016.00041

Kern, L. R., Perkins, T. K., Wyant, R. E. (1959). The mechanics of sand movement in fracturing. J. Petrol. Technol. 11:55–57. https://doi.org/10.2118/1108-G

Kern, L. R., Perkins, A. T. K., Member, J., Wyant, A. R. E. (1961). Propping Fractures with Aluminum Particles. Journal of Petroleum Technology 13:583–589. https://doi.org/10.2118/1573-G-PA

Kim, C. M., Han, R., Kim, J. S., Sohn, Y. K., Jeong, J. O., Jeong, G. Y., Yi, K., Kim, J. C. (2019). Fault zone processes during caldera collapse: Jangsan Caldera, Korea. J. Struct. Geol. 124:197-210. https://doi.org/10.1016/j.jsg.2019.05.002

Klinkenberg, L. J. (1941). The permeability of porous media to liquids and gases. In: Drilling and Production Practice. 200–213.

Kolzenburg, S., Heap, M. J., Lavallée, Y., Russell, J. K., Meredith, P. G., Dingwell, D. B. (2012). The strength and permeability of tuffisite-bearing andesite in volcanic conduits. Solid Earth Discussions 4:459–473. https://doi.org/10.5194/sed-4-459-2012

Kolzenburg, S., Russell, J. K. (2014). Welding of pyroclastic conduit infill: A mechanism for cyclical explosive eruptions. J. Geophys. Res. Solid Earth 119:5305–5323. https://doi.org/10.1002/2013JB010931

Kolzenburg, S., Ryan, A. G., and Russell, J. K. (2019). Permeability evolution during non-isothermal compaction in volcanic conduits and tuffisite veins: implications for pressure monitoring of volcanic edifices. Earth Planet. Sci. Lett. 527:115783. https://doi.org/10.1016/j.epsl.2019.115783

Kueppers, U., Perugini, D., Dingwell, D. B. (2006). "Explosive energy" during volcanic eruptions from fractal analysis of pyroclasts. Earth Planet Sci. Lett. 248:800–807. https://doi.org/10.1016/J.EPSL.2006.06.033

Kumagai, H., Chouet, B. A. (1999). The complex frequencies of long-period seismic events as probes of fluid composition beneath volcanoes. Geophys. J. Int. 138:F7–F12. https://doi.org/10.1046/j.1365-246X.1999.00911.x

Kumagai, H., Chouet, B. A. (2000). Acoustic properties of a crack containing magmatic or hydrothermal fluids. J. Geophys. Res. Solid Earth 105:25493– 25512. https://doi.org/10.1029/2000JB900273

Kushnir, A. R. L., Martel, C., Champallier, R., Wadsworth, F. B. (2017). Permeability Evolution in Variably Glassy Basaltic Andesites Measured Under Magmatic Conditions. Geophys. Res. Lett. 44:10262-10271. https://doi.org/10.1002/2017GL074042

Lara, L. E. (2009). The 2008 eruption of Chaitén volcano, Chile: a preliminary report. Andean Geology 36:125–129. http://dx.doi.org/10.5027/andgeoV36n1-a09

Lavallée, Y., Benson, P. M., Heap, M. J., Flaws, A., Hess, K.-U., Dingwell, D. B. (2012). Volcanic conduit failure as a trigger to magma fragmentation. Bull. Volcanol. 74:11–13. https://doi.org/10.1007/s00445-011-0544-2

Lavallée, Y., Benson, P. M., Heap, M. J., Hess, K.-U., Flaws, A., Schillinger, B., Meredith, P. G., Dingwell, D. B. (2013). Reconstructing magma failure and the degassing network of dome-building eruptions. Geology 41(4):515–518. https://doi.org/10.1130/G33948.1

le Heron, D. P., Etienne, J. L. (2005). A complex subglacial clastic dyke swarm, Sólheimajökull, southern Iceland. Sediment. Geol. 181:25–37. https://doi.org/10.1016/J.SEDGEO.2005.06.012

Lister, J. R., Kerr, R. C. (1991). Fluid-mechanical models of crack propagation and their application to magma transport in dykes. J. Geophys. Res. 96:10049. https://doi.org/10.1029/91JB00600

Lormand, C., Zellmer, G. F., Németh, K., Kilgour, G., Mead, S., Palmer, A. S., Sakamoto, N., Yurimoto, H., Moebis, A. (2018). Weka Trainable Segmentation Plugin in ImageJ: A Semi-Automatic Tool Applied to Crystal Size Distributions of Microlites in Volcanic Rocks. Microscopy and Microanalysis 24(6):667–675. https://doi.org/10.1017/S1431927618015428

Maltman, A. (1994). Deformation structures preserved in rocks. In: The Geological Deformation of Sediments. Springer Netherlands, Dordrecht, pp.261–307.

Maxwell, J. C. (1867). IV. On the dynamical theory of gases. Philos. Trans. R. Soc. Lond. 157:49–88. https://doi.org/10.1098/RSTL.1867.0004

McGowan, E. M. (2016). Magma Emplacement and Deformation in Rhyolitic Dykes: Insight Into Magmatic Outgassing. Doctoral dissertation. Lancaster: Lancaster University.

Molina, I., Kumagai, H., Yepes, H. (2004). Resonances of a volcanic conduit triggered by repetitive injections of an ash-laden gas. Geophys. Res. Lett. 31:L03603. https://doi.org/10.1029/2003GL018934

Mortimer, N., Gans, P. B., Foley, F. V., Turner, M. B., Daczko, N., Robertson, M., Turnbull, I. M. (2013). Geology and age of Solander Volcano, Fiordland, New Zealand. Journal of Geology 121(5) https://doi.org/10.1086/671397

Neuberg, J. W., Tuffen, H., Collier, L., Green, D., Powell, T., and Dingwell, D. (2006). The trigger mechanism of low-frequency earthquakes on Montserrat. J. Volcanol. Geoth. Res. 153:37–50. https://doi.org/10.1016/J.JVOLGEORES.2005.08.008

Niu, J., Song, T.-R. A. (2020). Real-time and in-situ assessment of conduit permeability through diverse long-period tremors beneath Aso volcano, Japan. Journal of Volcanology and Geothermal Research 401:106964. https://doi.org/10.1016/j.jvolgeores.2020.106964

Obermeier, S. F. (1996). Use of liquefaction-induced features for paleoseismic analysis

— An overview of how seismic liquefaction features can be distinguished from other features and how their regional distribution and properties of source sediment can be used to infer the location and strength of Holocene paleo-earthquakes. Eng Geol 44:1–76. https://doi.org/10.1016/S0013-7952(96)00040-3

Okumura, S., Sasaki, O. (2014). Permeability reduction of fractured rhyolite in volcanic conduits and its control on eruption cyclicity. Geology 42:843–846. https://doi.org/10.1130/G35855.1

Owen, J., Tuffen, H., McGarvie, D. W. (2013). Explosive subglacial rhyolitic eruptions in Iceland are fuelled by high magmatic H2O and closed-system degassing. Geology 41:251–254. https://doi.org/10.1130/G33647.1

Owen, J., Shea, T., Tuffen, H. (2019). Basalt, Unveiling Fluid-filled Fractures, Inducing Sediment Intra-void Transport, Ephemerally: Examples from Katla 1918. Journal of Volcanology and Geothermal Research 369:121–144. https://doi.org/10.1016/J.JVOLGEORES.2018.11.002

Özsan, A., and Akn, M. (2002). Engineering geological assessment of the proposed Uru¸s Dam, Turkey. Eng. Geol. 66:271–281. https://doi.org/10.1016/S0013-7952(02)00 047-9

Paisley, R., Berlo, K., Ghaleb, B., Tuffen, H. (2019a). Geochemical constraints on the role of tuffisite veins in degassing at the 2008–09 Chaitén and 2011– 12 Cordón Caulle rhyolite eruptions. J. Volcanol. Geoth. Res. 380:80–93. https://doi.org/10.1016/j.jvolgeores.2019.05.013

Paisley, R., Berlo, K., Whattam, J., Schipper, C. I., Tuffen, H. (2019b). Degassing-induced chemical heterogeneity at the 2011-2012 Cordón Caulle eruption. Volcanica 2:211–237. https://doi.org/10.30909/vol.02.02.211237

Paithankar, M. G. (1967). Tuffisite and Volcanic Phenomena Associated with the Glas Eilean vent, Ardnamurchan, Argyllshire, Scotland. GFF 89(1):15– 28. https://doi.org/10.1080/11035896709449231

Pallister, J. S., Cashman, K. V., Hagstrum, J. T., Beeler, N. M., Moran, S. C., Denlinger, R. P. (2013). Faulting within the Mount St. Helens conduit and implications for volcanic earthquakes. Bulletin of the Geological Society of America 125:359–376. https://doi.org/10.1130/B30716.1

Peterson, G. L. (1968). Flow structures in sandstone dikes. Sediment. Geol. 2:177–190. https://doi.org/10.1016/0037-0738(68)90024-9

Perkins, T. K., Kern, L. R. (1961). Widths of hydraulic fractures. J. Petrol. Technol. 13:937–949. https://doi.org/10.2118/89-PA

Phillips, E., Everest, J., Reeves, H. (2013). Micromorphological evidence for subglacial multiphase sedimentation and deformation during overpressurized fluid flow associated with hydrofracturing. Boreas 42:395–427. https://doi.org/10.1111/j.1502-3885.2012.00261.x

Phillips, E., Hughes, L. (2014). Hydrofracturing in response to the development of an overpressurised subglacial meltwater system during drumlin formation: an example from Anglesey, NW Wales. Proc. Geol. Associat. 125:296–311. https://doi.org/10.1016/J.PGEOLA.2014.03.004

Phillips, E., Kearsey, T. I. (2020). Mass flow and hydrofracturing during Late Devensian moraine emplacement, NE Scotland. Proc. Geol. Associat. 131:730–750. https://doi.org/10.1016/j.pgeola.2020.08.002

Ratté, J. C. (2004). A guide to the Mule Creek volcanic vent, the rhyolite of Potholes Country, and obsidian ledges, Gila National Forest, southwestern New Mexico. New Mexico Geology 26:111–122.

Ravier, E., Buoncristiani, J.-F., Guiraud, M., Menzies, J., Clerc, S., Goupy, B., Portier, E. (2014). Porewater pressure control on subglacial soft sediment remobilization and tunnel valley formation: a case study from the Alnif tunnel valley (Morocco). Sediment. Geol. 304:71–95. https://doi.org/10.1016/J.SEDGEO.2014.02.005

Ravier, E., Buoncristiani, J.-F., Menzies, J., Guiraud, M., Portier, E. (2015). Clastic injection dynamics during ice front oscillations: A case example from Sólheimajökull (Iceland). Sediment. Geol. 323:92–109. https://doi.org/10.1016/J.SEDGEO.2015.04.013

Reynolds, D. L. (1952). IV.—The Geology of Slieve Gullion, Foughill and Carrickcarnan: An Actualistic Interpretation of a Tertiary Gabbro-granophyre Complex. Transactions of the Royal Society of Edinburgh 62:85–143. https://doi.org/10.1017/S008045680000925X

Rijsdijk, K. F., Owen, G., Warren, W. P., McCarroll, D., van der Meer, J. J. (1999). Clastic dykes in over-consolidated tills: evidence for subglacial hydrofracturing at Killiney Bay, eastern Ireland. Sediment. Geol. 129, 111–126. https://doi.org/10.1016/S0037-0738(99)00093-7

Ripepe, M., Lacanna, G., Pistolesi, M., Silengo, M. C., Aiuppa, A., Laiolo, M., Massimetti, F., Innocenti, L., Della Schiava, M., Bitetto, M., La Monica, F. P., Nishimur, T., Rosi, M., Mangione, D., Ricciardi, A., Genco, R., Coppola, D., Marchetti, E., Delle Donne, D. (2021). Ground deformation reveals the scale-invariant conduit dynamics driving explosive basaltic eruptions. Nat Commun 12:1683. https://doi.org/10.1038/s41467-021-21722-2

Rivalta, E., Taisne, B., Bunger, A. P., Katz, R. F. (2015). A review of mechanical models of dike propagation: schools of thought, results and future directions. Tectonophysics 638:1–42. https://doi.org/10.1016/j.tecto.2014.10.003

Robertson, R., Cole, P., Sparks, R. S. J., Harford, C., Lejeune, A. M., McGuire, W. J., Miller, A. D., Murphy, M. D., Norton, G., Stevens, N. F., Young, S. R. (1998). The explosive eruption of Soufriere Hills Volcano, Montserrat, West Indies, 17 September, 1996. Geophys. Res. Lett. 25(18):3429–3432. https://doi.org/10.1029/98GL01442

Ross, P. S., White, J. D. L. (2006). Debris jets in continental phreatomagmatic volcanoes: A field study of their subterranean deposits in the Coombs Hills vent complex, Antarctica. Journal of Volcanology and Geothermal Research 149:62–84. https://doi.org/10.1016/j.jvolgeores.2005.06.007

Ross, J. A., Peakall, J., Keevil, G. M. (2014). Facies and flow regimes of sandstone hosted columnar intrusions: Insights from the pipes of Kodachrome Basin State Park. Sedimentology 61:1764–1792. https://doi.org/10.1111/sed.12115

Ross, P. S., Carrasco Núñez, G., Hayman, P. (2017). Felsic maar-diatreme volcanoes: a review. Bull. Volcanol. 79:1–33. https://doi.org/10.1007/s00445-016-1097-1

Rubin, A. M. (1993). Tensile fracture of rock at high confining pressure: Implications for dike propagation. J. Geophys. Res. 98(15919). https://doi.org/10.1029/93JB01391

Rubin, A. M. (1995). Propagation of magma-filled cracks. Annu. Rev. Earth Planet. Sci. 23:287–336.

Rust, A. C., Cashman, K. V., and Wallace, P. J. (2004). Magma degassing buffered by

vapor flow through brecciated conduit margins. Geology 32:349.
https://doi.org/10.1130/G20388.2

Rutter, E. H. (1986). On the nomenclature of mode of failure transitions in rocks.
Tectonophysics 122:381–387. https://doi.org/10.1016/0040-1951(86)90153-8

Sæmundsson, K., Noll, H. (1974). K-Ar ages of rocks from Husafell, western Iceland,
and the Development of the Husafell Central Volcano. Jökull 24:40–59.

Saffman, P. G., Taylor, G. I. (1958). The penetration of a fluid into a porous medium
or Hele-Shaw cell containing a more viscous liquid. Proc. R. Soc. Lond. Ser. A Math.
Phys. Sci. 245:312–329. https://doi.org/10.1098/rspa.1958.0085

Sahagian, D. L., Proussevitch, A. A. (1998). 3D particle size distributions from 2D
observations: stereology for natural applications. Journal of Volcanology and
Geothermal Research 84:173–196. https://doi.org/10.1016/S0377-0273(98)00043-2

Saubin, E., Tuffen, H., Gurioli, L., Owen, J., Castro, J. M., Berlo, K., McGowan, E.
M., Schipper, C. I., Wehbe, K. (2016). Conduit dynamics in transitional rhyolitic
activity recorded by tuffisite vein textures from the 2008–2009 Chaitén Eruption.
Front. Earth Sci. 4:59. https://doi.org/10.3389/feart.2016.00059

Saubin, E., Kennedy, B., Tuffen, H., Villeneuve, M., Davidson, J., Burchardt, S.
(2019). Comparative field study of shallow rhyolite intrusions in Iceland: emplacement
mechanisms and impact on country rocks. J. Volcanol. Geoth. Res. 388(106691).
https://doi.org/10.1016/j.jvolgeores.2019.106691

Schipper, C. I., Castro, J. M., Tuffen, H., James, M. R., How, P. (2013). Shallow vent
architecture during hybrid explosive–effusive activity at Cordón Caulle (Chile,
2011–12): Evidence from direct observations and pyroclast textures. Journal of
Volcanology and Geothermal Research 262:25–37.
https://doi.org/10.1016/J.JVOLGEORES.2013.06.005

Schipper, C. I., Castro, J. M., Tuffen, H., Wadsworth, F. B., Chappell, D., Pantoja, A.
E., Simpson, M. P., Le Ru, E. C. (2015). Cristobalite in the 2011–2012 Cordón Caulle
eruption (Chile). Bull.Volcanol. 77(34). https://doi.org/10.1007/s00445-015-0925-z

Schipper, C. I., Castro, J. M., Kennedy, B. M., Tuffen, H., Whattam, J., Wadsworth,
F. B., Paisley, R., Fitzgerald, R. H., Rhodes, E., Schaefer, L. N., Ashwell, P. A., Forte,
P., Seropian, G., Alloway, B. V. (2021). Silicic conduits as supersized tuffisites:
Clastogenic influences on shifting eruption styles at Cordón Caulle volcano (Chile).
Bull. Volcanol. 83(11). https://doi.org/10.1007/s00445-020-01432-1

Schmidt, R. A., Warpinski, N. R., Finley, S. J., Shear, R. C. (1981). Multi-frac test
series. Final report. Albuquerque, NM, and Livermore, CA (United States)

Schmiedel, T., Burchardt, S., Mattsson, T., Guldstrand, F., Galland, O., Palma, J. O.,
Skogby, H. (2021). Emplacement and Segment Geometry of Large, High-Viscosity
Magmatic Sheets. Minerals 11(10):1113. https://doi.org/10.3390/min11101113

Schneider, C. A., Rasband, W. S., Eliceiri, K. W. (2012). NIH Image to ImageJ: 25
years of image analysis. Nature Methods 9(7):671–675.
https://doi.org/10.1038/nmeth.2089

Scott, A., Vigorito, M., Hurst, A. (2009). The process of sand injection: internal
structures and relationships with host strata (Yellowbank Creek Injectite Complex,
California, U.S.A.). J. Sediment. Res. 79:568–583. https://doi.org/10.2110/jsr.
2009.062

Scholz, C. H. (1968). Experimental study of the fracturing process in brittle rock. J. Geophys. Res. 73:1447–1454. https://doi.org/10.1029/JB073i004p01447

SERNAGEOMIN-OVDAS (2011). Puyehue-Cordón Caulle: Reporte especial de actividad volcánica. Internal report 38, SERNAGEOMINOVDAS, Arica, Chile.

Shea, T., Houghton, B. F., Gurioli, L., Cashman, K. V., Hammer, J. E., Hobden, B. J. (2010). Textural studies of vesicles in volcanic rocks: An integrated methodology. Journal of Volcanology and Geothermal Research 190:271–289. https://doi.org/10.1016/j.jvolgeores.2009.12.003

Sherry, T. J., Rowe, C. D., Kirkpatrick, J. D., Brodsky, E. E. (2012). Emplacement and dewatering of the world's largest exposed sand injectite complex. Geochemistry, Geophysics, Geosystems 13(8). https://doi.org/10.1029/2012GC004157

Sigfúsdóttir T., Phillips, E., Benediktsson, Í. Ö. (2019). Micromorphological evidence for the role of pressurised water in the formation of large-scale thrust-block moraines in Melasveit, Western Iceland. Quaternary Research. 93:88–109. https://doi.org/10.1017/qua.2019.48

Simmons, J. H., Mohr, R. K., Montrose, C. J. (1998). Non-Newtonian viscous flow in glass. J. Appl. Phys. 53:4075. https://doi.org/10.1063/1.331272

Skilling, I. P., White, J. D. L., McPhie, J. (2002). Peperite: A review of magmasediment mingling. Journal of Volcanology and Geothermal Research 114:1–17. https://doi.org/10.1016/S0377-0273(01)00278-5

Sparks, R. S. J. (1976). Grain size variations in ignimbrites and implications for the transport of pyroclastic flows. Sedimentology 23:147–188. https://doi.org/10.1111/j.1365-3091.1976.tb00045.x

Stasiuk, M. V., Barclay, J., Carroll, M. R., Jaupart, C., Ratté, J. C., Sparks, R. S. J., et al. (1996). Degassing during magma ascent in the Mule Creek vent (USA). Bull. Volcanol. 58:117–130. https://doi.org/10.1007/s004450050130

Stix, J., Torres, C. R., Narváez, M. L, Cortés J., G. P., Raigosa, J. A., Gómez M., D., Castonguay, R. (1997). A model of vulcanian eruptions at Galeras volcano, Colombia. Journal of Volcanology and Geothermal Research 77:285–303. https://doi.org/10.1016/S0377-0273(96)00100-X

Stoppa, F., Lupini, L. (1993). Mineralogy and petrology of the Polino Monticellite Calciocarbonatite (Central Italy). Mineral Petrol 49:213–231. https://doi.org/10.1007/BF01164595

Stoppa, F., Rosatelli, G., Wall, P., le Bas, M. J. (2003). Texture and mineralogy of tuffs and tuffisites at Ruri Volcano in western Kenya: A carbonatite, melilitite, mantle-debris trio. Periodico di Mineralogia 72:181–204

Taguchi, K., Kumagai, H., Maeda, Y., Torres, R. (2018). Source properties and triggering processes of long-period events beneath volcanoes inferred from an analytical formula for crack resonance frequencies. J. Geophys. Res. Solid Earth. 123(9):7550–7565. https://doi.org/10.1029/2018JB015866

Taguchi, K., Kumagai, H., Maeda, Y., and Torres, R. (2021). Empirical formula for the quality factors of crack resonances and its application to the estimation of source properties of long-period seismic events at active volcanoes. Geophys. J. Int. 224:2131–2148. https://doi.org/10.1093/gji/ggaa519

Taisne, B., Jaupart, C. (2009). Dike propagation through layered rocks. J. Geophys.

Res. Solid Earth 114(B9). https://doi.org/10.1029/2008JB006228

Taylor, B. J. (1982). Sedimentary dykes, pipes and related structures in the Mesozoic sediments of south-eastern Alexander Island. British Antarctic Survey Bulletin 51:1–42.

Torres, R., Kumagai, H., Taguchi, K. (2021). Source models of long-period seismic events at Galeras volcano, Colombia. Geophys. J. Int. 227:2137–2155. https://doi.org/10.1093/GJI/GGAB325

Trafton, K. R., Giachetti, T. (2022). The pivotal role of Vulcanian activity in ending the explosive phase of rhyolitic eruptions: the case of the Big Obsidian Flow eruption (Newberry Volcano, USA). Bull. Volcanol. 84(104). https://doi.org/10.1007/s00445-022-01610-3

Trevelyan, P. M. J., Almarcha, C., De Wit, A. (2011). Buoyancy-driven instabilities of miscible two-layer stratifications in porous media and Hele-Shaw cells. J. Fluid Mech. 670:38–65. https://doi.org/10.1017/S0022112010005008

Tuffen, H., Dingwell, D. B., Pinkerton, H. (2003). Repeated fracture and healing of silicic magma generate flow banding and earthquakes? Geology 31(1089). https://doi.org/10.1130/G19777.1

Tuffen, H., Dingwell, D. (2005). Fault textures in volcanic conduits: Evidence for seismic trigger mechanisms during silicic eruptions. Bull. Volcanol. 67:370–387. https://doi.org/10.1007/s00445-004-0383-5

Tuffen, H., Castro, J. M. (2009). The emplacement of an obsidian dyke through thin ice: Hrafntinnuhryggur, Krafla Iceland. Journal of Volcanology and Geothermal Research 185:352–366. https://doi.org/10.1016/j.jvolgeores.2008.10.021

Van Der Meer, J. J. M., Kjaer, K. H., Krüger, J. (1999). Subglacial water-escape structures and till structures, Slettjokull, Iceland. J. Q. Sci. 14:191–205. https://doi.org/10.1002/(sici)1099-1417(199905)14:3<191::aid-jqs436<3.0.co;2-

Vachon, R., Hieronymus, C. F. (2017). Effect of host-rock rheology on dyke shape, thickness and magma overpressure. Geophys. J. Int. 208:1414–1429. https://doi.org/10.1093/gji/ggw448

Valentine, G. A., White, J. D. L. (2012). Revised conceptual model for maardiatremes: Subsurface processes, energetics, and eruptive products. Geology 40:1111–1114. https://doi.org/10.1130/G33411.1

Valentine, G. A., Cole, M. A. (2021). Explosive caldera-forming eruptions and debris-filled vents: Gargle dynamics. Geology 49:1240–1244. https://doi.org/10.1130/G48995.1

van der Meer, J. J. M., Kjær, K. H., Krüger, J., Rabassa, J., Kilfeather, A. A. (2009). Under pressure: clastic dykes in glacial settings. Q. Sci. Rev. 28, 708–720. https://doi.org/10.1016/j.quascirev.2008.07.017

Vasseur, J., Wadsworth, F. B., Lavallée, Y., Hess, K.-U., Dingwell, D. B. (2013). Volcanic sintering: Timescales of viscous densification and strength recovery. Geophys. Res. Lett. 40:5658–5664. https://doi.org/10.1002/2013GL058105

Vasseur, J., Wadsworth, F. B., Lavallée, Y., Dingwell, D. B. (2016). Dynamic elastic moduli during isotropic densification of initially granular media. Geophys. J. Int. 204:1721–1728. https://doi.org/10.1093/gji/ggv550

Vasseur, J., Wadsworth, F. B. (2019). Volcanic welding model: VolcWeld.

https://theghub.org/resources/4568

Vasseur, J., Wadsworth, F. B., Dingwell, D. B. (2020). Permeability of polydisperse magma foam. Geology 48:536–540. https://doi.org/10.1130/G47094.1

Vigorito, M., Hurst, A., Cartwright, J., Scott, A. (2008). Regional-scale subsurface sand remobilization: Geometry and architecture. J. Geol. Soc. London 165:609–612. https://doi.org/10.1144/0016-76492007-096

Voight, B., Sparks, R. S. J., Miller, A. D., Stewart, R. C., Hoblitt, R. P., Clarke, A., Ewart, J., Aspinall, W. P., Baptie, B., Calder, E. S., Cole, P., Druitt, T. H., Hartford, C., Herd, R. A., Jackson, P., Lejeune, A. M., Lockhart, A. B., Loughlin, S. C., Luckett, R., Lynch, Y., Norton, G. E., Robertson, R., Watson, I. M., Watts, R., Young, S. R. (1999). Magma flow instability and cyclic activity at Soufriere Hills volcano, Montserrat, British West Indies. Science. 283(5405):1138–1142. https://doi.org/10.1126/science.283.5405.1138

Voight, B., Hoblitt, R. P., Clarke, A. B., Lockhart, A. B., Miller, A. D., Lynch, L., McMahon, J. (1998). Remarkable cyclic ground deformation monitored in real-time on Montserrat, and its use in eruption forecasting. Geophys. Res. Lett. 25:3405–3408. https://doi.org/10.1029/98GL01160

Wadsworth, F. B., Vasseur, J., von Aulock, F. W., Hess, K.-U., Scheu, B., Lavallée, Y., Dingwell, D. B. (2014). Nonisothermal viscous sintering of volcanic ash. J. Geophys. Res. Solid Earth 119:8792–8804. https://doi.org/10.1002/2014JB011453

Wadsworth, F. B., Vasseur, J., Scheu, B., Kendrick, J. E., Lavallée, Y., Dingwell, D. B. (2016). Universal scaling of fluid permeability during volcanic welding and sediment diagenesis. Geology 44:219–222. https://doi.org/10.1130/G37559.1

Wadsworth, F. B., Vasseur, J., Llewellin, E. W., Dingwell, D. B. (2017). Sintering of polydisperse viscous droplets. Phys. Rev. E 95:033114. https://doi.org/10.1103/PhysRevE.95.033114

Wadsworth, F. B., Witcher, T., Vossen, C. E. J., Hess, K.-U., Unwin, H. E., Scheu, B., Castro, J. M., Dingwell, D. B. (2018). Combined effusive-explosive silicic volcanism straddles the multiphase viscous-to-brittle transition. Nature Communications, 9:1–8. https://doi.org/10.1038/s41467-018-07187-w

Wadsworth, F. B., Vasseur, J., Schauroth, J., Llewellin, E. W., Dobson, K. J., Havard, T., Scheu, B., von Aulock, F. B., Gardner, J. E., Dingwell, D. B., Hess, K.-U., Colombier, M., Marone, F., Tuffen, H., Heap, M. J. (2019). A general model for welding of ash particles in volcanic systems validated using in situ X-ray tomography. Earth Planet. Sci. Lett. 525(115726). https://doi.org/10.1016/j.epsl.2019.115726

Wadsworth, F. B., Llewellin, E. W., Vasseur, J., Gardner, J. E., and Tuffen, H. (2020). Explosive-effusive volcanic eruption transitions caused by sintering. Sci. Adv. 6:7940. https://doi.org/10.1126/sciadv.aba7940

Wadsworth, F. B., Vasseur, J., Llewellin, E. W., Brown, R. J., Tuffen, H., Gardner, J. E., Kendrick, J. E., Lavallée, Y., Dobson, K. J., Heap, M. J., Dingwell, D. B., Hess, K.-U., Schauroth, J., von Aulock, F. W., Kushnir, A. R. L., Marone, F. (2021). A model for permeability evolution during volcanic welding. J. Volcanol. Geoth. Res. 409(107118). https://doi.org/10.1016/j.jvolgeores.2020.107118

Wadsworth, F. B., Llewellin, E. W., Castro, J. M., Tuffen, H., Schipper, C. I., Gardner, J. E., Vasseur, J., Foster, A., Damby, D. E., McIntosh, I. M., Boettcher, S., Unwin, H. E., Heap, M. J., Farquharson, J. I., Dingwell, D. B., Iacovino, K., Paisley,

R., Jones, C., Whattam, J. (2022). A reappraisal of explosive–effusive silicic eruption dynamics: syn-eruptive assembly of lava from the products of cryptic fragmentation. Journal of Volcanology and Geothermal Research 432(107672). https://doi.org/10.1016/J.JVOLGEORES.2022.107672

Walker, G. P. L. (1984). Characteristics of dune-bedded pyroclastic surge bedsets. J. Volcanol. Geoth. Res. 20:281–296. https://doi.org/10.1016/0377-0273(84)90044-1

Walker, B. H., Francis, E. H. (1987). High-level emplacement of an olivine-dolerite sill into Namurian sediments near Cardenden, Fife. Trans. R. Soc. Edinb. Earth Sci. 77(4):295–307. https://doi.org/10.1017/S0263593300023191

Warpinski, N. R., Tyler, L. D., Vollendorf, W. C., Northrop, D. A. (1981). Direct observation of a sand-propped hydraulic fracture. Sandia National Labs., Albuquerque, N. Mex. Technical Report, SAND-81-0225, 6430566

Weaver, J., Lavallée, Y., Ashraf, M., Kendrick, J. E., Lamur, A., Schauroth, J., Wadsworth, F. B. (2022). Vesiculation and densification of pyroclasts: A clast-size dependent competition between bubble growth and diffusive outgassing. Journal of Volcanology and Geothermal Research 428(107550). https://doi.org/10.1016/j.jvolgeores.2022.107550

White, J. D. L., Ross, P. S. (2011). Maar-diatreme volcanoes: A review. Journal of Volcanology and Geothermal Research 201:1–29. https://doi.org/10.1016/J.JVOLGEORES.2011.01.010

White, F. M., Xue, H. (2020) Fluid mechanics. Ninth edn. Chapter 6 Viscous flow in ducts. New York, N.Y: McGraw Hill.

Wicks, C., de La Llera, J. C., Lara, L. E., Lowenstern, J. (2011). The role of dyking and fault control in the rapid onset of eruption at Chaitén volcano, Chile. Nature, 478:374–377. https://doi.org/10.1038/nature10541

Wilson, L., Head, J. W. (1981). Ascent and eruption of basaltic magma on the Earth and Moon. J. Geophys. Res. Solid Earth 86:2971–3001. https://doi.org/10.1029/JB086iB04p02971

Wright, H. M. N., Cashman, K. V., Rosi, M., Cioni, R. (2007). Breadcrust bombs as indicators of Vulcanian eruption dynamics at Guagua Pichincha volcano, Ecuador. Bull. Volcanol. 69:281–300. https://doi.org/10.1007/s00445-006-0073-6

Williams, C. L., Thompson, T. B., Powell, J. L., Dunbar, W. W. (2000). Gold-Bearing Breccias of the Rain Mine, Carlin Trend, Nevada. Economic Geology 95:391–404. https://doi.org/10.2113/gsecongeo.95.2.391

Woods, J., Winder, T., White, R. S., Brandsdóttir, B. (2019). Evolution of a lateral dike intrusion revealed by relatively-relocated dike-induced earthquakes: the 2014–15 Bárðarbunga–Holuhraun rifting event, Iceland. Earth Planet. Sci. Lett. 506:53–63. https://doi.org/10.1016/j.epsl.2018.10.0

Zhou, J., Chen, Y., Tang, H., Wang, L., Cardenas, M. B. (2019). Disentangling the Simultaneous Effects of Inertial Losses and Fracture Dilation on Permeability of Pressurized Fractured Rocks. Geophys. Res. Lett. 46:8862–8871. https://doi.org/10.1029/2019GL083355

A Appendices

A.1 Tuffisite explainer animation (Animation 1)

This explainer animation, produced by collaboration with Mair Perkins and Envision DTP, can be found on YouTube at: https://youtu.be/ZPkCrcmLRAA

This animation outlines the different hazards of explosive and effusive eruptions and the role that tuffisites might play in moderating eruption style. The animation explains the setting of tuffisites adjacent to volcanic conduits and their formation.

A.2 Untraced SEM images of Mule Creek tuffisites

a

b

20 μm

50 μm
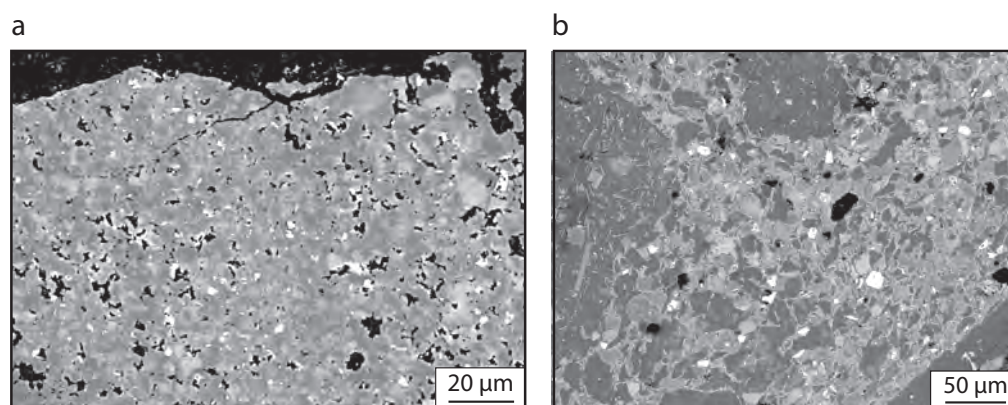
Figure A.1: Untraced images of a diffuse tuffisite within the pyroclastic breccia (a) and tuffisite within the vitrophyre breccia (b) that are used to collect the grain-size distributions in Figures 4.10a and 4.10c.

A.3 Animation of vent evolution (Animation 2)

An animated version of the schematic shown in Figure 4.12, demonstrating the evolution of the MCV. The animation can be found on YouTube at: https://youtu.be/X-m7Wqs_8tU

Vent evolution begins with high pressure gas-pyroclast mixtures opening fractures that are expanded to form a conduit and vent. Pyroclastic material is deposited within the vent to form subunits of pyroclastic breccia that are periodically eroded and overturned. Increasing temperature allows welding of the pyroclastic breccia,

increasing its strength, as well as the accretion of ash-sized particles on to the vent walls to produce the vitrophyre. Fracturing of the vent walls breaks the accreting vitrophyre to form the vitrophyre breccia until a waning of explosivity prevents the continual fracturing of the wall material, allowing the coherent vitrophyre to form. Tuffisites are shown to form throughout vent evolution.

A.4   Animation of tuffisite formation (Animation 3)

An animated schematic demonstrating the formation of tuffisites in the pyroclastic breccia, vitrophyre breccia, and vitrophyre. The animation can be found on Youtube at: https://youtu.be/irsF54m6Zcw

When the walls of the vent are permeable pyroclastic breccia, lateral outgassing can occur through the pore space of the breccia and fracturing would not be required to increase the wall permeability. As the welding of the pyroclastic breccia and accretion of the vitrophyre lower the permeability of the vent walls, lateral outgassing through pore space is limited. Fracturing, and the formation of fracture-hosted tuffisites, would now be required for lateral outgassing to occur. Tuffisites will weld together through time and this fracturing must therefore be repeated to create new pathways for lateral outgassing to continue.

A.5   Combining particle-size distributions

The particle-size distributions are produced by combining multiple images in nests of different magnifications. The magnification of the different images was chosen so that >100 particles of the largest and smallest sizes could be seen clearly in the image, with the other images within the nest at magnifications to allow for significant overlap between the combined particle-size distribution curves. Within each image, once the Python code has filtered the data to remove the particle-sizes that are too small (<10 pixels in diameter) or too large (>1% image area) to be correctly represented, the remaining particle-size distribution will be the true distribution for that image without distortion at both ends. Ensuring significant overlap between the particle-sizes in each image will ensure that the switch from one image to that of the next magnification in the combined particle-size distribution is in the most appropriate place, as well as imaging a larger sample area, allowing for better representation of the true

distribution.

Table A.1: Magnifications of the different images used in the image nests.

	Magnification			
Sample name	1	2	3	4
DM9B 1–3	x150	x450	x1000	
DM9B 4–5	x250	x1200		
DM9B 19–21	x120	x450	x1100	
DM11B 1-3	x220	x700	x1800	
DM11B 13-16	x180	x600	x1500	x2200
DM11B 24-26	x120	x400	x1100	
DM13B 4-6	x110	x400	x2200	
DM13B 12-14	x100	x400	x2200	
DM13B 24-26	x200	x500	x2200	
DM13B 30-32	x130	x500	x2200	
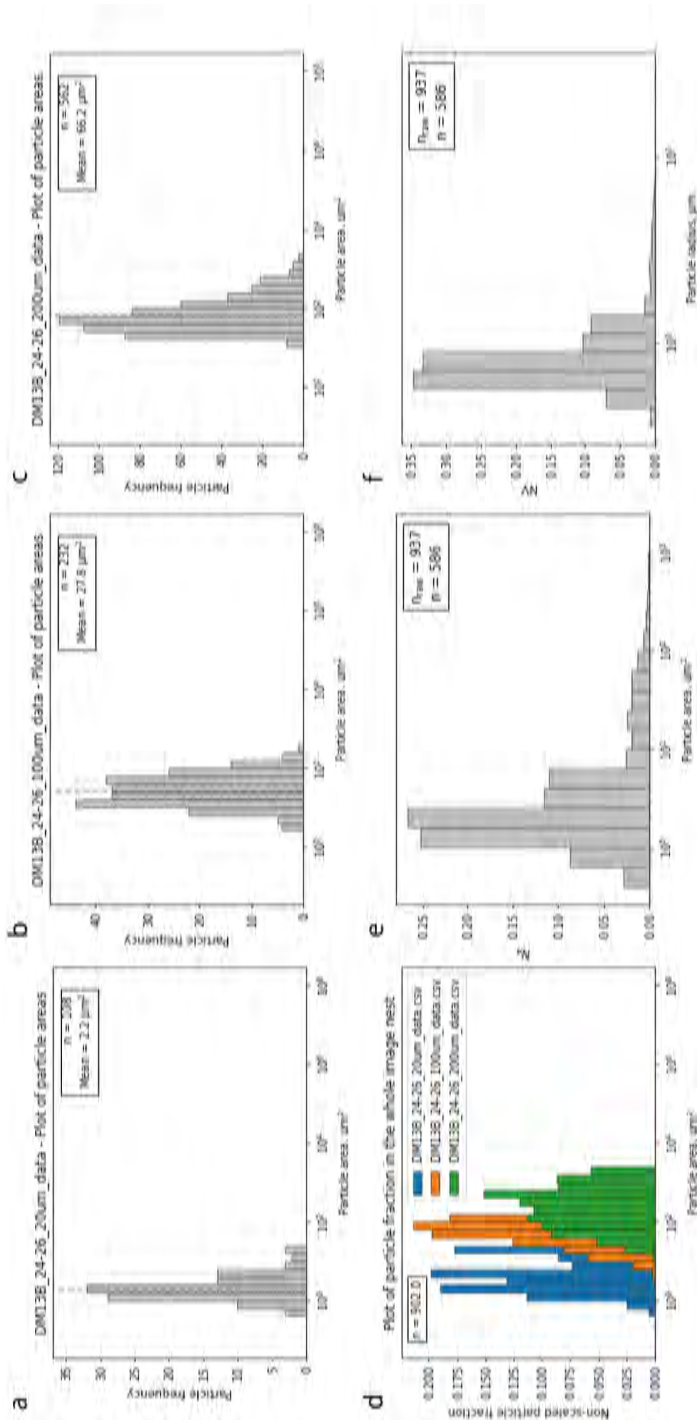
Figure A.2: The different stages involved in combining particle-size distributions to produce a single particle-size distribution for an image nest. See also the Jupyter notebooks. The frequency of particles in each area bin for the three individual images in order of decreasing magnification (a–c), the calculated particle fractions (per area) of the three distributions superimposed (d) and the calculated number density per unit area (N_A) and per unit volume (N_V).

A.5.1 Cumulative distribution curves
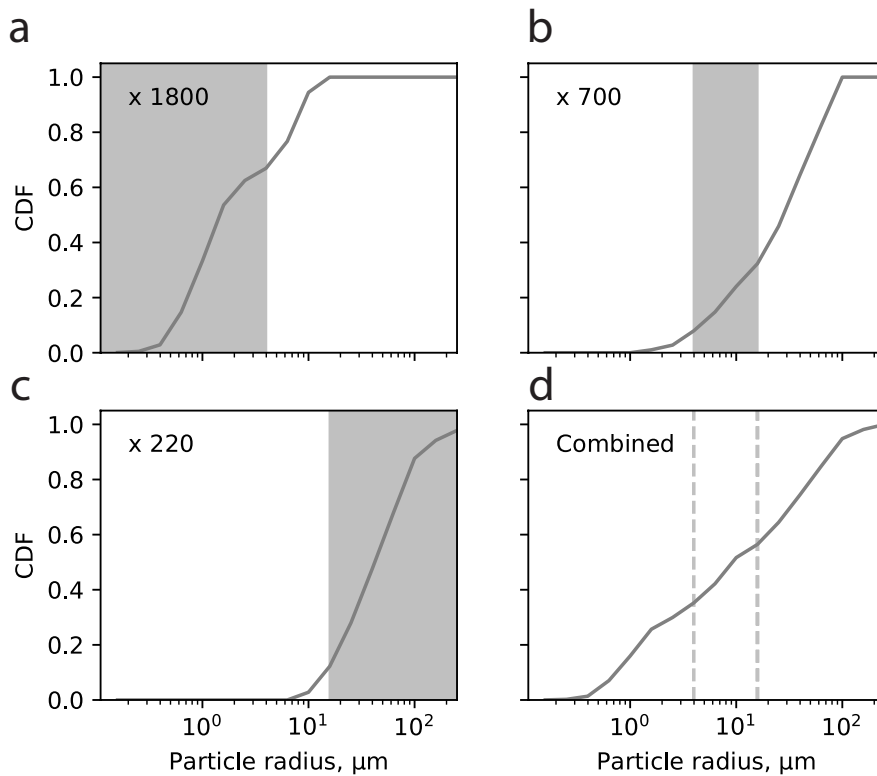
Figure A.3: Example cumulative distribution curves for each image within a nest (a-c) and the final combined distribution produced (d). Text in the image gives the magnification of the SEM image used in the particle-size analysis. The shaded area (or dashed lines in d) show the fraction of each particle-size distribution used to produce the final combined distribution.

A.6 Stereological conversions

Within a thin section, particles are only visible as a 2D slice through a structure that is actually 3D. A slice through a pack of particles is unlikely to sample each particle across its largest point (cut effect), and smaller particles also have a lower probability of being intersected by the slice than larger particles (intersection probability; Shea et al. 2010). These factors introduce error into particle size distributions calculated from 2D surfaces, and these are further accentuated if the particles sampled are elongate. Stereological conversions attempt to reduce these errors by taking into account the intersection probabilities of different particles (Sahagian and Proussevitch, 1998).

Sahagian and Proussevitch (1998) produced a method for a stereological conversion

that accounts for the intersection probabilities of the different particles in a 2D surface. Their technique calculates the number density of objects in different size classes per unit volume by successive iterations of the number density of larger objects. This approach assumes that the particles are spherical, and therefore particles that differ from perfect sphericity will introduce further errors into the particle-size distribution produced. The use of geometric size classes allows for particle sizes over several orders of magnitude, with smaller particle sizes better represented in the final distribution (Shea et al. 2010).

The number density of the smallest size class (N_{V1}) and the subsequent number densities (to N_i where i is the number of size classes) can be expressed using the equation

$$N_{Vi} = \frac{1}{P_i \bar{H}'_i} \times \left(N_{Ai} - \sum_{j=1}^{i-1} P_j + {}_1\bar{H}'_j + {}_1 N_{V(i-j)} \right) \tag{A.1}$$

where N_A is the measured number density per unit area, P is the probability of intersecting particles and $\bar{H}'_i$ is the mean projected height. For ease of computation, Sahagian and Proussevitch (1998) rewrite this equation as

$$N_{Vi} = \frac{1}{\bar{H}'_i} \times \left(\alpha_i N_{Ai} - \sum_{j=1}^{i-1} \alpha_j + {}_1 N_{A(i-j)} \right) \tag{A.2}$$

where the coefficients α_i are equal to

$$\alpha_i = \frac{1}{P_1} \left(\alpha_1 P_i - \sum_{j=1}^{i-2} \alpha_j + {}_1 P_{i-j} \right) \tag{A.3}$$

The probability of intersecting objects through a specific size for spherical particles can then be calculated as

$$P\left(r_1 < r < r_2\right) = \frac{1}{R} \left(\sqrt{R^2 - r_1^2} - \sqrt{R^2 - r_2^2} \right) \tag{A.4}$$

where r is the cross-section radius, r_1 and r_2 are the upper and lower size limits of the particular size class considered and R is the spherical radius.

Assumptions in the stereological conversion and associated errors The stereological conversion assumes that the particles are perfectly spherical, introducing a potential error in the resulting particle-size distribution. Analysis of particles of different shapes

(e.g. 2D cut-throughs of spheres, ellipsoids, and rectangular solids) has found that the shape of the particles with the same aspect ratios does not greatly effect the conversion coefficients produced by Equation A.3 and therefore does not have a large effect on the resulting distribution (Sahagian and Proussevitch, 1998). Altering the aspect ratio of a shape will however alter the conversion coefficients produced and will have a greater effect on the resulting distribution.

By measuring particle area, A, and then calculating the particle radius, r, using $A = \pi r^2$, the 2D particles are assumed to be circular. To estimate the error produced by this assumption that circularity of the particles measured can be considered. The average circularity of all of the particles measured in Chapter 5 is 0.75 and the distribution in circularity is plotted in Figure A.4a. If the particles are assumed to be rotational ellipsoids then the error in the calculated particle radius depends on whether in 3D the third axis is equal to the long or short axis of the particle. The circularity value found above suggests that the average aspect ratio between the long and short axes of a particle is 1.91 (Figure A.4b). The error in the calculation of a spherical area, rather than the area of a rotational ellipsoid is therefore 38% if the particle is rotated around the long axis (prolate spheroid) or 28% if rotated around the short axis (oblate ellipsoid; A.4c and d). A Jupyter Notebook with the error calculations can be found in Appendix B.5. Using computer generated particle-size distributions that are mathematically cut through the produce 10^6 thin sections in a numerical experiment, Sahagian and Proussevitch (1998) demonstrate that the error in the probability of each particle size generated by the stereological conversion is small for rotational ellipsoids but larger for non-rotational ellipsoids (Figure A.5). Figure A.4c and d show variation in the calculated particle volume and percentage error created by assuming that an elliptical particle of different aspect ratios is spherical, compared to a prolate or oblate spheroid. The percentage error increases with a greater particle aspect ratio. The ellipsoidal shape of the particles results in the underestimation of the smallest particle sizes and overestimation of the largest particle sizes in the final distribution (Sahagian and Proussevitch, 1998). With only 2D cut-throughs of the particles from thin sections, I am unable here to consider the proportion of particles in the actual distribution that are non-rotational, and this unknown factor will increase the error in the final distribution produced.

The model for the timescale of particle sintering (Wadsworth et al., 2019) is for spherical particles, and the assumption of sphericity needs to therefore be made. A
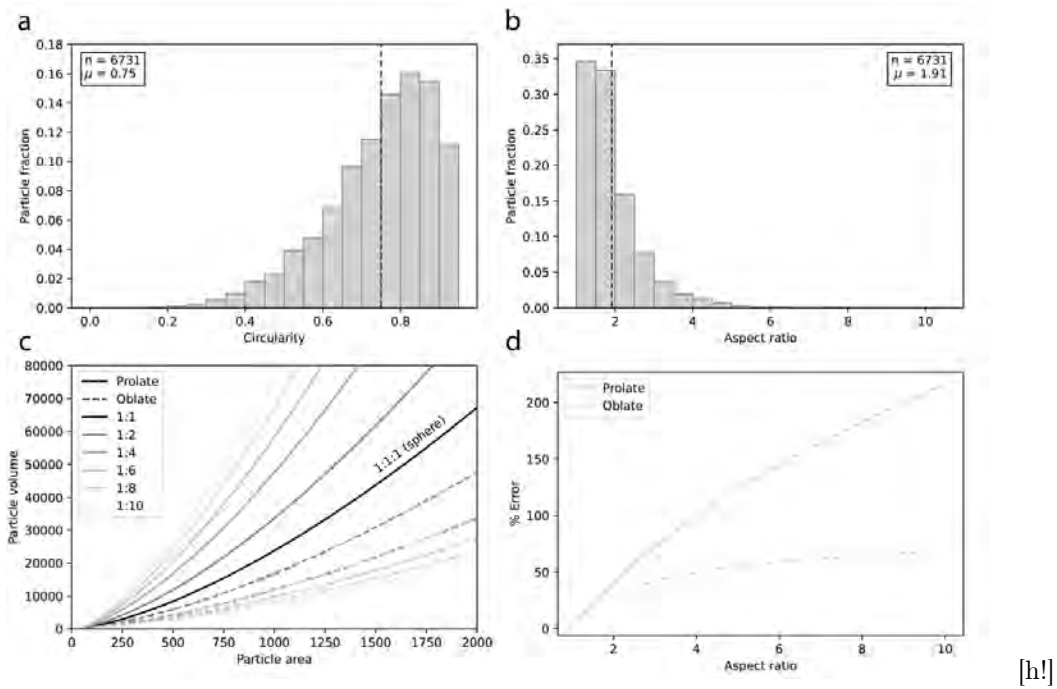
Figure A.4: The shape of measured particles and the expected percentage error caused by the assumption of spherical particles. a) The circularity of all particles measured, before filtering takes place. The particles have a mean circularity (μ) of 0.75. b) The aspect ratio of the particles measured in the images (2D). The mean aspect ratio (μ) of the particles is 1.91. c) The difference in calculated volume between the assumption that particles are spherical or prolate of oblate spheroids, plotted for different aspect ratios. The volume of prolate spheroids is underestimated by the spherical approximation while the volume of oblate spheroids is overestimated. d) The percentage error for calculations of particle volume assuming sphericity for particles that are prolate or oblate spheroids. The percentage error increases with increasing aspect ratio of the particles.

percentage error of 38% on the particle volume gives a % error on the particle radius of $\sim$13%.
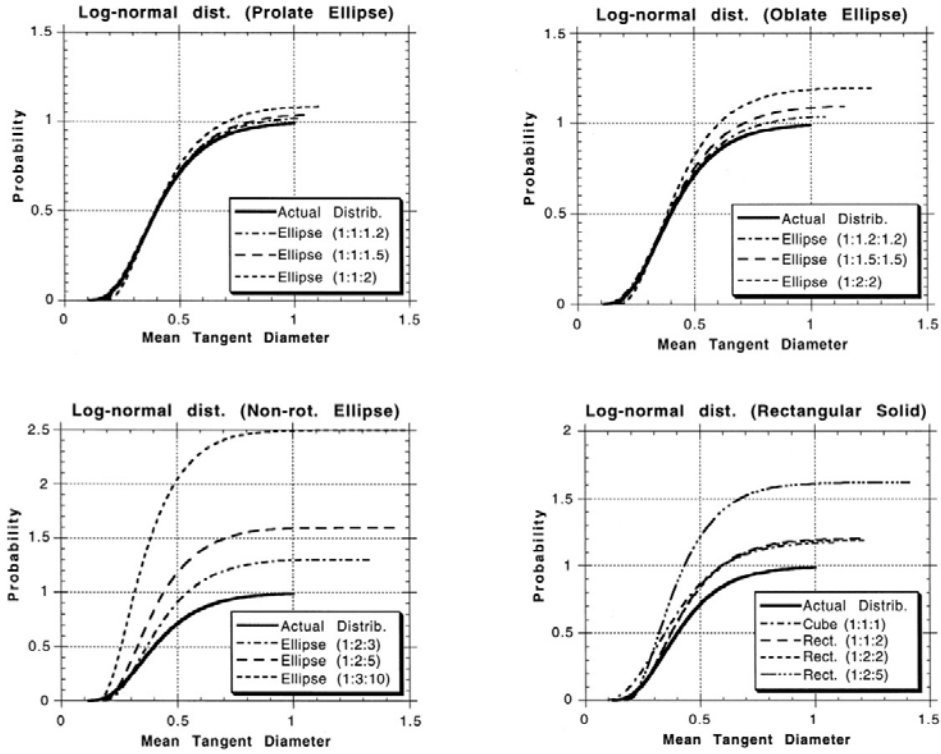
Figure A.5: Differences in the resulting particle-size distributions after stereological conversion assuming spherical conversion coefficients for particles of different shapes in a numerical experiment on 10^6 thin sections, compared to the actual particle-size distribution (Sahagian and Proussevitch, 1998). For rotational ellipsoids (a and b) the resulting error is small but increases for particles with a greater aspect ratio, causing the proportion of small particles to be overestimated and the proportion of large particles to be overestimated. For non-rotational ellipsoids and rectangular particles the resulting distribution deviates more greatly than for rotational ellipsoids. Reproduced from Sahagian and Proussevitch (1998).

A.7 Permeability measurements

The gas permeability of each sample was measured with nitrogen as the permeant. A confining pressure of 1 MPa was applied radially to each sample to ensure that the gas flows through the sample instead of between the jacket and the sample edge. Each sample was left for ~1 hour at this confining pressure to allow for any necessary microstructural equilibrium. During the measurement gas flows through the sample, with the values of the volumetric flow rate, Q, and the pressure differential across the sample, ∇P, being continuously monitored with a LabVIEW program.

The flow of gas entering the sample can be adjusted using a regulator attached to the gas bottle, allowing for a range of different values of ∇P to be produced. The volumetric flow rate was recorded once steady-state flow was achieved through the

223

sample. Using this data and the measured dimensions of the samples, the permeability can then be calculated using Equations 5.1 and 5.2. This measurement of permeability may then need to be corrected for the effects of gas turbulence and gas slippage. The need for corrections is checked for each individual measurement and the appropriate correction is then applied where required.

Python code used to process the data and example figures can be found as a Jupyter notebook in Appendix B.4.

A.7.1 Correcting for gas turbulence (Forchheimer correction)

Fluid flow experiments have shown that the relationship between the pressure differential and volumetric flow rate becomes non-linear at high fluid velocities due to turbulent, rather than laminar flow (Forchheimer, 1901). While Forchheimer corrections may be avoided by using lower volumetric flow rates, this may still prove to be an issue for samples with a high connected porosity and large pore networks. The Forchheimer correction is given as:

$$\frac{1}{k_{\mathrm{meas}}} = \frac{1}{k_{\mathrm{forch}}} + \zeta Q \tag{A.5}$$

where k_{meas} is the permeability calculated from the raw measured data, k_{forch} is the permeability given by the Forchheimer correction, and ζ is a constant encompassing the various geometric and viscosity constants in Darcy's Law (Kushnir et al., 2017). To assess the need for the Forchheimer correction, $\frac{1}{k_{meas}}$ is plotted against Q. A Forchheimer correction is required where this relationship is non-linear. An equation fitted to the linear portion of this curve (preferably at low Q to minimise the effects of turbulence) has a gradient equal to ζ and a y-intercept equal to the inverse of the permeability corrected for the Forchheimer effect, k_{forch}. Turbulence will introduce resistance to fluid flow and therefore the corrected permeability (k_{forch}) will be lower than the measured permeability (k_{meas}).

A.7.2 Correcting for gas slippage (Klinkenberg correction)

During laminar flow in liquids, the layer of molecules next to the pore walls is static. For laminar flow in gases, this layer of molecules is not static due to molecular diffusion

(also known as slip; Farquharson et al., 2017). The effect of slippage alters the fluid flow rate that results from the same pressure differential in measurements in a gas or a liquid. As the characteristic pore size approaches the mean free path length for a molecule of the permeant gas (the distance travelled between molecular collisions), interactions between the walls of the pores and the gas molecules will reduce the resistance to flow (Klinkenberg, 1941). Corrections for gas slippage are therefore necessary for samples that have a low permeability, and correct for the measurement of permeability being artificially higher than it would be if determined using a liquid.

The equation for the Klinkenberg correction is

$$k_{\text{meas}} = k_{\text{klink}} \left(1 + \frac{\psi}{P_m} \right), \qquad (A.6)$$

where k_{klink} is the permeability corrected for the Klinkenberg effect, ψ is a constant depending on the geometry of the flow path, and P_m is the mean pressure across the sample, where $P_m = \frac{P_{\text{up}} + P_{\text{down}}}{2}$. To apply the Klinkenberg correction, the measured permeability values for a sample at different values of ∇P, k_{meas}, are plotted against $1/P_m$. The corrected permeability, k_{klink}, is given by the y-intercept of an equation fitted to the linear portion of the plotted curve.

A.7.2.1 Experimental error in permeability measurements

Sources of error in the permeability measurements include the measurement of the dimensions of each sample and the resolution of the flowmeters and pressure tranducer. Repeat measurements of the sample dimensions suggest that the error in the calculated sample volume is <0.05 cm^3. As permeability is a function of a linear regression line fitted to the data on a plot of $\langle u \rangle = Q/A$ against ∇P, the relative precision of the flowmeters and pressure tranducer is encompassed by the coefficient of determination (r^2 value) of the regression line. The r^2 value of the regression lines for these measurements have always had a value >0.99, or do so after the appropriate correction has been applied to the data. Example plots can be seen in the Jupyter Notebook in Appendix B.4. Repeat measurements indicate that the experimental error is always smaller than the symbol size on a plot.
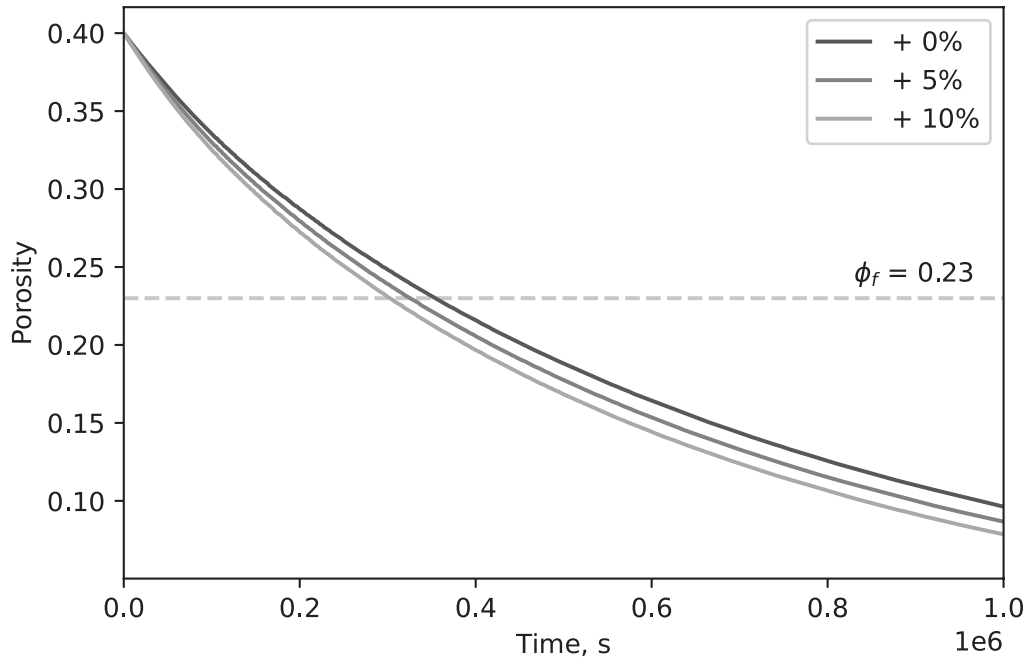
Figure A.6: The effect of adding different percentages of particles <1 μm in diameter to the particle-size distribution used to calculate sintering times for sample TF1 at 750 °C and $\Delta P = 0.1$ MPa. The dashed line shows the measured final porosity of the sample. Adding 5% or 10% extra <1 μm particles reduces the calculated sintering time by 7.5% and 15% respectively.

A.8   Sensitivity analysis for sintering time estimates

The measured particle-size distributions for each sample can only provide the final particle-size distribution, after sintering has taken place. This may therefore not represent the initial particle-size distribution that was deposited within the tuffisite, with fines perhaps being under-represented in the measured distribution. By adding different percentages of fine-grained material to the distributions it is possible to consider the effect that missing fine-grained particles may have on the calculated sintering time (Figure A.6). Adding 5% and 10% extra <0.1 μm diameter particles to the distribution reduces the calculated sintering time at 750 °C and $\Delta P = 0.1$ MPa by 7.5% and 15% respectively. While potentially altering the expected sintering value, these values with extra added fines still allow sintering at 750 °C to match the expected conductive cooling time of individual units (0.1 or 0.2 m thick) in the tuffisite.

B Jupyter notebooks

The Jupyter notebooks in this section contain the Python code used to process the data in this thesis. Interactive versions of this code can be found at:

https://github.com/hollyeunwin/unwin_PhD_thesis

B.1 Particle sorter: Worked example

This Python code is used to process the particle-size data from ImageJ for an individual image within an image nest. The interactive version of this code and the BSE images used can be found at:

https://github.com/hollyeunwin/unwin_PhD_thesis

Particle_sorter_worked_example

This notebook file gives details of the Particle_sorter function that does the initial data processing

NB: This notebook runs the Particle_sorter function for one inputted .csv file to demonstrate how it works. To combine data from multiple nested images the Particle_sorter function is run multiple times in a loop - see notebook Particle_size_analysis.ipynb for details.

This notebook contains the code in full, including the functions within it (bin_creator, size_filter and normalise_data) that can be found in Particle_functions_area_fixed.py

In [1]:
```python
import pandas as pd
import numpy as np
from pandas import Series
from pandas import DataFrame
import matplotlib.pyplot as plt
import math
from textwrap import wrap

from Particle_functions import bin_creator
from Particle_functions import size_filter
from Particle_functions import normalise_data
from Particle_errors import MinBinTooBig
```

1. Inputting particle size data

Import the file outputted from ImageJ/Fiji (only for demo purposes so this notebook can produce outputs - see notebook Particle_size_analysis.ipynb to see how to input data for multiple images).

In [2]:
```python
file_path = 'Results.csv'

# insert file name in the format
# pd.read_csv(r'Path to your file name here\File name'.csv)
size_data = pd.read_csv(file_path)

# Displays only first 5 rows of dataframe size_data
size_data.head(5)
```

		Area	Major	Minor	Angle	Circ.	Feret	FeretX	FeretY	FeretAngle	MinFeret	
0	1	0.812	1.484	0.697	60.215	0.743	1.508	291	260	60.124	0.733	2.1
1	2	0.853	1.059	1.026	166.796	0.911	1.091	485	212	109.359	1.034	1.0
2	3	1.715	1.763	1.238	142.296	0.850	1.762	557	228	158.703	1.251	1.4
3	4	0.527	0.986	0.680	105.799	0.853	1.039	865	212	110.376	0.696	1.4
4	5	1.355	1.644	1.050	127.455	0.851	1.648	1038	214	127.451	1.043	1.5

Give the image area and scale of image to allow data to be filtered (for demo purposes only - normally inputted as part of file_list.txt. See Particle_size_analysis.ipynb).

In [3]:

```python
im_area = 3600 # um^2   Give area of image here
pix_per_um = 36 # scale of the image in pixels per micron

# Give minimum pixel diameter of particles to consider
min_size_threshold = 10
```

2. Filtering particle size data

Particles that are too big to be properly represented or too small to be seen need to be filtered from the data. Particles > 1% of the image area or < 10 pixels across are discarded.

This is the code for the size_filter function found in Particle_functions_area.py

In [4]:

```python
# Changing minimum particle diameter above from
# pixels into microns
min_area = (min_size_threshold /(2*pix_per_um))**2 * math.pi

max_area = round(im_area / 100 , 1) # An area > 1% of the total image area

print("Particles smaller than", round(min_area,1), \
      "um^2 in area will be discarded.")
print("Particles larger than", max_area, \
      " um^2 will also be discarded.")
```

```
Particles smaller than 0.1 um^2 in area will be discarded.
Particles larger than 36.0  um^2 will also be discarded.
```

The equivalent diameters of each particles are calculated from the area data.

```python
# Calculates the equivalent diameter from the area of each particle
Eq_di = (size_data["Area"] / math.pi) ** (1/2) *2

# Copies dataframe size_data to allow
# calculated equivalent diameter data to be added
size_data=size_data.copy()

# places equivalent diameter (Eq Di) column into dataframe
size_data["Eq Di"] = Eq_di

size_data.head(5) # Displays first 5 rows of dataframe size_data
```

Out[5]:

	Area	Major	Minor	Angle	Circ.	Feret	FeretX	FeretY	FeretAngle	MinFeret	
0	1	0.812	1.484	0.697	60.215	0.743	1.508	291	260	60.124	0.733	2.1
1	2	0.853	1.059	1.026	166.796	0.911	1.091	485	212	109.359	1.034	1.0
2	3	1.715	1.763	1.238	142.296	0.850	1.762	557	228	158.703	1.251	1.4
3	4	0.527	0.986	0.680	105.799	0.853	1.039	865	212	110.376	0.696	1.4
4	5	1.355	1.644	1.050	127.455	0.851	1.648	1038	214	127.451	1.043	1.5

The calculated size thresholds are then used to filter out any data that is too large or too small and the area of measured particles is calculated.

The area of measured particles is considered to be the total area of particles excluding those that have been filtered from the data for being too large. Particles filtered out for being too small are considered to still be in the pore space between the other particles and so are not removed from the total area measured.

In [6]:

```python
# Finds the total area of all measured particles
# before filtering takes place
total_area = round(sum(size_data["Area"]), 1)
print("A total particle area of", total_area, "um^2 has been \
measured in the image")
```

A total particle area of 124.8 um^2 has been measured in the image

In [7]:

```python
# Filters out any values that are too big
data_not_bigs = size_data[ size_data["Area"] < max_area ]

# Calculates the number of particles that are filtered
# out for being too big
too_big = len(size_data) - len(data_not_bigs)

# Calculates the total area of all remaining particles
# now particles too large have been removed
total_area_not_bigs = round(sum(data_not_bigs["Area"]),1)

# Calculates the area of particles >1% image area that are excluded
area_too_big = total_area - total_area_not_bigs
```

```
In [8]:   # Filters out any values that are too small
          filtered_data = data_not_bigs[ data_not_bigs["Area"] > min_area]

          # Calculates the number of particles that are filtered
          # out for being too small
          too_small = len(data_not_bigs) - len(filtered_data)
```

```
In [9]:   # Calculates the total number of removed particles
          no_removed = too_small + too_big
          particles_remaining = len(size_data) - no_removed

          print(f"Filtering has removed {no_removed} particles from the data.")
          print(f"{too_small} particles were smaller than 10 pixels across.")
          print(f"{too_big} particles were larger than 1% of the image area")
          print("The remaining area of particles once those too large are \
          removed is", total_area_not_bigs, "um^2")
          print("There are", particles_remaining, "particles remaining")
```

```
Filtering has removed 1 particles from the data.
1 particles were smaller than 10 pixels across.
0 particles were larger than 1% of the image area
The remaining area of particles once those too large are removed is 124.8 u
m^2
There are 84 particles remaining
```

3. Sort data in equivalent diameter bins

The data are sorted into geometric bins, each $10^{0.1}$ larger than the previous bin.
Geometric bins are chosen so that the stereological conversion is simpler (Sahagrian & Proussevitch, 1998).
The first (smallest) bin is taken to be the minimum size threshold, beneath which any data has been filtered out.

This is the code for bin_creator found in Particle_functions_area.py

```
In [10]:    bins = np.zeros(46) # Creates empty array of bins to iterate over below
            # 10^(bin_multiplier) gives the size of the next bin
            # (See Sahagrian & Proussevitch, 1998)
            bin_multiplier = 0.1


            # The first bin value is the minimum diameter
            # (10 / scale of the image, as calculated above)
            bins[0] = min_area
            # The 2nd bin is 10^(bin_multiplier) larger than the first bin
            bins[1] = bins[0] * (10**bin_multiplier)

            for index, value in enumerate(bins): # Creates geometric bins
                if index < len(bins)-1:
                    bins[index+1] = value * 10**bin_multiplier
```

```
In [11]:    # Bin edges are sorted into lower and upper bounds
            # to display each bin clearly
            bins_lower = bins[:-1]
            bins_upper = bins[1:]

            # Bin edges are placed in the dataframe bins_df
            bins_df = pd.DataFrame(data = bins_lower, columns = ['Bins lower'])
            bins_df['Bins upper'] = bins_upper
            bins_df.head(5)
```

Out[11]:

	Bins lower	Bins upper
0	0.060602	0.076293
1	0.076293	0.096047
2	0.096047	0.120916
3	0.120916	0.152225
4	0.152225	0.191639

The data can then be sorted into the created bins.

```
In [12]:    # Places data into bins, outputting 2 arrays:
            # binned data (counts) and bins
            counts, bins_out = np.histogram(filtered_data["Area"], bins)

            # Checks that numbered of pieces of data binned matches
            # the expected number of data points

            if sum(counts) != len(filtered_data["Area"]):
                raise MinBinTooBig (min_bin_size)
            else:
                    print("All data binned successfully")

            # Places the count for each bin into the dataframe bins_df
            bins_df['Counts'] = counts

            bins_df.head(5) # Displays the first 5 rows of the dataframe bins_df
```

Out[12]:

	Bins lower	Bins upper	Counts
0	0.060602	0.076293	0
1	0.076293	0.096047	0
2	0.096047	0.120916	0
3	0.120916	0.152225	1
4	0.152225	0.191639	0

In this code the minimum bin size is set as the equivalent diameter of the particle of the minimum area that could be imaged. When combining different images (running this code in a loop in Particle_size_analysis.pynb) the bin size needs to be fixed across images. The minimum bin size is then defined by the user as an input and the code checks if the chosen minimum bin size will cause data to be discarded. If the minimum bin size is too large this causes an error and suggests to the user that they should reduce the minimum bin size.

In [13]:

```python
#Plots a histogram of the binned particle areas
plt.hist(bins[:-1], bins, weights=counts, color='silver', \
         density = False, edgecolor='black',
             linewidth=0.5)
plt.xscale('log')
plt.xlabel("Particle area, $\mathregular{\mu m^{2}}$")
plt.ylabel("Particle frequency")
#plt.xlim([1, 10**2])
plt.title("Plot of particle areas")
```

Out[13]: Text(0.5, 1.0, 'Plot of particle areas')
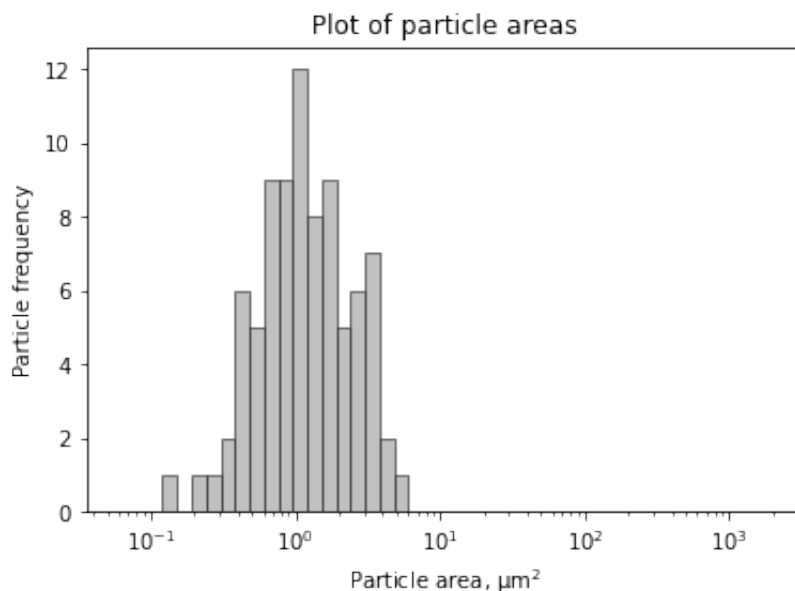
In [14]:
```python
#Finds the geometric mean of the data
a = sum(counts*np.log10(bins[:-1]))/sum(counts)
mean = 10**a
print("The geometric mean is", round(mean,2))

#Plots same histogram now with the value for the geometric mean added
ax = plt.figure()
#Plots a histogram of the binned particle areas
plt.hist(bins[:-1], bins, weights=counts, color='silver', \
         density = False, edgecolor='black', linewidth=0.5)
plt.xscale('log')
plt.xlabel("Particle area, $\mathregular{\mu m^{2}}$")
plt.ylabel("Particle frequency")

mean_y=[0.0, 15]
plt.plot([mean, mean],mean_y, color='grey', linestyle='dashed')
plt.ylim([0,15])
microns = "$\mathregular{\mu}$"
ax.text(.85, .85, f"n = {particles_remaining} \n \
Mean = {round(mean,1)} {microns}m", horizontalalignment="right", \
        verticalalignment="top", bbox=dict(boxstyle = "square",
                     facecolor = "white"))
```

The geometric mean is 1.02

Out[14]: Text(0.85, 0.85, 'n = 84 \n Mean = 1.0 $\\mathregular{\\mu}$m')
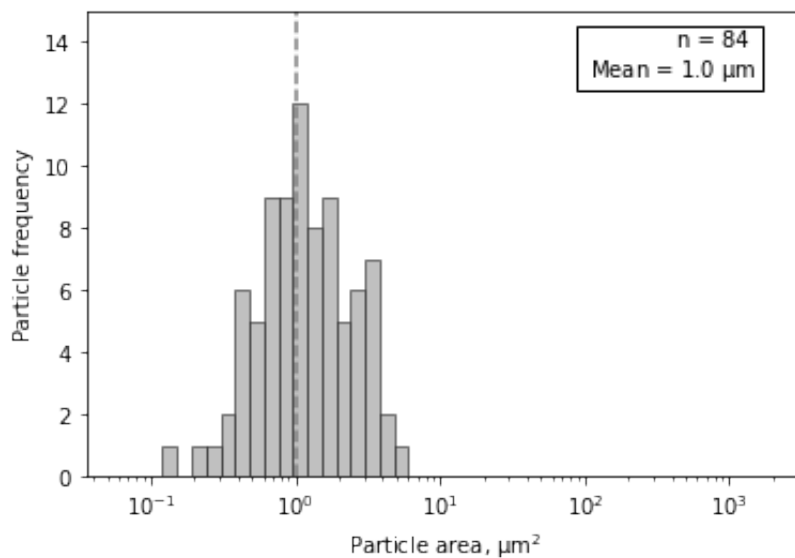
In [15]:
```python
#Outputs the filtered data as a .csv file
filtered_data.to_csv('filtered_data.csv', index=False)
```

4. Normalising data

The total area of particles in each bin is normalised by the image area measured to reduce the bias of small particles. The image area to normalised by is taken as:

Total particle area = total area of measured particles - area of large particles filtered out.

The large particles that are not sufficiently represented in the image are not considered to be part of the measured area. Particles too small to measure are assumed to still be present in the pore space between measured particles, and so are still included in this total measured area.

First, the total area of particles sorted into each bin is calculated.

In [16]:
```python
# Creates an array to hold the sum values of each bin
total_bin_values = np.zeros(len(bins)-1)

for index in range(0,len(bins)-1):
     # Takes values that are greater than or equal to the lower bin value
    bin_total = filtered_data[filtered_data["Area"] >= bins[index]]

    # Takes values that are less than the upper bin value
    bin_total = bin_total[bin_total["Area"] < bins[index+1]]

    # Sums the equivalent diameters for that bin
    # and places into an array of sum values
    total_bin_values[index]=sum(bin_total["Area"])
```

In [17]:
```python
# Checks that the total area in each bin matches that expected
if round(sum(total_bin_values),1) == round(sum(filtered_data["Area"]),1):
    print("The sum of each bin has been calculated successfully.")
else: print("ERROR: bin totals not calculated correctly.")
```

```
The sum of each bin has been calculated successfully.
```

In [18]:
```python
# Normalises the bin totals calculated by the measured particle area
normal_bin_values = total_bin_values / total_area_not_bigs

# Places the calculated bin totals and normalised
# values into the dataframe bins_df
bins_df["Total bin values"] = total_bin_values
bins_df["Normalised bin values"] = normal_bin_values

bins_df.head(5) # Displays the first 5 values of bins_df
```

	Bins lower	Bins upper	Counts	Total bin values	Normalised bin values
0	0.060602	0.076293	0	0.000	0.000000
1	0.076293	0.096047	0	0.000	0.000000
2	0.096047	0.120916	0	0.000	0.000000
3	0.120916	0.152225	1	0.129	0.001034
4	0.152225	0.191639	0	0.000	0.000000

In [19]:

```python
sum(bins_df["Total bin values"])
```

Out[19]: 124.75300000000001

In [20]:

```python
sum(bins_df["Normalised bin values"])
```

Out[20]: 0.9996233974358976

In [21]:

```python
#Plots a histogram of the binned area data
plt.figure()
plt.hist(bins[:-1], bins, weights=normal_bin_values, \
         color='silver', density = False, \
         edgecolor='black',linewidth=0.5)
plt.xscale('log')
plt.xlabel("Particle area, microns")
plt.ylabel("Particle fraction")
plt.title("Plot of the fraction of measured particles within each bin")
```

Out[21]: Text(0.5, 1.0, 'Plot of the fraction of measured particles within each bin'
)
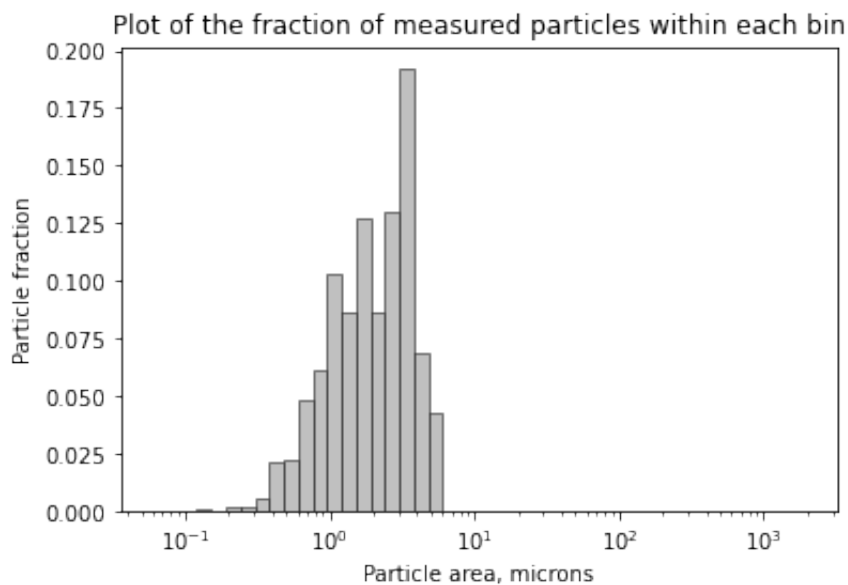
In [22]:
```python
#Finds the geometric mean of the data
a = sum(normal_bin_values*np.log10(bins[:-1]))/sum(normal_bin_values)
mean = 10**a
print("The geometric mean is", round(mean,2))

#Plots the same histogram as above, now with the
# value for the geometric mean added
plt.hist(bins[:-1], bins, weights=normal_bin_values, \
        color='silver', density = False, edgecolor='black',
            linewidth=0.5) #Plots the binned particle areas
plt.xscale('log')
plt.xlabel("Particle area, $\mathregular{\mu m^{2}}$")
plt.ylabel("Particle fraction")

mean_y=[0.0, 1]
plt.plot([mean, mean],mean_y, color='grey', linestyle='dashed')
plt.ylim([0,max(normal_bin_values)+0.05])
```

The geometric mean is 1.68

Out[22]: (0.0, 0.24220352564102565)
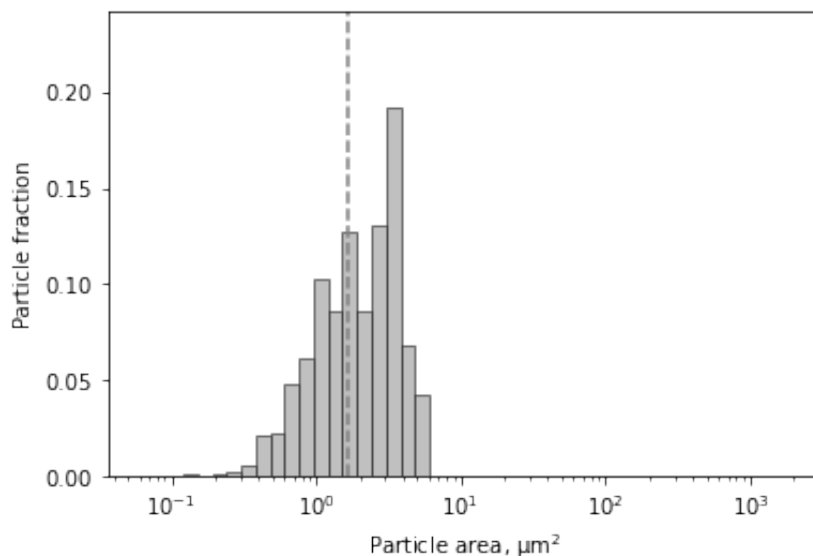
This is now the final distribution for one of the images within the image nest. This code is run in a loop to produce distributions for each image in the image nest by running Particle_analysis, which then also combines those to produce a single distribution.

B.2 Fixed bins controller: Combining particle-size distributions

This Python code processes the particle-size data for image nests by running the code in Appendix B.1 in a loop and performing the stereological conversion (Appendix A.6). The interactive version of this code can be found at:

https://github.com/hollyeunwin/unwin_PhD_thesis

Fixed bins controller: Combining particle-size distributions

This notebook explains the process of combining the different particle-size distributions within each image nest. For the creation of the particle-size distributions see Particle_sorter_worked_example for explanation of the Particle_sorter function.

```python
In [1]:
import pandas as pd
import numpy as np
from pandas import Series
from pandas import DataFrame
import matplotlib.pyplot as plt
import math
import openpyxl
from glob import glob
#As explained in notebook Particle_sorter_worked_example
from Particle_sorter_perarea_fixedbins import Particle_sorter

#Explanation for these functions can be found in
# Particle_sorter_worked_example as well as the .py file
from Particle_functions_area_fixedbins import bin_creator
from Particle_functions_area_fixedbins import size_filter
from Particle_functions_area_fixedbins import normalise_data

from Particle_errors import IncorrectNumberOfFiles
from Particle_errors import MinBinTooBig
from textwrap import wrap
import os
import seaborn as sns
```

1. Inputting data

The code requires values for min_size_threshold, min_bin_size, and bin_multiplier to be inputted below.

Place the output .csv files from ImageJ for the image nest that you would like to combine into a folder. These files do not need to be processed before running this code. Give the name of the folder containing the files below (as file_path).

The input .txt file needs to contain the names of the .csv files that you have placed in the folder, as well as the area of each image and its scale (see file_list.txt). An error will be raised if these do not match.

Note: Changing the titles of the individual columns in the .txt or .csv files (from ImageJ) inputted will break the code

```
In [2]:
min_size_threshold = 10 # Give minimum diameter of particles to consider
min_bin_size = 0.1 # Give the size of the lower bound of the smallest bin
bin_multiplier = 0.2 # Multiplier to make geometric bins

# Give the name of the .txt file containing the list of files,
# areas and scales
file_name = "file_list.txt"

# Give folder name containing data files to be inputted.
# The outputs will be saved here.
#Must be a folder within current working directory in
# terminal unless you add a folder structure below.
file_path = "DM9B_19-21_data"

#Imports the information from the .txt file (file names, areas and scales)
file_list = pd.read_csv(f'{file_path}/{file_name}', sep = "\t")
print(file_list)

# Takes all .csv files from the folder at the given file path
files = glob(f'{file_path}/*.csv')
print("Data will be taken from the files:", files)


# Takes the columns from file_list and creates named variables
filenames = file_list["Filename"]
im_areas = file_list["Image size"]
pix_per_ums = file_list["Scale"]

#Checks that the number of files found matches the number expected
# in the .txt file.
#If these do not match then the error is raised.
if len(files) != len(filenames):
    raise IncorrectNumberOfFiles(len(files))

# Checks if output folder exists in current directory
if not os.path.exists(f'{file_path}/Output'):
    # If does not exist, makes folder
    os.makedirs(f'{file_path}/Output')
```

```
               Filename   Image size   Scale
0    DM9B_19-21_50um.csv    8455.820   12.96
1   DM9B_19-21_100um.csv   55456.177    5.33
2   DM9B_19-21_400um.csv  781317.695    1.42
Data will be taken from the files: ['DM9B_19-21_data/DM9B_19-21_100um.csv',
'DM9B_19-21_data/DM9B_19-21_400um.csv', 'DM9B_19-21_data/DM9B_19-21_50um.cs
v']
```

```
In [3]:
#To create a non-fixed bin size if needed
#min_bin = (min_size_threshold/(2*max(pix_per_ums)))**2*math.pi

#Sorts the data from the .txt file so that the images
# are listed from high to low magnification
file_list.sort_values("Scale",ascending=False)
file_list.reset_index(drop=True)

file_list
```

	Filename	Image size	Scale
0	DM9B_19-21_50um.csv	8455.820	12.96
1	DM9B_19-21_100um.csv	55456.177	5.33
2	DM9B_19-21_400um.csv	781317.695	1.42

2. Running the Particle_sorter function for each image within the nest

The Particle_sorter function processes each .csv file within the chosen folder in a loop. See Particle_sorter_worked example for explanation.

This function outputs the filtered and binned data that can then be combined to produce a single particle-size distribution for the image nest.

Below each filename will be outputted alongside information on the number of particles filtered out. A frequency distribution of each particle-size distribtution is also plotted, with n giving the number of particles remaining after filtering. This information is saved within the "_stats.csv" file outputted for each image. The plots are also outputted as "_raw_hist".

The code can be edited to produce different plots - the code for each plot is within the Particle_sorter function.

In [4]:

```python
data_output = pd.DataFrame() #Creates empty dataframe to hold data
filtered_output = pd.DataFrame(index = range(1000))
no_filtered = np.zeros(len(filenames))
bin_counts = pd.DataFrame(index = range(45))
particles_too_big = np.zeros((len(filenames)))
total_inputted = 0
total_filtered_out = 0

# Creates loop to run the Particle_sorter function for the data
# from each inputted file (runs once per image)
for i in range(0, len(filenames)):
    print(filenames[i])
    (bins_df, bins, filtered_data, area_too_big, stats) = \
    Particle_sorter(file_path, filenames[i], im_areas[i], \
                    pix_per_ums[i], min_size_threshold, \
                    min_bin_size, bin_multiplier)

    # Places the normalised output for each image/inputted
    # file into the dataframe data_output
    data_output[filenames[i]] = bins_df["Normal bin values"]
    bin_counts[filenames[i]] = bins_df["Counts"]
    print(stats)

    # Counts the number of filtered particles
    no_filtered[i] = len(filtered_data["Area"])
    # Creates an array of the number of particles that are too large
    particles_too_big[i] = area_too_big
    # Counts the total number of inputted particles
    total_inputted += sum(stats["No inputted particles"])
    #Places the filtered data into a dataframe filtered_output
    filtered_output[filenames[i]] = filtered_data["Area"]

# Calculates the total number of particles remaining after
# filtering across all images
particles_post_filter = sum(no_filtered)
# Calculates the number of particles removed
total_filtered_out = total_inputted - particles_post_filter

print(f"The total number of particles inputted is {total_inputted}")
print(f"A total of {total_filtered_out} particles were filtered from \
the data leaving {particles_post_filter} particles for analysis")

# Converts the array of bin edges (bins) into 2 arrays that contain the
# lower and upper bounds of each bin. These are placed into
# the dataframe data_output
data_output["Bins lower"] = bins[:-1]
data_output["Bins upper"] = bins[1:]
bin_counts["Bins lower"] = bins[:-1]
bin_counts["Bins upper"] = bins[1:]

# Removes any empty rows created in the original dataframe
filtered_output = filtered_output.dropna(how = 'all')
```

```
DM9B_19-21_50um.csv
All data binned successfully
   Min particle area  Max particle area  No inputted particles  Inputted ar
ea  \
0           0.467606               84.6                    270             1502
.7
```

```
   No too small  No too big  Total particles removed  \
0            1          2                         3

   No particles after filtering  Area remaining particles
0                           267                 1102.164
DM9B_19-21_100um.csv
All data binned successfully
   Min particle area  Max particle area  No inputted particles  Inputted ar
ea  \
0          2.76462              554.6                    351         15671
.9

   No too small  No too big  Total particles removed  \
0           47          5                        52

   No particles after filtering  Area remaining particles
0                           299                 9790.515
DM9B_19-21_400um.csv
All data binned successfully
   Min particle area  Max particle area  No inputted particles  Inputted ar
ea  \
0         38.950514             7813.2                    954         280416
.7

   No too small  No too big  Total particles removed  \
0           71          0                        71

   No particles after filtering  Area remaining particles
0                           883                278343.198
The total number of particles inputted is 1575
A total of 126.0 particles were filtered from the data leaving 1449.0 parti
cles for analysis
```


DM9B_19-21_50um - Plot of particle areas

n = 267
Mean = 2.5 μm²

DM9B_19-21_100um - Plot of particle areas

DM9B_19-21_400um - Plot of particle areas

n = 883
Mean = 182.6 µm²

n = 883
Mean = 472.7 µm²
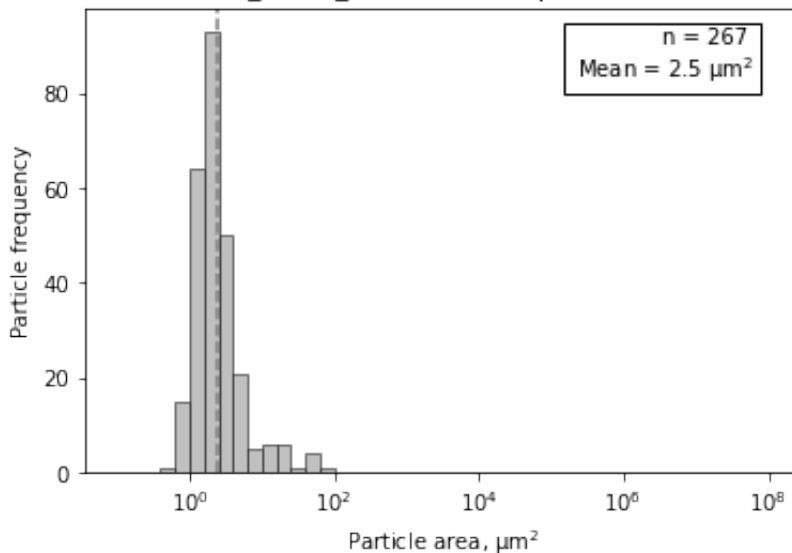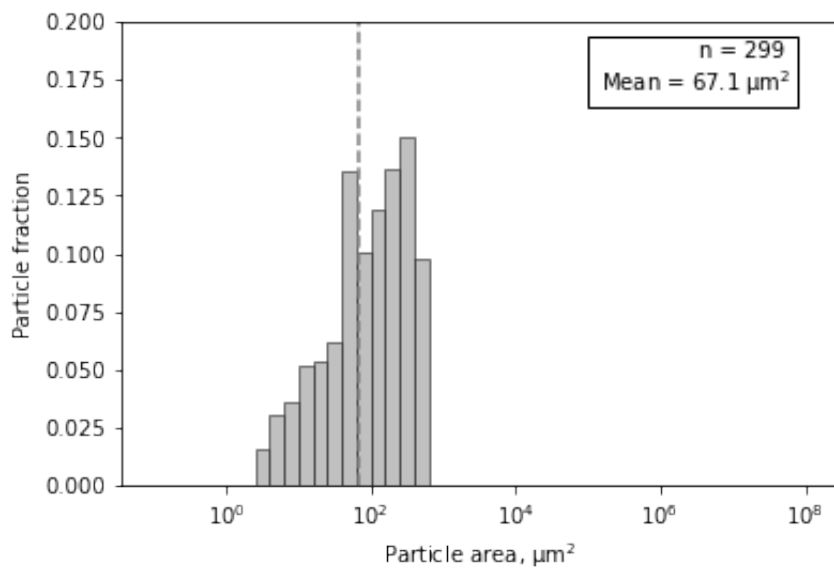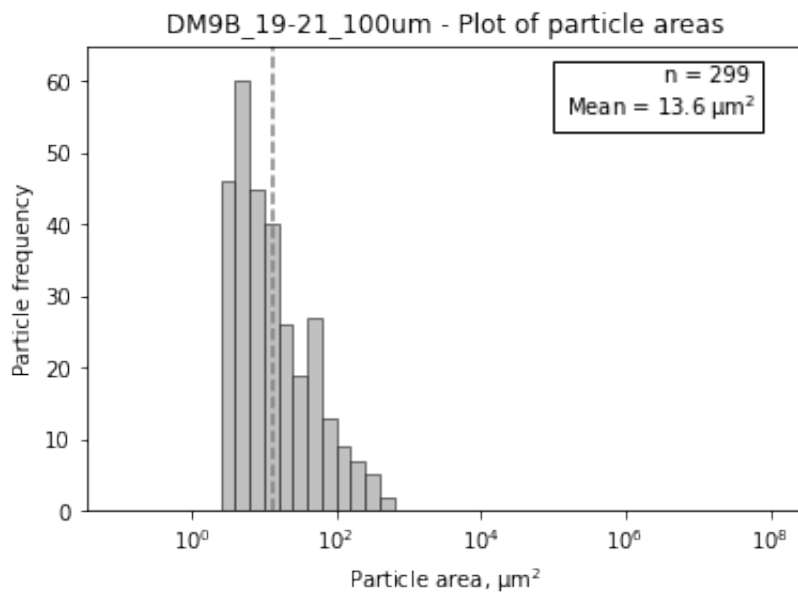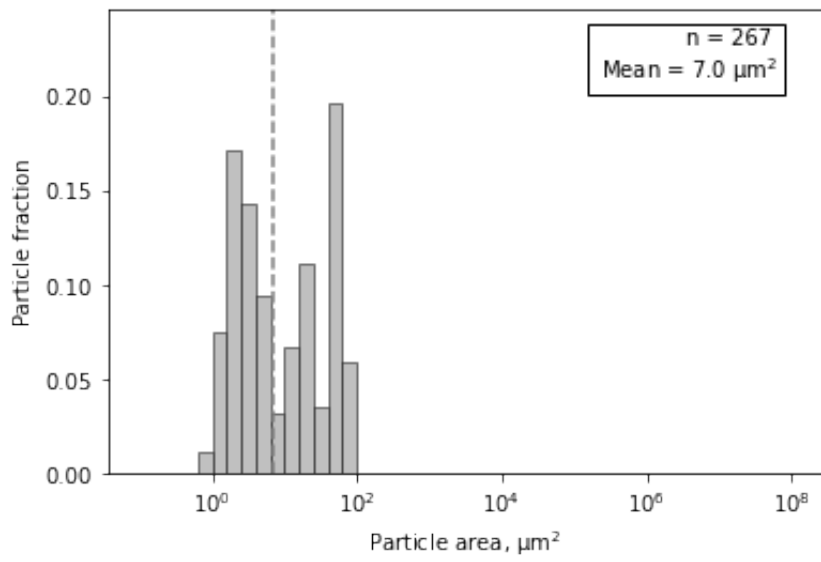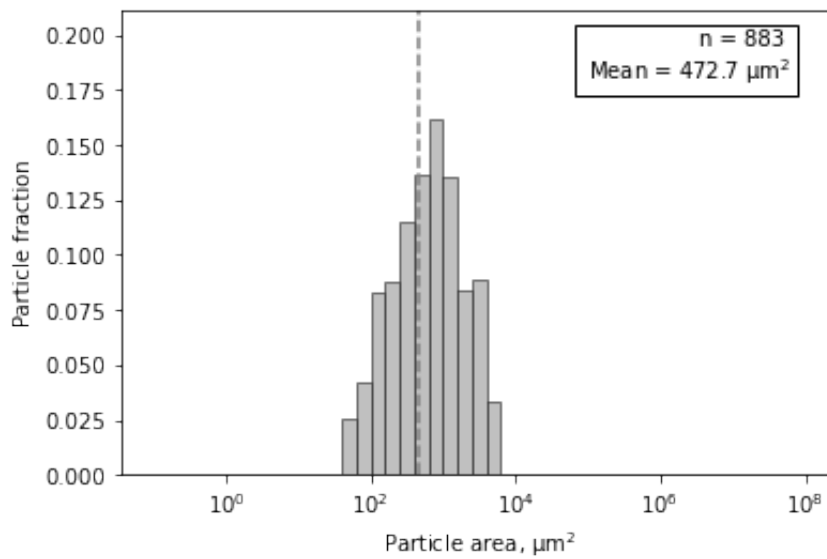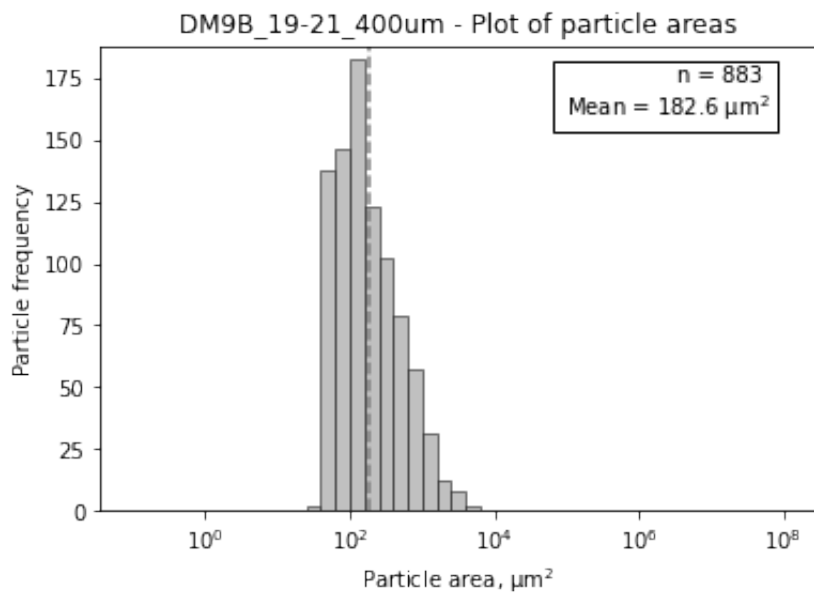
3. Combining particle-size distributions

The particle-size distributions within each image nest need to be combined. This requires each particle-size distribution to be scaled.

3.1 Identifying cutoffs and cleaning the data

First, we can lay the unscaled distributions over each other to check how they align.

```python
ax = plt.figure()
#Plots a histogram of the binned equivalent diameter data
for name in filenames:
    plt.hist(bins[:-1], bins, weights=bin_counts[name], \
             density = False, edgecolor='k', linewidth=0.5, \
             label=name)
plt.xscale('log')
plt.xlabel("Particle area, $\mathregular{\mu m^{2}}$")
plt.ylabel("Non-scaled counts")
plt.title("Plot of all particle areas in the image nest")
plt.legend(loc='upper right')
ax.text(.28, .85, f"n = {particles_post_filter}", \
        horizontalalignment="right", verticalalignment="top", \
        bbox=dict(boxstyle = "square", facecolor = "white"))
plt.savefig(f'{file_path}/Output/unscaled_counts')
```
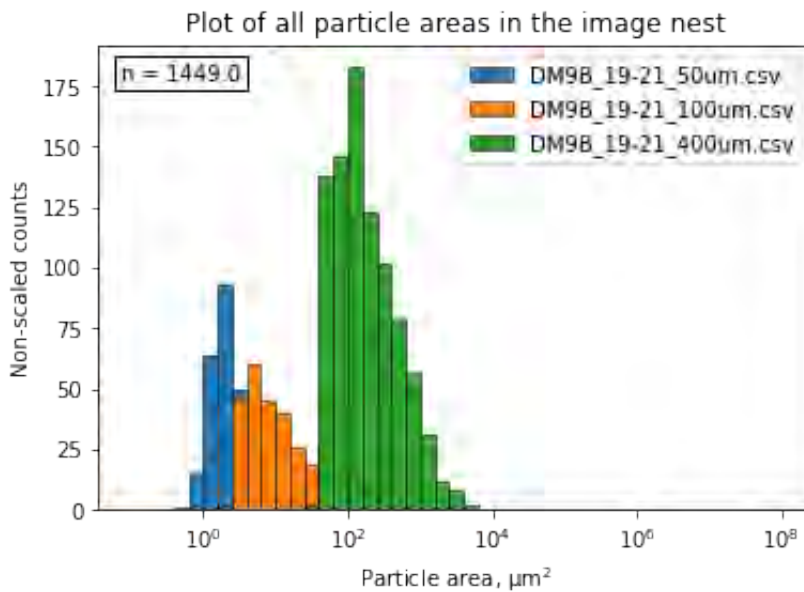

This plot looks at how the different particle fraction curves (normalised) align for each dataset.

```python
ax = plt.figure()
#Plots a histogram of the binned equivalent diameter data
for name in filenames:
    plt.hist(bins[:-1], bins, weights=data_output[name], \
             density = False, edgecolor='k', linewidth=0.5, \
             label=name)
plt.xscale('log')
plt.xlabel("Particle area, $\mathregular{\mu m^{2}}$")
#plt.xlim([1, 10])
plt.ylabel("Non-scaled particle fraction")
plt.title("Plot of particle fraction in the whole image nest")
plt.legend(loc='upper right')
ax.text(.28, .85, f"n = {particles_post_filter}", \
        horizontalalignment="right", verticalalignment="top", \
        bbox=dict(boxstyle = "square", facecolor = "white"))
plt.savefig(f'{file_path}/Output/normalised__unscaled_counts')
```

Plot of particle fraction in the whole image nest
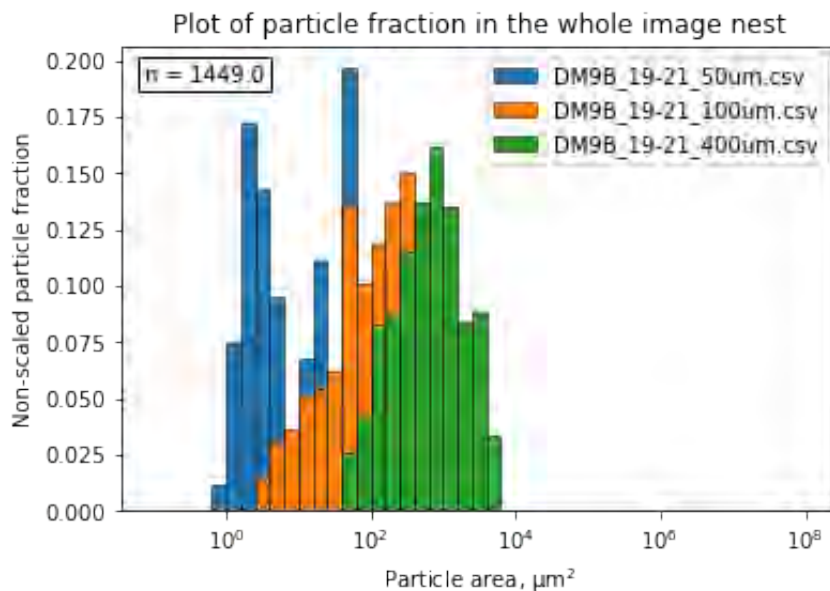
Combining the datasets requires the bin values in each dataset to be the same. In the dataframe data_output the particle fraction data show that there are some bins that only contain data from one image, others multiple images.

The data needs cleaning to remove any rows that contain no data (so bins that contain no particles from any of the images).

In [7]:
```python
data_output.head()
```

Out[7]:

	DM9B_19-21_50um.csv	DM9B_19-21_100um.csv	DM9B_19-21_400um.csv	Bins lower	Bins upper
0	0.000000	0.0	0.0	0.100000	0.158489
1	0.000000	0.0	0.0	0.158489	0.251189
2	0.000000	0.0	0.0	0.251189	0.398107
3	0.000567	0.0	0.0	0.398107	0.630957
4	0.011642	0.0	0.0	0.630957	1.000000

In [8]:
```python
# Checks for rows in data_output that contain no data
f = (data_output[filenames].T != 0).any()
f = f.where(f == True)

f =(f.dropna(how='all')) # Removes any rows that contain no data
index = f.index # Takes the index from f

# Uses the index from f to trim data_output, removing
# rows with no data while keeping bins aligned
data_output = data_output.loc[index[0]:index[-1]]
# Resets the index of data_output
data_output = data_output.reset_index(drop = True)
data_output.head()
```

	DM9B_19-21_50um.csv	DM9B_19-21_100um.csv	DM9B_19-21_400um.csv	Bins lower	Bins upper
0	0.000567	0.000000	0.0	0.398107	0.630957
1	0.011642	0.000000	0.0	0.630957	1.000000
2	0.075347	0.000000	0.0	1.000000	1.584893
3	0.171780	0.000000	0.0	1.584893	2.511886
4	0.143092	0.015776	0.0	2.511886	3.981072

3.2 Collecting the correct data from each image between cutoffs

The code combines the particle size distributions by switching from one curve to the next when the curve of the next magnification along exceeds the particle size fraction measured within a bin. This assumes that the next magnification has therefore imaged that particle size fraction better. This switching only occurs in one direction rather than continually switching back and forth between different curves.

First, we need to identify the image that has the maximum particle size fraction within each bin. This is then placed as a number in the dataframe (max_values) below.

In [9]:
```python
# Gives the name of the column with the max value in that row
names=data_output[filenames].idxmax(axis=1)

# Creates new dataframe max_values containing names
max_values=pd.DataFrame(data = names, columns = ['Names'])

for i in range(len(filenames)):
    # Replaces the names with a numerical column value
    # as named in the file "filenames"
    names = names.replace(to_replace = filenames[i], value=i)

# Adds the number of the column with the maximum value
# for each row to the dataframe
max_values["Column number"] = names

max_values.head(10)
```

	Names	Column number
0	DM9B_19-21_50um.csv	0
1	DM9B_19-21_50um.csv	0
2	DM9B_19-21_50um.csv	0
3	DM9B_19-21_50um.csv	0
4	DM9B_19-21_50um.csv	0
5	DM9B_19-21_50um.csv	0
6	DM9B_19-21_100um.csv	1
7	DM9B_19-21_50um.csv	0
8	DM9B_19-21_50um.csv	0
9	DM9B_19-21_100um.csv	1

The dataframe now contains the maximum value from each column. If we assume that the smaller particle sizes can only be better imaged by a larger magnification, then we want to only move from each image to the next magnification once rather than switching between images.

The code below creates an array (increasing) that contains the column numbers to take the data from for the final distirbution.

In [10]:

```python
# Creates empty array to hold values from loop
increasing = np.zeros(len(names))
increasing[0] = 0 # Sets first value of array to zero

# Creates another empty array to hold values from loop
switch = np.zeros(len(names))

# Changes any column values that are not increasing,
# so only moves from high mag to low mag image
for i in range(1,len(names)):
    if names[i] >= increasing[i-1]:
        increasing[i] = int(names[i])
    else:
        # Array of integer column values that show which
        # image provides data for each bin size
        increasing[i] = int(increasing[i-1])

    if increasing[i] != increasing[i-1]:
        # If the number has changed, record as True in the array switch
        switch[i] = True
```

In [11]:

```python
# Changes values in increasing to integers
increasing = increasing.astype(int)

increasing
```

Out[11]: `array([0, 0, 0, 0, 0, 0, 1, 1, 1, 1, 1, 1, 1, 1, 1, 2, 2, 2, 2, 2, 2])`

The array "increasing" now contains the number of the image that we would like to take the data from for each bin. The values in this array are now only increasing, and so we are only moving from each image to the next magnification once.

The code below now takes the data needed from each image between the cutoffs.

In [12]:
```python
output = np.zeros(len(increasing)) # Creates empty array output

# Loop passes through the rows of data_output,
# taking the value from the column given by the array increasing
for index, number in enumerate(increasing):
    # Takes the desired values from data_output and places into output
    output[index] = data_output.iloc[index, number]

# Places output array into the dataframe max_values
max_values["output"] = output
```

To help with filtering the data we need to collect the output values at which the particle size distribution switches from one dataset to another. These are then placed in the array switch_values_trim below.

In [13]:
```python
switch_values = np.zeros(len(switch)) # Creates array switch values

# Loop passes through switch and multiplies by output to only give
# the output values where switching from one image to
# another, rather than every value
for i in range(len(switch)):
    switch_values[i] = switch[i]*output[i]

    # Removes all zeros from array
    switch_values_trim = switch_values[switch_values != 0 ]

max_values["switch values"] = switch_values # Places into dataframe
max_values["Increasing"] = increasing # Places into dataframe

# These are the values where switch from one
# image to the next magnification
switch_values_trim
```

Out[13]: `array([0.03587796, 0.13655352])`

In [14]:
```python
max_values.head()
```

Out[14]:

	Names	Column number	output	switch values	Increasing
0	DM9B_19-21_50um.csv	0	0.000567	0.0	0
1	DM9B_19-21_50um.csv	0	0.011642	0.0	0
2	DM9B_19-21_50um.csv	0	0.075347	0.0	0
3	DM9B_19-21_50um.csv	0	0.171780	0.0	0
4	DM9B_19-21_50um.csv	0	0.143092	0.0	0

Removing some of the data while combining the particle size distributions means that not all of the original particles are now included in the final distribution. By looking at the original data we can calculate the number of particles still included.

In [15]:

```python
#Creates a new dataframe to hold the count data
post_bin_counts = np.zeros(len(output))

#Looks in the correct column in the original bin_counts data
# to collect the number of particles present in that bin
for i,j in enumerate(max_values["Increasing"]):
    post_bin_counts[i] = bin_counts.iloc[i,j]

# Finds the total number of particles still included in the distribution
final_particle_number = round(sum(post_bin_counts))
print(f'The particle-size distribution now contains \
{final_particle_number} particles')
```

The particle-size distribution now contains 931 particles

To plot the distributions separately to see where they have combined we need to separate the particle-size distribution values back out into their original columns for each image.

In [16]:

```python
# Creates new dataframe to hold the trimmed data
trim_output = pd.DataFrame()

# Gives indices at which switch from one image to the next
a = np.nonzero(switch_values)[0]

# Creates array indexes that holds the index values at
# which switch from one image to the next
indexes = np.zeros(len(a)+1)
for index, number in enumerate(a):
    indexes[index+1] = number


indexes = indexes.astype(int) # Makes sure array contains integers

# Creates new dataframe to hold the data split into images
split_max_values=pd.DataFrame(index=range(len(output)))

# Filters data to separate the max output values into the
# image columns that they were taken from
for i in range(len(filenames)):
    filter_column=max_values['Increasing']==i
    split_max_values[filenames[i]]=max_values['output'][filter_column]

# Adds bin columns to dataframe
split_max_values["Bins lower"] = data_output["Bins lower"]
split_max_values["Bins upper"] = data_output["Bins upper"]

split_max_values
```

	DM9B_19-21_50um.csv	DM9B_19-21_100um.csv	DM9B_19-21_400um.csv	Bins lower	Bins upper
0	0.000567	NaN	NaN	0.398107	0.630957
1	0.011642	NaN	NaN	0.630957	1.000000
2	0.075347	NaN	NaN	1.000000	1.584893
3	0.171780	NaN	NaN	1.584893	2.511886
4	0.143092	NaN	NaN	2.511886	3.981072
5	0.094730	NaN	NaN	3.981072	6.309573
6	NaN	0.035878	NaN	6.309573	10.000000
7	NaN	0.051529	NaN	10.000000	15.848932
8	NaN	0.053935	NaN	15.848932	25.118864
9	NaN	0.061770	NaN	25.118864	39.810717
10	NaN	0.135693	NaN	39.810717	63.095734
11	NaN	0.100740	NaN	63.095734	100.000000
12	NaN	0.118818	NaN	100.000000	158.489319
13	NaN	0.136643	NaN	158.489319	251.188643
14	NaN	0.150181	NaN	251.188643	398.107171
15	NaN	NaN	0.136554	398.107171	630.957344
16	NaN	NaN	0.161669	630.957344	1000.000000
17	NaN	NaN	0.135317	1000.000000	1584.893192
18	NaN	NaN	0.084197	1584.893192	2511.886432
19	NaN	NaN	0.088576	2511.886432	3981.071706
20	NaN	NaN	0.033364	3981.071706	6309.573445

3.3 Calculating the remaining particle areas

Now that the data has been filtered it will need scaling. This scaling will be done by the area of particles measured in each image.

Here the original particle area data is refiltered to give only the particles that are still present in the final distribution.

```python
# Creates empty array to hold loop output
order = np.zeros(len(indexes))

# confirms order that image data is in - only works for
# increasing values, otherwise calls error
for i in range(0,len(indexes)):
    order[i] = max_values.at[(indexes[i]),"Column number"]

order
```

`array([0., 1., 2.])`

The bin values at which the final particle-size distribution seitches from one image to another are found. These then allow the original particle-size data to be refiltered to remove extra data.

```python
# Finds the bin values at which need to switch from one image to the next.
# Creates new array to hold bin values
bin_filter = np.zeros((len(indexes)))

# Loop takes the bin values at which switch from one image to another
for i in range(0, len(indexes)):
    bin_filter[i] = split_max_values.at[(indexes[i]), "Bins lower"]

bin_filter = np.append(bin_filter, \
                 split_max_values.at[len(split_max_values)-1, "Bins upper"]
bin_filter
```

`array([3.98107171e-01, 6.30957344e+00, 3.98107171e+02, 6.30957344e+03])`

To calculate the area of measured particles in each image the particles that are now too large (beyond the top cutoff) are removed.

```python
# Creates new dataframe the length of filtered_output
too_big_post_cutoffs = pd.DataFrame(index=range(len(filtered_output)))

# Refilters the original particle area data

# Removes particles that are too big (above the top cutoff for each image)
for i in range(len(bin_filter)-1):

    # Places data column for each image into dataframe
    re_filtered = filtered_output[filenames[i]]

    # Removes values beyond top cutoffs
    re_filtered_filter=re_filtered > bin_filter[i+1]
    out = re_filtered[re_filtered_filter].dropna() # Removes Nas
    too_big_post_cutoffs[filenames[i]] = out.reset_index(drop = True)


too_big_post_cutoffs = too_big_post_cutoffs.dropna(how = 'all')
too_big_post_cutoffs # Contains the particles excluded for being too big
```

	DM9B_19-21_50um.csv	DM9B_19-21_100um.csv	DM9B_19-21_400um.csv
0	6.365	471.155	NaN
1	8.484	495.655	NaN
2	39.521	NaN	NaN
3	59.972	NaN	NaN
4	6.644	NaN	NaN
5	11.074	NaN	NaN
6	65.431	NaN	NaN
7	17.974	NaN	NaN
8	20.761	NaN	NaN
9	6.978	NaN	NaN
10	11.574	NaN	NaN
11	52.673	NaN	NaN
12	14.468	NaN	NaN
13	17.581	NaN	NaN
14	25.089	NaN	NaN
15	60.782	NaN	NaN
16	43.426	NaN	NaN
17	17.569	NaN	NaN
18	23.362	NaN	NaN
19	13.193	NaN	NaN
20	12.360	NaN	NaN
21	11.788	NaN	NaN
22	7.127	NaN	NaN

In [20]:
```python
# Creates empty array to place values for each image into
sum_too_big = np.zeros(len(filenames))

# Loop finds the total area of the remaining particles for each image
for i in range(len(filenames)):
    # Removes any NaNs from the array
    to_add = too_big_post_cutoffs[filenames[i]].dropna()
    sum_too_big[i] = sum(to_add) # Finds the sum of the array

sum_too_big # Area of particles removed for being too big
```

Out[20]: array([554.196, 966.81 ,   0.   ])

The data is then filtered to find the particles still present between each cutoff.

In [21]:
```python
# Creates new dataframe to hold refiltered particle areas
refiltered_particles = pd.DataFrame(index=range(len(filtered_output)))

# Loop filters particles so that only those between the
# cutoffs for each image remain (creating no size overlaps between images)
for i in range(len(bin_filter)-1):
    # Places data column for each image into dataframe
    re_filtered = filtered_output[filenames[i]]

    # Filters between upper and lower cutoff
    re_filtered_filter= (re_filtered < bin_filter[i+1]) \
    & (re_filtered >= bin_filter[i])

    # Removes values beyond cutoffs
    out = re_filtered[re_filtered_filter].dropna()

    # Resets index so particles are placed into top of dataframe
    refiltered_particles[filenames[i]] = out.reset_index(drop = True)

# Removes rows of all NaNs in the dataframe
refiltered_particles = refiltered_particles.dropna(how = "all")
refiltered_particles
```

Out[21]:

	DM9B_19-21_50um.csv	DM9B_19-21_100um.csv	DM9B_19-21_400um.csv
0	0.941	141.223	689.841
1	1.983	31.399	468.160
2	2.262	40.304	678.435
3	1.608	7.498	927.888
4	1.256	24.570	840.604
...	...	...	...
239	1.078	NaN	NaN
240	5.162	NaN	NaN
241	1.238	NaN	NaN
242	4.037	NaN	NaN
243	1.673	NaN	NaN

244 rows × 3 columns

The image of particles measured in each image between the cutoffs can then be calculated. This will be needed to scale the particle-size distributions.

```
In [22]:   image_particle_area = np.zeros(len(filenames))

           for i in range(len(filenames)):
               # Removes any NaNs from the array
               to_add = refiltered_particles[filenames[i]].dropna()
               image_particle_area[i] = sum(to_add) # Finds the sum of the array

           image_particle_area

Out[22]:   array([   547.968,    8361.774, 179376.055])
```

1.4 Scaling the particle-size distributions to combine

Using the area of particles in each image and the working image area, we can estimate the effective porosity of each image. The area not made of particles is scaled to be filled by the particle size distribution from the image of the next greatest magnification.

The data is scaled from low to high magnification by the porosity each image.

```
In [23]:   # Removes particles >1% image area and those greater than the
           # upper size cutoff for each image
           working_im_area = im_areas - particles_too_big - sum_too_big
```

```
In [24]:   # Calculates the fraction of each image made from measured particles
           particle_fraction = image_particle_area/working_im_area

           # Calculates the fraction of each image not made from measured particles,
           # effectively the image porosity
           im_porosities = 1 - particle_fraction
           im_porosities

Out[24]:   0    0.926949
           1    0.828339
           2    0.770419
           Name: Image size, dtype: float64
```

```
In [25]:   # Creates an empty array to place the porosities into
           porosities = np.zeros(len(filenames))

           # The image porosity of the highest magnification image
           # is the simply the porosity already calculated
           porosities[0] = im_porosities[0]

           for i in range(1, len(filenames)):
               # Scales the porosities for the lower magnification images
               porosities[i] = im_porosities[i] * porosities[i-1]

           porosities # Contains the porosity values

Out[25]:   array([0.92694855, 0.76782729, 0.59154838])
```

The filtered particle-size data for each image is now normalised again before scaling.

```
In [26]:   # Creates empty array and dataframe to hold values
           total_norms = np.zeros(len(filenames))
           scaled_values = pd.DataFrame()

           for i in range(len(filenames)):
               norms = split_max_values[filenames[i]]

               # Removes the NaNs from the normalised values of one image column
               total_norms[i] = sum(norms.dropna())

               # Normalises particle fraction and scales to make up the fraction
               # of the image that is actually particles
               scaled_values[filenames[i]] = norms/total_norms[i] * \
               particle_fraction[i]

           scaled_values.head() # Contains the scaled values for each image
```

Out[26]:

	DM9B_19-21_50um.csv	DM9B_19-21_100um.csv	DM9B_19-21_400um.csv
0	0.000083	NaN	NaN
1	0.001711	NaN	NaN
2	0.011071	NaN	NaN
3	0.025241	NaN	NaN
4	0.021026	NaN	NaN

```
In [27]:   # Creates new dataframe to hold the NaN-removed data
           scaled_values_squish = pd.DataFrame()

           for name in filenames:
               # Moves all values to the top of the dataframe
               scaled_values_squish[name] = scaled_values[name].dropna\
               (how = "all").reset_index(drop = True)

           # Removes unnecessary NANs to create trimmed dataframe
           scaled_values_squish = scaled_values_squish.dropna(how = "all")
           scaled_values_squish
```

Out[27]:

	DM9B_19-21_50um.csv	DM9B_19-21_100um.csv	DM9B_19-21_400um.csv
0	0.000083	0.007287	0.049009
1	0.001711	0.010466	0.058023
2	0.011071	0.010954	0.048566
3	0.025241	0.012546	0.030219
4	0.021026	0.027560	0.031790
5	0.013919	0.020461	0.011974

The data is then scaled by the porosities, starting at the lowest magnification. This first data is not scaled and so can be placed straight into the final dataframe.

```python
# Creates new dataframe
particles = pd.DataFrame(index=range(100))

# Places data from highest magnification image into the dataframe
particles[0] = scaled_values[filenames[order[0]]]
particles.head()
```

	0
0	0.000083
1	0.001711
2	0.011071
3	0.025241
4	0.021026

Each subsequent image is then scaled by the porosity of the previous image, going from lowest to highest magnification.

```python
for i in range(1,len(filenames)):
    # Scales the particle data by the image porosity
    accumulating = particles[i-1] * im_porosities[i]

    # Adds the data from the next image to the array
    accumulating = np.append(accumulating.dropna(), \
                            scaled_values[filenames[order[i]]].dropna())

    a = pd.Series(accumulating)

    # Adds the new column to the dataframe
    particles = pd.concat([particles, a], ignore_index=True, axis =1)

particles.head()
```

	0	1	2
0	0.000083	0.000069	0.000053
1	0.001711	0.001417	0.001092
2	0.011071	0.009171	0.007065
3	0.025241	0.020908	0.016108
4	0.021026	0.017416	0.013418

The distributions are then combined to produce one distribution. This distribution is then normalised.

```
In [30]:   # Creates new dataframe to hold the combined particle size distributions
           combined_distributions = pd.DataFrame(index = range(100))

           for i in range(len(filenames)):
               # Adds particle distributions with file names to the dataframe
               combined_distributions[filenames[order[i]]] = particles[i]

           # Removes any rows that are all NANs
           combined_distributions = combined_distributions.dropna(how = "all")

           # Takes final data column containing entire combined distribution
           to_normalise = combined_distributions[filenames[order[-1]]]

           # Adds upper and lower bin edges to dataframe
           combined_distributions["Bins lower"] = data_output["Bins lower"]
           combined_distributions["Bins upper"] = data_output["Bins upper"]
```

```
In [31]:   #Normalises the distribution so adds to 1

           # Finds N_A (number density per area
           a = to_normalise/\
           ((combined_distributions["Bins upper"]+\
             combined_distributions["Bins lower"])/2)

           norm_counts = a/sum(a)

           sum(norm_counts)

           combined_distributions["Normalised combined"] = norm_counts
```

```
In [32]:   #Plots the binned data
           ax = plt.figure()
           plt.hist(combined_distributions["Bins lower"],\
                    combined_distributions["Bins lower"] , \
                    weights=combined_distributions["Normalised combined"], \
                    color = 'Silver', edgecolor='k', linewidth=0.5, \
                    density=False)
           plt.xscale('log')
           plt.xlabel("Particle area, $\mathregular{\mu m^{2}}$")
           plt.ylabel("$N_A$")
           text = "$\mathregular{n_{raw}}$"
           ax.text(.72, .84, f"{text} = {total_inputted} \n n = \
           {final_particle_number}", horizontalalignment="left", \
                    verticalalignment="top", bbox=dict(boxstyle = "square",
                              facecolor = "white"), size = 12)
           plt.title=("DM9B_1-3_data")
           plt.savefig(f'{file_path}/Output/{file_path}_N_A.jpg')
```
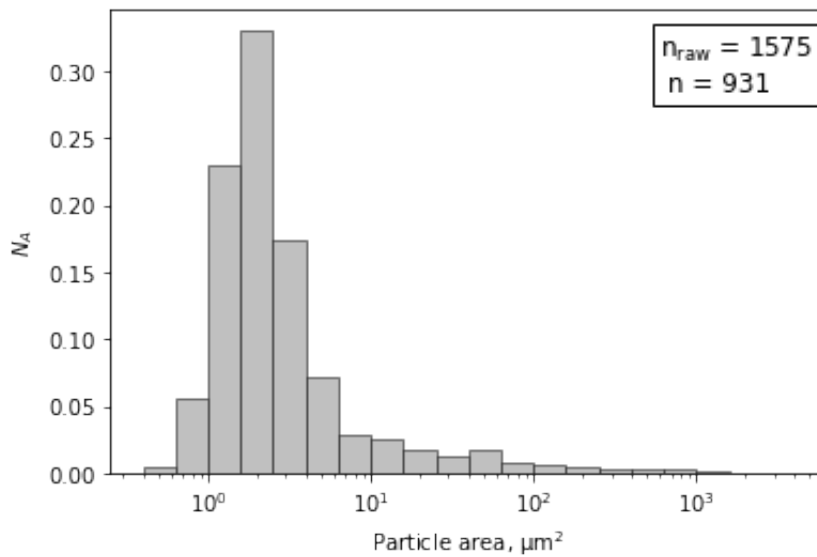
```python
area_fraction = to_normalise/sum(to_normalise)

ax = plt.figure()
plt.hist(combined_distributions["Bins lower"],\
         combined_distributions["Bins lower"] , \
         weights=area_fraction, \
         color = 'Silver', edgecolor='k', linewidth=0.5, \
         density=False)
plt.xscale('log')
plt.xlabel("Particle area, $\mathregular{\mu m^{2}}$")
plt.ylabel("Particle fraction")
text = "$\mathregular{n_{raw}}$"
ax.text(.15, .84, f"{text} = {total_inputted} \n n = \
{final_particle_number}", horizontalalignment="left", \
         verticalalignment="top", bbox=dict(boxstyle = "square",
                   facecolor = "white"), size = 12)
plt.title=("DM9B_1-3_data")
plt.savefig(f'{file_path}/Output/{file_path}_area_fraction.jpg')
```
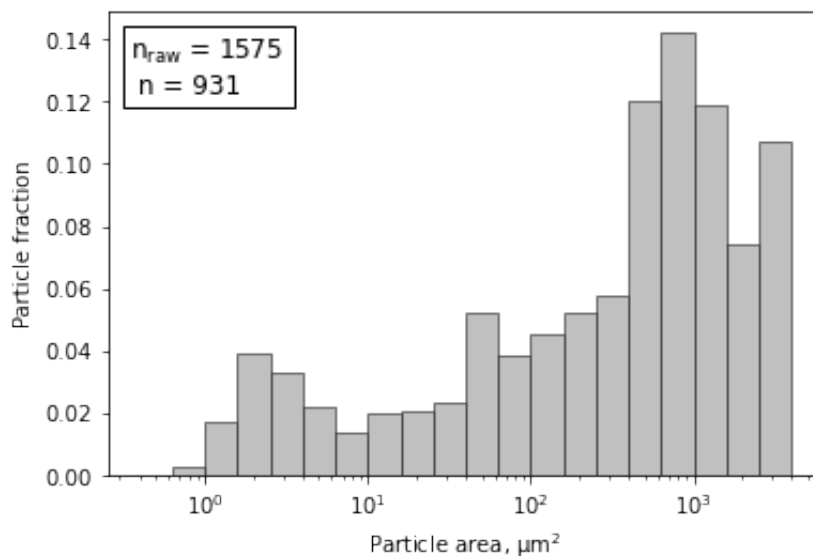
3.5 Stereological conversion

Now that the particle-size distribution has been produced from the image nest it can be converted to consider 3D particles rather than 2D intersection sizes.

In [34]:

```python
# Calculates equivalent particle radius of each bin from the area
r_bin_lower = (combined_distributions["Bins lower"]/math.pi)**0.5
r_bin_upper = (combined_distributions["Bins upper"]/math.pi)**0.5

v_bins_lower = (4/3)*math.pi*r_bin_lower**3 # Converts to volume bins
v_bins_upper = (4/3)*math.pi*r_bin_upper**3 # Converts to volume bins

r_bin_lower
stereo = pd.DataFrame()
```

In [35]:

```python
# Creates array of zeros to hold the calculated normalised bin edges
nbins = np.zeros(len(combined_distributions)+1)
nbins[0] = 1 # The upper bound of the largest bin is 1.

# Loop creates the array of normalised bin edges,
# each 10^(-0.1) smaller than the last
for i in range(0, len(nbins)-1):
    nbins[i+1] = nbins[i] * 10**-(bin_multiplier)

# Splits the normalised bin edges into lower
# and upper bounds for each bin
nbins_lower = nbins[1:]
nbins_upper = nbins[:-1]
```

```python
In [36]:    # # Creates an array of zeros for the calculated H_bar values to be added
            H_bar = np.zeros(len(nbins)-1)

            # Calculates the value of H_bar for each volume bin from
            # its upper and lower bounds
            for index in range(len(nbins)-1):
                H_bar[index] = ((v_bins_lower[index] + v_bins_upper[index])/2)**(1/3)

            # Creates an array of zeros to hold the probability values
            P = np.zeros(len(H_bar))

            # Calculates the probablity value for each normalised bin
            # and places in the array P
            for index in range(len(nbins)-1):
                P[index] = -math.sqrt( 1 - nbins_upper[index]**2) + \
                math.sqrt( 1 - nbins_lower[index]**2)


            # Inverts the volume bin bounds to order from largest
            # to smallest before placing in the stereo dataframe
            stereo["v bins lower"] = np.flip(v_bins_lower)
            stereo["v bins upper"] = np.flip(v_bins_upper)

            # Resets the dataframe index so that the values corresponding
            # to the largest bins are now at index 0.
            stereo.reset_index(inplace = True, drop = True)

            # Adds the arrays of lower and upper normalised bin bounds
            # to the stereo dataframe
            stereo["n bins lower"] = nbins_lower
            stereo["n bins upper"] = nbins_upper

            # Inverts the H_bar column so that the values corresponding
            # to the largest bins are at the column top.
            H_bar_flip = np.flip(H_bar)

            # Adds the inverted H_bar column to the stereo dataframe
            stereo["H_bar"] = H_bar_flip
            stereo["P"] = P
            stereo.head()
```

Out[36]:

	v bins lower	v bins upper	n bins lower	n bins upper	H_bar	P
0	188957.354628	377019.488826	0.630957	1.000000	65.653249	0.775818
1	94703.013840	188957.354628	0.398107	0.630957	52.150229	0.141521
2	47463.941522	94703.013840	0.251189	0.398107	41.424400	0.050599
3	23788.321549	47463.941522	0.158489	0.251189	32.904570	0.019423
4	11922.403070	23788.321549	0.100000	0.158489	26.137029	0.007627

```python
In [37]:    # Flips so the correct way around for conversion
            combi_flip = np.flip(combined_distributions["Normalised combined"])
            combi_flip.reset_index(inplace = True, drop = True) # Resets the index
            stereo["Normalised combined"] = combi_flip
            stereo.head()
```

	v bins lower	v bins upper	n bins lower	n bins upper	H_bar	P	Normalised combined
0	188957.354628	377019.488826	0.630957	1.000000	65.653249	0.775818	0.000098
1	94703.013840	188957.354628	0.398107	0.630957	52.150229	0.141521	0.000411
2	47463.941522	94703.013840	0.251189	0.398107	41.424400	0.050599	0.000620
3	23788.321549	47463.941522	0.158489	0.251189	32.904570	0.019423	0.001578
4	11922.403070	23788.321549	0.100000	0.158489	26.137029	0.007627	0.002988

In [38]:
```python
# Creates array of zeros to hold the alpha values
alpha = np.zeros(len(nbins)-1)

alpha[0] = 1/P[0] # Calculates the first alpha value

for i in range(1,len(alpha)): # Loop creates the rest of the alpha values
    alpha_sum = 0
    for j in range(1,i):
        alpha_sum += alpha[j]*P[i-j]

    # Alpha values are placed in the alpha array
    alpha[i] = (1/P[0])*(alpha[0]* P[i] - alpha_sum)

stereo["Alpha"] = alpha # Adds the alpha array to the stereo dataframe

# Creates an empty array to hold the calculated NV values
NV = np.zeros(len(nbins)-1)

for i in range(len(NV)): # Loop creates each NV value
    NV_sum = 0
    for j in range(i):
        NV_sum += alpha[i-j]*combi_flip[j]
    # Calculated NV values are placed in the array NV
    NV[i] = (1/H_bar_flip[i])*(alpha[0]*combi_flip[i] - NV_sum)


stereo["NV"] = NV # Adds the array NV to the dataframe stereo
NV_flip = np.flip(NV)
```

In [39]:
```python
for i in range(len(NV)):  # Sets any negative values in NV to 0
    if NV[i] < 0:
        NV[i] = 0

NV_no_neg = NV
```

In [40]:
```python
# Creates an array of all the volume bin edges
v_bin_edges = np.append(v_bins_lower[0], v_bins_upper)

# Converts volume bin edges to equivalent diameters
eq_di = 2*(v_bin_edges*(3/(4*math.pi)))**(1/3)
NV_norm = NV_flip/sum(NV_flip) # Normalises so sums to 1
```

```
In [41]:    ax=plt.figure()

            #Plots a histogram of the binned equivalent diameter data
            plt.hist(eq_di[:-1], eq_di, weights = NV_norm, color = 'Silver',\
                    edgecolor='k', linewidth=0.5, density = False)
            plt.xscale('log')
            plt.xlabel("Particle equivalent diameter, $\mathregular{\mu m}$")
            plt.ylabel("NV")
            ax.text(.72, .84, f"{text} = {total_inputted} \n \
            n = {final_particle_number}", horizontalalignment="left", \
                    verticalalignment="top", bbox=dict(boxstyle = "square",
                            facecolor = "white"), size = 12)
            plt.savefig(f'{file_path}/Output/{file_path}_NV_with_neg.jpg')
```
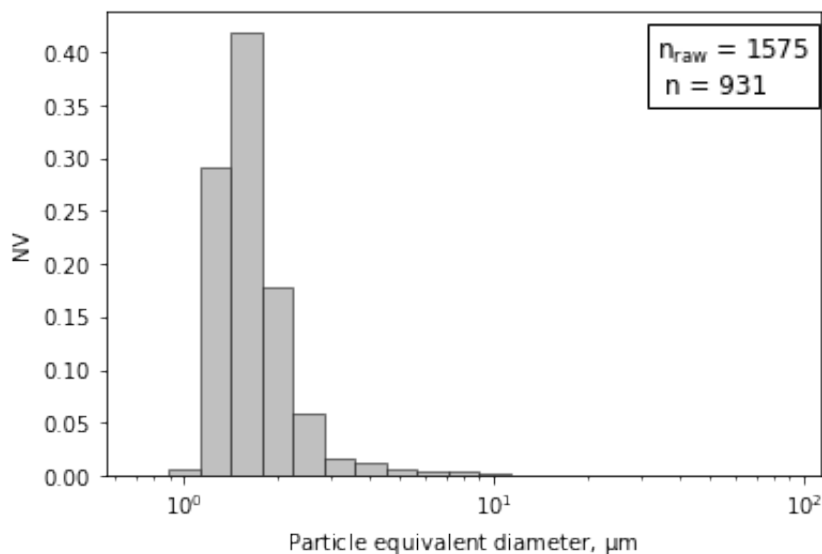


```
In [42]:    NV_no_neg_norm = NV_flip/sum(NV_flip) # Normalises so sums to 1
            NV_no_neg_norm
```

```
Out[42]:   array([0.00000000e+00, 5.31734232e-03, 2.90676532e-01, 4.18787485e-01,
                   1.78905806e-01, 5.91253253e-02, 1.66291662e-02, 1.26725259e-02,
                   6.44055538e-03, 3.20850024e-03, 4.40841482e-03, 1.53479739e-03,
                   9.09972205e-04, 5.20117598e-04, 2.47453979e-04, 3.03457022e-04,
                   1.89845324e-04, 8.17399036e-05, 2.42229651e-05, 1.39812902e-05,
                   2.75901084e-06])
```

```
In [43]:    ax = plt.figure()
            plt.hist(eq_di[:-1]/2, eq_di/2, weights = NV_no_neg_norm, \
                    color = 'Silver', edgecolor='k', linewidth=0.5, \
                    density = False) #Plots the binned data
            plt.xscale('log')
            plt.xlabel("Particle radius, $\mathregular{\mu m}$")
            plt.ylabel("NV")
            text = "$\mathregular{n_{raw}}$"
            ax.text(.72, .84, f"{text} = {total_inputted} \n n = \
            {final_particle_number}", horizontalalignment="left", \
                    verticalalignment="top", bbox=dict(boxstyle = "square",
                            facecolor = "white"), size = 12)
            #plt.xlim([0, 2])
            plt.savefig(f'{file_path}/Output/{file_path}_NV.jpg')
```
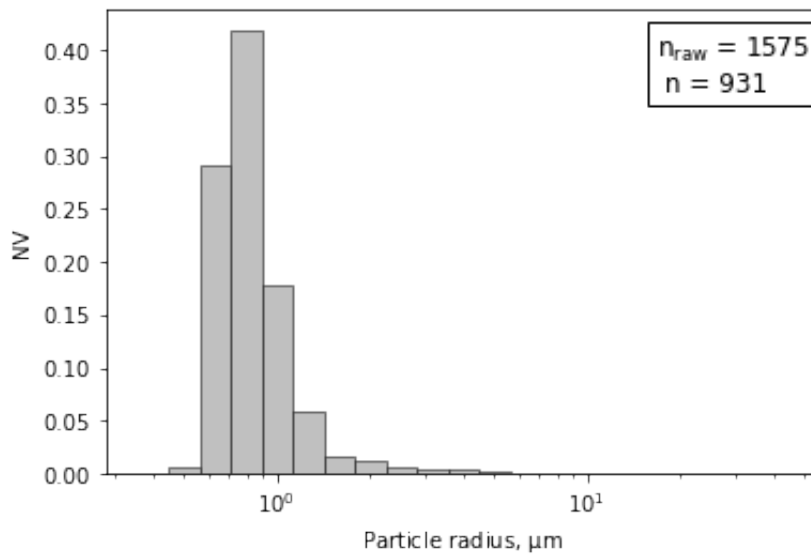
```
In [44]:    # Flips so that the largest values are at the start of the array
            NV_no_neg_norm_flip=np.flip(NV_no_neg_norm)

            # Adds to the dataframe stereo
            stereo["NV_norm_no_neg"] = NV_no_neg_norm_flip
            stereo.head()
```

Out[44]:

	v bins lower	v bins upper	n bins lower	n bins upper	H_bar	P	Normalised combined
0	188957.354628	377019.488826	0.630957	1.000000	65.653249	0.775818	0.000098
1	94703.013840	188957.354628	0.398107	0.630957	52.150229	0.141521	0.000411
2	47463.941522	94703.013840	0.251189	0.398107	41.424400	0.050599	0.000620
3	23788.321549	47463.941522	0.158489	0.251189	32.904570	0.019423	0.001578
4	11922.403070	23788.321549	0.100000	0.158489	26.137029	0.007627	0.002988

```
In [45]:    # Flips bins around so that the largest
            # values are at the start of the array
            r_bins_lower_flip = np.flip(r_bin_lower)
            r_bins_lower_flip = r_bins_lower_flip.reset_index(drop=True)
            r_bins_upper_flip = np.flip(r_bin_upper)
            r_bins_upper_flip = r_bins_upper_flip.reset_index(drop=True)
```

```
In [46]:    stereo["Radius (bins lower)"] = r_bins_lower_flip
            stereo["Radius (bins upper)"] = r_bins_upper_flip
            stereo.tail()
```

Out[46]:

	v bins lower	v bins upper	n bins lower	n bins upper	H_bar	P	Normalised combined	Alph
16	2.994772	5.975356	0.000398	0.000631	1.649135	1.198089e-07	0.173575	3.614968e 1(
17	1.500942	2.994772	0.000251	0.000398	1.309955	4.769680e-08	0.330251	9.815129e 1
18	0.752253	1.500942	0.000158	0.000251	1.040534	1.898844e-08	0.229583	2.664921e 1
19	0.377019	0.752253	0.000100	0.000158	0.826525	7.559432e-09	0.056222	7.235688e 1:
20	0.188957	0.377019	0.000063	0.000100	0.656532	3.009464e-09	0.004340	1.964738e 1:

In [47]:
```python
r = eq_di/2 # Converts equivalent diameters to radii
r =np.flip(r[:-1]+(np.diff(r)/2)) # Finds the midpoints of the bins
stereo["Radius midpoints"] = r # Adds midpoints to the dataframe stereo
stereo.head()
```

Out[47]:

	v bins lower	v bins upper	n bins lower	n bins upper	H_bar	P	Normalised combined	
0	188957.354628	377019.488826	0.630957	1.000000	65.653249	0.775818	0.000098	1
1	94703.013840	188957.354628	0.398107	0.630957	52.150229	0.141521	0.000411	(
2	47463.941522	94703.013840	0.251189	0.398107	41.424400	0.050599	0.000620	
3	23788.321549	47463.941522	0.158489	0.251189	32.904570	0.019423	0.001578	(
4	11922.403070	23788.321549	0.100000	0.158489	26.137029	0.007627	0.002988	(

In [48]:
```python
print(f'From the {total_inputted} particles inputted, \
{total_filtered_out} were removed at the first stage of \
filtering. After combining datasets \
{final_particle_number} particles are used in the final distribution.')
```

From the 1575 particles inputted, 126.0 were removed at the first stage of
filtering. After combining datasets 931 particles are used in the final dis
tribution.

In [49]:
```python
# Finds the midpoints of the volume bins
v_bin_mid = (stereo["v bins lower"] + stereo["v bins upper"])/2
```

In [50]:
```python
# Calculates the volume fraction of each particle size
vol_fraction = v_bin_mid*NV

# Normalises so sums to 1
vol_norm = vol_fraction/sum(vol_fraction)

# Adds the normalised volume fraction to the dataframe
stereo["Volume fraction"] = vol_norm

# Flips the array
vol_norm_flip = np.flip(vol_norm)
```

In [51]:
```python
#Plots the binned data against volume fraction
ax = plt.figure()
plt.hist(eq_di[:-1]/2, eq_di/2, weights = vol_norm_flip, color = 'Silver'\
         , edgecolor='k', linewidth=0.5, density= False)
plt.xscale('log')
plt.xlabel("Particle radius, $\mathregular{\mu m}$")
plt.ylabel("Volume fraction")
text = "$\mathregular{n_{raw}}$"
ax.text(.15, .84, f"{text} = {total_inputted} \n n = \
{final_particle_number}", horizontalalignment="left", \
        verticalalignment="top", bbox=dict(boxstyle = "square",
                    facecolor = "white"), size = 12)
plt.savefig(f'{file_path}/Output/{file_path}_vol.jpg')
```
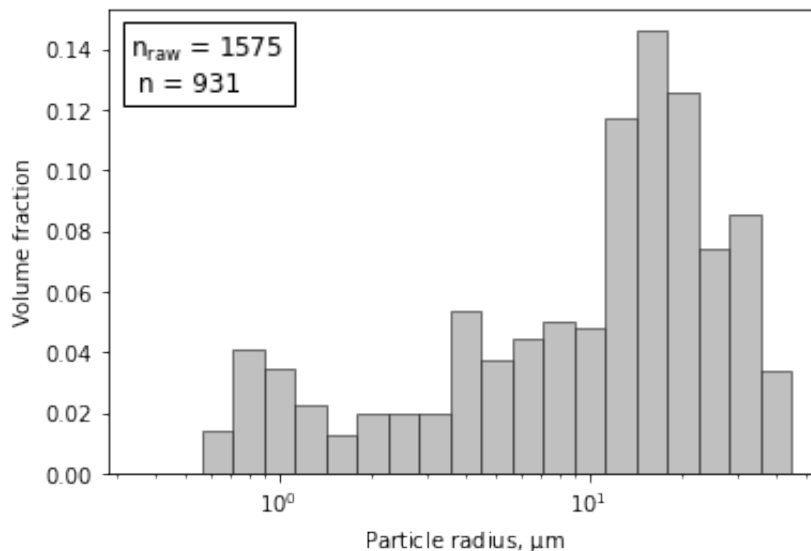

In [52]:
```python
data_output.to_csv\
(f'{file_path}/Output/{file_path}_raw_output.csv', \
 index=False)
stereo.to_csv\
(f'{file_path}/Output/{file_path}_stereo.csv', \
 index=False)
```

```python
# Name of the file to copy and save data into
name = 'for_output_data.xlsx'
xfile = openpyxl.load_workbook(name) # Opens the file
# Saves the file under a new name at the given file path
xfile.save(f'{file_path}/Output/output_calcs.xlsx')

# Writes dataframe stereo to a new sheet of
# the spreadheet named 'Data input'
with pd.ExcelWriter(f'{file_path}/Output/output_calcs.xlsx', \
                    engine='openpyxl', mode= 'a') as writer:
    stereo.to_excel(writer, sheet_name='Data input')
```

B.3 Scaling data to thin section

This Python code allows the particle-size distribution created for a sample to take into account different subunits of different particle size present in a thin section. The code combines multiple image nests generated by the code in Appendix B.2, scaling by the area of different units. The interactive version of this code can be found at:

https://github.com/hollyeunwin/unwin_PhD_thesis

Scaling data for thin sections

The particle-size distribution of a tuffisite sample can be made more representative by combining particle-size distributions for individual subunits within a sample.

This code requires area data for each subunit with a thin section to scale the particle-size distributions (after Farquharson & Wadsworth, 2018). See the example file 'DM9B_section_areas.csv'.

The code also requires the particle-size distribution outputs generated previously by Fixed_bins_controller.ipynb. These should all be contained within a single folder (e.g. DM9B_section_areas).

In [1]:
```python
import pandas as pd
import numpy as np
from pandas import Series
from pandas import DataFrame
import matplotlib.pyplot as plt
import math
import openpyxl
from Particle_functions_area_fixedbins import bin_creator
from glob import glob
import os
```

In [2]:
```python
# DM13B
print(675 +802 + 424 + 937)
print(521 + 446 + 139 + 586)

# DM9B
#print(1575 + 435 + 191)
#print( 931 + 272 + 90)
```

```
2838
1692
```

```
In [3]:   # Smallest bin size to consider
          bin_min_size = 0.1

          # Multiplier to produce bins
          bin_multiplier = 0.2

          # Total number of particles included before and after filtering
          total_particles_raw = 2838
          total_particles_used = 1692

          # Name of .csv file containing the area
          # data for the thin section and the folder containing
          # the outputs from Fixed_bins_controller
          area_csv = 'DM13B_section_areas'

          # Reads the .csv file
          section_areas = pd.read_csv(f"{area_csv}.csv")

          # Checks if output folder exists in current directory
          if not os.path.exists(f'{area_csv}_output'):
              # If does not exist, makes folder
              os.makedirs(f'{area_csv}_output')

          section_areas
```

Out[3]:

	Names	Area	Mean	Min	Max
0	DM13B_4-6_data	2276889	255	255	255
1	DM13B_12-14_data	1592494	255	255	255
2	DM13B_24-26_data	398770	255	255	255
3	DM13B_30-32_data	865679	255	255	255

```
In [4]:   # Creates an empty dataframe to hold the data
          all_vol = pd.DataFrame(index = range(100))

          for name in section_areas["Names"]:
              # Reads all .csv files from the folder
              file_load = pd.read_csv(f'{name}/Output/{name}_stereo.csv')
              all_vol[f"{name} bins lower"] = file_load["Radius (bins lower)"]
              all_vol[f"{name} bins upper"]  = file_load["Radius (bins upper)"]
              all_vol[f"{name} volume fraction"]=file_load["Volume fraction"]

          #  Removes all NaNs from the data
          all_vol.dropna(how='all')
          all_vol.head()
```

Out[4]:

	DM13B_4-6_data bins lower	DM13B_4-6_data bins upper	DM13B_4-6_data volume fraction	DM13B_12-14_data bins lower	DM13B_12-14_data bins upper	DM13B_12-14_data volume fraction	DM13B_24-26_data bins lower	DM bi
0	44.815172	56.418958	0.031620	44.815172	56.418958	0.069208	22.460792	2
1	35.597956	44.815172	0.190981	35.597956	44.815172	0.116233	17.841241	2
2	28.276462	35.597956	0.068099	28.276462	35.597956	0.079108	14.171802	
3	22.460792	28.276462	0.116411	22.460792	28.276462	0.132187	11.257062	
4	17.841241	22.460792	0.078057	17.841241	22.460792	0.090658	8.941802	1

In [5]:
```python
# Calculates the area fraction of the thin section
# composed of each subunit.
areas = section_areas["Area"]/sum(section_areas["Area"])

# Adds the area fraction to the DataFrame
section_areas["Area fraction"] = areas

section_areas
```

Out[5]:

	Names	Area	Mean	Min	Max	Area fraction
0	DM13B_4-6_data	2276889	255	255	255	0.443507
1	DM13B_12-14_data	1592494	255	255	255	0.310196
2	DM13B_24-26_data	398770	255	255	255	0.077675
3	DM13B_30-32_data	865679	255	255	255	0.168622

```python
In [6]:    # Creates a new DataFrame to hold the scaled data
           scaled_vol = pd.DataFrame(index = range(100))

           # Variable to check the area fractions add to 1
           total = 0


           for index, name in enumerate(section_areas["Names"]):

               # Takes the lower bin edges from the all_vol DataFrame and
               # places into the new scaled_vol DataFrame.
               scaled_vol[f"{name} bins lower"] = \
               all_vol[f"{name} bins lower"]

               # Takes the lower bin edges from the all_vol DataFrame and
               # places into the new scaled_vol DataFrame.
               scaled_vol[f"{name} bins upper"] = \
               all_vol[f"{name} bins upper"]

               # Calculates the scaled volume fraction for each subunit.
               scaled_vol[f"{name} scaled volume fraction"] = \
               all_vol[f"{name} volume fraction"] * areas[index]

               # Makes an array with the volume fractions to add together
               to_add = scaled_vol\
               [f"{name} scaled volume fraction"].dropna(how="all")

               # Adds the volum fraction together
               total += sum(to_add)

           # Checks that the volume fraction adds to 1
           if round(total) == 1:
               print("Data has been successfully scaled to thin section")
           else:
               print("There is an error in scaling, check \
               the names given in the csv file match folder names")

           scaled_vol.head(10)
```

```
Data has been successfully scaled to thin section
```

Out[6]:

	DM13B_4-6_data bins lower	DM13B_4-6_data bins upper	DM13B_4-6_data scaled volume fraction	DM13B_12-14_data bins lower	DM13B_12-14_data bins upper	DM13B_12-14_data scaled volume fraction	DM13B_24-26_data bins lower	DM bi
0	44.815172	56.418958	0.014023	44.815172	56.418958	0.021468	22.460792	2
1	35.597956	44.815172	0.084701	35.597956	44.815172	0.036055	17.841241	2
2	28.276462	35.597956	0.030202	28.276462	35.597956	0.024539	14.171802	
3	22.460792	28.276462	0.051629	22.460792	28.276462	0.041004	11.257062	
4	17.841241	22.460792	0.034619	17.841241	22.460792	0.028122	8.941802	1
5	14.171802	17.841241	0.041822	14.171802	17.841241	0.021500	7.102726	
6	11.257062	14.171802	0.037904	11.257062	14.171802	0.014398	5.641896	
7	8.941802	11.257062	0.025897	8.941802	11.257062	0.034421	4.481517	
8	7.102726	8.941802	0.039835	7.102726	8.941802	0.022851	3.559796	
9	5.641896	7.102726	0.033925	5.641896	7.102726	0.012337	2.827646	

In [7]:
```python
# Runs the bin_creator function (see Particle_sorter_worked_example)
bins_df, bins = bin_creator(bin_min_size, bin_multiplier)
```

In [8]:
```python
# Converts area bins to radius bins
r_bins = (bins_df/math.pi)**0.5
r_bins.head()
```

Out[8]:

	Bins lower	Bins upper
0	0.178412	0.224608
1	0.224608	0.282765
2	0.282765	0.355980
3	0.355980	0.448152
4	0.448152	0.564190

```
In [9]:   # Creates a new DataFrame to hold data
          align = pd.DataFrame()

          # Places bins into the new Dataframe in decreasing size

          align["Radius bins lower"] = \
          (np.flip(r_bins["Bins lower"])).reset_index(drop=True)

          align["Radius bins upper"] = \
          (np.flip(r_bins["Bins upper"])).reset_index(drop=True)

          align["Diameter bins lower"] = \
          align["Radius bins lower"]*2

          align["Diameter bins upper"] = \
          align["Radius bins upper"]*2

          align.tail()
```

Out[9]:

	Radius bins lower	Radius bins upper	Diameter bins lower	Diameter bins upper
40	0.448152	0.564190	0.896303	1.128379
41	0.355980	0.448152	0.711959	0.896303
42	0.282765	0.355980	0.565529	0.711959
43	0.224608	0.282765	0.449216	0.565529
44	0.178412	0.224608	0.356825	0.449216

```
In [10]:  # Creates new empty array
          to_fill = []

          # Compares the largest bin in each image
          # with those in the align DataFrame to align
          # the data with bin sizes that are offset
          for j in range(len(section_areas["Names"])):
              for index, bin in enumerate(align["Radius bins lower"]):
                  if round(bin,2) == round(scaled_vol.iat[0,3*j],2):

                      # Places each index in the to_fill array
                      to_fill.append(index)
```

```
In [11]:    # Creates an array with the names of each image
            names = section_areas["Names"]

            # Creates an empty array to hold the volume
            # fractions of each image set in the thin section
            fraction_total = []

            # For each image set, places the scaled volumme fraction
            # into the array fraction_total
            for i in range(len(names)):

                # Creates an array of zeros with a length equal
                # to the number of bins in the particle-size distribution
                # in each image set
                zeros = np.zeros(int(to_fill[i]))

                # Adds the scaled volume fraction to an array
                # so that all data is aligned to the correct bins
                with_zeros = \
                np.append(zeros, scaled_vol[f"{names[i]} scaled volume fraction"])

                # Places the data for each image set against
                # the correct bins in the Dataframe
                align[names[i]] = \
                with_zeros[:len(align["Radius bins lower"])]

                # Places the scaled volume fraction for each
                # image nest in the array
                fraction_total.append(sum(align[names[i]].dropna()))

            # Replaces the NaNs in the dataframe with zeros
            align = align.fillna(0)
```

```
In [12]:    # Creates a new column of zeros in the DataFrame
            align["Average"] = np.zeros(len(align))

            # Sums the scaled volume fraction for each image
            # nest to give the fraction for the whole thin section
            for name in names:
                align["Average"] += align[name]

            align.head()
```

Out[12]:

	Radius bins lower	Radius bins upper	Diameter bins lower	Diameter bins upper	DM13B_4-6_data	DM13B_12-14_data	DM13B_2 26_da
0	4481.517159	5641.895835	8963.034319	11283.791671	0.0	0.0	(
1	3559.795614	4481.517159	7119.591228	8963.034319	0.0	0.0	(
2	2827.646166	3559.795614	5655.292332	7119.591228	0.0	0.0	(
3	2246.079188	2827.646166	4492.158375	5655.292332	0.0	0.0	(
4	1784.124116	2246.079188	3568.248232	4492.158375	0.0	0.0	(

```
In [13]:    # Removes the zeros from the align DataFrame
            align= align[align['Average'] != 0]
            align.head()
```

Out[13]:

	Radius bins lower	Radius bins upper	Diameter bins lower	Diameter bins upper	DM13B_4-6_data	DM13B_12-14_data	DM13B_24-26_data	DM
20	44.815172	56.418958	89.630343	112.837917	0.014023	0.021468	0.000000	C
21	35.597956	44.815172	71.195912	89.630343	0.084701	0.036055	0.000000	(
22	28.276462	35.597956	56.552923	71.195912	0.030202	0.024539	0.000000	C
23	22.460792	28.276462	44.921584	56.552923	0.051629	0.041004	0.003148	(
24	17.841241	22.460792	35.682482	44.921584	0.034619	0.028122	0.004439	

```
In [14]:    # Adds the bins to the DataFrame align
            bins_lower = np.flip(align["Radius bins lower"])
            bins_lower.reset_index(drop = True)

            bins_upper = np.flip(align["Radius bins upper"])
            bins_upper.reset_index(drop = True)

            average_vol_frac = np.flip(align["Average"])
            average_vol_frac.reset_index(drop = True)
```

Out[14]: 0   0.000011
          1   0.000271
          2   0.002257
          3   0.007547
          4   0.005487
          5   0.006433
          6   0.008697
          7   0.017246
          8   0.027336
          9   0.025951
          10   0.037039
          11   0.042093
          12   0.060344
          13   0.079848
          14   0.076903
          15   0.079221
          16   0.082955
          17   0.084395
          18   0.116841
          19   0.077675
          20   0.125958
          21   0.035491
          Name: Average, dtype: float64
```

```python
# Calculates the geometric mean of the data
bins_mid = (align['Radius bins lower'] + align['Radius bins upper'])/2

a = sum(align["Average"]*np.log10(bins_mid))/sum(align["Average"])
mean = 10**a
mean
```

13.230052912699467

```python
# Plots the total volume fraction for the whole thin section

ax= plt.figure()
y = [0, 0.5]
plt.hist(bins_lower,bins_lower, weights=average_vol_frac, \
        color = 'Silver', edgecolor='k', linewidth=0.5, density = False)
plt.xscale('log')

# Plots the mean values
plt.plot([2.4,2.4],y, linestyle = 'dashed', color = 'dimgray')
plt.plot([mean,mean],y, linestyle = 'dashed', color = 'dimgray')


plt.ylim(0,0.2)
plt.xlabel("Particle radius, $\mathregular{\mu}$m")
plt.ylabel("Volume fraction")
text = "$\mathregular{N_{raw}}$"
a = "$\bar{r}$"
b = "$\mathregular{\mu m}$"

ax.text(.15, .835, f" {text} = {total_particles_raw} \n N = \
{total_particles_used}", horizontalalignment="left", \
        verticalalignment="top", bbox=dict(boxstyle = "square", \
                                        facecolor = "white"))

ax.text(0.40,0.69,"r = 2.4 $\mathregular{\mu m}$", rotation=90)

ax.text(0.655,0.67,\
        r"$\mathregular{\bar{r}}$ = 13.2 $\mathregular{\mu m}$", rotation=9
plt.savefig(f'{area_csv}_output/{area_csv}_combined_volume_fractions.eps')
```
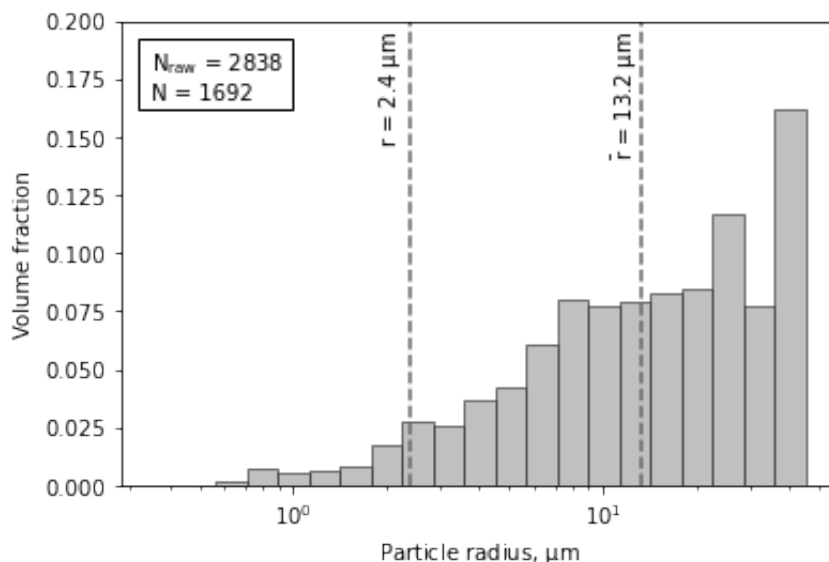
```
In [17]:   # Writes the align DataFrame to .csv
           align.to_csv(f'{area_csv}_output/{area_csv}_average_PSD.csv', index=False)
```

```
In [18]:   # Finds volume bins from the particle radius
           volbin = (4/3)*math.pi*(bins_lower)**3

           # Multiplies by the volume fraction to find
           # the frequency of each particle
           get_f = average_vol_frac/volbin
```

```
In [19]:   # Normalises the frequency data for number density per volume
           norm_f = get_f/sum(get_f)
```

```
In [20]:   # Calculates the geometric mean of the data

           a = sum(get_f*np.log10(bins_mid))/sum(get_f)
           mean = 10**a
           mean
```

Out[20]:   0.9881259309375203

```
In [21]:   # Plots the normalised frequency data with the labelled mean

           plt.hist(bins_lower,bins_lower, weights=norm_f, \
                   color = 'Silver', edgecolor='k', \
                   linewidth=0.5, density = False)
           plt.xscale('log')
           plt.plot([mean,mean],[0,0.7], linestyle = 'dashed', \
                   color = 'dimgray')
           plt.ylim(0,0.52)
           plt.text(14.5, 0.495,f" {text} = {total_particles_raw} \n N = \
           {total_particles_used}", horizontalalignment="left", \
                   verticalalignment="top", bbox=dict(boxstyle = "square", \
                                                    facecolor = "white"))

           plt.text(0.78,0.382\
                   ,r"$\mathregular{\bar{r}}$ = 1.0 $\mathregular{\mu m}$",\
                   rotation=90)

           plt.xlabel('Particle radius, $\mathregular{\mu m}$')
           plt.ylabel('$N_v$')
           plt.savefig(f'{area_csv}_output/{area_csv}_norm_freq.eps')
```
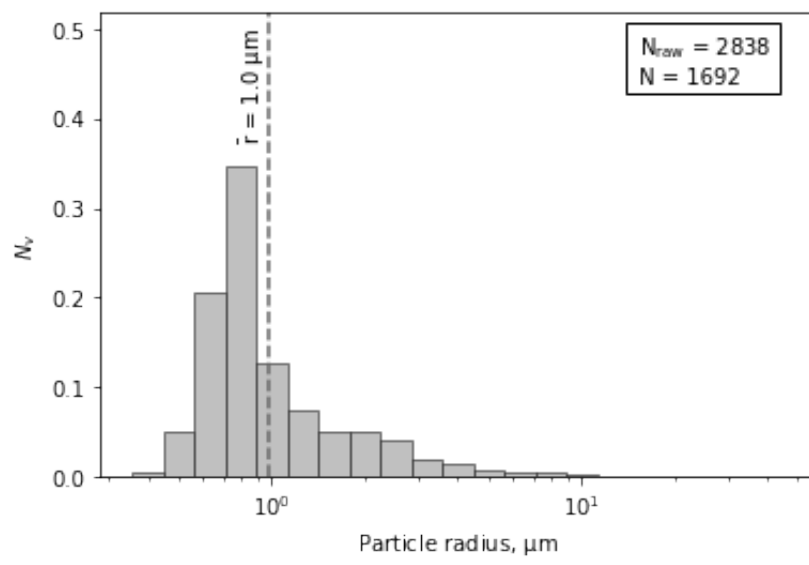
B.4   Correcting permeability data

This Python code processes the permeability data, providing the method for applying different corrections to the data. See also Appendix A.7.2.1. The interactive version of this code and the raw flow data can be found at:

https://github.com/hollyeunwin/unwin_PhD_thesis

Plotting and correcting permeablity data

Here is the method to process the raw volumetic flow and pressure differential data to calculate permeability. This data is then corrected where needed for gas turbulence and gas slippage. See Appendix A5 for details of the different corrections applied to permeability data.

In [1]:
```python
import pandas as pd
import numpy as np
from pandas import Series
from pandas import DataFrame
import matplotlib.pyplot as plt
import math
```

Three samples have been chosen to demonstrate the changes that corrections make to the permeability measurement calculated from the raw data. These samples were selected to include an example of each of the following sitations:

1. No correction is required (TF1_1)
2. The Forchheimer correction is required (TF1_2)
3. The Klinkenberg correction is required (TF2_1)

In [2]:
```python
TF1_1 = pd.read_csv("TF1_1.csv") # Reads each of the raw data files
TF1_2 = pd.read_csv("TF1_2.csv")
TF2_1 = pd.read_csv("TF2_1.csv")
TF2_1 # Here is an example of a raw data file.
```

Out[2]:

	dP_(mBar)	Q_(ml/min)	dP_(Pa)	Q_(m^3/s)
0	1505.2	37.60	150520	6.266670e-07
1	1424.5	34.85	142450	5.808330e-07
2	1290.2	30.42	129020	5.070000e-07
3	1143.1	25.77	114310	4.295000e-07
4	1010.2	21.84	101020	3.640000e-07
5	907.8	19.00	90780	3.166670e-07

In [3]:
```python
names = [TF1_1,TF1_2,TF2_1] # Creates a list of the dataframe names to loop
```

We also need measurements of the dimensions of each sample.

In [4]:
```python
characteristics = pd.read_csv("example_characteristics.csv")
characteristics
```

	name	length	diameter	bulk_volume	pycnometer_volume	sd
0	TF1_1	39.89	19.90	12.406808	9.5933	0.0066
1	TF1_2	39.92	19.92	12.441109	9.3876	0.0083
2	TF2_1	40.01	19.95	12.510000	11.2358	0.0106

```python
# Calculates cross-sectional area in m^2
characteristics["area"] = (characteristics["diameter"]/(2*1000))**2 * math
characteristics
```

	name	length	diameter	bulk_volume	pycnometer_volume	sd	area
0	TF1_1	39.89	19.90	12.406808	9.5933	0.0066	0.000311
1	TF1_2	39.92	19.92	12.441109	9.3876	0.0083	0.000312
2	TF2_1	40.01	19.95	12.510000	11.2358	0.0106	0.000313

The calculations below require values for atmospheric pressure as well as the viscosity and density of nitrogen at room temperature.

```python
P_atm = 101325 # Atmospheric pressure in Pa
mu_N = 0.0000176 # Viscosity of nitrogen in Pa.s
rho = 1.16 # Density of Nitrogen
```

Measurements of the pressure differential are taken but here we require the values of the upstream (P_up) and downstream (P_down) pressure. The downstream pressure (P_down) is assumed to be atmospheric pressure (P_atm). The upstream pressure is therefore calculated using:

```python
for name in names:
    #Creates a new P_up column in each dataframe using dP_(Pa) + P_atm
    name['P_up'] = name.iloc[:,2] + P_atm
```

We can then calculate the values for nabla_P (Eq. 5.1):

```python
for i in range(3):
    # Takes each of the samples in turn
    name = names[i]
    # Calculates the top of the fraction in Eq. 5.1
    sq_diff = name['P_up']**2 - P_atm**2
    # Calculates the base of the fraction in Eq. 5.2
    base = 2 * P_atm * (characteristics.iloc[i,1]*0.001)
    # Divides one by the other and adds to the dataframe
    name['nabla_P'] = sq_diff/base
names
```

```
[     dP_(mBar)  Q_(ml/min)  dP_(Pa)       Q_(m^3/s)    P_up        nabla_P
 0      1887.3        3.00    188730   5.000000e-08   290055   9.137532e+06
 1      1746.1        2.69    174610   4.483330e-08   275935   8.148905e+06
 2      1626.3        2.45    162630   4.083330e-08   263955   7.348791e+06
 3      1473.6        2.14    147360   3.566670e-08   248685   6.380422e+06
 4      1313.3        1.81    131330   3.016670e-08   232655   5.425925e+06
 5      1137.6        1.48    113760   2.466670e-08   215085   4.452758e+06,
       dP_(mBar)  Q_(ml/min)  dP_(Pa)       Q_(m^3/s)    P_up        nabla_P
 0      1879.4        4.57    187940   7.616670e-08   289265   9.074092e+06
 1      1741.3        4.10    174130   6.833330e-08   275455   8.110064e+06
 2      1620.7        3.71    162070   6.183330e-08   263395   7.306764e+06
 3      1464.6        3.22    146460   5.366670e-08   247785   6.320394e+06
 4      1327.9        2.82    132790   4.700000e-08   234115   5.506087e+06
 5      1181.8        2.39    118180   3.983330e-08   219505   4.686858e+06,
       dP_(mBar)  Q_(ml/min)  dP_(Pa)       Q_(m^3/s)    P_up        nabla_P
 0      1505.2       37.60    150520   6.266670e-07   251845   6.556361e+06
 1      1424.5       34.85    142450   5.808330e-07   243775   6.063065e+06
 2      1290.2       30.42    129020   5.070000e-07   230345   5.277741e+06
 3      1143.1       25.77    114310   4.295000e-07   215635   4.468621e+06
 4      1010.2       21.84    101020   3.640000e-07   202345   3.783503e+06
 5       907.8       19.00     90780   3.166670e-07   192105   3.285334e+06]
```

The value for u is defined as Q/A.

In [9]:

```
for i in range(3):
    name = names[i] # Takes each of the samples in turn
    # Calculates u for each sample and adds as a new column in the datafram
    name['u'] = name.iloc[:,3]/characteristics.iloc[i,6]
```

The permeability of each sample can be calculated by finding gradient of the line of best fit on a plot of u against nabla_P. In the code below, a least squares regression is used to fit a line through the data with a y-intercept of zero. The data and the fitted line are then plotted in the figures.

```
predictions = pd.DataFrame()
fit = pd.DataFrame(index = range(2))
a_values = np.zeros(3)

fig, axs = plt.subplots(1,3,figsize=[12,3]) # Creates subplots for each sa
plt.subplots_adjust(wspace = 0.25)
for i,name in enumerate(names): # Runs through each sample in a loop
    # Plots <u> against nabla_P for each sample
    axs[i].scatter(name['u']*1000,name['nabla_P']/(10**6), color='silver')
    # Adds axis labels
    axs[i].set(xlabel='<u> x $10^{-3}$ ($ms^{-1}$)', ylabel=''r'$\nabla$ P

    x = name['u'].to_numpy() # Changes DataFrame columns to numpy arrays
    y = name['nabla_P'].to_numpy()

    X = x[:,np.newaxis] # Changes the orientation of the x array
    # Minimises to fit a line to the data with y-intercept of 0
    a, _, _, _ = np.linalg.lstsq(X,y, rcond=-1)

    # Plots the fitted line on the graph
    axs[i].plot(x*1000, (x*a)/(10**6), color='gray')
    y_predict = a*x # Creates variable of the predicted y values

    # Places each of the values for a in an array
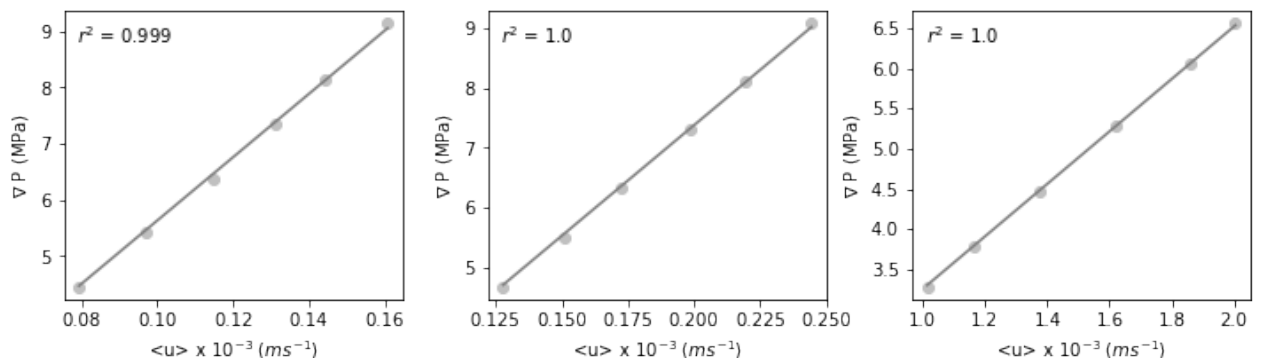    a_values[i] = a

    # Finds the r value of the fit
    corr_matrix = np.corrcoef(name['nabla_P'],a*x)
    corr = corr_matrix[0,1]
    R_sq = corr**2 # Square to find the r^2 value

    # Adds the value of R_sq as text on each subplot
    axs[i].text(0.04,0.96,f'$r^2$ = {round(R_sq,3)}',
                ha='left', va='top', transform=axs[i].transAxes)
    print(f' a = {a}, r^2 = {round(R_sq,3)}')
```

```
a = [5.63017579e+10], r^2 = 0.999
a = [3.68840525e+10], r^2 = 1.0
a = [3.25927777e+09], r^2 = 1.0
```


The permeability of the sample can be found from the gradient of the fitted line, a, using Darcy's law.

```python
k = np.zeros(3) # Creates new empty array to hold the permeability values

for i in range(len(k)):
    k[i] = mu_N/a_values[i] # Calculates the permeability of each sample.
k # Array holding the permeability of each sample
```

`array([3.12601252e-16, 4.77170994e-16, 5.39996932e-15])`

Now the permeability has been calculated from the raw measured data, each the data for each sample can be checked to see if a Forchheimer or Klinkenberg correction are required. See Appendix A5 for details on each correction.

Forchheimer correction

To check if the Forchheimer correction is required, the permeability (k_meas) first needs to be calculated from each data point for a sample, using Eq. 5.2.

```python
for i in range(3):
    name = names[i] # Takes each of the samples in turn
    # Calculates the Darcian permeability of each sample (Eq. 5.2)
    name['k_meas'] = (name['Q_(m^3/s)']* mu_N)/ \
    (characteristics.iloc[i,6]*name['nabla_P'])
```

The need for the Forchheimer correction is checked by seeing if the fit between 1/k_meas and Q is linear. The y-intercept of a equation fitted to the linear portion of this curve is equal to the inverse of the Forchheimer corrected permeability (1/k_forch)

In [13]:
```python
# Creates empty array to hold the values of b found,
# needed to find corrected permeability
b_values = np.zeros(3)

fig, axs = plt.subplots(1,3,figsize=[12,3]) # Creates subplots for each sar
plt.subplots_adjust(wspace = 0.4)
for i,name in enumerate(names): # Runs through each sample in a loop
    # Plots Q against 1/k_meas for each sample
    axs[i].scatter(name['Q_(m^3/s)'],1/(name['k_meas']), color='silver')
    # Adds axis labels
    axs[i].set(xlabel='Q ($m^3s^{-1}$)', ylabel='${k_{meas}}^{-1}, m^{-2}$

    # Fits a straight line to the data
    a, b = np.polyfit(name['Q_(m^3/s)'],1/(name['k_meas']), 1)
    # Plots the fitted line on the graph
    axs[i].plot(name['Q_(m^3/s)'], name['Q_(m^3/s)']*a+b, color='gray')

    b_values[i] = b # Places b_value for each sample into the array

    # Finds the r value of the fit
    corr_matrix = np.corrcoef(1/(name['k_meas']),a*name['Q_(m^3/s)']+b)
    corr = corr_matrix[0,1]
    R_sq = corr**2 # Square to find the r^2 value

    # Adds the value of R_sq as text on each subplot
    axs[i].text(0.04,0.96,f'$r^2$ = {round(R_sq,3)}',
                ha='left', va='top', transform=axs[i].transAxes)
    print(f' a = {a}, b = {b}, r^2 = {round(R_sq,3)}')
```

```
a = 1.7105151573702452e+21, b = 3127520187282468.5, r^2 = 0.422
a = 8.634595549555313e+20, b = 2041251323600802.8, r^2 = 0.837
a = 4.4389758876701184e+18, b = 182870799652751.12, r^2 = 0.935
```
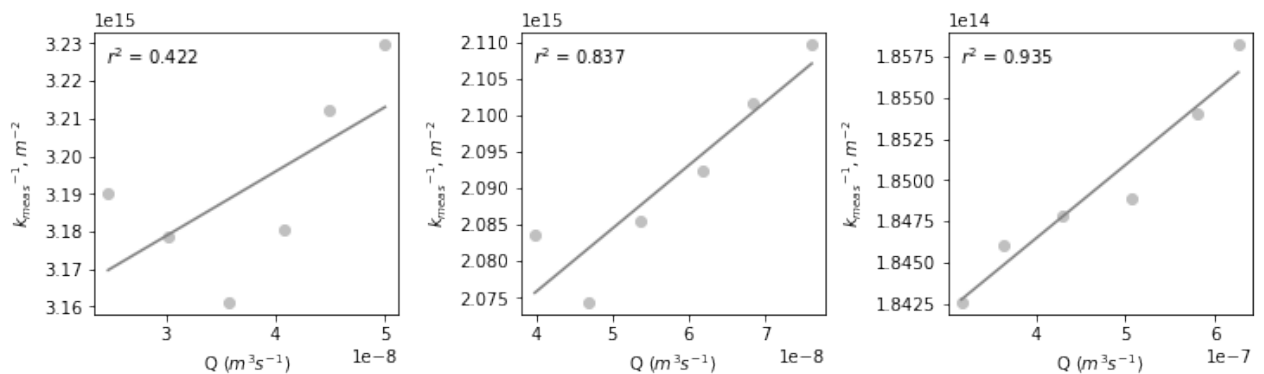

Here the first sample shows a low r^2 value, indicating that this does not require a Forchheimer correction. The other two samples show a stronger correlation and their Forchheimer corrected permeabilities can be found from the fit above.

The permeability of the first sample that does not need correcting can be taken from above.

In [14]:
```python
print(f' The permeability of TF1_1 is {k[0]} m^2')
```

```
The permeability of TF1_1 is 3.1260125179985756e-16 m^2
```

```
k_forch = 1/b_values
k_forch

print(f'The Forchheimer corrected permeability of the second two samples is
```

```
The Forchheimer corrected permeability of the second two samples is 4.89895
5794605353e-16 m^2 for TF1_2 and 5.468341593621702e-15 m^2 for TF2_1.
```

Klinkenberg correction

The data can also be checked to see if the Klinkenberg correction needs to be applied. To do this, the inverse of the mean pressure of each measurement needs to be calculated.

In [16]:

```
for name in names:
    name['P_m'] = (name['P_up'] + P_atm)/2
    name['P_m_inv'] = 1/name['P_m']
```

In [17]:

```
b_values_klink = np.zeros(3)

fig, axs = plt.subplots(1,3,figsize=[12,3]) # Creates subplots for each sam
plt.subplots_adjust(wspace = 0.3)
for i,name in enumerate(names): # Runs through each sample in a loop
    # Plots 1/P_m against k_meas for each sample
    axs[i].scatter(name['P_m_inv'],name['k_meas'], color='silver')
    # Adds axis labels
    axs[i].set(xlabel='${P_m}^{-1} (Pa^{-1}$)', ylabel='$k_{meas}, m^2$')

    # Fits a straight line to the data
    a, b = np.polyfit(name['P_m_inv'],name['k_meas'], 1)
    # Plots the fitted line on the graph
    axs[i].plot(name['P_m_inv'], name['P_m_inv']*a+b, color='gray')

    b_values_klink[i] = b # Places b_value for each sample into the array

    # Finds the r value of the fit
    corr_matrix = np.corrcoef(name['k_meas'],a*name['P_m_inv']+b)
    corr = corr_matrix[0,1]
    R_sq = corr**2 # Square to find the r^2 value

    # Adds the value of R_sq as text on each subplot
    axs[i].text(0.04,0.96,f'$r^2$ = {round(R_sq,3)}',
                ha='left', va='top', transform=axs[i].transAxes)
    print(f' a = {a}, b = {b}, r^2 = {round(R_sq,3)}')
```

```
a = 3.179797437684518e-12, b = 2.953279377312609e-16, r^2 = 0.348
a = 6.222515697405162e-12, b = 4.4312534753800817e-16, r^2 = 0.786
a = 3.455868675281651e-11, b = 5.192332387762109e-15, r^2 = 0.911
```
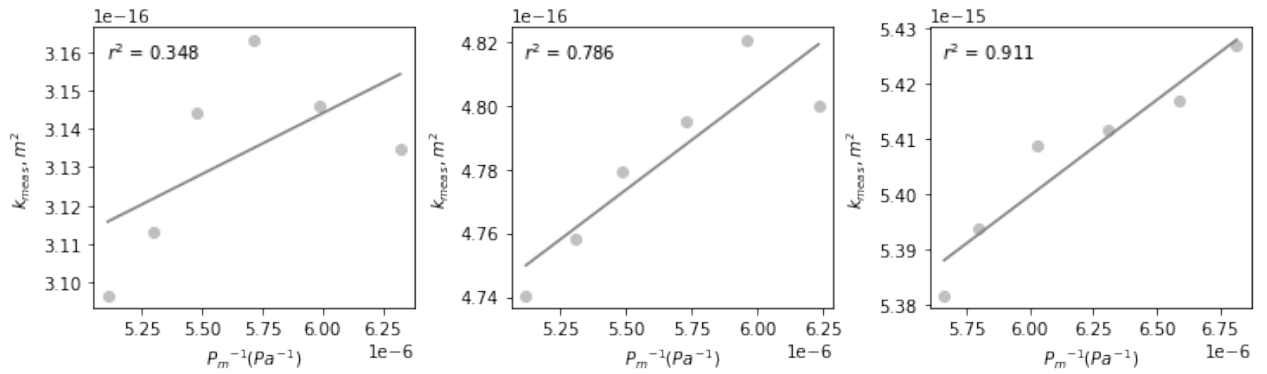

In the above data the first two samples do not show a strong correlation, suggesting that a Klinkenberg correction is only required for the third sample. The corrected permeability, k_klink, is given by the y-intercept of the best fit line above.

In [18]:
```
print(f'The corrected permeability of the third sample would be {b_values_]
```

The corrected permeability of the third sample would be 5.192332387762109e-15 m^2

B.5 Assumptions: Circularity and stereological conversion

This Python code takes the raw particle-size data for all measured particles and calculates the average circularity and the magnitude of error generated by the spherical assumption in the stereological conversion. The interactive version of this code can be found at: https://github.com/hollyeunwin/unwin_PhD_thesis

Circularity, aspect ratios and area errors

In [1]:
```python
import pandas as pd
import numpy as np
from pandas import Series
from pandas import DataFrame
import matplotlib.pyplot as plt
import math
```

In [2]:
```python
# Reads .csv containing all the particle data
raw_data = pd.read_csv("All_particle_data.csv")
raw_data.head()
```

Out[2]:

	Area	Major	Minor	Angle	Circ.	Feret	FeretX	FeretY	FeretAngle	MinFeret	AR
0	1.971	1.783	1.407	33.746	0.933	1.884	133	169	34.992	1.473	1.267
1	1.351	1.623	1.060	14.771	0.867	1.685	186	162	15.945	1.122	1.531
2	1.101	1.580	0.888	149.132	0.759	1.669	243	153	146.310	1.035	1.780
3	1.762	1.973	1.137	16.385	0.840	2.006	348	165	22.620	1.195	1.735
4	13.533	4.477	3.849	150.831	0.826	4.834	387	158	151.390	4.129	1.163

Circularity

Here the circularity data are plotted for all of the measured particles.

In [3]:
```python
circ_bins = np.linspace(0,1,21) # Creates bins for the circularity data
```

In [4]:
```python
# Places data into bins, outputting 2 arrays:
# binned data (counts) and bins
circ_counts, circ_bins_out = np.histogram(raw_data['Circ.'], circ_bins)

#Creates new dataframe to hold the circularity data
circ_data = pd.DataFrame()
circ_data['Bins_lower'] = circ_bins_out[:-1]
circ_data['Counts'] = circ_counts
# Creates column with particle fraction data
circ_data['norm_counts'] = circ_counts/len(raw_data)
```

In [5]:
```python
# Finds the mean circularity of the raw data
mean_circ = sum(raw_data['Circ.'])/len(raw_data)
```

```python
# Plots the circularity data against particle fraction
ax = plt.figure()
plt.hist(circ_bins_out[:-1], circ_bins_out[:-1], \
         weights=circ_data['norm_counts'], \
         color='silver', density=False, edgecolor='dimgrey')
plt.xlabel('Circularity')
plt.ylabel('Particle fraction')

# Plots a line for the mean of the data
plt.plot([mean_circ, mean_circ],[0,1], linestyle='dashed', color='black')
max_bin_height = round(circ_data['norm_counts'].max(),2)
plt.ylim([0,max_bin_height+0.02])

# Adds a box with the total particle count and mean of the data
ax.text(.15, .85, f"n = {len(raw_data)}\n$\mu$ = \
{round(mean_circ,2)}", horizontalalignment="left", \
        verticalalignment="top", bbox=dict(boxstyle = "square",
                    facecolor = "white"))
#plt.savefig('Circularity', format='eps')
```

```
Text(0.15, 0.85, 'n = 6731\n$\\mu$ = 0.75')
```
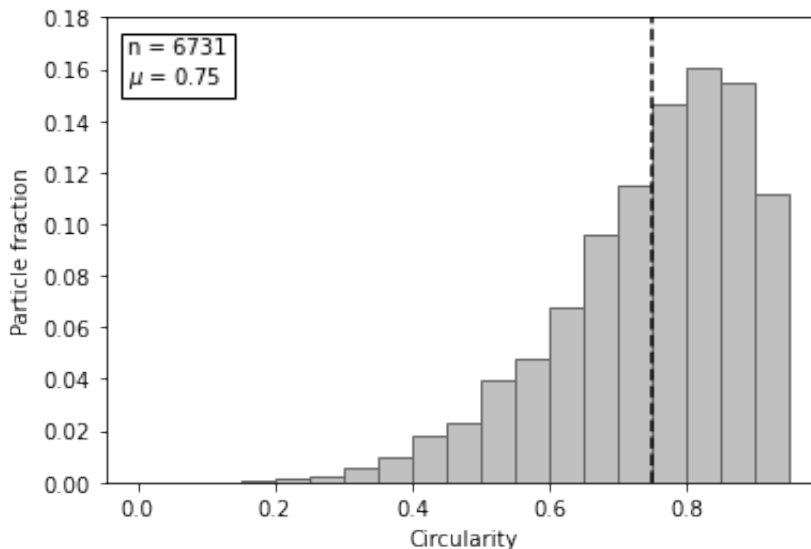

Particle aspect ratios

Here the aspect ratios of all the particle data are plotted

```python
# Finds the maximum aspect ratio of all particles
max_AR = raw_data['AR'].max()
# Rounds the maximumm aspect ratio up to the nearest integer
max_AR_bin = math.ceil(max_AR)

# Creates bins to hold the aspect ratio data
AR_bins = np.linspace(1,max_AR_bin,(max_AR_bin*2)-1)
```

```
In [8]:    # Places data into bins, outputting 2 arrays:
           # binned data (counts) and bins
           AR_counts, AR_bins_out = np.histogram(raw_data['AR'], AR_bins)

           #Creates new dataframe to hold the aspect ratio data
           AR_data = pd.DataFrame()
           AR_data['Bins_lower'] = AR_bins_out[:-1]
           AR_data['Counts'] = AR_counts
           # Creates column with particle fraction data
           AR_data['norm_counts'] = AR_counts/len(raw_data)
```

```
In [9]:    # Finds the mean aspect ratio of the raw data
           mean_AR = sum(raw_data['AR'])/len(raw_data)
```

```
In [10]:   # Plots the aspect ratio data against particle fraction
           ax = plt.figure()
           plt.hist(AR_bins_out[:-1], AR_bins_out[:-1], \
                    weights=AR_data['norm_counts'], \
                    color='silver', density=False, edgecolor='dimgrey')
           plt.xlabel('Aspect ratio')
           plt.ylabel('Particle fraction')

           # Plots a line for the mean of the data
           plt.plot([mean_AR, mean_AR],[0,1], linestyle='dashed', color='black')
           max_bin_height = round(AR_data['norm_counts'].max(),2)
           plt.ylim([0,max_bin_height+0.02])

           # Adds a box with the total particle count and mean of the data
           ax.text(.87, .85, f"n = {len(raw_data)}\n$\mu$ = \
           {round(mean_AR,2)}", horizontalalignment="right", \
                   verticalalignment="top", bbox=dict(boxstyle = "square",
                              facecolor = "white"))
           #plt.savefig('Aspect_ratio', format='eps')
```

Out[10]:   Text(0.87, 0.85, 'n = 6731\n$\\mu$ = 1.91')
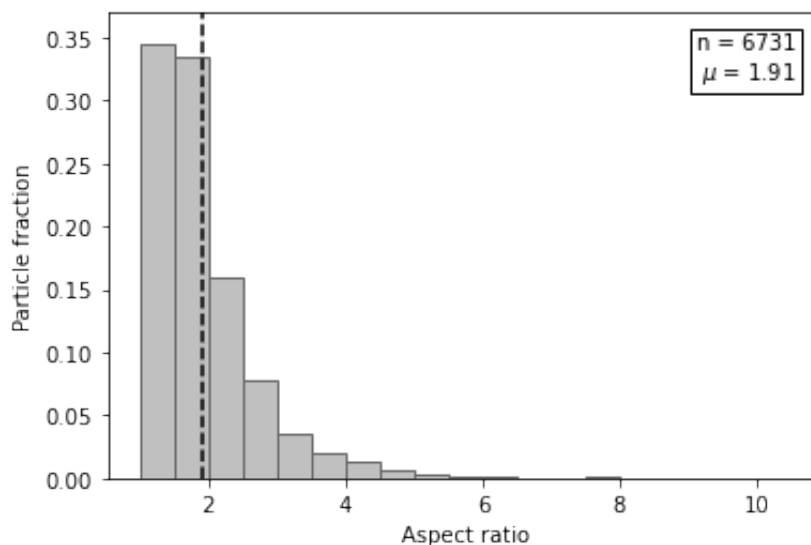
Area errors from spherical assumption

As particles are not truly spherical there will be an error associated with this assumption made for the stereological conversion and sintering calculations. Here this error is quantified by considering the effects on the volume calculations of the particle data above.

When constructing a particle-size distribution from 2D images the third (depth) dimension of the particles will always be unconstrained and therefore only rotational ellipsoids can be considered. Here we consider the volume errors created by sphericity for oblate or prolate spheroids.

The average particle

First, the average particle in the dataset is considered. The volume of this particle can be calculated from its area, assuming that the particle is perfectly spherical.

In [11]:
```python
# Calculates the mean area of a particle
mean_area = sum(raw_data['Area'])/len(raw_data)

# Assuming perfectly circular particles, the mean radius is calculated
mean_r = (mean_area/ math.pi)**0.5
round(mean_r,2)
```

Out[11]: 9.64

In [12]:
```python
# Assuming spherical particles, the mean volume can be calculated
mean_volume = 4/3 * math.pi * mean_r**3
mean_volume
```

Out[12]: 3757.7764307575003

The aspect ratio of each particle indicate how far from sphericity each particle is. Using the mean aspect ratio we can calculate the volume of the oblate and prolate spheroids formed by the average particle.

In [13]:
```python
# Finds the axes (a and b) of an ellipse with the mean particle area
ab = mean_area/math.pi
b = (ab / mean_AR)**0.5
a = mean_AR * b
```

In [14]:
```python
# Finds volume of prolate ellipsoid
v_pro = 4/3 * math.pi * a**2 * b
# Finds volume of prolate ellipsoid
v_ob = 4/3 * math.pi * b**2 * a
```

```python
# Calculates the % error on both volumes
er_pro = abs(((v_pro - mean_volume)/mean_volume)*100)
er_ob = abs(((v_ob - mean_volume)/mean_volume)*100)

print(f'The % error on the prolate spheroid is {round(er_pro,2)} \
% and the % error on the oblate spheroid is {round(er_ob,2)} %')
```

```
The % error on the prolate spheroid is 38.34 % and the % error on the oblat
e spheroid is 27.72 %
```

Particle packs of different areas

The code below calculates the volume of particles of a range of sizes and different aspect ratios, as well as the % error from the spherical assumption.

```python
# Generates a range of particle sizes to calculate volumes for
areas = np.linspace(0,10000,1000)

# Generates a range of aspect ratios to plot
#ARs = np.linspace(1.1,10,100)
ARs = [2, 4, 6, 8, 10]
```

```python
volume_data = pd.DataFrame()
volume_data['Areas'] = areas
AR = 1
volume_data['sph_r'] = (areas/ math.pi)**0.5
volume_data[f'vol_1'] = 4/3 * math.pi * volume_data['sph_r']**3

for AR in ARs:
    ab = areas/math.pi
    b = (ab / AR)**0.5
    a = AR * b

    volume_data[f'short_axis_{AR}'] = b

    volume_data[f'vol_pro_{AR}'] = 4/3 * math.pi * b * a**2

    volume_data[f'vol_ob_{AR}'] = 4/3 * math.pi * b**2 * a

volume_data
```

	Areas	sph_r	vol_1	short_axis_2	vol_pro_2	vol_ob_2
0	0.00000	0.000000	0.000000	0.000000	0.000000e+00	0.000000
1	10.01001	1.785017	23.824049	1.262198	3.369229e+01	16.846146
2	20.02002	2.524395	67.384586	1.785017	9.529619e+01	47.648097
3	30.03003	3.091740	123.793388	2.186190	1.750703e+02	87.535144
4	40.04004	3.570034	190.592389	2.524395	2.695383e+02	134.769171
...	...	...	...	...	...	...
995	9959.95996	56.305894	747739.268940	39.814280	1.057463e+06	528731.507627
996	9969.96997	56.334182	748866.797249	39.834282	1.059058e+06	529528.790541
997	9979.97998	56.362455	749994.891729	39.854274	1.060653e+06	530326.473797
998	9989.98999	56.390714	751123.552095	39.874256	1.062249e+06	531124.557195
999	10000.00000	56.418958	752252.778064	39.894228	1.063846e+06	531923.040535

1000 rows × 18 columns

```python
ax = plt.figure()

plt.plot(volume_data['Areas'], volume_data[f'vol_pro_{ARs[0]}'],\
         label='Prolate',color='0')
plt.plot(volume_data['Areas'], volume_data[f'vol_ob_{ARs[0]}'],\
         linestyle='dashed', label='Oblate',color='0')
plt.plot(volume_data['Areas'], volume_data['vol_1'],\
         label=f'1:1',color='0')

colour=np.linspace(0.4,0.9,len(ARs))

for i,AR in enumerate(ARs):
    plt.plot(volume_data['Areas'], volume_data[f'vol_pro_{AR}'],\
             label=f'1:{AR}',c=str(colour[i]))
    plt.plot(volume_data['Areas'], volume_data[f'vol_ob_{AR}'],\
             linestyle='dashed',c=str(colour[i]))

plt.xlim([0,2000])
plt.ylim([0,80000])
plt.xlabel('Particle area')
plt.ylabel('Particle volume')
plt.legend(loc='upper left')
ax.text(0.7,0.74,'1:1:1 (sphere)', ha='left', va='top', rotation=37)
#plt.savefig('Aspect_ratio_volumes', format='eps')
```

`Text(0.7, 0.74, '1:1:1 (sphere)')`
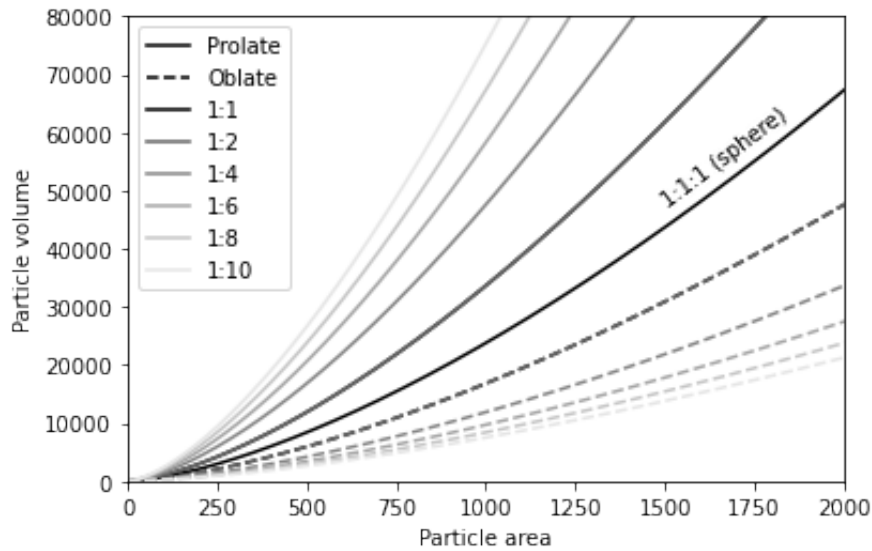
In [19]:
```python
error_data = pd.DataFrame()
# Calculates the % error for each aspect ratio
for AR in ARs:
    error_data[f'er_pro_{AR}'] = abs(((volume_data[f'vol_pro_{AR}']- \
        volume_data[f'vol_1'])/volume_data[f'vol_1'])*100)
    error_data[f'er_ob_{AR}'] = abs(((volume_data[f'vol_ob_{AR}']- \
        volume_data[f'vol_1'])/volume_data[f'vol_1'])*100)

error_data.head(2)
```

Out[19]:

	er_pro_2	er_ob_2	er_pro_4	er_ob_4	er_pro_6	er_ob_6	er_pro_8	er_ob_8
0	NaN	NaN	NaN	NaN	NaN	NaN	NaN	NaN
1	41.421356	29.289322	100.0	50.0	144.948974	59.175171	182.842712	64.644661

In [20]:
```python
# Creates two new arrays to separate out the dataframe columns
across_ARs_pro = np.zeros(len(ARs)+1)
across_ARs_ob = np.zeros(len(ARs)+1)

# Collects the prolate and oblate values into separate arrays
for i in range(1,len(across_ARs_pro)):
    across_ARs_pro[i] = error_data.iloc[1,2*(i)-2]
    across_ARs_ob[i] = error_data.iloc[1,2*(i)-1]
```

In [21]:
```python
# Plots the prolate and oblate errors against aspect ratio
plt.plot(ARs, across_ARs_pro[1:], color='silver', label='Prolate')
plt.plot(ARs, across_ARs_ob[1:], color='silver',\
        linestyle='dashed', label='Oblate')
plt.xlabel('Aspect ratio')
plt.ylabel('% Error')
plt.legend(loc='upper left')
#plt.savefig('aspect_ratio_error', format='eps')
```

`<matplotlib.legend.Legend at 0x7f852e1420d0>`